AGH University of Science and Technology

Faculty of Electrical Engineering, Automatics, Computer Science
and Biomedical Engineering

Doctoral Dissertation in Computer Science

Non-stationary noise estimation in accelerated parallel MRI data

Tomasz Pięciak, M.Sc.

Supervisor: Professor Piotr Augustyniak

Co-supervisor: Santiago Aja-Fernández, Ph.D.
(Universidad de Valladolid, Spain)

Kraków, 2016

Akademia Górniczo-Hutnicza
im. Stanisława Staszica w Krakowie

Wydział Elektrotechniki, Automatyki, Informatyki
i Inżynierii Biomedycznej

Rozprawa doktorska w dyscyplinie Informatyka

Estymacja niestacjonarnego szumu w przyspieszonym równoległym obrazowaniu metodą rezonansu magnetycznego

mgr inż. Tomasz Pięciak

Promotor: Profesor Piotr Augustyniak

Kopromotor: Dr Santiago Aja-Fernández
(Universidad de Valladolid, Hiszpania)

Kraków, 2016

Contents

El autor del presente trabajo quería expresar su agradecimiento al **Dr. Santiago Aja-Fernández** (Universidad de Valladolid, España) así como al **Dr. Gonzalo Vegas Sánchez-Ferrero** (Harvard Medical School, Boston, MA), quienes le introdujeron a la estimación de ruido no estacionario en imagen por resonancia magnética y le enseñaron la relevancia de dicho ámbito en la investigación y la práctica clínica. Ambos mostraron una increíble paciencia y brindaron un gran apoyo frente a las cuestiones examinadas en la tesis, resolviendo multitud de problemas relativos tanto al funcionamiento del código fuente como a otros aspectos técnicos.

Tarnów, 08.05.2016,

Tomasz Pięciak

Acknowledgements

The author of the thesis would like to acknowledge **Santiago Aja-Fernández, Ph.D.** (Universidad de Valladolid, Spain) and **Gonzalo Vegas Sánchez-Ferrero, Ph.D.** (Harvard Medical School, Boston, MA), who introduced the author to non-stationary noise estimation in magnetic resonance imaging and justified the importance of these topics by research and clinical communities. They showed an incredible patience and an outstanding assistance with the problems considered in the thesis, running the codes and solving other technical difficulties.

The author acknowledges **Professor Piotr Augustyniak** for reading the manuscipt and helping with all red tape while registering the thesis.

This work was supported by Ministerio de Ciencia e Innovación (Spain) with research grant TEC2013-44194-P and by AGH University of Science and Technology (Poland) under the faculty research grant No. 15.11.120.494.

The author of the thesis thanks **Karsten Tabelow, Ph.D.** from Weierstrass Institut for Applied Analysis and Stochastics (Berlin, Germany) and **Matteo Maggioni, Ph.D.** from Department of Signal Processing at Tampere University of Technology (Tampere, Finland) for sharing their source codes of noise estimation methods and the assistance with solving technical problems. Author acknowledges also **Alessandro Foi, Ph.D.** from Department of Signal Processing at Tampere University of Technology (Tampere, Finland) for interesting discussion about variance-stabilizing approach at IEEE International Conference on Image Processing 2014 (Paris, France).

The author thanks also **Daniel Argibay Quiñones, Ph.D.** (Universidad de Valladolid, Spain) for a great assistance with the acquisition of *in vivo* brain MRI data.

The author acknowledges **Mrs Jolanta Dziedzic-Grzesik** for reading the manuscript and her valuable comments. The author would like to acknowledge also **Mateusz Komorkiewicz, Ph.D.** and **Miss Joanna Sabik**, who motivated the author to hard work.

Finally, special thanks to all people, who helped the author while staying in Valladolid: **Mr Gonzalo Barrio Arranz**, **Mr Javier Royuela del Val**, **Mr. Iñaki Rabanillo Viloria**, **Beatriz Carramolino-Arranz, Ph.D.** (a great help with accomodation), **Miss Susana Merino Caviedes**, **Ariel Hernan Curiale, Ph.D.**, **Antonio Tristán Vega, Ph.D.**, **Federico Simmross-Wattenberg, Ph.D.**, **Marcos Martin-Fernandez, Ph.D.** and **Diego Martín-Martínez, Ph.D.** (thanks for spending many hours at La Liga matches).

Tarnów, 08.05.2016,

Tomasz Pięciak

Mamie która do samego końca wierzyła w ukończenie pracy.

List of abbreviations

1D-SENSE – one-dimensional SENSE,
2D-SENSE – two-dimensional SENSE,
2D – two-dimensional,
3D – three-dimensional,
χ^2-test – Chi-square Goodness-of-fit Test,
ACS – Auto Calibration Signal,
AD – Anderson-Darling (statistical test),
ALOHA – Annihilating filter based LOw-rank Hankel matrix Approach,
ARC – Autocalibrating Reconstruction for Cartesian imaging,
ASSET – Array Spatial Sensitivity Encoding Technique,
AWGN – Additive White Gaussian Noise,
BM3D – Block-matching and 3D (filtering),
BM4D – Block-matching and 4D (filtering),
c-χ – central Chi (distribution),
CCD – Charge-coupled Device,
CDF – Cumulative Distribution Function,
CI – Confidence Interval,
CINE – Cinematographic (cardiac imaging),
CMS – Composite Magnitude Signal,
CNR – Contrast-to-Noise Ratio,
db7 – Daubechies7 (wavelet),
DC – Direct Current,
DCT – Discrete Cosine Transformation,
DFT – Discrete Fourier Transform,
DKI – Diffusion Kurtosis Imaging,
DTI – Diffusion Tensor Imaging,
DWI – Diffusion-weighted Imaging,
EM – Expectation-Maximization,

EPI – Echo Planar Imaging,
FFE – Fast Field Echo,
FFT – Fast Fourier Transform,
FGRE – Fast Gradient Echo,
FSPGR – Fast Spoiled Gradient Echo,
FPGA – Field-Programmable Gate Array,
fMRI – functional Magnetic Resonance Imaging,
FOV – Field of View,
GPU – Graphics Processing Unit,
GRAPPA – GeneRalized Autocalibrating Partially Parallel Acquisition,
HARDI – High Angular Resolution Diffusion Imaging,
HH – High-High (subband),
INU – Intensity Non-Uniformity,
i.i.d. – Independent and identically distributed (data),
LL – Low-Low (subband),
LMMSE – Linear Minimum Mean Square Error (estimator),
LPF – Low-Pass Filter,
MAD – Median Absolute Deviation,
MAP – Maximum a Posteriori (estimator),
mSENSE – modified SENSE,
ML – Maximum Likelihood (estimator),
MR – Magnetic Resonance,
MRI – Magnetic Resonance Imaging,
nc-χ – noncentral Chi (distribution),
nc-χ^2 – noncentral Chi-square (distribution),
NLM – Non-local Means,
NMR – Nuclear Magnetic Resonance,
OLS – Ordinary Least Squares,
PCA – Principal Component Analysis,
PD – Proton Density,
PDF – Probability Density Function,
POCS – Projection-onto-convex-sets,
PROBER – Parallel MRI Reconstruction using B-spline Approximation,
QQ – Quantile-Quantile (plot),
RE – Relative Error,

RF – Radiofrequency (pulse),
RV – Random Variable,
RSPIRiT – Robust SPIRiT,
SAR – Synthetic Aperture Radar,
SENSE – SENSitivity Encoding,
SMASH – SiMultaneous Acquisition of Spatial Harmonics,
SMF – Spatial Matched Filter,
SNR – Signal-to-Noise Ratio,
SoS – Sums of Squares,
SPACE RIP – Sensitivity Profiles From an Array of Coils
– for Encoding and Reconstruction in Parallel,
SPIRiT – iTerative Self-consistent Parallel Imaging Reconstruction,
SWT – Stationary Wavelet Transformation,
TFE – Turbo Field Echo,
TE – Echo Time,
TSE – Turbo Spin Echo,
TR – Repetition Echo,
VAR – VARiance,
VST – Variance-stabilizing Transformation,
WLS – Weighted Least Squares.

Notations

The notations included in this section mainly refer to the contribution part of the thesis. The most important and frequently used symbols in this work are presented. Since many other symbols are defined in the thesis, especially in background chapters, we decided not to include them all in this section. The symbols introduced in the background chapters are mainly employed to explain the methods and algorithms, and they are usually not used anymore in the remaining part of the thesis. The notation is kept to be uniform for the whole manuscript as far as it is possible.

A_T – noncentrality parameter (Rician/nc-χ distribution),
$A_T(\mathbf{x})$ – noncentrality parameter (non-stationary Rician/nc-χ distribution),
$\mathbb{E}\{\cdot\}$ – expectation operator,
${}_1F_1(\cdot,\cdot,\cdot)$ – confluent hypergeometric function of the first kind,
FOV_x, FOV_y – sizes of the FOV,
H_0 – null hypothesis in statistical tests,
H_1 – alternative hypothesis in statistical tests,
$I_k(\cdot)$ – modified Bessel function of the first kind and $k-$th order ($k \geqslant 0$),
$J(\cdot,\cdot)$ – the functional being optimized to achieve a robust version of VST (Rician/nc-χ distribution),
L – number of receiver coils,
$L_{\mathrm{eff}}(\mathbf{x})$ – effective number of receiver coils,
$\mathrm{LPF}_{\sigma_{\mathrm{f}}}\{\cdot\}$ – low-pass filtering procedure (used in the homomorphic filter),
M – real-valued Rician RV (a realization of Rician distributed RV),
M_L – real-valued nc-χ RV (a realization of nc-χ distributed RV),
$M(\mathbf{x})$ – non-stationary Rician distributed RV (noisy image),
$M_L(\mathbf{x})$ – non-stationary nc-χ distributed RV (noisy image),
$\widetilde{M}(\mathbf{x})$, $\widetilde{M_L}(\mathbf{x})$ – variance-stabilized noisy images $M(\mathbf{x})$ and $M_L(\mathbf{x})$,
$\widetilde{M_{\mathrm{C}}}(\mathbf{x})$, $\widetilde{M_{L_{\mathrm{C}}}}(\mathbf{x})$ – centered versions of the stabilized noisy images $\widetilde{M}(\mathbf{x})$ and $\widetilde{M_L}(\mathbf{x})$,

$\mathcal{N}(0,1)$ – standard normal distribution,

$\mathcal{N}(0,\sigma^2)$ – Gaussian distributed noise component with zero mean and the variance σ^2,

$N_{\mathrm{re}}(\mathbf{x})$, $N_{\mathrm{im}}(\mathbf{x})$ – Gaussian distributed noise components $\mathcal{N}(0,\sigma^2(\mathbf{x}))$ real and imaginary parts, respectively,

$\mathcal{S}$ – structuring element (used in morphological operations),

SNR – SNR level (stationary Rician/nc-χ distribution),

$\mathrm{SNR}(\mathbf{x})$ – SNR map of the image $M(\mathbf{x})$,

$\mathrm{SNR}_{M_L}(\mathbf{x})$ – SNR map of the image $M_L(\mathbf{x})$,

$\mathrm{SNR}_{\mathrm{max}}$ – maximum level of $\mathrm{SNR}(\mathbf{x})$ in the foregorund area of the image $M(\mathbf{x})$,

$\mathrm{SNR}_{\mathrm{modified}}(\mathbf{x})$ – modified SNR map (used in the SNR mismatch analysis),

R – number of (repeated) experiments,

$\mathrm{RE}_i(\mathbf{x})$ – relative error of the estimator at $i-$th repetition of the experiment,

$\mathrm{RE}(\mathbf{x})$ – (averaged) relative error of the estimator along the replicas,

$\overline{\mathrm{RE}}$ – spatially averaged $\mathrm{RE}(\mathbf{x})$,

$\mathrm{Var}\{M\}$ – the variance of Rician RV,

$\mathrm{Var}\{M|A_T,\sigma\}$ – the conditional variance of Rician RV,

$\mathrm{Var}\{f_{\mathrm{stab}}(M|\sigma)\}$ – the variance of stabilized Rician RV,

$\mathrm{Var}\{M_L^2\}$ – the variance of squared nc-χ RV,

$\mathrm{Var}\{M_L^2|A_T,\sigma,L\}$ – the conditional variance of squared nc-χ RV,

$\mathrm{Var}\{f_{\mathrm{stab}}(M_L^2|\sigma,L)\}$ – the variance of stabilized squared nc-χ RV,

$\mathrm{VAR}(\mathbf{x})$ – the variance of the estimator,

$\overline{\mathrm{VAR}}$ – spatially averaged $\mathrm{VAR}(\mathbf{x})$,

$f_{\mathrm{stab}}(M|\sigma)$ – VST (Rician distribution),

$f_{\mathrm{stab}}(M|\sigma,\mathbf{\Theta})$ – parametrized version of VST (Rician distribution)

$f_{\mathrm{stab}}(M|\sigma,L)$ – VST (nc-χ distribution),

$f_{\mathrm{stab}}(M|\sigma,L,\mathbf{\Theta})$ – parametrized version of VST (nc-χ distribution)

j – unit imaginary number ($j^2=-1$),

m_r – $r-$th raw moment of the parametrized VST,

n_b – number of bins (used in χ^2-test),

$p(M|A_T, \sigma)$ – PDF of Rician distributed RV,

$p(M|A_T, \sigma, L)$ – PDF of nc-χ distributed RV,

$p(M_L^2|A_T, \sigma, L)$ – PDF of squared nc-χ distributed RV,

r – reduction factor (SENSE, GRAPPA),

$\mathbf{x}$ – spatial location at the image/noise map ($\mathbf{x} \subset \mathbb{R}^2$),

$\Psi(\mathbf{x})$ – filtered version of variance-stabilized image $\widetilde{M}(\mathbf{x})$
using the bilateral filter,

Ω_Δ – the foreground area of the image,

$\mathbf{\Theta} = (\theta_1, \theta_2)$ – the parameters used in the optimization procedure
of the functional $J\colon \mathbb{R}^2 \mapsto \mathbb{R}$ (Rician/nc-χ distribution),

$\mathbf{\Theta}_{\mathrm{opt}} = (\theta_{1\mathrm{opt}}, \theta_{2\mathrm{opt}})$ – the optimal parameters θ_1 and θ_2,

γ – Euler-Mascheroni constant,

$\eta(\mathbf{x})$ – neighbourhood centered at the pixel $\mathbf{x}$,

$\lambda_1, \lambda_2, \lambda_3$ – the weighting parameters used in the optimization procedure
of the functional $J\colon \mathbb{R}^2 \mapsto \mathbb{R}$,

ρ, $\rho_{i,j}$ – the correlations between $i-$th and $j-$th receiver coils,

σ – the underlying noise level,

$\sigma(\mathbf{x})$ – spatially variant noise map (non-stationary Rician distribution),

$\sigma^2_{\mathrm{eff}}(\mathbf{x})$ – spatially variant (effective) noise variance map
– (non-stationary nc-χ distribution),

$\sigma_0(\mathbf{x})$ – the initial noise map $\sigma(\mathbf{x})$,

$\sigma^2_l(\mathbf{x})$ – the variance of the noise at $l-$th receiver coil,

$\widehat{\sigma(\mathbf{x})}$, $\widehat{\sigma_{\mathrm{eff}}(\mathbf{x})}$ – the estimated noise maps,

$\widehat{\sigma_i(\mathbf{x})}$ – the noise map estimate at $i-$th iteration of the experiment,

$\psi_{\sigma_{\mathrm{g}}}$, $\psi_{\sigma_{\mathrm{r}}}$ – geometric and radiometric distances (used by bilateral filter).

Chapter 1

Introduction

Contents

1.1 Introduction

The magnetic resonance imaging (MRI) is one of the most relevant medical modality, which enables to inspect a human body in a non-invasive way. It allows investigating both the structural and functional properties of the tissues. A typical MRI acquisition is affected by inherent noise, whether a static or dynamic image series is considered. The noise in MRI occurs under different forms including physiological (Triantafyllou et al. 2011, Fratini et al. 2014) and thermal noise also called Johnson-Nyquist noise (Macovski 1996, Aja-Fernández and Tristán-Vega 2013). The physiological noise results from the patient itself (mainly from cardiac and respiratory processes). In this thesis, however, we are interested in thermal noise. It orginates from a stochastic motion of free electrons in the radiofrequency coil and by eddy current losses in the patient, which are inductively coupled to the coil (Henkelman 1985, McVeigh et al. 1985, Macovski 1996).

The thermal noise is one of the most crucial deterioration source in MRI data significantly reducing the quality of the images. Apart from the quality impoverishment of the data, the noise[1] affects further stages of data processing pipeline, e.g., image segmentation and registration procedures (Zhang et al. 2001, Rohde et al. 2005), accuracy of parameter estimation in diffusion tensor imaging (DTI) (Anderson 2001, Tristán-Vega et al. 2012a, Gahm et al. 2014), fiber tracts reconstructions in diffusion tensor tractography (Reichenbach et al. 2014) and accuracy of quantitative parameters in cardiovascular imaging (Sandino et al. 2015). Furthermore, the disturbed MRI data sets might have even more serious consequences in a diagnostic performance of the image-derived metrics like signal-to-noise ratio (SNR) and contrast-to-noise ratio (CNR) (Yu et al. 2011), or a precise evaluation of tumour tissues (Dikaios et al. 2014).

---

[1] For the sake of simplicity we will henceforth use the term *noise* referring to thermal noise.

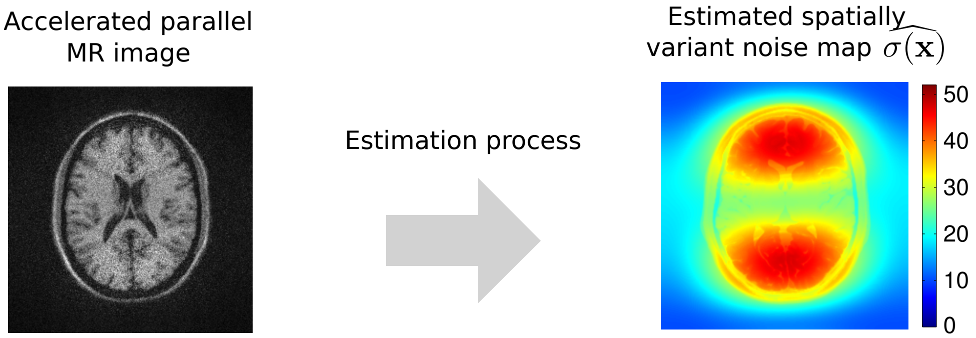

Figure 1.1: Spatially variant noise estimation from a single accelerated parallel MR image.

Typically, the noise is assumed to be homogeneous in single-coil acquisitions (Aja-Fernández et al. 2008, Aja-Fernández et al. 2009, Pieciak 2014). We refer to this kind of noise as a *stationary* noise, since the variance of the noise is assumed not to change with the position in the reconstructed magnitude MRI data. Over the last decade multiple-coil scanners have systematically been replacing single-coil devices. The main reason behind this is to improve the SNR of the magnitude MR image, while keeping a large field-of-view (FOV) (Constantinides et al. 1995, Constantinides et al. 1997). Another potential possibility of the multiple-coil system is to speed-up the acquisition. This is especially important feature for breath-hold cinematographic (CINE) cardiac imaging and diffusion-weighted imaging (DWI) of fibrous tissues like white matter of the brain or spinal cord.

Nowadays, however, more sophisticated accelerated parallel image reconstruction techniques like SENSE (SENSitivity Encoding) (Pruessmann et al. 1999) or GRAPPA (GeneRalized Autocalibrating Partially Parallel Acquisition) (Griswold et al. 2002) have been commonly used in clinical and research practices. These modalities collect the MR signal not only in a parallel fashion, but they also subsample raw MRI data. Specifically, these techniques enable to reconstruct the final MR image from partial information acquired by each receiver coil. This improvement over multiple-coil acquisitions significantly reduces acquisition time and consequently raises the patient comfort. For accelerated parallel MRI techniques the stationarity of the noise can no longer be assumed (Aja-Fernández et al. 2011, Aja-Fernández et al. 2014a, Aja-Fernández et al. 2014b). This means that the noise is not represented by a single value like in single-coil acquisitions, but it is now a non-stationary process and it changes over the FOV.

This PhD thesis concerns the comprehensive statistical modelling of the noise in accelerated parallel MRI acquisitions. Since the noise component in magnitude data obtained from SENSE MRI and GRAPPA MRI cannot simply be assumed as additive white Gaussian process, there is a clear and urgent need to use advanced statistical models, which take signal-dependency and non-stationarity of the noise into account. The non-stationary Rician and non-stationary noncentral Chi (nc-χ) models became the fundamental part of modern adaptive noise-driven digital image processing tools in accelerated parallel MRI as they show considerable effectiveness improvements of the algorithms over Gaussian models.

In this thesis, the author proposes a new theoretical framework to deal with non-Gaussian distributed signals using variance-stabilizing transformations (VSTs). The VST changes a signal-dependent nature of non-Gaussian noise into a signal-independent one. To put it differently, the noise component in variance-stabilized data might be considered as additive white Gaussian noise. Consequently, complicated non-Gaussian models or empirical corrections to Rician/nc-χ distributions are no longer necessary as they can be replaced by calculations in variance-stabilized domain of the image.

The statistics-oriented thinking about the noise leads to the key application of the proposed VST in context of non-stationary signal-dependent noise estimation. In this thesis, we focus on the estimation of noise patterns from non-stationary Rician and nc-χ distributed data. As stated in previous paragraph these types of noise can be found in accelerated parallel MRI data like SENSE MRI and GRAPPA MRI. Consequently, **the purpose of this PhD thesis is to retrieve spatially variant noise patterns from accelerated parallel MRI data using only a single image** (see Fig. 1.1).

1.2 Motivation

A proper noise modelling is an inherent task of almost every stage of MRI data processing pipeline. The accurate knowledge about the noise affecting the data can be employed in adaptive image processing procedures (Aja-Fernández et al. 2008, Krissian and Aja-Fernández 2009), SNR/CNR quantifications (Yu et al. 2011) or quality assurance testing of the MRI scanner (Davids et al. 2014). The noise estimation is a particularly desirable procedure for a retrospectively reconstructed magnitude MRI data, where no information about the parameters of the acquisition process is available.

The applications of the estimated noise patterns can be found at different stages of MRI data processing pipeline including:

- image denoising – Adaptive image denoising procedures employ noise estimates to modify the characteristics of the filters. In context of MRI such approaches usually take distributional properties of the signal into account and estimate the underlying noise-free signal, e.g., linear minimum mean square error (LMMSE) estimator (Aja-Fernández et al. 2008, Aja-Fernández et al. 2009, Tristán-Vega and Aja-Fernández 2010), majorize-minimize framework (Varadarajan and Haldar 2015) or maximum likelihood (ML) estimator (He and Greenshields 2009). On the other hand, image processing approaches, like the non-local means filter (Manjón et al. 2010, Tristán-Vega et al. 2012b), utilize the noise estimates to set the strength (intensity) of the filtering process.

- parameter estimation in diffusion tensor (kurtosis) imaging – Although fundamental techniques in diffusion MRI use least squares approach to retrieve the parameters of directionality of water diffusion, more advanced concepts like ML estimator (Veraart et al. 2011, Veraart et al. 2013) or sequential estimator (Casaseca-de-la Higuera et al. 2012) require noise variance to carry out the fitting procedure.

- image segmentation – Image segmentation methods based on mixture models use the noise variance estimates in the expectation-maximization (EM) framework to fit the models to the data, e.g., Rician mixture model (Roy et al. 2012), Gaussian mixture model (Greenspan et al. 2006, Czajkowska and Pietka 2014),

- estimation of diffusion profiles from high angular resolution diffusion imaging (HARDI) – The noise estimates are used to fit a spherical harmonic to the MRI data. This enables to provide a continuous representation of the diffusion profile at each voxel of the data (Tristan-Vega et al. 2010, Varadarajan and Haldar 2015).

1.3 The proved thesis

In this work, the following thesis is defined and proved:

Maps of non-stationary noise generated by parallel MRI reconstruction can be accurately estimated from a single acquisition without any additional information needed.

1.4 Related papers to the author

The author of the thesis contributed to the following journal papers:

1. **Pieciak, T.**, Vegas-Sánchez-Ferrero, G., Aja-Fernández, S., *Non-stationary Rician noise estimation in parallel MRI using a single image: A variance-stabilizing approach*, IEEE Transactions on Pattern Analysis and Machine Intelligence, (Impact factor: 5.781) (Pieciak et al. 2016a) – second review,

2. Aja-Fernández, S., **Pieciak, T.**, and Vegas-Sánchez-Ferrero, G., *Spatially variant noise estimation in MRI: A homomorphic approach.*, Medical Image Analysis, 20(1), 2015, 184–197. (Impact factor: 3.654) (Aja-Fernández et al. 2015b),

and the conference papers:

1. **Pieciak, T.**, Vegas-Sánchez-Ferrero, G., Aja-Fernández, S., *Variance stabilization of noncentral-Chi data: application to noise estimation in MRI*, In: IEEE International Symposium on Biomedical Imaging (ISBI), 2016, 1376–1379. Prague, Czech Republic (Acceptance ratio for oral presentation: 20.5%). (Pieciak et al. 2016b),

2. **Pieciak T.**, *The maximum spacing noise estimation in single-coil background MRI data*, In: IEEE International Conference on Image Processing (ICIP), 2014, 1743–1747. Paris, France (Acceptance Ratio: 43%). (Pieciak 2014).

1.5 The signpost of the thesis

This PhD thesis is divided into two parts: the **background** and the **contributions**. The former part is devoted to presenting basic information about image reconstruction processes in MRI and statistical distributions employed in modelling the noisy data. We also review the state-of-the-art in spatially variant noise estimation in accelerated parallel MRI. In the latter part of the thesis, we demonstrate our contributions to spatially variant noise estimation in accelerated parallel MRI. We evaluate then our proposals using synthetic and real MRI data in comparison with the state-of-the-art algorithms.

Below, we provide the details of each section of the thesis. The following topics are raised in the **the background part** of the thesis:

- **section 2** – In this section, a physical phenomena behind the MRI is presented. Then, we focus on reconstruction processes of the data in single-coil, multiple-coil and accelerated parallel MRI acquisitions particularly with attention to SENSE and GRAPPA.
- **section 3** – This section is devoted to inspecting the statistical models commonly used to represent the data coming from MRI acquisitions. We present the statistical properties of the underlying noise in raw MRI data, and then we investigate how the noise propagates in the image reconstruction pipeline depending on the algorithm used to obtain the magnitude image.
- **section 4** – We provide the most up-to-date review of the state-of-the-art in non-stationary Gaussian, Rician and nc-χ noise estimation algorithms developed for MRI. This analysis will serve us to establish the main drawbacks of current approaches and then verify our proposals in the contribution part of the thesis.

In the **the contribution part**, we investigate the topics:

- **section 5** – The non-stationary Rician noise estimation.
  We derive the numerical transformation within the variance-stabilizing framework for the case of Rician distributed data. We later introduce the spatially variant noise estimation method for non-stationary Rician distributed data employing proposed VST and Gaussian homomorphic filtering process. Finally, our proposal is compared to fourteen state-of-the-art methods estimating the noise patterns from a single MR image and four methods arranging repeated scans.
- **section 6** – The non-stationary nc-χ noise estimation.
  We analytically derive an asymptotic stabilizer for squared nc-χ distributed random variable and we propose a robust numerical model to improve the performance of the asymptotic transformation for low SNRs. Then, we present a spatially variant noise estimation algorithm in the variance-stabilizing framework intended for non-stationary nc-χ distributed data. The comparison is made against five state-of-the-art methods. We additionally show that any Gaussian method can be employed now for spatially variant noise estimation in non-stationary nc-χ data using the proposed variance-stabilizing framework.

Part I

Background

Chapter 2

Image reconstruction in magnetic resonance imaging

Contents

2.1 Introduction

In this chapter, we provide the fundamentals of MRI technique focusing on the nuclear magnetic resonance physical phenomenon. Although the physical aspects of MRI are not used in the contribution part of the thesis, we explain basic physical phenomenon behind the MRI for clarity the information given later in this chapter. We define the magnetic momentum of hydrogen nucleus, which is induced by a nuclear spin and therefore we present the excitation and relaxation phenomena being part of the NMR signal formation.

Then, we focus on image reconstruction algorithms used to obtain the magnitude images from a signal processing perspective. We illustrate reconstruction processes in single-coil and in multiple-coil MRI acquisitions, since their introduction allows us a better understanding the topics connected with accelerated parallel MRI. We focus then on more advanced concepts, i.e., accelerated parallel MRI. We particularly investigate SENSE and GRAPPA methods being two most popular accelerated parallel MRI acquisition techniques in clinical and research communities.

2.2 Nuclear magnetic resonance physical phenomenon

The theoretical foundations of MRI technique has been proposed by Paul C. Lauterbur[1] (Lauterbur 1973) and Sir Peter Mansfield[2] (Mansfield and Grannell 1973). The scientists were honored by the Nobel Prize in *Physiology or Medicine* in 2003 by Karolinska Institutet for "*their discoveries concerning magnetic resonance imaging*". In comparison with X-radiation imaging (X-ray), computed tomography (X-ray CT) and positron emission tomography (PET), the MRI does not use ionizing radiation or radioactive nuclides. This means that MRI scanning is safe for a biological cell provided that the patient and a technician follow MRI safety policies and procedures.

The MRI is based on a nuclear magnetic resonance (NMR) physical phenomenon, which was independently observed by Felix Bloch[3] (Bloch 1946) and Edward Mills Purcell[4] (Purcell et al. 1946). In 1952, the scientists were honored by the Nobel Prize in *Physics* for "*their development of new ways and methods for nuclear magnetic precision measurements*". The NMR phenomenon states that if a sample is placed in a static magnetic field and then it is subjected to a radiofrequency (RF) pulse at the appropriate frequency, the nuclei in that sample absorbs the energy. After the end of the RF pulse, the nuclei generate the signal, which is therefore measured by a receiver coil.

In the context of MRI, we are particularly interested in hydrogen nuclei because their abundance in water and fat – the main components of human body (Berger 2002). The hydrogen nucleus ^1H (a single proton) can be described by four main parameters, namely the mass, electric charge, angular momentum (called spin) and an associated magnetic momentum. The fundamental role in NMR phenomenon plays the magnetic momentum of the proton, which is induced by the nuclear spin.

The NMR phenomenon arises in the external static magnetic field with induction $\mathbf{B}_0$ and the time-varying magnetic field (RF pulse) $\mathbf{B}_1$ (see Fig. 2.1a). Initially, in the absence of the external magnetic field $\mathbf{B}_0$, the magnetic moments (vectors) of the protons are oriented randomly leading to the null net magnetization (Fig. 2.1b). When the external static magnetic field $\mathbf{B}_0$ is applied, the magnetic moments are aligned parallelly or anti-parallelly to the direction of $\mathbf{B}_0$ (Fig. 2.1b). Furthermore, the magnetic moments precess about the axis

---

[1] `http://www.nobelprize.org/nobel_prizes/medicine/laureates/2003/lauterbur-bio.html`

[2] `http://www.nobelprize.org/nobel_prizes/medicine/laureates/2003/mansfield-bio.html`

[3] `http://www.nobelprize.org/nobel_prizes/physics/laureates/1952/purcell-bio.html`

[4] `http://www.nobelprize.org/nobel_prizes/physics/laureates/1952/bloch-bio.html`

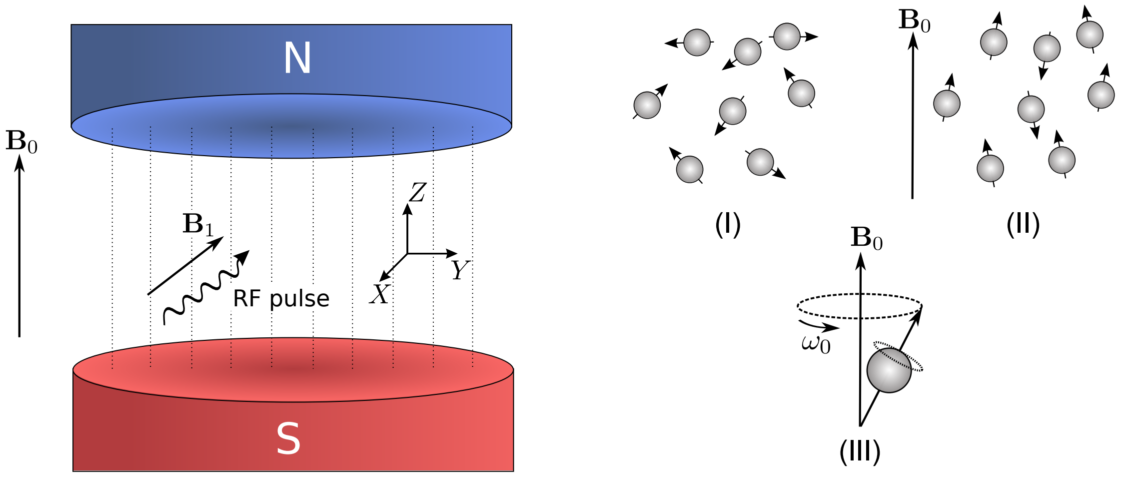

(a) (b)

Figure 2.1: (a) The orientations of the external static magnetic field $\mathbf{B}_0$ and the RF pulse $\mathbf{B}_1$. (b) – (I) Randomly oriented magnetic moments of the protons, (II) parallelly or anti-parallelly to the direction of $\mathbf{B}_0$ oriented magnetic moments, and (III) the precession of an individual magnetic moment about the axis of the magnetic field $\mathbf{B}_0$ with the frequency ω_0.

of the field $\mathbf{B}_0$ with the frequency $\omega_0 = \gamma\,|\mathbf{B}_0|$ (called Larmor frequency), where γ is the gyromagnetic ratio and $|\mathbf{B}_0|$ is the magnitude of the magnetic field $\mathbf{B}_0$ (Fig. 2.1b). In a thermodynamic equilibrium, however, the magnetic moments oriented parallelly to the field $\mathbf{B}_0$ predominate over those oriented anti-parallelly to $\mathbf{B}_0$ and therefore they lead to the net magnetization vector $\mathbf{M}$ pointing along the field $\mathbf{B}_0$ (see Fig. 2.2a). Note although individual magnetic moments precess about the field $\mathbf{B}_0$, the net magnetization vector $\mathbf{M}$ (which is the vector sum of the individual moments) does not precess. This is because magnetic moments are not phase-related with each other and therefore they cancel their phases with each other, when we sum them all up (Hashemi et al. 2012). This net magnetization vector $\mathbf{M}$ can be featured by two components namely longitudinal $\mathbf{M}_\mathrm{z}$ (along $\mathbf{B}_0$) and transverse $\mathbf{M}_\mathrm{xy}$ (orthogonal to $\mathbf{B}_0$):

$$\mathbf{M} = \mathbf{M}_\mathrm{z} + \mathbf{M}_\mathrm{xy}. \tag{2.1}$$

Now, the second magnetic field (RF pulse) $\mathbf{B}_1$[5] is applied perpendicularly to the static magnetic field $\mathbf{B}_0$, i.e., along the x-axis (see Fig. 2.1a). The magnetic moments, which are aligned with the external magnetic field $\mathbf{B}_0$, will start now to precess about the x-axis with the frequency $\omega_1 = \gamma\,|\mathbf{B}_1|$ ($\omega_1 \ll \omega_0$).

Consequently, the net magnetization vector $\mathbf{M}$ flips into the perpendicular to $\mathbf{B}_0$ plane (XY plane) in a spiral motion. The flip angle θ of this change depends on the strength and the duration of the RF pulse (Hashemi et al. 2012). Typically, the flip angle θ is assumed to be $\theta = 90°$ leading the net magnetization vector $\mathbf{M}$ into the XY plane (see Fig. 2.2b). This is because the energy from the RF pulse boosts the protons from lower energy state to the higher energy state and therefore the protons in both states can be equalized (Hashemi et al. 2012). Additionally note that in comparison with the previous state (before the RF pulse), the magnetic moments tend to line up their phases now. Clearly, if the frequency ω of the RF pulse matches the Larmor frequency ω_0 (i.e., $\omega = \omega_0$), the resonance occurs. The hydrogen nuclei absorb the energy and the longitudinal component of the vector $\mathbf{M}$ no longer exist. This process is called *excitation*.

---

[5] While the static magnetic field $\mathbf{B}_0$ is strong (e.g., 1.5T, 3T or even 7T), the second magnetic field $\mathbf{B}_1$ is weak (e.g., 50mT).

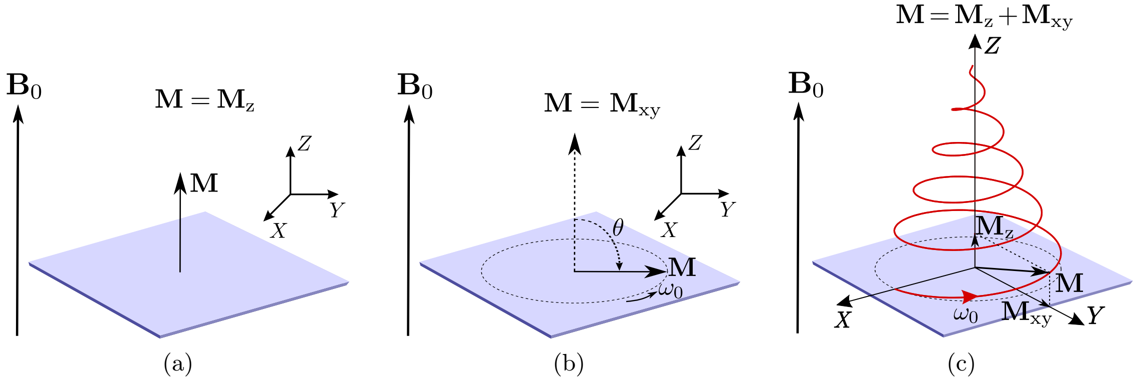

(a) (b) (c)

Figure 2.2: The net magnetization vector $\mathbf{M}$ in the external static magnetic field $\mathbf{B}_0$: (a) the net magnetization vector $\mathbf{M}$ before the RF excitation pulse, (b) the net magnetization vector $\mathbf{M}$ during the RF excitation pulse with flip angle $\theta = 90^\circ$ and frequency ω_0, and (c) the trajectory of the excited magnetization vector $\mathbf{M}$ going towards the equilibrium. The $\mathbf{M}_\mathrm{z}$ and $\mathbf{M}_\mathrm{xy}$ are the parallel and perpendicular to the magnetic field $\mathbf{B}_0$ components of $\mathbf{M}$, respectively.

Once the RF pulse is turned off, the net magnetization vector $\mathbf{M}$ returns to the initial state, i.e., before the excitation (see Fig. 2.2c). The protons go back from their high energy state to the low energy state and they start to get out of the common phase. Consequently, the value of transverse component $\mathbf{M}_\mathrm{xy}$ of the magnetization vector $\mathbf{M}$ decays in time t following the equation:

$$M_\mathrm{xy}(t) = M_0 \mathrm{exp}\left(-\frac{t}{T_2}\right), \tag{2.2}$$

while the value of longitudinal component $\mathbf{M}_\mathrm{z}$ recovers in time t according to the formula:

$$M_\mathrm{z}(t) = M_0\left(1 - \exp\left(-\frac{t}{T_1}\right)\right) \tag{2.3}$$

with T_1 and T_2 being longitudinal and transverse relaxation times, respectively (see Fig. 2.3) and M_0 is the initial value of transverse component $\mathbf{M}_\mathrm{xy}$.

For the sake of considerations in this chapter, we use the first-order Taylor expansion of the net magnetization vector $\mathbf{M}$ (Ying and Liang 2010):

$$M_0 \approx \frac{\gamma^2 h |\mathbf{B}_0| N_s}{4 k_B T_s}, \tag{2.4}$$

where h is the Planck constant divided by 2π, N_s is the total number of polarized protons in the object, k_B is Boltzmann's constant and T_s is the absolute temperature of the object.

2.3 Single-coil acquisition

In this section, we provide basic details about image reconstruction in single-coil devices from a signal processing perspective.

Without going into all the details, the raw MR signal in the $\mathbf{k}$–space domain at the location $\mathbf{k}$ can be modelled using Fourier imaging equation (Sodickson and Manning 1997, Hoge et al. 2005, Ying and Liang 2010):

$$s(\mathbf{k}) = \int_\mathrm{FOV} C(\mathbf{r})\varrho(\mathbf{r}) \exp(-j2\pi\mathbf{k}^T\mathbf{r}) d\mathbf{r}, \tag{2.5}$$

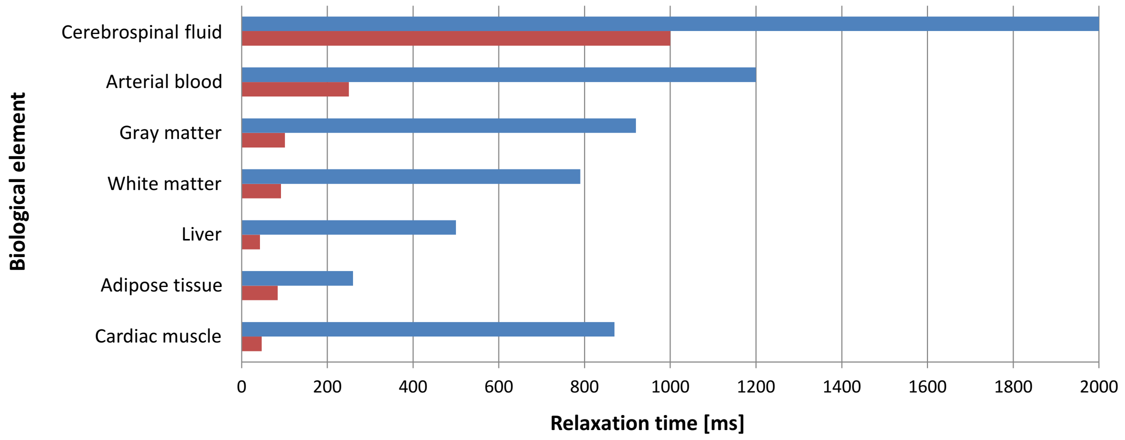

	Cardiac muscle	Adipose tissue	Liver	White matter	Gray matter	Arterial blood	Cerebrospinal fluid
🟦 T_1 [ms]	870	260	500	790	920	1200	2000
🟥 T_2 [ms]	47	84	43	92	101	250	1000

Figure 2.3: Comparison of T_1 and T_2 relaxation time constants in human tissues for $\mathbf{B_0}$ magnetic field of 1.5 T *(based on McRobbie et al. 2003 and Vymazal 2004).*

where $s(\mathbf{k}) = s_{\text{re}}(\mathbf{k}) + j \cdot s_{\text{im}}(\mathbf{k})$ is the acquired complex raw MRI data, $\mathbf{r}$ is the vector referring to the spatial position within the field of view (FOV), $C(\mathbf{r})$ is the coil sensitivity profile at the location $\mathbf{r}$, $\varrho(\mathbf{r})$ is the excited spin density function throughout the FOV and $j^2 = -1$ is the unit imaginary number. The first-order Taylor expansion of the net magnetization vector, M_0 (2.4), recently introduced in section 2.2, is proportional to the excited spin density function $\varrho(\mathbf{r})$ (Ying and Liang 2010):

$$M_0 \propto \int \varrho(\mathbf{r}) d\mathbf{r}. \tag{2.6}$$

For single-coil devices, the same RF coil is responsible for RF signal excitation and MR signal acquisition. The sensitivity profile of that receiver coil is relatively homogeneous over the FOV, i.e., $C(\mathbf{r}) \approx 1$ (Sodickson and Manning 1997). Therefore, the eq. (2.5) can be simplified to:

$$s(\mathbf{k}) = \int_{\text{FOV}} \varrho(\mathbf{r}) \exp(-j2\pi \mathbf{k}^T \mathbf{r}) d\mathbf{r}. \tag{2.7}$$

The goal of the image reconstruction step is to retrieve a spatial representation of the signal $s(\mathbf{k})$, i.e., the equivalent signal $S(\mathbf{x})$ in the $\mathbf{x}$–space domain (Fig. 2.4). To this end, the signal $s(\mathbf{k})$ is assumed to be uniformly sampled on a Cartesian grid (Fig. 2.5a) and then the inverse discrete Fourier transform (DFT) of eq. (2.7) is employed to obtain $S(\mathbf{x})$:

$$S(\mathbf{x}) = \mathcal{F}^{-1}\{s(\mathbf{k})\} = S_{\text{re}}(\mathbf{x}) + j \cdot S_{\text{im}}(\mathbf{x}), \tag{2.8}$$

where $\mathcal{F}^{-1}\{\cdot\}$ is the inverse DFT operator, $S_{\text{re}}(\mathbf{x})$ and $S_{\text{im}}(\mathbf{x})$ are real and imaginary parts of the signal $S(\mathbf{x})$, respectively. In clinical and research scenarios, however, we are particularly interested in magnitude signal rather than its complex representation. To this end, the magnitude information can be easily obtained using the absolute value operator of the complex signal $S(\mathbf{x})$ (2.8) (Henkelman 1985):

$$M(\mathbf{x}) = |S(\mathbf{x})| = \sqrt{S_{\text{re}}^2(\mathbf{x}) + S_{\text{im}}^2(\mathbf{x})}. \tag{2.9}$$

The pipeline of the aforementioned data processing is summarized in Fig. 2.4. Note that we additionally introduced the size of the FOV defined as $\text{FOV}_x \times \text{FOV}_y$ and the size of a single

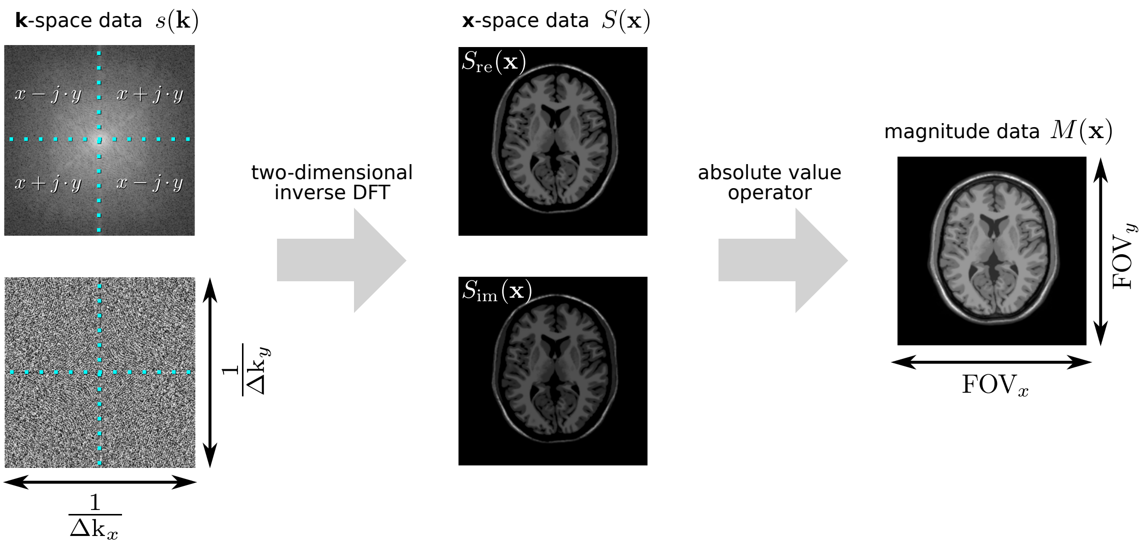

Figure 2.4: Image reconstruction pipeline in single-coil devices. The raw MRI data are represented in $\mathbf{k}$–space domain as a complex image $s(\mathbf{k}) = s_{\mathrm{re}}(\mathbf{k}) + j \cdot s_{\mathrm{im}}(\mathbf{k})$ with $\Delta \mathrm{k}_x$ and $\Delta \mathrm{k}_y$ being pixel sizes in frequency and phase encoding direction, respectively. Then, the two-dimensional inverse DFT operator is applied leading to the $\mathbf{x}$–space domain representation, $S(\mathbf{x}) = S_{\mathrm{re}}(\mathbf{x}) + j \cdot S_{\mathrm{im}}(\mathbf{x})$, and finally, the absolute value operator provides the magnitude image $M(\mathbf{x})$. The parameters FOV_x and FOV_y determine the size of FOV in frequency and phase encoding direction, respectively. To make the scheme more readable, we show log-amplitude image $\log(|s(\mathbf{k})| + 1)$ and phase image $\mathrm{arctg}\left(\frac{s_{\mathrm{im}}(\mathbf{k})}{s_{\mathrm{re}}(\mathbf{k})}\right)$ as the $\mathbf{k}$–space domain representation. The conjugate symmetries of $\mathbf{k}$–space are depicted in log-amplitude image.

pixel given by $\Delta \mathrm{k}_x \times \Delta \mathrm{k}_y$. The size of a single pixel $\Delta \mathrm{k}_x \times \Delta \mathrm{k}_y$ is defined to be a reciprocal of the FOV size, i.e., $\Delta \mathrm{k}_x \times \Delta \mathrm{k}_y = 1/\mathrm{FOV}_x \times 1/\mathrm{FOV}_y$. These parameters will be used at further stages of the thesis[6].

For practical considerations, however, a fast Fourier transform (FFT) is arranged to retrieve the image $S(\mathbf{x})$. Since two-dimensional Fourier transform is linearly separable, multiple one-dimensional Fourier transforms can be arranged here, i.e., along the rows and then along the columns of the image $s(\mathbf{k})$. The complexity of multiple FFTs is defined to be $\mathcal{O}(N^2 \log N)$ rather than $\mathcal{O}(N^4)$ for two-dimensional DFT. Note that Fourier-based approach requires Cartesian sampled data in $\mathbf{k}$–space domain. Nevertheless, other than Cartesian sampling schemes of $\mathbf{k}$–space domain can be employed in the acquisition procedure as well. For this kind of non-Cartesian sampling the Fourier operator will not work. The reconstruction becomes more complicated, since the non-Cartesian measurements must be regridded onto a rectilinear grid prior to the reconstruction step (see Jackson et al. 1991 and Sedarat and Nishimura 2000) or a non-uniform FFT scheme must be applied (Fessler and Sutton 2003).

2.4 Multiple-coil acquisition

In multiple-coil MRI acquisition, the raw data are acquired simultaneously using a phased array system comprised of L receiver coils (Roemer et al. 1990). In comparison to single-coil devices, the intensity profiles of receiver coils are not uniform across the FOV.

In the analogy to eq. (2.5), the fully-sampled raw data in l-th receiver coil ($l = 1, \ldots, L$)

---

[6] Note that we interchangeably use the parameters FOV_x and FOV_y to denote the size of FOV both in centimeters and in pixels depending on the context.

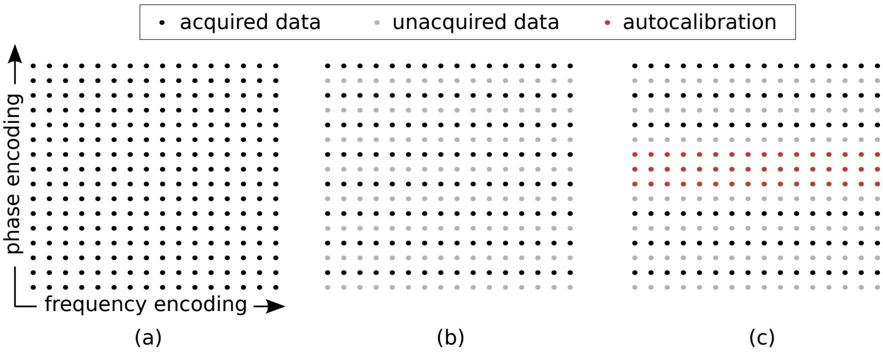

Figure 2.5: The comparison of different coverages of **k**–space domain: (a) fully sampled **k**–space (single-coil and multiple-coil acquisitions), (b) subsampled **k**–space in phase encoding direction with subsampling rate $r = 2$ (SENSE) and (c) subsampled **k**–space in phase encoding direction with subsampling rate $r = 2$ and with acquired autocalibration signal (GRAPPA).

in the **k**-space domain at the location **k** can be modelled as (Wang 2000, Hoge et al. 2005):

$$s_l(\mathbf{k}) = \int_{\text{FOV}} C_l(\mathbf{r})\varrho(\mathbf{r}) \exp(-j2\pi\mathbf{k}^T\mathbf{r})d\mathbf{r}, \tag{2.10}$$

where $s_l(\mathbf{k}) = s_{l_{\text{re}}}(\mathbf{k}) + j \cdot s_{l_{\text{im}}}(\mathbf{k})$ is the complex raw MRI data in the Fourier domain at the location **k**, $C_l(\mathbf{r})$ is a non-uniform sensitivity profile of l-th receiver coil at **r** and $\varrho(\mathbf{r})$ is again the excited spin density function over the FOV. Note that the sensitivity profiles $C_1(\mathbf{x}), \ldots, C_L(\mathbf{x})$ are complementary for each point in the FOV, i.e.,

$$\bigwedge_{\mathbf{x}\in\text{FOV}} \sum_{l=1}^{L} C_l(\mathbf{x}) = \text{const.} \tag{2.11}$$

Since the **k**–space domain is again sampled on a Cartesian grid (see Fig. 2.5a) and **k**–space/**x**–space domains are related with each other by the Fourier transform, we can rewrite eq. (2.10) as follows:

$$s_l(\mathbf{k}) = \int_{\text{FOV}} C_l(\mathbf{x})S(\mathbf{x}) \exp(-j2\pi\mathbf{k}^T\mathbf{x})d\mathbf{x}. \tag{2.12}$$

Then, using a substitution $S_l(\mathbf{x}) = C_l(\mathbf{x})S(\mathbf{x})$ we finally have:

$$s_l(\mathbf{k}) = \int_V S_l(\mathbf{x}) \exp(-j2\pi\mathbf{k}^T\mathbf{x})d\mathbf{x}. \tag{2.13}$$

It is clear now that in multiple-coil systems the image $S_l(\mathbf{x})$ in l-th receiver coil in the **x**–space domain can be modelled as the non-weighted target image $S(\mathbf{x})$ multiplied element-by-element by the sensitivity profile of the receiver coil $C_l(\mathbf{x})$.

Eventually, we apply the inverse DFT to each raw MR image $s_l(\mathbf{k})$ (2.13) leading to the **x**–space domain representation $S_l(\mathbf{x})$:

$$S_l(\mathbf{x}) = \mathcal{F}^{-1}\{s_l(\mathbf{k})\} = S_{l_{\text{re}}}(\mathbf{x}) + j \cdot S_{l_{\text{im}}}(\mathbf{x}) \quad \text{for} \quad l = 1, \ldots, L, \tag{2.14}$$

where $S_{l_{\text{re}}}(\mathbf{x})$ and $S_{l_{\text{im}}}(\mathbf{x})$ are real and imaginary parts of the signal $S_l(\mathbf{x})$, respectively. The general scheme for multiple-coil acquisition is summarized in Fig. 2.6. Note that we still need a reconstruction algorithm to obtain a single magnitude image from the collections of the images $S_1(\mathbf{x}), \ldots, S_L(\mathbf{x})$. Two such approaches are presented in sections 2.4.1 and 2.4.2.

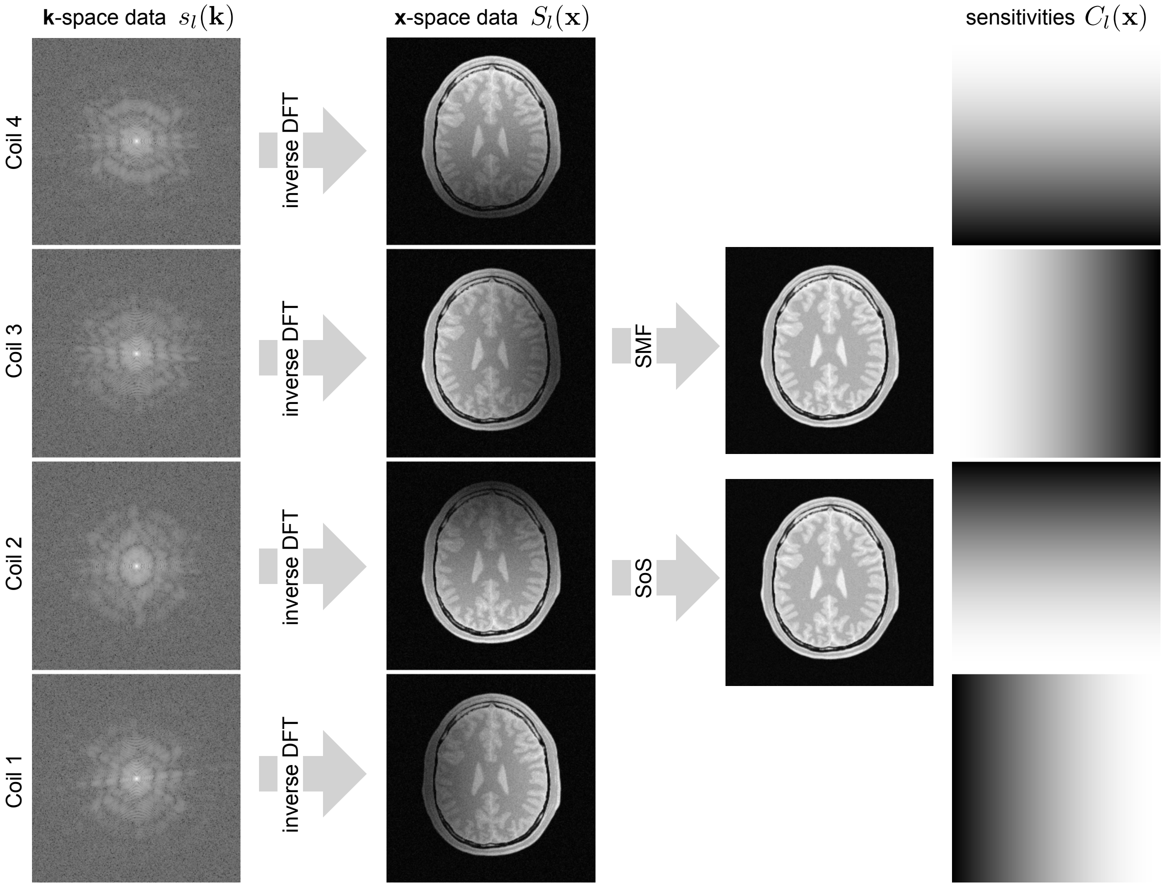

Figure 2.6: Image reconstruction scheme in multiple-coil acquisition for four receiver coils ($L = 4$). The two-dimensional inverse DFT operator is applied to the raw MRI data from each receiver coil $s_l(\mathbf{k})$ individually to obtain $\mathbf{x}$–space domain representation $S_l(\mathbf{x})$ (2.14). Then, the final magnitude image is obtained using either a sum of squares (SoS) formula (2.15) or a spatial matched filter (SMF) approach (2.18–2.19). The SMF approach requires the sensitivity maps $C_l(\mathbf{x})$ to be estimated (right column presents the artificial sensitivities). Finally, note although the representations $s_l(\mathbf{k})$ and $S_l(\mathbf{x})$ are in complex domain, we provide the magnitude images only for the sake of the readability of the scheme, i.e., $\log(|s_l(\mathbf{k})| + 1)$ and $|S_l(\mathbf{x})|$, respectively.

2.4.1 Sum of squares (SoS)

In the most primordial variant, the final composite magnitude signal (CMS) is recovered by means of sums of squares (SoS) procedure aggregating the data from all receiver coils $S_l(\mathbf{x})$ (Roemer et al. 1990, Constantinides et al. 1997, Aja-Fernández and Tristán-Vega 2012):

$$M_L(\mathbf{x}) = \sqrt{\sum_{l=1}^{L} |S_l(\mathbf{x})|^2} = \sqrt{\sum_{l=1}^{L} \left(S^2_{l_{\mathrm{re}}}(\mathbf{x}) + S^2_{l_{\mathrm{im}}}(\mathbf{x})\right)}. \tag{2.15}$$

The key advantage of this simple approach is that it does not require sensitivity profiles of the receiver coils $C_l(\mathbf{x})$ to be known in the reconstruction process.

2.4.2 Spatial matched filter (SMF)

The spatial matched filter (SMF) is another computational technique, which allows for reconstructing the final magnitude image in the $\mathbf{x}$–space domain from the data $S_1(\mathbf{x}), \ldots, S_L(\mathbf{x})$ (Roemer et al. 1990). The method was shown to produce the image with a maximized SNR

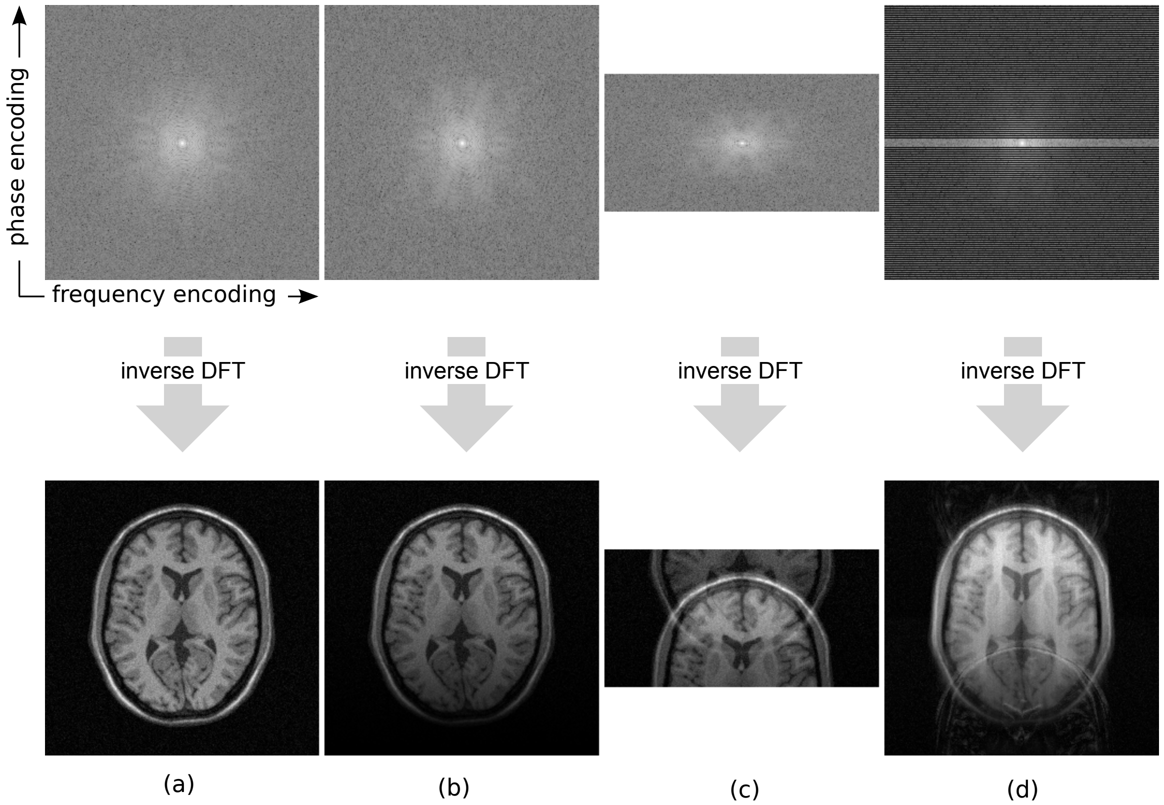

Figure 2.7: The comparison of different image reconstruction schemes in MRI acquisitions: (a) single-coil, (b) multiple-coil, (c) SENSE and (d) GRAPPA.

level, and additionally it enables to take the correlations between receiver coils into account (Walsh et al. 2000). Note that in comparison to SoS, the SMF method requires the sensitivity coils $C_l(\mathbf{x})$ to be known or at least to be estimated.

The SMF linearly combines the complex data from all receiver coils $S_l(\mathbf{x})$ weighted by the sensitivity profiles $C_l(\mathbf{x})$ to retrieve the image $S(\mathbf{x})$. The acquired data $S_l(\mathbf{x})$ and the target image $S(\mathbf{x})$ can be related as follows:

$$S_l(\mathbf{x}) = C_l(\mathbf{x})S(\mathbf{x}) \quad \text{for} \quad l = 1, \dots, L. \tag{2.16}$$

The eqs. (2.16) can be rewritten then in a matrix form:

$$\mathbf{S}(\mathbf{x}) = \mathbf{C}(\mathbf{x})S(\mathbf{x}) \tag{2.17}$$

with $\mathbf{S}(\mathbf{x}) = [S_1(\mathbf{x}), \dots, S_L(\mathbf{x})]^T$ being a $L \times 1$ column vector of acquired data at the location $\mathbf{x}$ and $\mathbf{C}(\mathbf{x}) = [C_1(\mathbf{x}), \dots, C_L(\mathbf{x})]^T$ is a $L \times 1$ column vector of sensitivities of receiver coils. Since we have an overdetermined system of equations (more equations than variables), we resort to the minimization procedure of $\|\mathbf{S}(\mathbf{x}) - \mathbf{C}(\mathbf{x})S(\mathbf{x})\|_2^2$ with $\| \cdot \|_2$ being the 2-norm (Trefethen and Bau III 1997). This can be solved using the ordinary least squares (OLS) formula under Gaussian noise assumptions (Kay 1993):

$$\widehat{S(\mathbf{x})} = \left(\mathbf{C}^*(\mathbf{x})\mathbf{C}(\mathbf{x})\right)^{-1} \mathbf{C}^*(\mathbf{x})\mathbf{S}(\mathbf{x}), \tag{2.18}$$

where $\mathbf{C}^*(\mathbf{x})$ is the conjugate transpose of the matrix $\mathbf{C}(\mathbf{x})$. Eventually, the magnitude image $M(\mathbf{x})$ is obtained using the absolute value operator of $\widehat{S(\mathbf{x})} = \widehat{S_{\text{re}}(\mathbf{x})} + j \cdot \widehat{S_{\text{im}}(\mathbf{x})}$:

$$M(\mathbf{x}) = |\widehat{S(\mathbf{x})}| = \sqrt{\widehat{S^2_{\text{re}}(\mathbf{x})} + \widehat{S^2_{\text{im}}(\mathbf{x})}}. \tag{2.19}$$

Some remarks are worth being made about the SMF method:

1. The algebraic solution (2.18) requires the matrix $\mathbf{C}^*(\mathbf{x})\mathbf{C}(\mathbf{x})$ to be invertible.
2. The estimation procedure (2.18) must be performed for each point of the FOV individually, which might be computationally intensive for large number of receiver coils, e.g., $L \geqslant 64$.
3. The sensitivity maps $C_1(\mathbf{x}), \ldots, C_L(\mathbf{x})$ must be estimated from the data itself or using an additional pre-scan (see e.g., Ling et al. 2014).
4. Finally, since the correlation between receiver coils affect the data as it was demonstrated by Aja-Fernández and Tristán-Vega 2012, the weighted least squares (WLS) formula can be arranged instead of OLS (2.18) (Kay 1993):

$$\widehat{S(\mathbf{x})} = \left(\mathbf{C}^*(\mathbf{x})\mathbf{\Sigma}^{-1}\mathbf{C}(\mathbf{x})\right)^{-1}\mathbf{C}^*(\mathbf{x})\mathbf{\Sigma}^{-1}\mathbf{S}(\mathbf{x}), \tag{2.20}$$

   where $\mathbf{\Sigma}$ is the positive definite covariance matrix.

2.5 Accelerated parallel MRI

In this section, we present accelerated parallel MRI techniques with a particular attention to SENSE and GRAPPA. These two techniques collect the MR signal not only in a parallel fashion, but they also subsample raw data in the **k**–space domain usually in phase encoding direction (see Fig. 2.5b, c and Fig. 2.7). The fundamental differences between SENSE and GRAPPA are the following:

- SENSE – applies inverse DFT operator to each subsampled **k**–space raw image individually, and then, it reconstructs the final image from **x**–space equivalents (reconstruction in **x**–space domain),
- GRAPPA – reconstructs images in **k**–space domain from subsampled **k**–space raw images, and then, it applies the inverse DFT operator to each reconstructed image individually (reconstruction in **k**–space domain).

Our attention in this thesis is particularly held on SENSE and GRAPPA imaging, and it arises directly from a distinctive MRI community interest in these modalities. Over the last decade, SENSE and GRAPPA reconstructions became *de facto* standard in most accelerated parallel MRI acquisitons[7]. Up till now, multifarious SENSE-derived and GRAPPA-derived imaging techniques confirm their serviceableness and wide clinical applicability including functional MRI (fMRI) analysis (Moeller et al. 2010), high-resolution diffusion tensor imaging (DTI) (Heidemann et al. 2012, Jeong et al. 2013) and real-time cardiac imaging (Feng et al. 2013). Although new modifications of SENSE and GRAPPA are still emerging in the literature (see some recent advances in this field in Aja-Fernández et al. 2015a and Muckley et al. 2015), the meticulous details and differences between them are beyond the scope of this thesis. Nevertheless, we refer the reader to the papers by Hoge and Brooks 2006 and Uecker et al. 2014, which clarify the relations and complementarities between SENSE and GRAPPA.

---

[7] The MRI vendors commonly provide their own modifications of SENSE and GRAPPA algorithms (Brau 2007, PhilipsHealthcare 2012). For instance, the SENSE algorithm is implemented in MRI scanners from Philips Healthcare (called dS-SENSE), Siemens Healthcare (mSENSE – modified SENSE) and General Electric Healthcare (ASSET – Array Spatial Sensitivity Encoding Technique), while GRAPPA is used by General Electric Healthcare (ARC – Autocalibrating Reconstruction for Cartesian imaging) and Siemens Healthcare.

2.5.1 SENSitivity Encoding (SENSE)

In this section, we present SENSE imaging algorithm in Cartesian coordinates usually referred as Cartesian SENSE. In SENSE method, the **k**–space domain is typically subsampled in phase encoding direction. The subsampling in **k**–space domain causes aliasing artifacts in spatial domain of the image along the subsampled direction (Pruessmann et al. 1999, Aja-Fernández et al. 2014a) (see Fig. 2.7c). The SENSE algorithm corrects these artifacts providing a full FOV image, which aggregates the information from all receiver coils (with reduced FOVs) and sensitivity profiles.

Let us assume now that $s_l^{\mathcal{S}}(\mathbf{k})$ is the subsampled signal (2.10) in phase encoding direction given the subsampling rate r $(1 < r < L)$. The inverse DFT-reconstructed equivalent $S_l^{\mathcal{S}}(\mathbf{x})$ in the $\mathbf{x}$–space domain (with reduced FOV) at the location $\mathbf{x} = (x, y)$ is represented then as follows (Blaimer et al. 2004, Larkman and Nunes 2007):

$$S_l^{\mathcal{S}}(x, y) = \sum_{i=1}^{r} C_l\left(x, y_i\right) S^{\mathcal{R}}\left(x, y_i\right) \quad \text{for} \quad l = 1, \ldots, L, \tag{2.21}$$

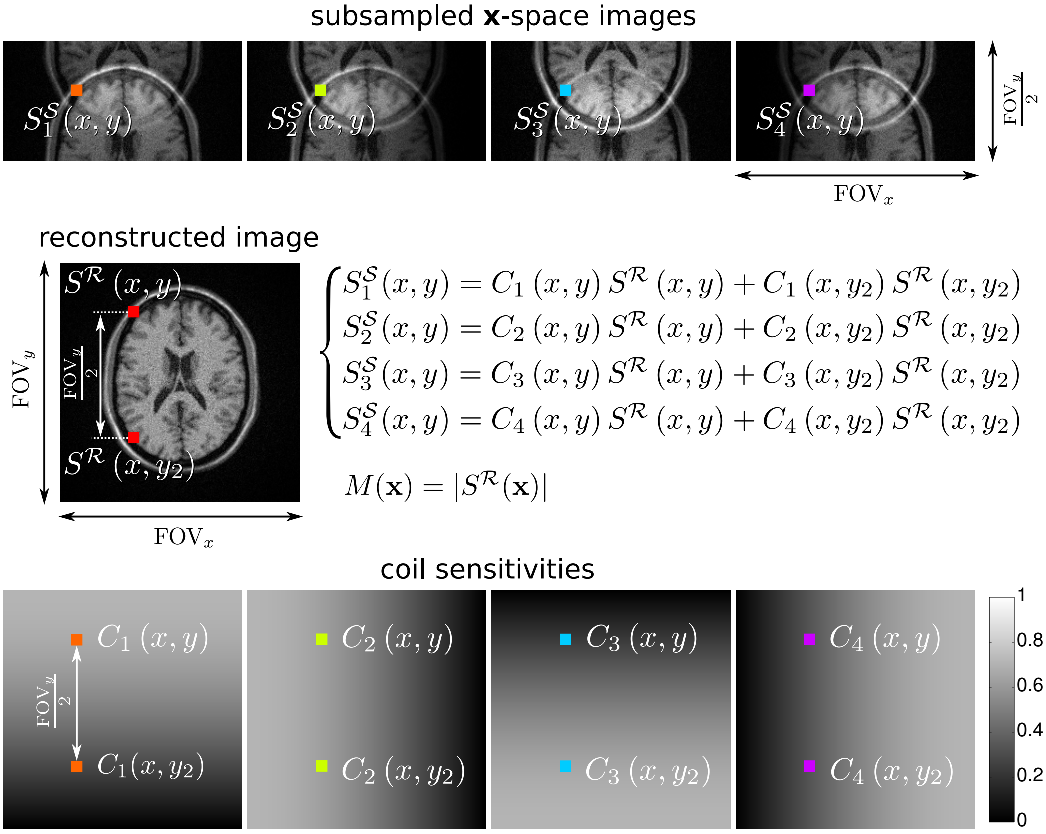

Figure 2.8: The graphical explanation of Cartesian SENSE reconstruction procedure using four receiver coils ($L = 4$) and the subsampling rate $r = 2$. Subsampling in phase encoding direction decreases the FOV size FOV_y by two and additionally it causes aliasing artifacts in the subsampled direction in the $\mathbf{x}$–space domain images $S_l^{\mathcal{S}}(x, y)$. Two red pixels of the reconstructed image $S^{\mathcal{R}}(x, y)$ are unfolded using coil sensitivity profiles $C_l(x, y)$ (the points are marked using orange, green, blue and purple, respectively) and the corresponding folded pixels $S_l^{\mathcal{S}}(x, y)$. For the sake of readability of the figure, we used the coordinates (x, y) instead of (x, y_1) (assume $i = 1$ in eq. (2.22)). Note that the subsampled $\mathbf{x}$–space domain images $S_l^{\mathcal{S}}(x, y)$ and the reconstructed image $S^{\mathcal{R}}(x, y)$ are complex images rather than scalar as it is shown in this scheme.

where $S^{\mathcal{R}}(x, y_1), \ldots, S^{\mathcal{R}}(x, y_r)$ are the pixels of the full FOV image to be reconstructed and (x, y_i) are the coordinates of the unfolded pixels with y_i given by:

$$y_i = y + \frac{\mathrm{FOV}_y}{r}(i-1) \quad \text{for} \quad i = 1, \ldots, r \tag{2.22}$$

with FOV_y being the size of FOV (in pixels) of the reconstructed image $S^{\mathcal{R}}(\mathbf{x})$ in phase encoding direction. A graphical interpretation of Cartesian SENSE using four receiver coils ($L = 4$) and the subsampling ratio $r = 2$ is depicted in Fig. 2.8.

The eqs. (2.21) can be rewritten then in a matrix form:

$$\mathbf{S}^{\mathcal{S}}(\mathbf{x}) = \mathbf{C}(\mathbf{x})\mathbf{S}^{\mathcal{R}}(\mathbf{x}) \tag{2.23}$$

with $\mathbf{S}^{\mathcal{S}}(\mathbf{x}) = \left[S_1^{\mathcal{S}}(x, y), \ldots, S_L^{\mathcal{S}}(x, y)\right]^T$ being a $L \times 1$ column vector of the acquired data at the location $\mathbf{x} = (x, y)$, $\mathbf{S}^{\mathcal{R}}(\mathbf{x}) = \left[S^{\mathcal{R}}(x, y_1), \ldots, S^{\mathcal{R}}(x, y_r)\right]^T$ is a $r \times 1$ column vector representing the pixels from full FOV image to be reconstructed at the locations $(x, y_1), \ldots, (x, y_r)$ and $\mathbf{C}(\mathbf{x})$ is a $L \times r$ matrix representing the sensitivities of receiver coils at the locations $(x, y_1), \ldots, (x, y_r)$:

$$\mathbf{C}(\mathbf{x}) = \begin{bmatrix} C_1(x, y_1) & C_1(x, y_2) & \ldots & C_1(x, y_r) \\ C_2(x, y_1) & C_2(x, y_2) & \ldots & C_2(x, y_r) \\ \vdots & \vdots & \ddots & \vdots \\ C_L(x, y_1) & C_L(x, y_2) & \ldots & C_L(x, y_r) \end{bmatrix}. \tag{2.24}$$

Since we have an overdetermined system, we again resort to WLS procedure under Gaussian noise assumptions (Kay 1993, Pruessmann et al. 1999, Aja-Fernández et al. 2014a):

$$\widehat{\mathbf{S}^{\mathcal{R}}(\mathbf{x})} = \left(\mathbf{C}^*(\mathbf{x})\mathbf{\Sigma}^{-1}\mathbf{C}(\mathbf{x})\right)^{-1}\mathbf{C}^*(\mathbf{x})\mathbf{\Sigma}^{-1}\mathbf{S}^{\mathcal{S}}(\mathbf{x}), \tag{2.25}$$

where $\widehat{\mathbf{S}^{\mathcal{R}}(\mathbf{x})} = \left[\widehat{S^{\mathcal{R}}(x, y_1)}, \ldots, \widehat{S^{\mathcal{R}}(x, y_r)}\right]^T$, $\mathbf{C}^*(\mathbf{x})$ is the conjugate transpose of the matrix $\mathbf{C}(\mathbf{x})$ and $\mathbf{\Sigma}$ is the positive definite covariance matrix of size $L \times L$ defining the correlations between receiver coils (Pruessmann et al. 1999, Aja-Fernández et al. 2014a). Finally, the magnitude image $M(\mathbf{x})$ is recovered using the absolute value operator of the reconstructed image $\widehat{S^{\mathcal{R}}(\mathbf{x})}$:

$$M(\mathbf{x}) = |\widehat{S^{\mathcal{R}}(\mathbf{x})}|. \tag{2.26}$$

Although the estimator (2.25) gives the implicit formula for $S^{\mathcal{R}}(\mathbf{x})$, it can lead to numerical instabilities due to the inherent noise component in the data $S_l^{\mathcal{S}}(\mathbf{x})$ and a bias in estimated coil sensitivity profiles $C_l(\mathbf{x})$. Such instabilities can usually be observed for higher values of subsampling rate r at the center of the FOV and especially for low magnetic fields $\mathbf{B}_0$. Exemplary distortions in the final magnitude image $M(\mathbf{x})$, which was obtained with SENSE algorithm and Turbo Spin Echo (TSE) sequence, are shown in Fig. 2.9.

To improve the results of this ill-conditioned problem some regularization techniques have been proposed (Ying et al. 2004, Liu et al. 2009, Liang et al. 2011, Chaâri et al. 2011). Generally, these regularizations consider the estimation of $S^{\mathcal{R}}(\mathbf{x})$ as a minimization procedure and additionally they take a penalization term in the minimization functional into account:

$$\widehat{\mathbf{S}^{\mathcal{R}}(\mathbf{x})} = \underset{\mathbf{S}^{\mathcal{R}}(\mathbf{x})}{\operatorname{argmin}} \|\mathbf{S}^{\mathcal{S}}(\mathbf{x}) - \mathbf{C}(\mathbf{x})\mathbf{S}^{\mathcal{R}}(\mathbf{x})\|_2^2 + \kappa\|\mathbf{A}(\mathbf{S}^{\mathcal{R}}(\mathbf{x}) - \mathbf{S}_{\mathrm{r}}^{\mathcal{R}}(\mathbf{x}))\|_2^2, \tag{2.27}$$

where $\kappa \in \mathbb{R}_+$ is the regularization parameter to balance the trade-off between the data fidelity term and the penalty (regularization) term, $\mathbf{A}$ is a positive semidefinite matrix

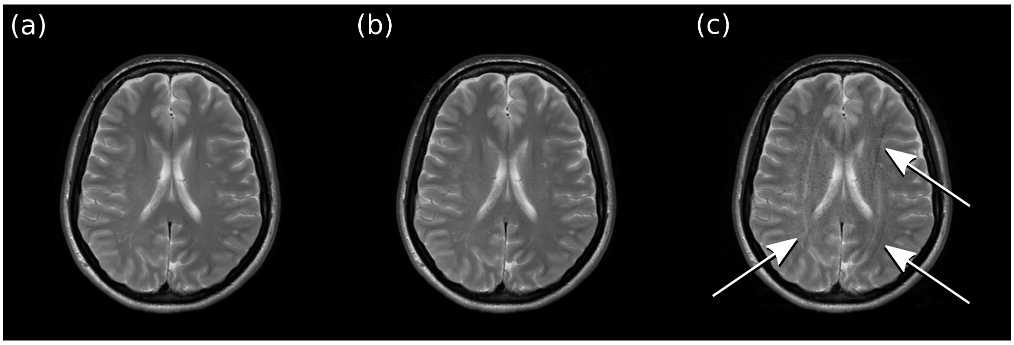

Figure 2.9: The SENSE reconstruction procedure for T_2-weighted TSE sequence with $L = 32$ and different subsampling rates r: (a) no subsampling, (b) $r = 2$ and (c) $r = 4$. The white arrows indicate the artifacts, which are the consequences of numerical instabilities of SENSE algorithm.

and $\mathbf{S}_{\mathrm{r}}^{\mathcal{R}}(\mathbf{x})$ is the prior information about the solution. The parameter κ is usually set heuristically or automatically using the L-curve method (Liu et al. 2009). The regularization methods need a fast convex optimization algorithm to obtain the estimate (2.27), though, the Tikhonov regularization can be expressed in a closed-form formula (Ying et al. 2004).

Finally, some remarks about SENSE are worth making:

1. For Cartesian SENSE, the matrix $\mathbf{C}^*(\mathbf{x})\mathbf{\Sigma}^{-1}\mathbf{C}(\mathbf{x})$ in eq. (2.25) must be nonsingular.
2. Sensitivity profiles of the coils $C_l(\mathbf{x})$ must be identified in order to estimate the full FOV image. They can be obtained from a reference low-resolution pre-scan using a body coil (Pruessmann et al. 1999) or jointly with the image $S^{\mathcal{R}}(\mathbf{x})$ in the estimation procedure (Ying and Sheng 2007). Note, however, that the estimation of the sensitivity profiles becomes a challanging problem especially for abdominal imaging, where a low spin density regions affect the estimation accuracy.
3. Presented SENSE algorithm is also called one-dimensional SENSE (1D-SENSE) as opposed to two-dimensional (2D-SENSE) (Weiger et al. 2002), where the subsampling is performed over two phase-encoding directions of three-dimensional (3D) MRI data.
4. The SENSE reconstruction method has evolved towards different sampling trajectories of the MR signal in the **k**–space domain (Pruessmann et al. 2001, Wright et al. 2014) and the powerful mathematical concept called *compressive sensing*, which takes the advantage of the sparsity of the MR signal (Lustig et al. 2007, Feng et al. 2013). This enables to obtain great results, when recovering the full FOV image, however, the schemes are usually computationally intensive.

2.5.2 GeneRalized Autocalibrating Partially Parallel Acquisition (GRAPPA)

In GRAPPA imaging, the reconstruction process takes place in the **k**–space domain. However, note that additional low-frequency lines sampled at Nyquist rate in the center of the **k**–space domain are acquired as it is shown in Fig. 2.5c. We call these lines auto calibration signal (ACS), since it allows to *calibrate* (identify) the reconstruction parameters used in GRAPPA. Contrary to SENSE imaging, where the size of the FOV in phase encoding direction is reduced by the factor r (i.e., $\mathrm{FOV}_y/2$), here, the missing lines are filled with zeros providing the full FOV image in the **k**–space domain (see Fig. 2.7d).

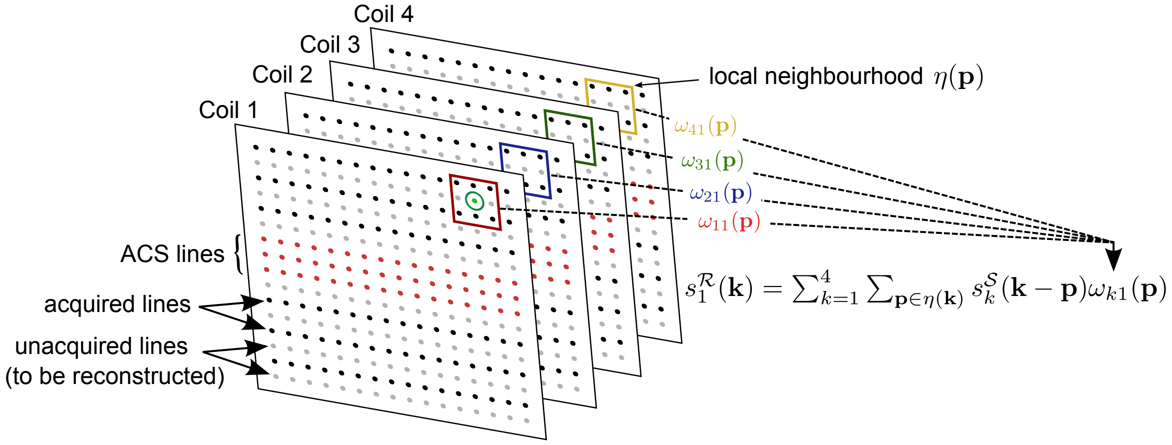

Figure 2.10: The GRAPPA reconstruction scheme for four receiver coils ($L = 4$) and 3×3 local neighbourhoods $\eta(\mathbf{k})$. The reconstruction of a single missing point in the first receiver coil $s_1^{\mathcal{R}}(\mathbf{k})$ (a green dot with a circle) involves a linear combination of the sampled points from local neighbourhoods from all receiver coils $s_k^{\mathcal{S}}(\mathbf{k}-\mathbf{p})$ with corresponding weights $\omega_{k1}(\mathbf{p})$. The scheme is repeated over all missing points in the $\mathbf{k}$–space domain and then over all receiver coils ($k = 1, \ldots, L$).

Let us assume again that $s_l^{\mathcal{S}}(\mathbf{k})$ is the subsampled signal (2.10) in phase encoding direction given the subsampling rate r ($1 < r < L$). In GRAPPA algorithm, the signal $s_l^{\mathcal{S}}(\mathbf{k})$ remains untouched, while the missing data $s_l^{\mathcal{R}}(\mathbf{k})$ are reconstructed using a linear combination of neighbouring points along all receiver coils (Griswold et al. 2002, Aja-Fernández et al. 2015a, Fig. 2.10):

$$s_l^{\mathcal{R}}(\mathbf{k}) = \sum_{k=1}^{L} \sum_{\mathbf{p}\in\eta(\mathbf{k})} s_k^{\mathcal{S}}(\mathbf{k}-\mathbf{p})\omega_{kl}(\mathbf{p}), \tag{2.28}$$

where $s_l^{\mathcal{R}}(\mathbf{k})$ is the reconstructed point in l-th receiver coil at the location $\mathbf{k}$, $\eta(\mathbf{k})$ is a local neighbourhood centered at $\mathbf{k}$ and $\omega_{kl}(\mathbf{p})$ is a (complex) weight being a contribution of the acquired sample $s_k^{\mathcal{S}}(\mathbf{k}-\mathbf{p})$ from k-th receiver coil to $s_l^{\mathcal{R}}(\mathbf{k})$. The eq. (2.28) can be rewritten then using a sum of convolution operators (Breuer et al. 2009):

$$s_l^{\mathcal{R}}(\mathbf{k}) = \sum_{k=1}^{L} s_k^{\mathcal{S}}(\mathbf{k}) \circledast \overline{w}_{kl}(\mathbf{k}), \tag{2.29}$$

where $\overline{w}_{kl}(\mathbf{k})$ is a GRAPPA convolution kernel, which is built upon the coefficients $\omega_{kl}(\mathbf{k})$. Using the convolution theorem, which states that a circular convolution in Fourier domain is equivalent to element-by-element multiplication in spatial domain of the signal, we can further rewrite eq. (2.29) as follows:

$$S_l^{\mathcal{R}}(\mathbf{x}) = \mathrm{FOV}_x \cdot \mathrm{FOV}_y \sum_{k=1}^{L} S_k^{\mathcal{S}}(\mathbf{x}) \odot W_{kl}(\mathbf{x}), \tag{2.30}$$

where the symbol "$\odot$" denotes the Hadamard product of two matrices (i.e., element-by-element multiplication), $S_k^{\mathcal{S}}(\mathbf{x})$ is the $\mathbf{x}$–space equivalent to $s_k^{\mathcal{S}}(\mathbf{k})$ and $W_{kl}(\mathbf{x})$ is the full FOV inverse DFT corresponding to $\overline{w}_{kl}(\mathbf{k})$.

The magnitude image from (2.30) can be obtained using both SoS (2.15) and SMF (2.18–2.19), though, the SoS is used in the orginal implementation of GRAPPA (Griswold et al. 2002). To apply GRAPPA method, however, we still need GRAPPA coefficients $\omega_{kl}(\mathbf{p})$

specified in (2.28). These coefficients can be obtained using the OLS procedure:

$$\sum_{k=1}^{L} S_k^{\mathcal{ACS}}(k_x, k_y - l\Delta k_y) = \sum_{k=1}^{L} \omega_{kl} S_k^{\mathcal{S}}(k_x, k_y), \tag{2.31}$$

where (k_x, k_y) is the position in the $\mathbf{k}$–space (i.e., $\mathbf{k} = (k_x, k_y)$), $S_k^{\mathcal{ACS}}(\mathbf{x})$ are the ACS lines and ω_{kl} is a GRAPPA weight for k-th receiver coil while recovering the missing data in l-th coil (see Fig. 2.10).

Recently, the conventional GRAPPA algorithm was extended towards a non-linear reconstruction (Chang et al. 2012). The method maps the sampled data $s_l^{\mathcal{S}}(\mathbf{k})$ onto a high dimensional feature space and therefore it applies the OLS principle to obtain GRAPPA coefficients ω_{kl}. This procedure can be seen as an extension of the phased array matrix to many additional virtual channels. Latterly, Aja-Fernández et al. 2015a shown that conventional GRAPPA can be significantly improved with almost no additional computational cost by a frequency discrimination in the ACS lines. Specifically, the low-frequency areas of the ACS lines are excluded from the estimation process of the weights ω_{kl}, since their inclusion along with a direct current component may lead to biased weights.

Eventually, some remarks about GRAPPA method are worth making:

1. The formula (2.30) is correct for non-stochastic weights $\omega_{kl}(\mathbf{p})$ only.
2. The conventional GRAPPA method was generalized also to the 3D MRI data undersampled in two phase-encoding directions (Blaimer et al. 2006).
3. The GRAPPA method does not require the sensitivity maps to be estimated. The ACS lines are still required whether a linear or a non-linear combination of the neighbourhoods are used to retrieve the signal $s_l^{\mathcal{R}}(\mathbf{k})$ (2.28).

2.5.3 Other accelerated parallel MRI reconstruction algorithms

In previous two sections, we limited ourselves to present two most crucial accelerated parallel MRI techniques used in clinical and research scenarios, i.e., SENSE and GRAPPA. Certainly, many other approaches were also proposed in the literature like SMASH (SiMultaneous Acquisition of Spatial Harmonics) (Sodickson and Manning 1997), SPACE RIP (Sensitivity Profiles From an Array of Coils for Encoding and Reconstruction in Parallel) (Kyriakos et al. 2000) or PROBER (Parallel MRI Reconstruction using B-spline Approximation) (Petr et al. 2007), however, mostly, they are not so relevant as SENSE and GRAPPA. This is because they generate spatial images with artifacts or low SNR parameter of the data (Blaimer et al. 2004). Another aspect of the algorithms is lack of flexibility to extend them towards a non-Cartesian sampling of the $\mathbf{k}$–space domain or exploit the sparsity of the MR signal.

On the other hand, recent advances in this field like SPIRiT (iTerative Self-consistent Parallel Imaging Reconstruction) (Uecker et al. 2014), ALOHA (Annihilating filter based LOw-rank Hankel matrix Approach) (Jin et al. 2015) or RSPIRiT (Robust SPIRiT) (Peng et al. 2016) enable to significantly improve the results. Nevertheless, they are non-linear techniques and the statistical models of the magnitude data cannot be derived.

Finally, we focus on one technique called PILS (Partially Parallel Imaging With Localized Sensitivities) (Griswold et al. 2000). Contrary to SENSE and GRAPPA, the PILS method assumes that the receiver coils are positioned linearly along the phase encoding direction and their geometrical positions are *a priori* known (see Fig. 2.11). Each receiver coil should have a non-negative sensitivity profile $C_l(\mathbf{x})$ only for a distinct region limited by Y_{C_l}, while it should equal zero elsewhere. The method employs the fact that the subimages are periodically

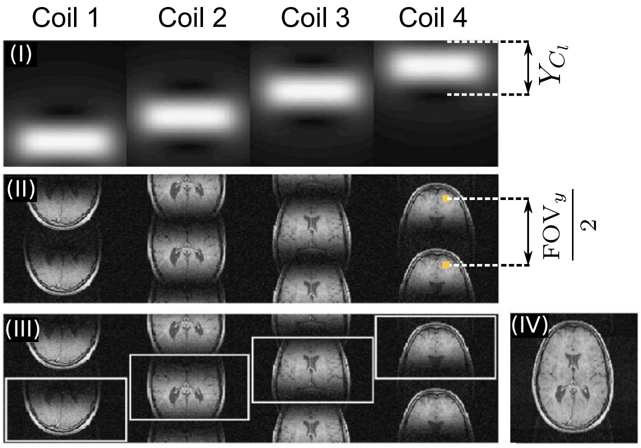

Figure 2.11: The PILS method: (I) sensitivity profiles of the coils $C_l(\mathbf{x})$ positioned along the phase encoding direction and covering distinct regions of size Y_{C_l}, (II) periodically repeated subimages obtained from subsampled data (replicas present every $\mathrm{FOV}_y/2$ pixels), (III) the subimages forming the final image (retrieved using sensitivity profiles $C_l(\mathbf{x})$) and (IV) the final magnitude image obtained using the SoS formula (2.15).

repeated along the phase encoding direction and they are separable as long as $\mathrm{FOV}_y/r > Y_{C_l}$, where r is the subsampling ratio (see Fig. 2.11 for $r = 2$). The subimages are extracted then using element-wise product of sensitivity profiles and the images with replicas. The magnitude image is obtained using the SoS procedure (2.15).

2.6 Conclusions and remarks

In this chapter, we presented the nuclear magnetic resonance physical phenomenon underlie magnetic resonance imaging. We introduced the concept of the net magnetization vector subjected to the time-varying radiofrequency pulse in the external static magnetic field. The changes of net magnetization vector in hydrogen nucleus during the excitation and relaxation phenomena finally lead to the magnetic resonance signal.

The rest part of the chapter is devoted to the explanation of image reconstruction algorithms used in single-coil, multiple-coil and accelerated parallel MRI acquisitions especially SENSE and GRAPPA. Although the chapter is the review over various reconstruction methods, it will be convenient for the reader, while studying the statistical models of the magnitude MRI data.

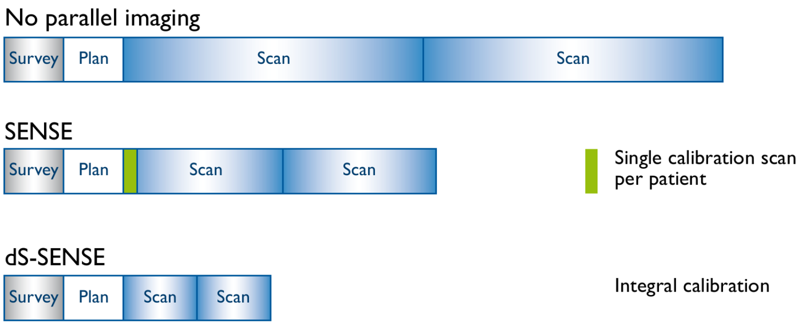

Figure 2.12: Comparison of acquisition times for different variants of MR imaging: no acceleration, SENSE and dS-SENSE (adapted from PhilipsHealthcare 2012).

One can ask if **the accelerated parallel MRI technique really *accelerates* the acquisition?** Actually, it does. However, due to different factors like the calibration procedure of the device or a low-resolution pre-scan the subsampling rate r does not lead to have r times faster acquisition process than the single-coil acquisition. This is depicted in Fig. 2.12, where various procedures are needed, whether we use a single-coil or accelerated parallel MRI acquisition. An exemplary scan times of human brain[8] for different acquisitions using Philips Achieva 3.0T TX device provided with a 32-channel coil system (Philips Medical Systems, Best, the Netherlands) are included in Table 2.1. However, note that we used dS-SENSE accelerated parallel MRI method, which is the brand product of Philips Healthcare. Finally, note that some recent advances in parallel imaging especially for CINE cardiac imaging (e.g., Royuela-Del-Val et al. 2016) enable to subsample the $\mathbf{k}$–space domain using even the acceleration rate of $r = 12$. In Table 2.2, we compared SENSE and GRAPPA accelerated parallel MRI reconstructions schemes presented in this chapter.

Some general remarks about accelerated parallel MRI techniques:

1. SENSE and GRAPPA as opposed to PILS do not require spatially localization of the receiver coils. They can be applied for a coil array both with a linear and a circularly symmetric geometry.
2. Accelerated parallel MRI techniques are not always used to *accelerate* the acquisition. In fMRI with Echo Planar Imaging (EPI) sequence, for instance, they can be arranged to acquire higher resolution data at the expense of time reduction (Chaâri et al. 2011).

Table 2.1: Comparison of the examination times in minutes for various acquisitions with dS-SENSE using Philips Achieva 3.0T TX device (Philips Medical Systems, Best, the Netherlands) with respect to subsampling rate r, Echo Time (TE) and Repetition Echo (TR) of the sequence.

Imaging	Sequence parameters	Slices	No subsampling	$r = 2$	$r = 4$
T_1-weighted	TE=3.7 ms, TR=7.5 ms	54	03:25.9	01:52.9	0:55.9
T_2-weighted	TE=80 ms, TR=3000 ms	50	06:36.0	03:24.0	01:48.0
T_2*-weighted	TE=16 ms, TR=553 ms	50	04:41.2	02:25.1	01:14.2

Table 2.2: Comparison of SENSE and GRAPPA reconstruction techniques.

Method	Reconstruction domain	Additional parameters required to reconstruct the data
SENSE	$\mathbf{x}$–space	sensitivity profiles $C_l(\mathbf{x})$
GRAPPA	$\mathbf{k}$–space	ACS lines $S_l^{ACS}(\mathbf{x})$, reconstruction coefficients $\omega_{kl}(\mathbf{k})$

---

[8] Actually, it the author's brain.

Chapter 3

Statistical modelling of the noise

Contents

3.1 Introduction

In this chapter, we present basic information about the underlying noise in MRI. We introduce various statistical models employed to represent the noise both in **k**–space and **x**–space domains. We are particularly interested in non-stationary Rician and on-stationary noncentral Chi distributed noise since they appear in magnitude data obtained with accelerated parallel MRI techniques. Nevertheless, we start the chapter with the simplest model used in single-coil acquisitions, and then we generalize it to support more advanced concepts.

3.2 Noise in MRI

The variance of the fluctuating noise voltage is proportional to the resistive impedance of the receiver coil and it is defined as follows (Brown et al. 2014; Chapter 15):

$$\sigma^2_{\text{thermal}} \propto 4k_B T_s R_{\text{eff}} B_W, \tag{3.1}$$

where $\sigma^2_{\text{thermal}}$ is the variance of the noise voltage, k_B is Boltzmann's constant, T_s is the absolute temperature of the resistor, R_{eff} is the effective resistance of the coil, and B_W is the bandwidth of the noise-voltage detecting system.

The thermal noise affects the raw data in **k**–space domain and then the noise is propagated to magnitude MRI data according to the reconstruction pipeline. We will explain now how the noise affects the magnitude MRI data assuming different acqusition schemes including single-coil, multiple-coil and accelerated parallel MRI.

3.3 Data distributions in MRI

The noise component in the **k**–space domain in a single-coil of the MRI device is assumed to be Gaussian distributed and it has approximately constant variance over the domain (Henkelman 1985, McVeigh et al. 1985). The noise is then *pro rata* transformed to the **x**–space domain preserving the Gaussianity due to linearity property of the DFT operator (Henkelman 1985, Aja-Fernández et al. 2009). A statistical distribution of the noise in final magnitude MR signal and its stationarity over the FOV, however, strictly depends on the acquisition system configuration and image reconstruction algorithm (Gudbjartsson and Patz 1995, Constantinides et al. 1997, Dietrich et al. 2008, Aja-Fernández et al. 2009, Aja-Fernández et al. 2011, Aja-Fernández and Tristán-Vega 2012, Aja-Fernández and Tristán-Vega 2013, Aja-Fernández et al. 2014b, den Dekker and Sijbers 2014).

For single-coil systems, the magnitude signal $M(\mathbf{x})$ (2.9) follows a stationary Rician distribution (Gudbjartsson and Patz 1995). In the background areas, due to lack of water proton density, the Rician distribution reduces to stationary Rayleigh case (Aja-Fernández et al. 2010). For multiple-coil systems, the distribution of the final magnitude signal depends on employed reconstruction algorithm and correlations between receiver coils. For SoS method (2.15), the magnitude signal $M_L(\mathbf{x})$ follows a noncentral Chi distribution (nc-χ) (Constantinides et al. 1997). However, as it was shown by Aja-Fernández and Tristán-Vega 2012, the nc-χ model must be corrected using the *effective values* to take the correlations between the coils into account. The nc-χ model also simplifies in the background areas of the MR image, i.e., the central Chi distribution (c-χ) is used instead (Aja-Fernández et al. 2009).

For accelerated parallel MRI acquisitions like SENSE or GRAPPA a situation becomes more and more complicated. For Cartesian SENSE imaging, the final magnitude data follows a non-stationary Rician distribution (Aja-Fernández et al. 2014a, Aja-Fernández et al. 2014b), while for Cartesian GRAPPA the magnitude signal obtained with SoS formula can be approximated well enough by a non-stationary nc-χ distribution corrected with the *effective values* (Aja-Fernández et al. 2011). Note that in comparison to single-coil acquisition, where the noise level is assumed to be homogeneous across the FOV, in accelerated parallel MRI, it becomes spatially variant, i.e., it varies across the FOV.

This section is a thorough guide to statistical distributions employed in modelling the magnitude MRI data for different reconstruction methods including single-coil, multiple-coil and accelerated parallel MRI imaging.

3.3.1 Single-coil acquisition

The raw noisy MRI data in the **k**–space domain in single-coil acquisitions can be modelled using additive white Gaussian noise (AWGN) process (Ying and Liang 2010, Aja-Fernández et al. 2009, den Dekker and Sijbers 2014):

$$s(\mathbf{k}) = a(\mathbf{k}) + n(\mathbf{k}; 0, \sigma^2_{\mathcal{K}}), \tag{3.2}$$

where $s(\mathbf{k})$ is the noisy MR signal, $a(\mathbf{k}) = a_{\text{re}}(\mathbf{k}) + j \cdot a_{\text{im}}(\mathbf{k})$ is the noise-free MR signal and $n(\mathbf{k}; 0, \sigma^2_{\mathcal{K}})$ is the complex Gaussian noise component given by:

$$n(\mathbf{k}; 0, \sigma^2_{\mathcal{K}}) = n_{\text{re}}(\mathbf{k}; 0, \sigma^2_{\mathcal{K}}) + j \cdot n_{\text{im}}(\mathbf{k}; 0, \sigma^2_{\mathcal{K}}) \tag{3.3}$$

with $n_{\text{re}}(\mathbf{k}; 0, \sigma^2_{\mathcal{K}})$ and $n_{\text{im}}(\mathbf{k}; 0, \sigma^2_{\mathcal{K}})$ being real and imaginary parts of $n(\mathbf{k}; 0, \sigma^2_{\mathcal{K}})$, respectively. These two components of (3.3) are Gaussian distributed with the expectation value zero and constant variance $\sigma^2_{\mathcal{K}}$ across the **k**–space domain. Formally, we define the components of (3.3) as follows:

$$n_{\text{re}}(\mathbf{k}; 0, \sigma^2_{\mathcal{K}}),\ n_{\text{im}}(\mathbf{k}; 0, \sigma^2_{\mathcal{K}}) \sim \mathcal{N}(0, \sigma^2_{\mathcal{K}}). \tag{3.4}$$

The raw **k**–space data (3.2) is now transformed to the **x**–space domain using inverse DFT operator (2.8). Since the inverse Fourier transform is a linear operator, the **x**–space domain equivalent to (3.2) is also AWGN process:

$$S(\mathbf{x}) = A(\mathbf{x}) + N(\mathbf{x}; 0, \sigma^2_{\mathcal{X}}) \tag{3.5}$$

with $S(\mathbf{x})$ being the noisy MR signal, $A(\mathbf{x}) = A_{\text{re}}(\mathbf{x}) + j \cdot A_{\text{im}}(\mathbf{x})$ being the noise-free MR signal, and $N(\mathbf{x}; 0, \sigma^2_{\mathcal{X}})$ is the complex Gaussian noise component:

$$N(\mathbf{x}; 0, \sigma^2_{\mathcal{X}}) = N_{\text{re}}(\mathbf{x}; 0, \sigma^2_{\mathcal{X}}) + j \cdot N_{\text{im}}(\mathbf{x}; 0, \sigma^2_{\mathcal{X}}), \tag{3.6}$$

where $N_{\text{re}}(\mathbf{x}; 0, \sigma^2_{\mathcal{X}}),\ N_{\text{im}}(\mathbf{x}; 0, \sigma^2_{\mathcal{X}}) \sim \mathcal{N}(0, \sigma^2_{\mathcal{X}})$. The relation between the variance in **k**–space and **x**–space domains is given by the equation (Ying and Liang 2010, Aja-Fernández et al. 2014a):

$$\sigma^2_{\mathcal{X}} = \frac{1}{\text{FOV}_x \cdot \text{FOV}_y} \sigma^2_{\mathcal{K}}, \tag{3.7}$$

where $\text{FOV}_x \cdot \text{FOV}_y$ is the number of pixels in FOV used to calculate the inverse DFT. Now, the data must be reconstructed using the absolute value operator of (3.5). We rewrite the eq. (3.5) in a complex form employing the noise component (3.6):

$$S(\mathbf{x}) = A_{\text{re}}(\mathbf{x}) + N_{\text{re}}(\mathbf{x}; 0, \sigma^2_{\mathcal{X}}) + j \cdot (A_{\text{im}}(\mathbf{x}) + N_{\text{im}}(\mathbf{x}; 0, \sigma^2_{\mathcal{X}})). \tag{3.8}$$

Finally, the magnitude image $M(\mathbf{x})$ is obtained using the absolute operator of (3.8):

$$M(\mathbf{x}) = \sqrt{\left(A_{\text{re}}(\mathbf{x}) + N_{\text{re}}(\mathbf{x}; 0, \sigma^2_{\mathcal{X}})\right)^2 + \left(A_{\text{im}}(\mathbf{x}) + N_{\text{im}}(\mathbf{x}; 0, \sigma^2_{\mathcal{X}})\right)^2}. \tag{3.9}$$

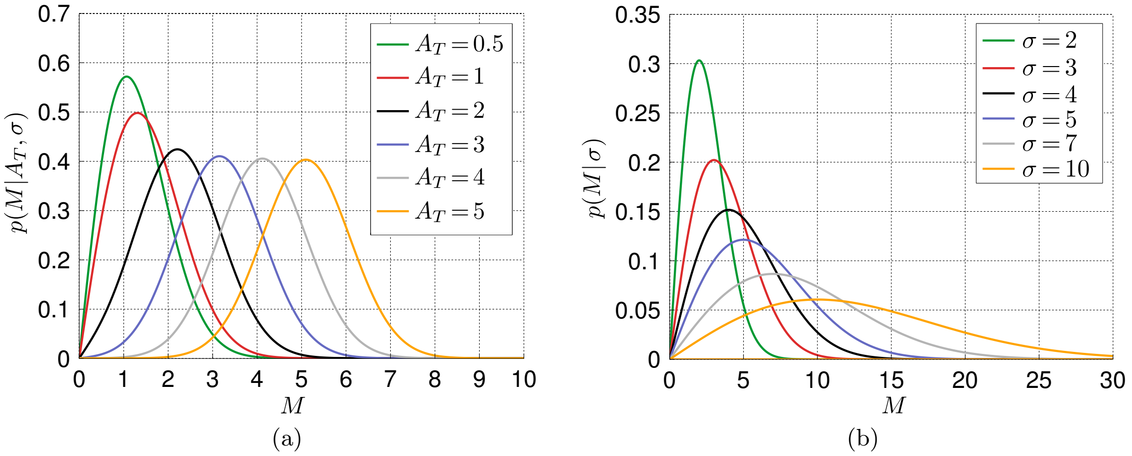

Figure 3.1: Probability density functions of (a) Rician distribution (3.10) and (b) Rayleigh distribution (3.19) for different configuration of distributional parameters. For Rician distribution the parameter σ is set to $\sigma = 1$.

The magnitude MRI data $M = M(\mathbf{x})$ (3.9) follows a stationary Rician distribution with a probability density function (PDF) given by (Rice 1944, Gudbjartsson and Patz 1995; see Fig. 3.1a):

$$p(M|A_T,\sigma) = \frac{M}{\sigma^2}\exp\left(-\frac{M^2+A_T^2}{2\sigma^2}\right) I_0\left(\frac{A_T M}{\sigma^2}\right), \quad M \geqslant 0, \tag{3.10}$$

where $A_T = A_T(\mathbf{x}) = \sqrt{A_{\text{re}}^2(\mathbf{x}) + A_{\text{im}}^2(\mathbf{x})}$ is the envelope of the amplitude signal, $\sigma^2 = \sigma_{\mathcal{X}}^2$ is the underlying noise variance in the $\mathbf{x}$–space domain (σ^2 is assumed to be constant across the FOV), and $I_0(\cdot)$ is the modified Bessel function of the first kind and zeroth order defined as follows (Zwillinger 2014):

$$I_0(x) = \sum_{n=0}^{\infty} \frac{\left(\frac{1}{4}x^2\right)^n}{(n!)^2}, \quad x \in \mathbb{R}_+ \cup \{0\}. \tag{3.11}$$

We can define now the r–th raw moment for Rician distributed random variable (RV) M, i.e., $M \sim \text{Rice}(A_T,\sigma)$:

$$\mathbb{E}\left\{M^r\right\} = \int_0^\infty M^r p(M|A_T,\sigma)dM, \tag{3.12}$$

which becomes then (Sijbers et al. 1998):

$$\mathbb{E}\left\{M^r\right\} = \left(2\sigma^2\right)^{\frac{r}{2}}\Gamma\left(1+\frac{r}{2}\right){}_1F_1\left(-\frac{r}{2};1;-\frac{A_T^2}{2\sigma^2}\right), \tag{3.13}$$

where $\Gamma(\cdot)$ is the gamma function[1]:

$$\Gamma(t) = \int_0^\infty x^{t-1}e^{-x}\,dx \tag{3.14}$$

and ${}_1F_1(\cdot;\cdot;\cdot)$ denotes the confluent hypergeometric function of the first kind:

$${}_1F_1\left(a;b;x\right) = \sum_{n=0}^{\infty}\frac{(a)_n}{(b)_n}\frac{x^n}{n!} \tag{3.15}$$

---

[1] The gamma function reduces to $\Gamma(n) = (n-1)!$ for positive integer n.

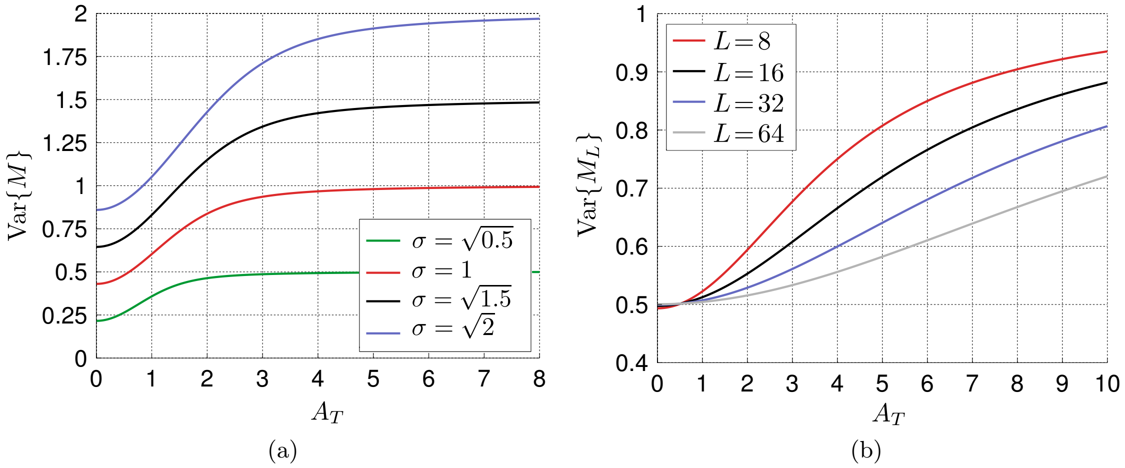

(a) (b)

Figure 3.2: Signal-dependency of the variance operator of the underlying amplitude A_T for (a) Rician and (b) nc-χ distribution with $\sigma = 1$.

with Pochhammer symbol $(\alpha)_n$ defined as follows:

$$(\alpha)_n = \frac{\Gamma(\alpha+n)}{\Gamma(\alpha)} = \prod_{i=0}^{n-1}(\alpha+i). \tag{3.16}$$

From eq. (3.12) we can define the expectation operator $\mathbb{E}\{M\}$ and the variance $\mathrm{Var}\{M\}$ of Rician distributed RV M (den Dekker and Sijbers 2014):

$$\mathbb{E}\{M\} = \sigma\sqrt{\frac{\pi}{2}}\,{}_1F_1\left(-\frac{1}{2};1;-\frac{A_T^2}{2\sigma^2}\right), \tag{3.17}$$

$$\mathrm{Var}\{M\} = A_T^2 + 2\sigma^2 - \frac{\pi\sigma^2}{2}{}_1F_1^2\left(-\frac{1}{2};1;-\frac{A_T^2}{2\sigma^2}\right). \tag{3.18}$$

The variance in Rician distribution is signal-dependent contrary to Gaussian distribution, where the variance is signal-independent parameter. This means that the variance $\mathrm{Var}\{M\}$ strongly depends on the underlying signal amplitude A_T (see Fig. 3.2a). Additionally, note that even-order raw moments in Rician distribution have closed-form analytical solutions as it was shown and effectively used to obtain a linear minimum mean square error (LMMSE) estimator for Rician RV in the milestone paper by Aja-Fernández et al. 2008. The Rician distribution reduces to Rayleigh distribution for $A_T = 0$ (Aja-Fernández et al. 2010). The PDF of Rayleigh distributed RV M is given then by (see Fig. 3.1b):

$$p(M|\sigma) = \frac{M}{\sigma^2}\exp\left(-\frac{M^2}{2\sigma^2}\right),\ M \geqslant 0. \tag{3.19}$$

Both PDFs are defined for non-negative variable M only, i.e., $M \geqslant 0$. To have no doubts: the Rician distribution is used to model the magnitude MRI data in the foreground regions of the image, while the Rayleigh distribution is employed to describe the background areas with lack of water proton density. Finally, since dealing with Rician distribution becomes computationally intensive, a simplification for higher SNR ($\mathrm{SNR} = A_T/\sigma$) was proposed by Gudbjartsson and Patz 1995:

$$p(M|A_T,\sigma) \approx \frac{1}{\sqrt{2\pi\sigma^2}}\exp\left(-\frac{(M-\sqrt{A_T^2+\sigma^2})^2}{2\sigma^2}\right). \tag{3.20}$$

3.3.2 Multiple-coil acquisition

In multiple-coil systems, the noise is processed in a similar fashion to single-coil acquisitions. In what follows, we assume that the raw signal in l–th receiver coil in the $\mathbf{k}$–space domain can be modelled again as the AWGN process (Aja-Fernández et al. 2009, Aja-Fernández and Tristán-Vega 2012):

$$s_l(\mathbf{k}) = a_l(\mathbf{k}) + n_l(\mathbf{k}; 0, \sigma^2_{\mathcal{K}_l}), \quad l = 1, \ldots, L \tag{3.21}$$

with $s_l(\mathbf{k})$ being a noisy MR signal, $a_l(\mathbf{k})$ is the noise-free MR signal and $n_l(\mathbf{k}; 0, \sigma^2_{\mathcal{K}_l}) = n_{l_{\text{re}}}(\mathbf{k}; 0, \sigma^2_{\mathcal{K}_l}) + j \cdot n_{l_{\text{im}}}(\mathbf{k}; 0, \sigma^2_{\mathcal{K}_l})$ is the complex Gaussian noise component (all in l–th receiver coil). After the inverse DFT applied to each signal $s_l(\mathbf{k})$ individually, the additivity and Gaussianity of the noise is still preserved:

$$S_l(\mathbf{x}) = A_l(\mathbf{x}) + N_l(\mathbf{x}; 0, \sigma^2_{\mathcal{X}_l}) \tag{3.22}$$

with $S_l(\mathbf{x})$ being the noisy MR signal, $A_l(\mathbf{x}) = A_{l_{\text{re}}}(\mathbf{x}) + j \cdot A_{l_{\text{im}}}(\mathbf{x})$ being the noise-free MR signal, and $N_l(\mathbf{x}; 0, \sigma^2_{\mathcal{X}_l}) = N_{l_{\text{re}}}(\mathbf{x}; 0, \sigma^2_{\mathcal{X}_l}) + j \cdot N_{l_{\text{im}}}(\mathbf{x}; 0, \sigma^2_{\mathcal{X}_l})$ is the complex Gaussian noise component (all in l–th receiver coil). The relation between the variance in $\mathbf{k}$–space and $\mathbf{x}$–space domains, which is given by the equation (3.7) also holds for multiple-coil acquisition.

While the noise component $N_l(\mathbf{x}; 0, \sigma^2_{\mathcal{X}_l})$ is spatially independent and identically distributed (i.i.d.) over the $\mathbf{x}$–space domain like in a single-coil acquisition, it becomes correlated between the receiver coils. These correlations are defined in the covariance matrix $\mathbf{\Sigma}$ (Aja-Fernández and Tristán-Vega 2012):

$$\mathbf{\Sigma} = \begin{bmatrix} \sigma_1^2 & \sigma_{12} & \ldots & \sigma_{1L} \\ \sigma_{21} & \sigma_2^2 & \ldots & \sigma_{2L} \\ \vdots & \vdots & \ddots & \vdots \\ \sigma_{L1} & \sigma_{L2} & \ldots & \sigma_L^2 \end{bmatrix}, \tag{3.23}$$

where $\sigma_{kl} = \rho_{kl}\sigma_k\sigma_l$ with ρ_{kl} being the coefficient of correlation between k–th and l–th receiver coil and $\sigma_l^2 = \sigma^2_{\mathcal{X}_l}$ is the noise variance in l–th receiver coil. The correlations between receiver coils included in the covariance matrix (3.23) can be obtained using an acquisition without the RF pulse $\mathbf{B}_1$, and then calculated as follows (Chaâri et al. 2011):

$$\sigma_{kl} = \frac{1}{\text{FOV}_x \cdot \text{FOV}_y} \sum_{\mathbf{p} \in \text{FOV}} S_k(\mathbf{p}) S_l^*(\mathbf{p}), \quad \text{for} \quad l, k = 1, \ldots, L. \tag{3.24}$$

Note that if the correlations between the receiver coils are assumed to be zero for all $k \neq l$ and the noise variances are the same for all coils (i.e., $\sigma_k^2 = \sigma_l^2$ for $k \neq l$), the covariance matrix (3.23) is simply given by $\mathbf{\Sigma} = \sigma^2 \mathbf{I}$.

Sum of squares

In SoS reconstruction, the final magnitude image $M_L(\mathbf{x})$ is obtained using the formula (2.15). The combination of squared Gaussian RVs is defined then by the nc-χ distribution with a PDF given by (Aja-Fernández and Tristán-Vega 2012; see Fig. 3.3a):

$$p(M_L | A_T, \sigma, L) = \frac{A_T^{1-L}}{\sigma^2} M_L^L \exp\left(-\frac{M_L^2 + A_T^2}{2\sigma^2}\right) I_{L-1}\left(\frac{A_T M_L}{\sigma^2}\right), \; M_L \geqslant 0, \tag{3.25}$$

where $M_L = M_L(\mathbf{x})$ is the CMS (2.15), $\sigma_l^2 = \sigma^2$ is the underlying noise variance (the same variance for all channels), L is the number of receiver coils, $A_T = A_T(\mathbf{x})$ is the noise-free signal given now by:

$$A_T(\mathbf{x}) = \sqrt{\sum_{l=1}^{L} |A_l(\mathbf{x})|^2} \tag{3.26}$$

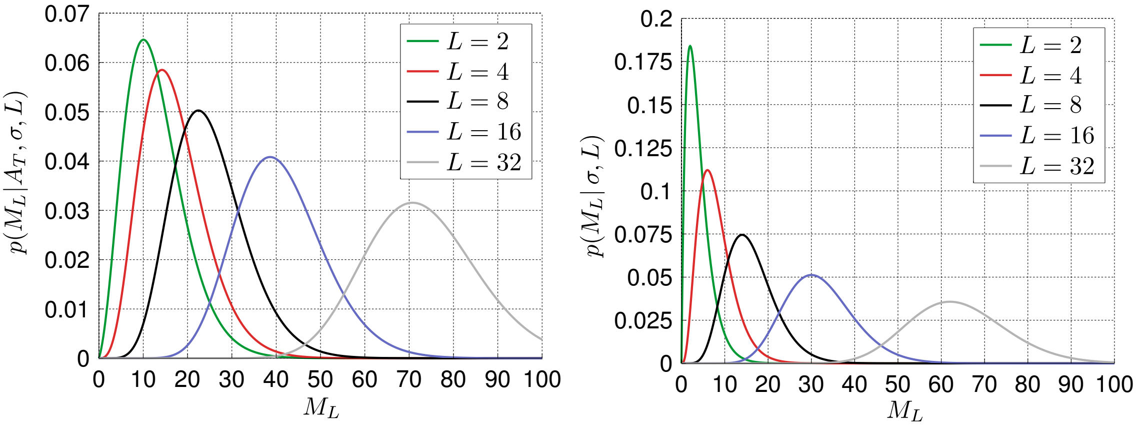

(a) (b)

Figure 3.3: Probability density functions of (a) nc-χ distribution (3.25) and (b) c-χ distribution (3.30) for different values of the parameter L. Other distributional parameters are: (a) $A_T = 3$, $\sigma = 1$ and (b) $\sigma = 1$.

and $I_k(\cdot)$ is the modified Bessel function of the first kind and k–th order (Zwillinger 2014):

$$I_k(x) = \left(\frac{1}{2}x\right)^k \sum_{n=0}^{\infty} \frac{\left(\frac{1}{4}x^2\right)^n}{n!(k+n)!}, \quad x \in \mathbb{R}_+ \cup \{0\}. \tag{3.27}$$

The expectation operator $\mathbb{E}\{M_L\}$ and the variance $\mathrm{Var}\{M_L\}$ of nc-χ distributed RV M_L are defined respectively as:

$$\mathbb{E}\{M_L\} = \sigma\sqrt{2}\,\frac{\Gamma\left(L+\frac{1}{2}\right)}{\Gamma(L)}\,{}_1F_1\left(-\frac{1}{2}; L; -\frac{A_T^2}{2\sigma^2}\right), \tag{3.28}$$

$$\mathrm{Var}\{M_L\} = A_T^2 + 2L\sigma^2 - 2\sigma^2\left(\frac{\Gamma\left(L+\frac{1}{2}\right)}{\Gamma(L)}\right)^2 {}_1F_1^2\left(-\frac{1}{2}; L; -\frac{A_T^2}{2\sigma^2}\right). \tag{3.29}$$

The variance for nc-χ distributed RV is also in the functional dependence of the underlying signal amplitude A_T (see Fig. 3.2b). Again, we refer to the variance (3.29) to be a signal-dependent parameter.

The nc-χ distribution with the PDF (3.25) reduces to c-χ distribution in the background areas, i.e., for $A_T = 0$ (Fig. 3.3b):

$$p(M_L|\sigma, L) = \frac{2^{1-L}}{(L-1)!}\frac{M_L^{2L-1}}{\sigma^{2L}}\exp\left(-\frac{M_L^2}{2\sigma^2}\right), \quad M_L \geqslant 0. \tag{3.30}$$

However, the nc-χ model is biased, when the underlying data $s_l(\mathbf{k})$ are affected by non-zero correlations between the channels, i.e., $\mathbf{\Sigma} \neq \sigma^2\mathbf{I}$. To still use the nc-$\chi$ model, Aja-Fernández and Tristán-Vega 2012 introduced *effective parameters*, which substitute the original values L and σ (see Fig. 3.4):

1. the effective (decreased) number of receiver coils L_{eff}:

$$L_{\text{eff}}(\mathbf{x}) = \frac{A_T^2(\mathbf{x})\mathrm{tr}(\mathbf{\Sigma}) + (\mathrm{tr}(\mathbf{\Sigma}))^2}{\mathbf{A}^*(\mathbf{x})\mathbf{\Sigma}\mathbf{A}(\mathbf{x}) + \|\mathbf{\Sigma}\|_F^2}, \tag{3.31}$$

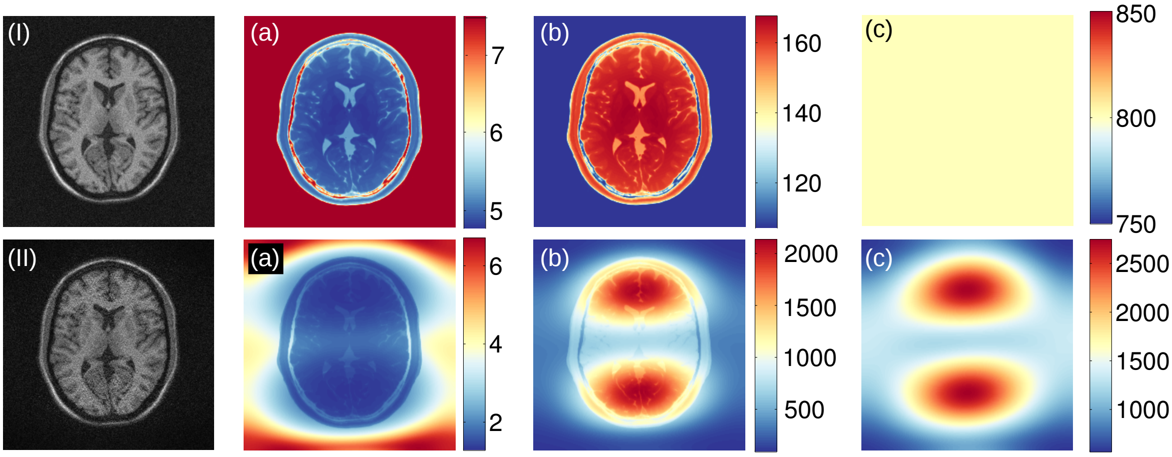

Figure 3.4: Effective parameters for (I) multiple-coil and (II) accelerated parallel GRAPPA MRI acquisition: (a) $L_{\text{eff}}(\mathbf{x})$, (b) $\sigma^2_{\text{eff}}(\mathbf{x})$ and (c) $L_{\text{eff}}(\mathbf{x})\sigma^2_{\text{eff}}(\mathbf{x})$. The image reconstruction parameters are: $L = 8$, $\sigma^2 = 100$, $\rho = 0.1$ and $r = 2$ (GRAPPA only).

2. the effective (increased) variance of noise σ^2_{eff}:

$$\sigma^2_{\text{eff}}(\mathbf{x}) = \frac{\operatorname{tr}(\mathbf{\Sigma})}{L_{\text{eff}}(\mathbf{x})}, \tag{3.32}$$

where $\mathbf{\Sigma}$ is the covariance matrix (3.23), $\operatorname{tr}(\cdot)$ is the trace of a matrix, $\mathbf{A}^*$ is a conjugate vector obtained from $\mathbf{A} = [A_1(\mathbf{x}), \ldots, A_L(\mathbf{x})]^T$ and $\|\mathbf{\Sigma}\|_F$ is the Frobenius norm of the matrix $\mathbf{\Sigma}$ given by:

$$\|\mathbf{\Sigma}\|_F = \sqrt{\sum_{l=1}^{L}\sum_{k=1}^{L} |\sigma_{kl}|^2}. \tag{3.33}$$

Note that the corrections (3.31) and (3.32) are position dependent (i.e., $\sigma^2_{\text{eff}} = \sigma^2_{\text{eff}}(\mathbf{x})$ and $L_{\text{eff}} = L_{\text{eff}}(\mathbf{x})$) and they must be tuned for each point of the image individually (see Aja-Fernández et al. 2013). Furthermore, element-by-element multiplication of these parameters is constant across the FOV, i.e., $L_{\text{eff}}(\mathbf{x})\sigma^2_{\text{eff}}(\mathbf{x}) = \text{const}$ (Fig. 3.4).

3.3.3 Accelerated parallel MRI acquisition (SENSE)

In accelerated parallel SENSE MR imaging, the noise component in the subsampled $\mathbf{k}$–space raw data $s^{\mathcal{S}}_l(\mathbf{k})$ is also assumed to be a stationary complex AWGN process. However, the relation between the variance in the $\mathbf{k}$–space and $\mathbf{x}$–space domain is now given by the formula (Aja-Fernández et al. 2014a):

$$\sigma^2_{\mathcal{X}_l} = \frac{r}{\text{FOV}_x \cdot \text{FOV}_y}\sigma^2_{\mathcal{K}_l} \quad \text{for} \quad l = 1, \ldots, L \tag{3.34}$$

with r being the subsampling rate. The relation (3.34) means that the noise is amplified in the $\mathbf{x}$–space domain and this intensification merely depends on the subsampling rate r.

The noise component $N^{\mathcal{R}}(\mathbf{x}; \sigma^2_{\mathcal{R}}(\mathbf{x}))$ in the reconstructed (complex) image $S^{\mathcal{R}}(\mathbf{x})$ (2.25) becomes spatially variant over the FOV, i.e., a non-stationary complex AWGN process (Aja-Fernández et al. 2014a, Aja-Fernández et al. 2014b):

$$S^{\mathcal{R}}(\mathbf{x}) = A^{\mathcal{R}}(\mathbf{x}) + N^{\mathcal{R}}(\mathbf{x}; 0, \sigma^2_{\mathcal{R}}(\mathbf{x})), \tag{3.35}$$

where $A^{\mathcal{R}}(\mathbf{x})$ is the noise-free amplitude. The Gaussianity of the signal (3.35) comes from the reconstruction step (2.25), i.e., the linear combination of Gaussian distributed signals $S^{\mathcal{S}}_l$.

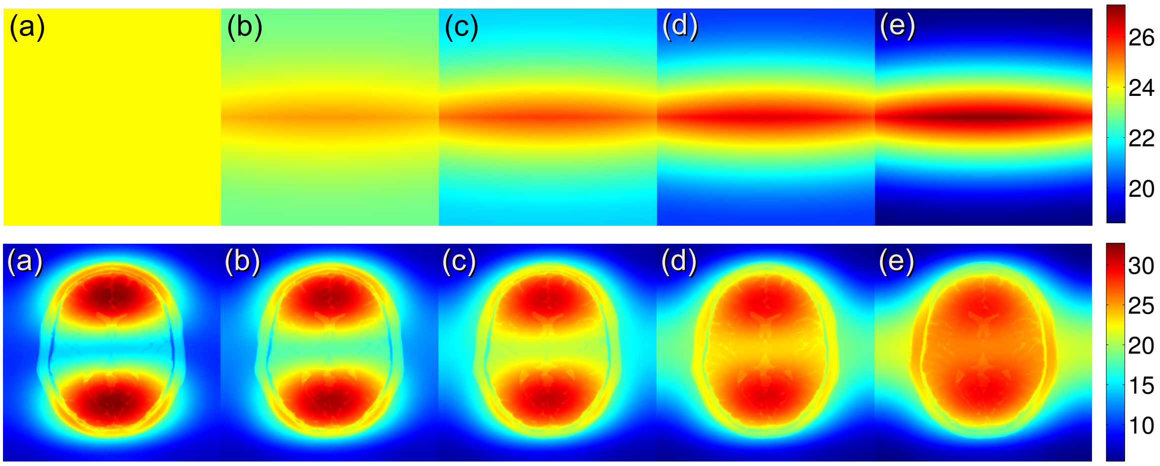

Figure 3.5: The spatially variant noise maps for accelerated parallel SENSE MRI (top row) and GRAPPA MRI with SoS (bottom row) for different correlation ratio between receiver coils: (a) $\rho = 0$, (b) $\rho = 0.1$, (c) $\rho = 0.2$, (d) $\rho = 0.3$ and (e) $\rho = 0.4$. The parameters of the reconstructions are: $L = 8$, $r = 2$ and $\sigma^2 = 100$.

The non-stationarity of the noise in eq. (3.35) arises at the reconstruction stage and it merely depends on correlations between receiver coils comprised in the matrix $\mathbf{\Sigma}$. Furthermore, the greater correlations are, the higher the level of the noise in the reconstructed image and the variability of the map are observed (see Fig. 3.5). In SENSE MR imaging, there also exist spatial correlations between adjacent lines used in the unfolding process of the signal $S^{\mathcal{R}}(\mathbf{x})$, i.e., the sample $S^{\mathcal{R}}(x, y_i)$ is correlated with the remaining samples $S^{\mathcal{R}}(x, y_j)$ for $i \neq j$ (Aja-Fernández et al. 2014b).

The final magnitude image $M(\mathbf{x})$ is recovered by the absolute value of the signal (3.35) as it was presented in section 2.5.1:

$$M(\mathbf{x}) = |S^{\mathcal{R}}(\mathbf{x})|. \tag{3.36}$$

The magnitude data (3.36) follows now a non-stationary Rician distribution with the underlying parameters $A_T(\mathbf{x})$ and $\sigma^2_{\mathcal{R}}(\mathbf{x}) = \sigma^2(\mathbf{x})$, i.e., $M(\mathbf{x}) \sim \text{Rice}(A_T(\mathbf{x}), \sigma(\mathbf{x}))$. The PDF is given then by:

$$p(M(\mathbf{x})|A_T(\mathbf{x}), \sigma(\mathbf{x})) = \frac{M(\mathbf{x})}{\sigma^2(\mathbf{x})} \exp\left(-\frac{M^2(\mathbf{x}) + A_T^2(\mathbf{x})}{2\sigma^2(\mathbf{x})}\right) I_0\left(\frac{A_T(\mathbf{x})M(\mathbf{x})}{\sigma^2(\mathbf{x})}\right), \quad M(\mathbf{x}) \geqslant 0. \tag{3.37}$$

In comparison to eq. (3.10), the underlying noise variance $\sigma^2(\mathbf{x})$ changes over the FOV, i.e., it is position-dependent parameter (Fig. 3.5). We remark that the moments defined in (3.17) and (3.18) also depend on the spatial position even though the image presents the homogeneous region, i.e., the same spin densities are observed for different areas in FOV.

3.3.4 Accelerated parallel MRI acquisition (GRAPPA)

In accelerated parallel GRAPPA MRI, the noise component in the subsampled $\mathbf{k}$–space raw data $s_l^S(\mathbf{k})$ is also assumed to be a stationary complex AWGN process. In a similar fashion to eq. (3.34), we can define the relation between the noise variance in $\mathbf{k}$–space and $\mathbf{x}$–space domains as follows (Aja-Fernández et al. 2014a):

$$\sigma^2_{\mathcal{X}_l} = \frac{1}{r \cdot \text{FOV}_x \cdot \text{FOV}_y} \sigma^2_{\mathcal{K}_l} \quad \text{for} \quad l = 1, \ldots, L. \tag{3.38}$$

Contrary to (3.34), the noise variance is now reduced in the $\mathbf{x}$–space domain. To explain the noise behaviour in GRAPPA MR imaging, let us recall the eq. (2.30):

$$S_l^{\mathcal{R}}(\mathbf{x}) = \mathrm{FOV}_x \cdot \mathrm{FOV}_y \sum_{k=1}^{L} S_k^{\mathcal{S}}(\mathbf{x}) \odot W_{kl}(\mathbf{x}), \tag{3.39}$$

where the symbol "$\odot$" denotes the Hadamard product of two matrices, $S_k^{\mathcal{S}}(\mathbf{x})$ is the $\mathbf{x}$–space equivalent to $s_k^{\mathcal{S}}(\mathbf{k})$ and $W_{kl}(\mathbf{x})$ is the full FOV inverse DFT corresponding to $\overline{w}_{kl}(\mathbf{k})$.

Since the inverse DFT preserves the Gaussianity of the noise, the eq. (3.39) can be rewritten assuming the formula $S_k^{\mathcal{S}}(\mathbf{x}) = A_k^{\mathcal{S}}(\mathbf{x}) + N_k(\sigma_{\mathcal{X}}^2)$ (Aja-Fernández et al. 2011):

$$\begin{aligned} S_l^{\mathcal{R}}(\mathbf{x}) &= \mathrm{FOV}_x \cdot \mathrm{FOV}_y \sum_{k=1}^{L} \left(A_k^{\mathcal{S}}(\mathbf{x}) + N_k(\sigma_{\mathcal{X}}^2)\right) \odot W_{kl}(\mathbf{x}) \\ &= \underbrace{\mathrm{FOV}_x \cdot \mathrm{FOV}_y \sum_{k=1}^{L} A_k^{\mathcal{S}}(\mathbf{x}) \odot W_{kl}(\mathbf{x})}_{\text{Reconstructed signal}} + \underbrace{\mathrm{FOV}_x \cdot \mathrm{FOV}_y \sum_{k=1}^{L} N_k(\sigma_{\mathcal{X}}^2) \odot W_{kl}(\mathbf{x})}_{\text{Gaussian noise}} \\ &= A_l^{\mathcal{R}}(\mathbf{x}) + N_l^{\mathcal{R}}(\mathbf{x}). \end{aligned} \tag{3.40}$$

Note that eq. (3.40) assumes same variance for each channel, i.e., $\sigma_{\mathcal{X}_l}^2 = \sigma_{\mathcal{X}}^2$.

Sum of squares

In GRAPPA MR imaging, the final magnitude image $M_L(\mathbf{x})$ is usually obtained with SoS formula (2.15). Since the components in SoS reconstruction are Gaussian distributed, the magnitude signal $M_L(\mathbf{x})$ follows the nc-χ distribution. However, note that the effective parameters are necessary to use the nc-χ model properly. For GRAPPA MRI and SoS reconstruction, the effective parameters are defined as follows (Aja-Fernández et al. 2011; see also Fig. 3.4):

1. the effective (decreased) number of receiver coils L_{eff}:

$$L_{\text{eff}}(\mathbf{x}) = \frac{A_T^2(\mathbf{x})\mathrm{tr}(\mathbf{C}_X) + (\mathrm{tr}(\mathbf{C}_X))^2}{\mathbf{A}^*(\mathbf{x})\mathbf{C}_X\mathbf{A}(\mathbf{x}) + \|\mathbf{C}_X\|_F^2}, \tag{3.41}$$

2. the effective (increased) variance of noise σ_{eff}^2:

$$\sigma_{\text{eff}}^2(\mathbf{x}) = \frac{\mathrm{tr}(\mathbf{C}_X)}{L_{\text{eff}}(\mathbf{x})}, \tag{3.42}$$

where $\mathbf{A}$ is given by $\mathbf{A} = [A_1^{\mathcal{R}}(\mathbf{x}), \ldots, A_L^{\mathcal{R}}(\mathbf{x})]^T$, $A_T^2(\mathbf{x}) = \sum_{l=1}^{L} |A_l^{\mathcal{R}}(\mathbf{x})|^2$ and $\mathbf{C}_X$ is the covariance matrix of the interpolated data given by $\mathbf{C}_X(\mathbf{x}) = \mathbf{W}(\mathbf{x})\mathbf{\Sigma}\mathbf{W}^*(\mathbf{x})$ with the matrix $\mathbf{W}(\mathbf{x})$ composed of the weights $W_{kl}(\mathbf{x})$:

$$\mathbf{W}(\mathbf{x}) = \begin{bmatrix} W_{11}(\mathbf{x}) & W_{12}(\mathbf{x}) & \ldots & W_{1L}(\mathbf{x}) \\ W_{21}(\mathbf{x}) & W_{22}(\mathbf{x}) & \ldots & W_{2L}(\mathbf{x}) \\ \vdots & \vdots & \ddots & \vdots \\ W_{L1}(\mathbf{x}) & W_{L2}(\mathbf{x}) & \ldots & W_{LL}(\mathbf{x}) \end{bmatrix}. \tag{3.43}$$

Note that in comparison with the effective parameters in multiple-coil acquisition (3.31–3.32), the multiplication of effective parameters $L_{\text{eff}}(\mathbf{x})\sigma_{\text{eff}}^2(\mathbf{x})$ is no longer constant across the FOV and it depends on the covariance matrix $\mathbf{C}_X = \mathbf{C}_X(\mathbf{x})$, i.e., $L_{\text{eff}}(\mathbf{x})\sigma_{\text{eff}}^2(\mathbf{x}) = \mathrm{tr}(\mathbf{C}_X(\mathbf{x}))$ (see Fig. 3.4).

3.4 Conclusions and remarks

In this chapter, we introduced various statistical models used to represent the magnitude MRI data. We started with the most fundamental stationary Rician model used in single-coil acquisitions (Gudbjartsson and Patz 1995), and then we generalized it to stationary nc-χ model arranged in multiple-coil acquisitions (Constantinides et al. 1997). However, if the correlations between the receiver coils are non-zero, the nc-χ model must be corrected by *effective parameters* to fit the magnitude data obtained with SoS formula (Aja-Fernández and Tristán-Vega 2012).

More advanced concepts arise in accelerated parallel MRI acquisition. For these modalities, the noise becomes non-stationary, i.e., it is spatially variant over the FOV (Aja-Fernández et al. 2014a). For SENSE MR imaging, the noise is given by a non-stationary Rician distribution (Aja-Fernández et al. 2014b), while for GRAPPA MR imaging and SoS reconstruction, it is represented by a non-stationary nc-χ distribution. Again, we must employ *effective parameters* to take the correlations between receiver coils into account in the nc-χ model (Aja-Fernández et al. 2011). We summarize the statistical models presented in this chapter in Table 3.1.

Two final remarks are worth making:

1. All statistical models introduced in this chapter are valid for Cartesian sampling of **k**–space domain. Even if the image reconstruction employs a projection-onto-convex-sets (POCS) method like Sabati et al. 2013, it still assumes Cartesian sampling of the raw MR signal.

2. Theoretical models are derived provided that the algorithms employ linear operators to reconstruct the full FOV image. For the non-linear reconstructions like Chang et al. 2012 the noise distribution can be evaluated using empirical studies only.

3. The nc-χ distribution with effective parameters approximates the magnitude MR signal for multiple-coil and GRAPPA MRI (both obtained with SoS).

4. The value of the variance of noise in SENSE MRI depends on the covariance matrix $\mathbf{\Sigma}$ and the sensitivity maps $C_l(\mathbf{x})$.

5. The value of the variance of noise in GRAPPA MRI with SoS depends on the covariance matrix $\mathbf{\Sigma}$ and the reconstruction coefficients $W_{kl}(\mathbf{x})$.

Table 3.1: Statistical distributions used in modelling the magnitude MRI data.

Modality	Magnitude reconstruction	Statistical model	Stationarity	Parameters
single-coil	absolute operator	Rician	stationary	σ^2
multiple-coil (uncorrelated)	SoS	nc-χ	stationary	L, σ^2
multiple-coil (correlated)	SoS	nc-χ (approx.)	non-stationary	$L_{\text{eff}}(\mathbf{x})$, $\sigma^2_{\text{eff}}(\mathbf{x})$
SENSE	absolute operator	Rician	non-stationary	$\sigma^2(\mathbf{x})$
GRAPPA	SoS	nc-χ (approx.)	non-stationary	$L_{\text{eff}}(\mathbf{x})$, $\sigma^2_{\text{eff}}(\mathbf{x})$

Chapter 4

Non-stationary noise estimation in Rician, nc-χ and Gaussian distributed signals

Contents

4.1 Introduction

In this chapter, we go over the state-of-the-art in non-stationary noise estimation in MRI. The review focuses on computational methods for Rician, nc-χ and Gaussian distributed signals. These methods allow estimating spatially variant noise patterns in accelerated parallel MRI acquisitions like SENSE MRI or GRAPPA MRI. We compare the methods in terms of noise type assumptions, estimation domain and additional requirements, which must be taken into account during the estimation process. We extensively illustrate all the methods, which are arranged then in our numerical experiments in the contribution part of the thesis. Next, the quantitative measures employed in the validation processes of the estimators are briefly explained. Eventually, some general remarks about spatially variant noise estimators in MRI are drawn.

4.2 Non-stationary noise estimation in MRI

One of the first attempts for spatially variant noise estimation in Rician distributed data was proposed by Marzetta 1995 and subsequently adapted to single-polarization synthetic aperture radar (SAR) images by DeVore et al. 2000. In these iterative schemes, the expectation-maximization (EM) algorithm is used to find maximum likelihood (ML) estimates of the parameters of a Rician distribution, i.e., the noise variance $\sigma^2(\mathbf{x})$ and the underlying signal amplitude $A_T(\mathbf{x})$. Although DeVore et al. 2000 require multiple samples of the receiving signal to estimate the noise level, it can also be related to the estimation process in a local neighbourhood from a single MR image. In the MRI field, the pioneers of spatially variant noise estimation are Samsonov and Johnson 2004, defining the method to obtain the noise map from the receiver coil noise matrix, which, actually, is not always available in a typical clinical routine.

In Delakis et al. 2007, the stationary wavelet transform (SWT) of the image at the first scale is used to suppress the underlying signal component, i.e., to remove the low-low (LL) subband coefficients. Then, the estimation is carried out assuming that inverse SWT of the remaining signal follows Rayleigh distribution. This assumption is not true for low SNR as it can be easily proved in the experimental way (see Fig. 4.1). Landman et al. 2009a and Landman et al. 2009b proposed general frameworks to deal with spatially variant noise using robust scale Q_n estimator (see Rousseeuw and Croux 1993 for more details), followed by

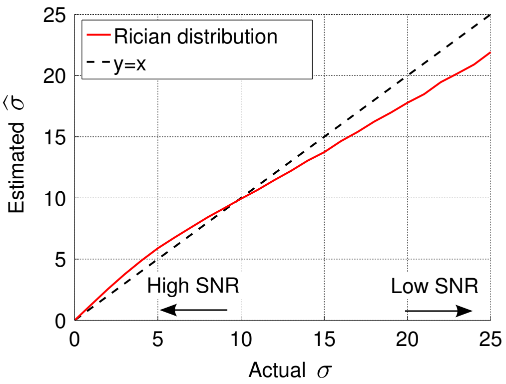

Figure 4.1: Mismatch between the actual σ and the estimated value $\widehat{\sigma}$ assuming that low-low subband coefficients of the SWT of the Rician signal were suppressed and the remaining signal follows Rayleigh distribution. The estimation is highly biased for low SNRs. The underlying signal level for Rician distribution is set to $A_T = 25$.

outliers rejection and regularization procedure. Although the methods have been proposed to cope with multiple independent scans and different signal contrast examinations (e.g., DWI data, T_1/T_2 relaxometry), in the basic scenario, they can be employed to estimate the noise map using a single image provided the biophysical model of the data.

In the context of general images, Goossens et al. 2006 presented a simple method to estimate the noise map assuming that the image is corrupted by a non-stationary AWGN process. The SWT is used to separate the noise assuming that the high-high (HH) subband is strictly the noise component. Guo and Huang 2009 proposed local sample variance as a noise level estimator after edges exclusion by means of local mutual information and k-means segmentation algorithm. Nevertheless, the estimator is fixed in the total variation regularization scheme and it suffers from the overestimations near to the edges. In Ding et al. 2010, a random noise in dynamic MR image series, e.g., cardiac function imaging or blood flow velocity mapping, has been considered. This approach utilizes a temporal redundancy between the acquisitions and it uses random matrix theory (Marchenko-Pastur distribution) to model the noise level. The method does not require any specific data distribution or image reconstruction technique assumptions. In Pan et al. 2012, a blind local noise estimation procedure has been proposed assuming that the kurtosis of the MR image is constant across different discrete cosine transformation (DCT) bands (Zoran and Weiss 2009). The method provides a closed-form expression of the noise estimator for AWGN channel and it can be efficiently implemented as a series of two-dimensional (2D) convolutions. Glenn et al. 2015 showed a simple estimation procedure for diffusion kurtosis imaging (DKI) using averaged sample variances over the repeated acquisitions and diffusion-sensitizing gradients directions followed by a bias correction and Gaussian smoothing of raw estimates. The proposed algorithm is fast, though, it requires multiple acquisitions and any data misalignment might result in biased results.

Rajan et al. 2011 presented the noise variance estimation scheme employing the ML estimator for Rician distribution, previously proposed in the milestone paper by Sijbers et al. 1998 and extensively investigated in Sijbers and Dekker 2004. The noise variance $\sigma^2(\mathbf{x})$ is estimated along with the amplitude signal $A_T(\mathbf{x})$ in a restricted local likelihood, thus, the pixels corresponding to the edges and different tissues in the neighbourhood are eliminated from the estimation process. Maggioni and Foi 2012 exploit the sparsity of the representation of similar 2D patches (neighbourhoods) in the non-local scheme using Gaussian and Rician assumptions. A beneficial factor of these two methods over most of the aforementioned noise estimation techniques so far is the possibility to simultaneously estimate the noise map and denoise the image. Aja-Fernández et al. 2013 studied the practical implications of the correlations between receiver coils and proposed the noise estimation approach for SoS reconstruction from correlated multiple-coil MRI data.

Unlike previously cited methodologies, the following techniques initially calculate the noise maps assuming Gaussian distribution, and then correct them to Rician/nc-χ case in the low SNR regions (usually for SNR < 5). This correction is usually done using the algorithm presented by Koay and Basser 2006. Note that all these techniques require the estimation of an extra measure, the SNR, which also is position dependent, i.e., SNR($\mathbf{x}$). Sharing this strategy, Manjón et al. 2010 modelled the noise variance as a minimal distance between local patch of the current pixel and the remaining patches in the non-local means (NLM) scheme. This approach uses the difference between noisy and low-pass filtered image to determine distances between the patches. The method is based on the experimental reasoning rather than grounded mathematical theory. In a similar fashion, Borrelli et al. 2014 handle the difference between noisy and a NLM prefiltered image to obtain local sample variances followed by median filtering and Rician adaptation. Maximov et al. 2012 generalized median absolute deviation (MAD) robust estimator (see Hampel 1974 for details), initially proposed for stationary Rician case by Coupé et al. 2010, to estimate non-stationary Rician noise in DTI. A very similar procedure, except the MAD estimator is calculated in the HH subband of the SWT of spherically interpolated DWI data, has been proposed by Veraart et al. 2013. The MAD estimator has also been adapted to non-stationary noise estimation procedure from a single MR image by Liu et al. 2014. Although there are several modifications of Coupé's method, this methodology has gained a lot of interest in MRI community. Recently, Dikaios et al. 2014 generalized the correction scheme presented by Koay and Basser 2006 to approximate the sum of the Rician PDFs leading to a closed-form formula for noise estimation in averaged DWI data. Finally, Veraart et al. 2016 presented another scheme to estimate the spatially variant noise map in diffusion MR imaging using the redundancy of the signal in multi-directional DWI data. The method identifies the noise level using the combination of local principal component analysis (PCA) with random matrix theory.

We note here that some previously cited methods (e.g., Landman et al. 2009a,b, Maximov et al. 2012, Veraart et al. 2013, Dikaios et al. 2014, Glenn et al. 2015 and Veraart et al. 2016) estimate the noise maps in a voxelwise scheme. This is a particularly important procedure in multiple contrast type techniques, e.g., DWI, perfusion imaging or T_1/T_2 relaxometry. Specifically, the methods take the MRI data from all diffusion-sensitizing gradient directions or contrast type into account to provide a single noise level for a given point of the image.

For the last two years, the number of new non-stationary noise estimators in MRI notably increased. This is a clear sign of the awareness of the importance of this topic by the magnetic resonance imaging community.

Aja-Fernández et al. 2014a presented comprehensive statistical noise analyses in SENSE MRI and GRAPPA MRI providing closed form expressions for the spatially variant variance of noise for both modalities. The noise estimation techniques have also been proposed, however, the methods require extra information like sensitivity coil profiles or reconstruction coefficients for SENSE and GRAPPA, respectively. In a similar fashion, Hansen et al. 2015 developed another scheme to measure the noise level of any linear combination of the complex, magnitude, or phase pixel values of a Cartesian MRI acquisition. Nevertheless, the method requires access to the raw MRI data and additional technical details about the acquisition process, i.e., the image reconstruction matrix and the sampling pattern of the data in **k**–space domain.

Lately, Tabelow et al. 2015 adapted the propagation-separation approach (Polzehl and Spokoiny 2006) for nc-χ distributed MRI data. The method estimates spatially variant noise maps by means of the weighted ML estimator, which is restricted to homogeneous regions. The method is well-founded from the theoretical point of view, however, it is a computationally intensive procedure. At the same time, Aja-Fernández et al. 2015b proposed a homomorphic approach to separate spatially variant noise into two terms: a stationary noise term and the low-frequency component corresponding to the noise pattern. In comparison with Landman et al. 2009a,b, Borrelli et al. 2014, Glenn et al. 2015 and Tabelow et al. 2015, where the relaxation of the raw estimates is performed next to the estimation process, in the homomorphic approach, the estimator uses a low-pass filter to model the noise pattern. The homomorphic filter avoids the granular effect and it allows implementing the noise estimation procedure as a 2D convolution. This is a great advantage over the previously presented noise estimation methods. In Aja-Fernández and Vegas-Sánchez-Ferrero 2015, the homomorphic filter has been further extended towards a blind noise estimation in GRAPPA imaging. Although, the method assumes Gaussian distributed signal, it can be directly applied to the GRAPPA MR image without *a priori* knowledge on the acquisition process.

Table 4.1: Comparison of spatially variant noise estimation techniques in Rician, nc-χ and Gaussian distributed data.

Method	Year	Imaging type	Imaging weighting	Spatially variant noise	Noise type assumptions	Estimation domain	Repeated acquisitions	Additional data
Marzetta 1995	1995	SAR	-	yes	Rician	-	-	no
DeVore et al. 2000	2000	SAR	-	yes	Rician	image	yes	no
Samsonov and Johnson 2004	2004	SENSE	T_1, T_2	yes	Gaussian	image ($\mp$)	no	yes ($\ominus$)
Sijbers and Dekker 2004	2004	No pMRI	–	yes ($\divideontimes$)	Rician	image	no	no
Goossens et al. 2006	2006	–	–	yes	Gaussian	wavelet	no	no
Delakis et al. 2007	2007	SENSE	not available	yes	Rayleigh	wavelet – image	no	no
Landman et al. 2009a	2009	SENSE	diffusion	yes ($\star$)	Gaussian ($\multimap$) + correction at low SNR	image	yes	yes ($\circledast$, $\otimes$)
Landman et al. 2009b	2009	SENSE	T_2 relaxometry, diffusion	yes ($\star$)	Gaussian ($\bowtie$, $\multimap$) + correction at low SNR	image	yes ($\dagger$)	yes ($\circledast$, $\otimes$)
Guo and Huang 2009	2009	SENSE, GRAPPA	T_1	yes	Gaussian	image ($\pm$)	no	no
Ding et al. 2010	2010	No pMRI, SoS, SENSE	T_1	yes	Gaussian ($\diamond$)	image	no ($\ddagger$)	no
Manjón et al. 2010	2010	No pMRI, SENSE GRAPPA	T_1, T_2, PD	yes	Gaussian + Rician adaptation	image	no	no
Rajan et al. 2011	2011	No pMRI	T_1, diffusion	yes	Rician	image	no	no
Maximov et al. 2012	2012	No pMRI	diffusion	yes ($\star$)	Gaussian + Rician adaptation	image	yes	no
Maggioni and Foi 2012	2012	No pMRI	T_1	yes	Gaussian, Rician	image	no	no
Pan et al. 2012	2012	SENSE	T_1	yes	Gaussian	image	no	no
Aja-Fernández et al. 2013	2013	SoS	T_1, diffusion	yes	nc-χ	image	no	no
Veraart et al. 2013	2013	SENSE, SoS	diffusion	yes ($\star$)	Gaussian + Rician/nc-χ adaptation	wavelet	yes ($\times$)	no
Aja-Fernández et al. 2014a	2014	SENSE, GRAPPA, SoS	T_1	yes	Rayleigh, c-χ	image	no	yes ($\odot$)
Liu et al. 2014	2014	No pMRI, SENSE	T_1, T_2, PD, diffusion	yes	Gaussian + Rician adaptation	wavelet	no	no
Borrelli et al. 2014	2014	SENSE, GRAPPA	T_2	yes	Gaussian + Rician adaptation	image	no	no
Dikaios et al. 2014	2014	SENSE, GRAPPA	diffusion	yes ($\star$)	Gaussian + Rician adaptation	wavelet	yes	no
Glenn et al. 2015	2015	No pMRI	diffusion	yes ($\star$)	Rician	image	yes	no
Hansen et al. 2015	2015	pMRI ($\div$)	perfusion	yes	Gaussian	image	no	yes ($\oslash$)
Aja-Fernández et al. 2015b	2015	SENSE	T_1	yes	Gaussian, Rayleigh, Rician	image	no	no
Tabelow et al. 2015	2015	SENSE, GRAPPA, zoomed GRAPPA	T_1, diffusion	yes	nc-χ	image	no	no
Aja-Fernández and Vegas-Sánchez-Ferrero 2015	2015	GRAPPA	T_1	yes	Gaussian	wavelet	no	no
Manjón et al. 2015	2015	SENSE	T_1	yes	Gaussian + Rician adaptation	image	no	no
Poot and Klein 2015	2015	No pMRI, SENSE	diffusion	yes ($\star$)	Rician	image	no	no
Veraart et al. 2016	2016	GRAPPA	diffusion	yes ($\star$)	Gaussian + nc-χ adaptation ($\diamond$)	image	no ($\times$)	no
Proposal (section 5)	2016	SENSE	T_1, T_2, PD	yes	Rician	image	no	no
Proposal (section 6)	2016	GRAPPA	T_1, T_2, PD	yes	nc-χ	image	no	no

Legend (Table 4.1):
pMRI – accelerated parallel MRI.
(÷) The method can measure the noise level for any linear combination of the pixels in an MR image.
(⋇) The general scheme is presented which can be employed to estimate spatially variant noise.
(⋆) Noise is measured in a voxelwise scheme.
(⊸) The method assumes that the difference between repeated acquisitions follows Gaussian distribution.
(⋈) The method assumes that the residuals (difference between the noisy and the prefiltered data) follows Gaussian distribution.
(♢) Noise is modeled assuming that the eigenvalues of the covariance matrix of a high-dimensional data follows Marchenko-Pastur distribution.
(∓) Noise level is represented as a local conductance parameter in the anisotropic diffusion filter.
(±) Noise level is estimated indirectly as a smoothing weight in the total variation regularization.
(†) In the basic variant, the method requires a biophysical model of the imaging data instead of repeated acquisitions.
(‡) The method is intended for successive dynamic image series rather than repeated acquisitions.
(×) The method uses the information of different DWIs to estimate the noise.
(⊖) The method uses a receiver noise matrix and it requires additional samples from the air background.
(⊛) The coil sensitivity model for the regularization procedure is required.
(⊗) The method requires multiple contrast type MR images.
(⊙) The method requires sensitivity maps for SENSE; reconstruction coefficients and correlations between channels for GRAPPA.
(⊘) The image reconstruction matrix, sampling pattern of the **k**–space and the complex MR images are required.

Manjón et al. 2015, in their recent work, proposed another noise estimation technique using sparseness and self-similarity of MR images. They utilize the PCA in the NLM scheme to extract the noise component. The noise level is obtained then as a median operator of the eigenvalues of the PCA decomposition and it is subsequently corrected to deal with the Rician case. In Poot and Klein 2015, a spatially regularized ML estimator was proposed to simultaneously estimate the noise pattern and diffusion tensor parameters. The method enables to set the regularization degree of the noise map by incorporating a maximum a posteriori (MAP) estimator.

To sum up, most of the spatially variant noise estimation methods published in the literature so far (and summarized in Table 4.1) show the following drawbacks:

1. The estimated noise maps are characterized by a certain level of granularity. Specifically, the estimates vary due to a small number of samples in local neighbourhoods. Moreover, the inhomogeneity of the tissues leads to highly biased estimates near to the edges.

2. The state-of-the-art methods do not take the signal-dependency of the noise in magnitude MRI data into account. This means that the noise component is usually assumed

to be Gaussian distributed and the preliminary estimates are further adapted to the Rician/nc-χ case (see the column *Noise type assumptions* in Table 4.1).

3. The methods significantly under- or overestimate the noise levels for low SNR areas, i.e., for SNR < 5, where the signal tends to be Rayleigh/c-χ distributed.

4. The methods require multiple acquisitions, a biophysical model of the data and/or additional information from the acquisition process (sensitivity maps for SENSE or reconstruction coefficients for GRAPPA). These varietes of extra parameters are usually not available in conventional clinical routines (see columns *Repeated acquisitions* and *Additional data* in Table 4.1).

5. The numerical procedures presented by some authors are computationally intensive schemes (Rajan et al. 2011, Tabelow et al. 2015, Manjón et al. 2015).

6. Finally, some methods have originally been proposed to estimate the noise from stacked images instead of separate estimations for each 2D slice (Rajan et al. 2011, Maggioni and Foi 2012, Tabelow et al. 2015, Manjón et al. 2015). Since the SENSE/GRAPPA reconstruction is different for each slice, the estimation cannot be done in three-simensional (3D) data for *in vivo* acquisitions.

4.3 State-of-the-art methods used in the experiments

For the sake of comparisons of our proposals we use **eighteen spatially variant noise estimation methods** from the state-of-the-art. The methods can be applied to a retrospectively reconstructed magnitude SENSE MRI and/or GRAPPA MRI data, and they are divided into two categories:

- estimation from a single image $M(\mathbf{x})$ (fourteen methods – section 4.3.1),
- estimation from multiple repeated scans $M_{(k)}(\mathbf{x})$[1] (four methods – section 4.3.2).

Our implementations of the methods follow a meticulous analyses of the algorithms, and they were prepared in MATLAB scientific environment (The MathWorks, Inc., Natick, MA), except Tabelow et al. 2015, where the source code in GNU R scientific package was provided by the autors[2]. For Aja-Fernández et al. 2015b and Maggioni and Foi 2012 we used already supplied MATLAB codes obtained from the authors homepages[3] [4].

4.3.1 Estimation from a single MR image

All these methods estimate the spatially variant noise map $\sigma(\mathbf{x})$ (or equivalently the noise variance map $\sigma^2(\mathbf{x})$) from a single magnitude MR image $M(\mathbf{x})$ without any additional information about the acquisition process.

1. DeVore et al. 2000
   The EM algorithm previously proposed by Marzetta 1995 is used to find the ML estimates for the parameters of the Rician distribution. The noise variance map $\sigma^2(\mathbf{x})$

---

[1] We use the symbol $M_{(k)}(\mathbf{x})$ to denote the repeated k–th acquisition.

[2] http://cran.r-project.org/web/packages/dti/index.html

[3] http://www.mathworks.com/matlabcentral/fileexchange/48762-noise-estimator-for-sense-mri

[4] http://www.cs.tut.fi/~foi/GCF-BM3D/

is estimated simultaneously with the underlying signal amplitude $A_T(\mathbf{x})$ in an iterative way:

$$\widehat{A_{k+1}(\mathbf{x})} = \left\langle \frac{I_1\left(\frac{\widehat{A_k(\mathbf{x})}}{\widehat{\sigma_k^2(\mathbf{x})}} M(\mathbf{x})\right)}{I_0\left(\frac{\widehat{A_k(\mathbf{x})}}{\widehat{\sigma_k^2(\mathbf{x})}} M(\mathbf{x})\right)} M(\mathbf{x}) \right\rangle_{\mathbf{x}}, \tag{4.1}$$

$$\widehat{\sigma_{k+1}^2(\mathbf{x})} = \max\left\{\frac{1}{2}\langle M^2(\mathbf{x})\rangle_{\mathbf{x}} - \frac{1}{2}\widehat{A_k^2(\mathbf{x})},\ 0\right\}, \tag{4.2}$$

where $I_k(\cdot)$ is the modified Bessel function of the first kind and k–th order, and $\langle M^p(\mathbf{x})\rangle_{\mathbf{x}}$ is the local sample estimator of p–th raw moment defined as:

$$\langle M^p(\mathbf{x})\rangle_{\mathbf{x}} = \frac{1}{|\eta(\mathbf{x})|} \sum_{\mathbf{p}\in\eta(\mathbf{x})} M^p(\mathbf{p}), \quad p \in \mathbb{N} \tag{4.3}$$

with $\eta(\mathbf{x})$ being a local neighbourhood centered at the pixel $\mathbf{x}$ and $|\eta(\mathbf{x})|$ is the cardinality (number of pixels) of the patch $\eta(\mathbf{x})$. The initialization process of the EM algorithm is obtained by the method of moments:

$$\widehat{A_0(\mathbf{x})} = \left[2\left(\langle M^2(\mathbf{x})\rangle_{\mathbf{x}}\right)^2 - \langle M^4(\mathbf{x})\rangle_{\mathbf{x}}\right]^{\frac{1}{4}}, \tag{4.4}$$

$$\widehat{\sigma_0^2(\mathbf{x})} = \frac{1}{2}\left[\langle M^2(\mathbf{x})\rangle_{\mathbf{x}} - \widehat{A_0^2(\mathbf{x})}\right]. \tag{4.5}$$

The algorithm stops after reaching $k_{\max}$ iterations.

2. Goossens et al. 2006
   The method estimates the noise variance map $\sigma^2(\mathbf{x})$ from HH subband coefficients of the SWT of the magnitude image at the first scale $M^{(1,\mathrm{HH})}(\mathbf{x})$:

$$\widehat{\sigma^2(\mathbf{x})} = \left\langle \left(M^{(1,\mathrm{HH})}(\mathbf{x})\right)^2 \right\rangle_{\mathbf{x}}, \tag{4.6}$$

   where $\left\langle M^{(1,\mathrm{HH})}(\mathbf{x})\right\rangle_{\mathbf{x}}$ is the local sample estimator of the mean as defined in eq. (4.3).

3. Delakis et al. 2007
   The method makes use of the SWT of the image $M(\mathbf{x})$ at the first scale and LL subband coefficients suppression to expose the noise component. Then, the noise variance map $\sigma^2(\mathbf{x})$ is estimated in spatial domain of the image provided the inverse SWT $\breve{M}(\mathbf{x})$:

$$\widehat{\sigma^2(\mathbf{x})} = \left(2 - \frac{\pi}{2}\right)^{-1} \left(\langle \breve{M}^2(\mathbf{x})\rangle_{\mathbf{x}} - \left(\langle \breve{M}(\mathbf{x})\rangle_{\mathbf{x}}\right)^2\right), \tag{4.7}$$

   where $\breve{M}(\mathbf{x})$ is the image with suppressed LL subband coefficients and $\langle \breve{M}^p(\mathbf{x})\rangle_{\mathbf{x}}$ is defined as in eq. (4.3). If however the image $M(\mathbf{x})$ contains an edge in a local neighbourhood $\eta(\mathbf{x})$, Delakis et al. 2007 suggest applying the directional analysis to correct the preliminary noise variance level (4.7). Specifically, the averages along four directions (horizontal, vertical and two diagonal) in a local neighbourhood $\eta(\mathbf{x})$ from $\breve{M}(\mathbf{x})$ map are calculated and then compared to the pixel $\breve{M}(\mathbf{x})$. Finally, the new noise level at $\mathbf{x}$ is calculated along the direction, which presents the closest average to the central point $\breve{M}(\mathbf{x})$.

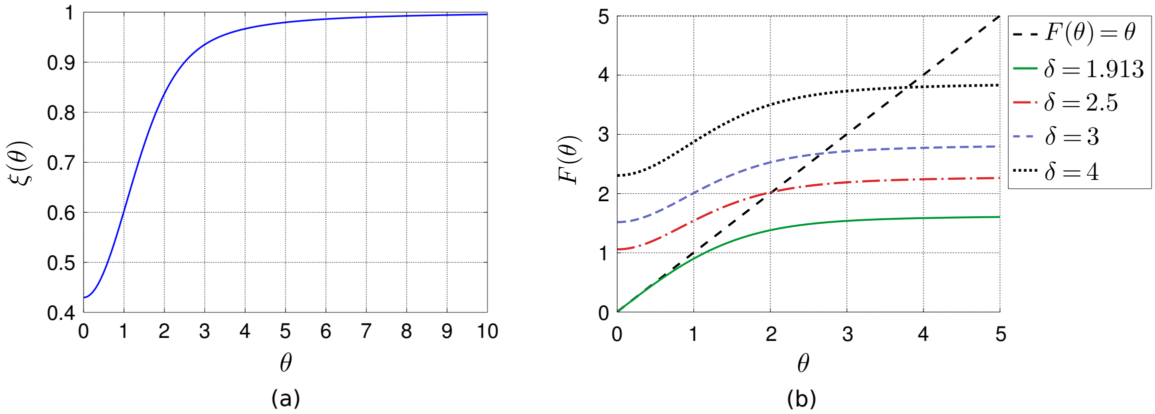

Figure 4.2: (a) The correction function $\xi(\theta)$ (4.16) in terms of SNR level θ and (b) the transcendental equation (4.17) for different values of $\delta = \frac{\langle M(\mathbf{x})\rangle_{\mathbf{x}}}{\widehat{\sigma_{\text{raw}}(\mathbf{x})}}$. For $\delta = 1.913$, the solution of (4.17) equals $\theta = 0$.

4. Landman et al. 2009b
   The general framework uses robust Q_n estimator (Rousseeuw and Croux 1993) to estimate the spatially variant noise map $\sigma(\mathbf{x})$. In the basic scenario, the method can be applied to a single slice $M(\mathbf{x})$ provided a biophysical model of the data:

$$\widehat{\sigma(\mathbf{x})} = Q_n\left(\{\mathbf{p} \in \eta(\mathbf{x})\colon \varepsilon(\mathbf{p})\}\right), \tag{4.8}$$

   where $\varepsilon(\mathbf{x})$ is the difference (residual) between noisy magnitude data $M(\mathbf{x})$ and a biophysical model projection onto data:

$$\varepsilon(\mathbf{x}) = M(\mathbf{x}) - M_{\text{model}}(\mathbf{x}) \tag{4.9}$$

   with $M_{\text{model}}(\mathbf{x})$ being the biophysical model of the data. The Q_n is the scale estimator defined as:

$$Q_n(\{x_1, \ldots, x_n\}) = 2.2219 \cdot \{|x_i - x_j|; i < j\}_{(k)}, \tag{4.10}$$

   where the symbol $\{\cdot\}_{(k)}$ denotes k–th element in the ascending ordered data (order statistics) and here $k = \frac{\lfloor n/2\rfloor(\lfloor n/2\rfloor+1)}{8}$ with $\lfloor x\rfloor$ being the largest integer not larger than x [5]. Finally, to mitigate the impact of the outliers, Landman et al. 2009b proposed to re-estimate the noise map by removing the observations with lower SNR than the adaptive computed threshold $t(\mathbf{x})$:

$$t(\mathbf{x}) = \min\left\{5,\ \underset{\mathbf{p}\in\eta(\mathbf{x})}{\text{median}}\left(\frac{M(\mathbf{p})}{\widehat{\sigma(\mathbf{x})}}\right) - 3\right\}. \tag{4.11}$$

5. Manjón et al. 2010
   The raw local noise variance $\sigma^2_{\text{raw}}(\mathbf{x})$ is modelled as a minimal distance between local neighbourhood (patch) of the current pixel $R(\mathbf{x})$ and the remaining patches $R(\mathbf{p})$ in the NLM scheme (Buades et al. 2005):

$$\widehat{\sigma^2_{\text{raw}}(\mathbf{x})} = \min_{\mathbf{p}\in V(\mathbf{x})\colon \mathbf{p}\neq\mathbf{x}} \|R(\mathbf{x}) - R(\mathbf{p})\|_2^2, \tag{4.12}$$

   where $V(\mathbf{x})$ ($V(\mathbf{x}) \supset R(\mathbf{x})$) is the search window and the patches $R(\mathbf{x})$ and $R(\mathbf{p})$ are obtained from $\varepsilon(\mathbf{x})$:

$$\varepsilon(\mathbf{x}) = M(\mathbf{x}) - \langle M(\mathbf{x})\rangle_{\mathbf{x}}. \tag{4.13}$$

---

[5] For n being an odd number we can define $k = \frac{n^2-1}{16}$.

The distance between the patches $R(\mathbf{x})$ and $R(\mathbf{p})$ in eq. (4.12) is calculated using the ℓ^2–norm as follows:

$$\mathrm{dist}(R(\mathbf{x}), R(\mathbf{p})) = \|R(\mathbf{x}) - R(\mathbf{p})\|_2 = \sqrt{\sum_j \left(R(\mathbf{x}^j) - R(\mathbf{p}^j)\right)^2} \tag{4.14}$$

with $R(\mathbf{x}^j)$ being the intensity of j–th pixel in the patch $R(\mathbf{x})$. In low SNR regions the raw map $\widehat{\sigma^2_{\mathrm{raw}}(\mathbf{x})}$ is underestimated and it is corrected then using the procedure described by Koay and Basser 2006[6]:

$$\widehat{\sigma(\mathbf{x})} = \frac{\widehat{\sigma_{\mathrm{raw}}(\mathbf{x})}}{\sqrt{\xi(\theta)}}, \tag{4.15}$$

where the function $\xi(\theta)$ is defined as follows (Fig. 4.2a):

$$\xi(\theta) = 2 + \theta^2 - \frac{\pi}{8} \exp\left(-\frac{\theta^2}{2}\right) \left[\left(2 + \theta^2\right) I_0\left(\frac{\theta^2}{4}\right) + \theta^2 I_1\left(\frac{\theta^2}{4},\right)\right]^2 \tag{4.16}$$

and the local SNR parameter $\theta = \mathrm{SNR}(\mathbf{x})$ is obtained from the solution of the transcendental equation (Fig. 4.2b):

$$\theta = F(\theta), \quad F(\theta) = \sqrt{\xi(\theta)\left(1 + \left(\frac{\langle M(\mathbf{x})\rangle_{\mathbf{x}}}{\widehat{\sigma_{\mathrm{raw}}(\mathbf{x})}}\right)^2\right) - 2}. \tag{4.17}$$

The transcendental equation (4.17) is usually solved in the iterative way using the Newton's method of root finding until $|\theta_{k+1} - \theta_k| > \theta_{\mathrm{ERR}}$ (see Koay and Basser 2006 for more details).

6. Rajan et al. 2011
   The local noise variance $\sigma^2(\mathbf{x})$ is calculated using Rician ML estimator (Sijbers and Dekker 2004):

$$\left\{\widehat{A_T(\mathbf{x})}, \widehat{\sigma^2(\mathbf{x})}\right\} = \underset{A_T,\sigma^2}{\mathrm{argmax}} \left(\log \mathcal{L}(A_T, \sigma^2 | \left\{M(\mathbf{p})\colon \mathbf{p} \in \overline{\eta}(\mathbf{x})\right\})\right), \tag{4.18}$$

where the log-likelihood function $\log \mathcal{L}(A_T, \sigma^2|\cdot)$ is defined as:

$$\begin{aligned}\log \mathcal{L}(A_T, \sigma^2| \left\{M(\mathbf{p})\colon \mathbf{p} \in \overline{\eta}(\mathbf{x})\right\}) = \sum_{\mathbf{p}\in\overline{\eta}(\mathbf{x})} \log\left(\frac{M(\mathbf{p})}{\sigma^2}\right) - \sum_{\mathbf{p}\in\overline{\eta}(\mathbf{x})} \frac{M^2(\mathbf{p}) + A_T^2}{2\sigma^2} \\ + \sum_{\mathbf{p}\in\overline{\eta}(\mathbf{x})} \log I_0\left(\frac{A_T M(\mathbf{p})}{\sigma^2}\right)\end{aligned} \tag{4.19}$$

and $\overline{\eta}(\mathbf{x})$ is the restricted local likelihood:

$$\overline{\eta}(\mathbf{x}) = \left\{\mathbf{p} \in V(\mathbf{x})\colon |M_{\mathrm{NLM}}(\mathbf{x}) - M_{\mathrm{NLM}}(\mathbf{p})| < t\right\}, \tag{4.20}$$

where $M_{\mathrm{NLM}}(\mathbf{x})$ is the image $M(\mathbf{x})$ filtered by NLM algorithm (Buades et al. 2005) and $V(\mathbf{x})$ is the search window in the NLM scheme. Threshold t in eq. (4.20) is obtained from the histogram of all local ranges of the image $M_{\mathrm{NLM}}(\mathbf{x})$ using the mode operator:

$$t = \underset{\mathbf{p}\in\Omega_\Delta}{\mathrm{mode}} \left(\mathrm{Histogram}_{n_b}\left(M_{\mathrm{range}}(\mathbf{p})\right)\right), \tag{4.21}$$

---

[6] Although the correction function was published by Koay and Basser 2006, the approach had been proposed a few years earlier by Marcos Martín-Fernández in his PhD thesis (see Martín-Fernández et al. 2009a and Martín-Fernández et al. 2009b for more details).

where Ω_{Δ} is the foreground area of the image. The histogram in eq. (4.21) is defined for n_b bins and it is derived from the image representing local ranges $M_{\text{range}}(\mathbf{x})$:

$$M_{\text{range}}(\mathbf{x}) = \max_{\mathbf{p}\in\eta(\mathbf{x})}\Big(M_{\text{NLM}}(\mathbf{p})\Big) - \min_{\mathbf{q}\in\eta(\mathbf{x})}\Big(M_{\text{NLM}}(\mathbf{q})\Big). \tag{4.22}$$

7. Pan et al. 2012
   At first, the response images $M_{\text{DCT}_k}(\mathbf{x})$ are obtained by convolving the noisy image $M(\mathbf{x})$ with each DCT basis:

$$M_{\text{DCT}_k}(\mathbf{x}) = \sum_{\mathbf{p}\in\eta(\mathbf{x})} M(\mathbf{p}) \cdot \text{DCT}_k(\mathbf{x}-\mathbf{p}) \quad \text{for} \quad k \in \{1, 2, \ldots, N \times N\}, \tag{4.23}$$

   where $\text{DCT}_k(\mathbf{x})$ is the k–th filter from $N \times N$ DCT basis. The noise variance map $\sigma^2(\mathbf{x})$ is estimated then using the relation between the variance and the kurtosis of noise-free and noisy data assuming the AWGN channel (Pauluzzi and Beaulieu 2000):

$$\widehat{\sigma^2(\mathbf{x})} = \frac{1}{\left\langle \frac{1}{\tilde{\sigma}_k^2(\mathbf{x})} \right\rangle_k} - \frac{\left\langle \frac{1}{\left(\tilde{\sigma}_k^2(\mathbf{x})\right)^2} \right\rangle_k - \left(\left\langle \frac{1}{\tilde{\sigma}_k^2(\mathbf{x})} \right\rangle_k\right)^2}{\left\langle \sqrt{\tilde{\kappa}_k(\mathbf{x})} \right\rangle_k \left\langle \frac{1}{\left(\tilde{\sigma}_k^2(\mathbf{x})\right)^2} \right\rangle_k - \left\langle \frac{\sqrt{\tilde{\kappa}_k(\mathbf{x})}}{\tilde{\sigma}_k^2(\mathbf{x})} \right\rangle_k \left\langle \frac{1}{\tilde{\sigma}_k^2(\mathbf{x})} \right\rangle_k} \cdot \frac{\left\langle \sqrt{\tilde{\kappa}_k(\mathbf{x})} \right\rangle_k}{\left\langle \frac{1}{\tilde{\sigma}_k^2(\mathbf{x})} \right\rangle_k}, \tag{4.24}$$

   where $\langle \cdot \rangle_k$ is the pointwise average along all $N \times N$ bands. The variance $\tilde{\sigma}_k^2(\mathbf{x})$ and the kurtosis $\tilde{\kappa}_k(\mathbf{x})$ of k–th response image $M_{\text{DCT}_k}(\mathbf{x})$ are defined in terms of local sample estimators of p–th raw moments (4.3):

$$\tilde{\sigma}_k^2(\mathbf{x}) = \left\langle M_{\text{DCT}_k}^2(\mathbf{x}) \right\rangle_{\mathbf{x}} - \left(\left\langle M_{\text{DCT}_k}(\mathbf{x}) \right\rangle_{\mathbf{x}}\right)^2 \tag{4.25}$$

   and

$$\begin{aligned} \tilde{\kappa}_k(\mathbf{x}) = {} & \frac{\left\langle M_{\text{DCT}_k}^4(\mathbf{x}) \right\rangle_{\mathbf{x}} - 4 \left\langle M_{\text{DCT}_k}^3(\mathbf{x}) \right\rangle_{\mathbf{x}} \left\langle M_{\text{DCT}_k}(\mathbf{x}) \right\rangle_{\mathbf{x}}}{\left(\tilde{\sigma}_k^2(\mathbf{x})\right)^2} \\ & + \frac{6 \left\langle M_{\text{DCT}_k}^2(\mathbf{x}) \right\rangle_{\mathbf{x}} \left(\left\langle M_{\text{DCT}_k}(\mathbf{x}) \right\rangle_{\mathbf{x}}\right)^2 - 3 \left(\left\langle M_{\text{DCT}_k}(\mathbf{x}) \right\rangle_{\mathbf{x}}\right)^4}{\left(\tilde{\sigma}_k^2(\mathbf{x})\right)^2}. \end{aligned} \tag{4.26}$$

8. Maggioni and Foi 2012[7]
   The method is based on BM4D algorithm (Maggioni et al. 2013), which is the generalization of the milestone in digital image processing BM3D algorithm to volumetric data (Dabov et al. 2007). At first, the cubes $C(\mathbf{p})$ are stacked together and the photometric distances to the reference (center) cube $C(\mathbf{x})$ are calculated:

$$\text{dist}(C(\mathbf{x}), C(\mathbf{p})) = \frac{\|C(\mathbf{x}) - C(\mathbf{p})\|_2^2}{L^3}, \tag{4.27}$$

   where $L \times L \times L$ $(L \in \mathbb{N})$ is the size of the cube and $\|\cdot\|_2$ is the ℓ^2–norm measured using the corresponding intensities in the input two cubes (see eq. (4.14)). Next, the set of indices of the cubes that are similar to $C(\mathbf{x})$ are defined as:

$$\Xi(\mathbf{x}) = \{\mathbf{p} \colon \text{dist}(C(\mathbf{x}), C(\mathbf{p})) \leqslant \tau_{\text{match}}\} \tag{4.28}$$

---

[7] The method has been initially proposed to deal with stacked images (3D cubes).

with τ_{match} denoting a predefined threshold. The set of indices (4.28) is used then to build the group $\mathcal{G}_{\Xi(\mathbf{x})}$ associated to the reference cube $C(\mathbf{x})$ using the disjoint union operation:

$$\mathcal{G}_{\Xi(\mathbf{x})} = \bigsqcup_{\mathbf{p}\in\Xi(\mathbf{x})} C(\mathbf{p}) = \{(C(\mathbf{p}), \mathbf{p})\colon \mathbf{p} \in \Xi(\mathbf{x})\}\,. \tag{4.29}$$

Finally, the noise level at $\mathbf{x}$ for Gaussian distributed data is estimated using MAD estimator, which is applied to the high-frequency coefficients $\Phi_{\Xi(\mathbf{x})}$ in the group $\mathcal{G}_{\Xi(\mathbf{x})}$:

$$\widehat{\sigma(\mathbf{x})} = 1.4826 \cdot \operatorname*{median}_{\phi_k\in\Phi_{\Xi(\mathbf{x})}} \left| \phi_k - \operatorname*{median}_{\phi_l\in\Phi_{\Xi(\mathbf{x})}}(\phi_l) \right|, \tag{4.30}$$

where ϕ_k is the k–th coefficient of the high-passed spectrum $\Phi_{\Xi(\mathbf{x})}$ given by:

$$\Phi_{\Xi(\mathbf{x})} = \mathcal{H}\left(\mathfrak{I}\left(\mathcal{G}_{\Xi(\mathbf{x})}\right)\right). \tag{4.31}$$

Two operations are needed for (4.31):

- the decorrelating linear transform $\mathfrak{I}$, which is separably applied to every dimension of the group $\mathcal{G}_{\Xi(\mathbf{x})}$,
- a high-pass filter $\mathcal{H}$ that discards the hyperplane representing the DC component[8].

9. Maximov et al. 2012
The method uses MAD estimator (Hampel 1974) previously adapted to stationary noise estimation in MRI by Coupé et al. 2010. Although the estimator was proposed to deal with repeated scans, it can also be related to the estimation process from a single slice $M(\mathbf{x})$ as follows:

$$\widehat{\sigma_{\mathrm{raw}}(\mathbf{x})} = 1.4826 \cdot \operatorname*{median}_{\mathbf{p}\in\eta(\mathbf{x})} \left| M(\mathbf{p}) - \operatorname*{median}_{\mathbf{q}\in\eta(\mathbf{x})}\Big(M(\mathbf{q})\Big) \right|. \tag{4.32}$$

In the same way as Manjón et al. 2010, the correction factor (4.15) is needed to obtain the final noise map $\widehat{\sigma(\mathbf{x})}$ from (4.32).

10. Liu et al. 2014
The method estimates the raw noise map $\sigma_{\mathrm{raw}}(\mathbf{x})$ using MAD estimator from HH subband coefficients of the SWT of the image at the first scale $M^{(1,\mathrm{HH})}(\mathbf{x})$:

$$\widehat{\sigma_{\mathrm{raw}}(\mathbf{x})} = 1.4826 \cdot \operatorname*{median}_{\mathbf{p}\in\eta(\mathbf{x})} \left| M^{(1,\mathrm{HH})}(\mathbf{p}) - \operatorname*{median}_{\mathbf{q}\in\eta(\mathbf{x})}\left(M^{(1,\mathrm{HH})}(\mathbf{q})\right) \right|. \tag{4.33}$$

The correction factor (4.15) is also necessary to obtain $\widehat{\sigma(\mathbf{x})}$ from (4.33).

11. Borrelli et al. 2014
The raw noise variance map $\widehat{\sigma^2_{\mathrm{raw}_1}(\mathbf{x})}$ is estimated from the image $\varepsilon(\mathbf{x})$ using the second order central moment:

$$\widehat{\sigma^2_{\mathrm{raw}_1}(\mathbf{x})} = \langle\varepsilon^2(\mathbf{x})\rangle_{\mathbf{x}} - \left(\langle\varepsilon(\mathbf{x})\rangle_{\mathbf{x}}\right)^2, \tag{4.34}$$

where $\varepsilon(\mathbf{x})$ is defined as:

$$\varepsilon(\mathbf{x}) = M(\mathbf{x}) - M_{\mathrm{NLM}}(\mathbf{x}) \tag{4.35}$$

---

[8] Although the abbreviation DC refers to *direct current* term in electrical engineering, it is also used in context of digital image processing. However, here the term DC relates to the "*average*" hyperplane in the data.

with $M_{\mathrm{NLM}}(\mathbf{x})$ being the prefiltered image $M(\mathbf{x})$ by the NLM filter (Buades et al. 2005). Then, the raw noise variance map (4.34) is smoothed using median filter:

$$\widehat{\sigma^2_{\mathrm{raw}_2}(\mathbf{x})} = \operatorname*{median}_{\mathbf{p}\in\eta(\mathbf{x})} \left(\widehat{\sigma^2_{\mathrm{raw}_1}(\mathbf{p})}\right). \tag{4.36}$$

Finally, the correction factor (4.15) is applied to (4.36) to get the final noise variance map $\widehat{\sigma^2(\mathbf{x})}$.

12. Tabelow et al. 2015
    The method estimates local noise level $\sigma(\mathbf{x})$ using the iterative propagation-separation approach (Polzehl and Spokoiny 2006). Specifically, the estimation procedure is restricted to adaptively refined homogeneous regions and the weighted ML estimator is applied then as follows:

$$\widehat{\sigma_{\mathrm{raw}_k}(\mathbf{x})} = \sqrt{\frac{N_k(\mathbf{x})}{N_k(\mathbf{x})-1}} \operatorname*{argmax}_{\sigma\colon \sigma^2 \geqslant \frac{\zeta}{2L}} \Big(\mathcal{L}(\sigma|\left\{M(\mathbf{p})\colon \mathbf{p}\in\overline{\eta}(\mathbf{x})\right\},\left\{w_k(\mathbf{p})\colon \mathbf{p}\in\overline{\eta}(\mathbf{x})\right\})\Big), \tag{4.37}$$

where the likelihood function $\mathcal{L}(\sigma|\cdot,\cdot)$ is defined as follows:

$$\begin{aligned} &\mathcal{L}(\sigma|\left\{M(\mathbf{p})\colon \mathbf{p}\in\overline{\eta}(\mathbf{x})\right\},\left\{w_k(\mathbf{p})\colon \mathbf{p}\in\overline{\eta}(\mathbf{x})\right\}) = \\ &\qquad - N_k(\mathbf{x})\left(\frac{\zeta}{\sigma^2} + 2\log\sigma + \frac{L-1}{2}\log\left(\zeta - 2L\sigma^2\right)\right) \\ &\qquad\qquad + \sum_{\mathbf{p}\in\overline{\eta}(\mathbf{x})} w_k(\mathbf{p}) \log I_{L-1}\left(\frac{M(\mathbf{p})}{\sigma^2}\sqrt{\zeta - 2L\sigma^2}\right) \end{aligned} \tag{4.38}$$

with I_{L-1} being the modified Bessel function of the first kind and $(L-1)$–th order. The parameter ζ in (4.38) is given by:

$$\zeta = \frac{1}{N_k(\mathbf{x})} \sum_{\mathbf{p}\in\overline{\eta}(\mathbf{x})} w_k(\mathbf{p}) M^2(\mathbf{p}), \tag{4.39}$$

where $N_k(\mathbf{x}) = \sum_{\mathbf{p}\in\overline{\eta}(\mathbf{x})} w_k(\mathbf{p})$ and $w_k(\mathbf{p})$ being the weight of the pixel $M(\mathbf{p})$ at position $\mathbf{p}$ in k–th iteration of the inference process. Finally, the raw noise estimates $\widehat{\sigma_{\mathrm{raw}_k}(\mathbf{x})}$ are corrected using local median filter:

$$\widehat{\sigma_k(\mathbf{x})} = \operatorname*{median}_{\mathbf{p}\in\eta(\mathbf{x})} \left(\widehat{\sigma_{\mathrm{raw}_k}(\mathbf{p})}\right). \tag{4.40}$$

The algorithm stops after reaching $k_{\max}$ iterations.

Two important issues are remarkable about Tabelow's algorithm:

- the weights $w_k(\mathbf{p})$ at the position $\mathbf{x}$ are computed adaptively in each k–th iteration of the algorithm (see Polzehl and Spokoiny 2006 and Tabelow et al. 2015 for more details),
- the number of coils L must be tuned locally to avoid nc-χ model misspecification. Such correction was proposed for accelerated parallel GRAPPA MRI (Aja-Fernández et al. 2011) and multiple-coil acquisitions (Aja-Fernández et al. 2013).

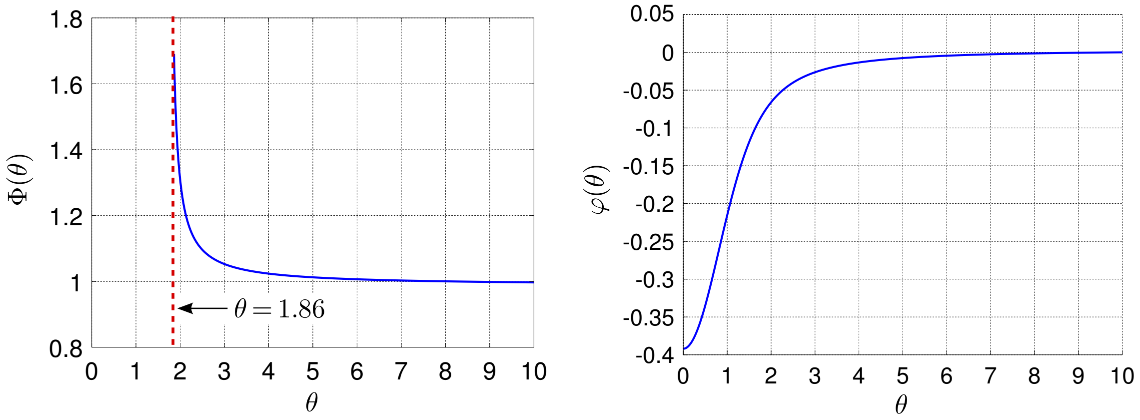

(a) (b)

Figure 4.3: The correction function $\Phi(\theta)$ (4.46) and $\varphi(\theta)$ (4.48) in terms of SNR level θ.

13. Manjón et al. 2015
    The method estimates local noise level $\sigma(\mathbf{x})$ using PCA in NLM scheme. Specifically, for each point of the data $\mathbf{x}$ a set of N the most similar patches $P(\mathbf{p})$ to the current patch $P(\mathbf{x})$ from the search window $V(\mathbf{x})$ ($V(\mathbf{x}) \supset P(\mathbf{x})$) are reordered as row vectors to form a matrix $\mathbf{X}$:

$$\mathbf{X} = \begin{bmatrix} P(\mathbf{p}_1^1) & P(\mathbf{p}_1^2) & \dots & P(\mathbf{p}_1^K) \\ P(\mathbf{p}_2^1) & P(\mathbf{p}_2^2) & \dots & P(\mathbf{p}_2^K) \\ \dots & \dots & \dots & \dots \\ P(\mathbf{p}_N^1) & P(\mathbf{p}_N^2) & \dots & P(\mathbf{p}_N^K) \end{bmatrix}, \tag{4.41}$$

where K is the number of elements in a single patch ($N = K$) and $P(\mathbf{p}_i^j)$ denotes the intensity of j–th pixel in i–th the most similar patch to $P(\mathbf{x})$. The similarity (distance) between two patches $P(\mathbf{x})$ and $P(\mathbf{p})$ is calculated using ℓ^2–norm:

$$\text{dist}(P(\mathbf{x}), P(\mathbf{p})) = \|P_{\text{G}}(\mathbf{x}) - P_{\text{G}}(\mathbf{p})\|_2 = \sqrt{\sum_{j=1}^{K} \left(P_{\text{G}}(\mathbf{x}^j) - P_{\text{G}}(\mathbf{p}^j)\right)^2}, \tag{4.42}$$

where the patch $P_{\text{G}}(\mathbf{p})$ is an equivalent to the patch $P(\mathbf{p})$, however, it is obtained from a guided image $M_{\text{G}}(\mathbf{x})$[9]:

$$M_{\text{G}}(\mathbf{x}) = \underset{\mathbf{p}\in\eta(\mathbf{x})}{\text{median}}\Big(M(\mathbf{p})\Big). \tag{4.43}$$

The PCA is applied therefore to the matrix $\mathbf{X}$ and the raw local noise map $\sigma_{\text{raw}}(\mathbf{x})$ is estimated as follows:

$$\widehat{\sigma_{\text{raw}}(\mathbf{x})} = 1.29 \cdot \sqrt{\underset{\lambda\in\lambda_t}{\text{median}}(\lambda)} \quad \text{where} \quad \lambda_t = \left\{\lambda_i\colon \sqrt{\lambda_i} < 2 \cdot \underset{\lambda}{\text{median}}(\sqrt{\lambda})\right\} \tag{4.44}$$

with λ being the eigenvalues of the PCA decomposition at $\mathbf{x}$. Finally, the raw noise map (4.44) is corrected to Rician case as follows:

$$\widehat{\sigma(\mathbf{x})} = \widehat{\sigma_{\text{raw}}(\mathbf{x})}\Phi(\theta), \tag{4.45}$$

---

[9] Compare to Maggioni and Foi 2012, where the similarity between two cubes (patches) is derived from the noisy image.

where the correction function $\Phi(\theta)$ is defined in terms of SNR (Fig. 4.3a):

$$\Phi(\theta) = \begin{cases} \frac{0.9846(\theta-1.86)+0.1983}{(\theta-1.86)+0.1175} & \text{if } \theta > 1.86 \\ 0 & \text{otherwise} \end{cases} \tag{4.46}$$

with $\theta = \mathrm{SNR}(\mathbf{x})$ being the local SNR level at $\mathbf{x}$. As the final step of the algorithm, the low-pass filter is applied to (4.45) to get a more realistic noise pattern.

14. Aja-Fernández et al. 2015b, Aja-Fernández and Vegas-Sánchez-Ferrero 2015
Two estimators are proposed for Gaussian and Rician noise, respectively:

$$\widehat{\sigma(\mathbf{x})} = \sqrt{2}\exp\left(\mathrm{LPF}_{\sigma_\mathrm{f}}\left\{\log\left|M(\mathbf{x}) - \mathbb{E}\left\{M(\mathbf{x})\right\}\right|\right\} + \frac{\gamma}{2}\right), \tag{4.47}$$

$$\widehat{\sigma(\mathbf{x})} = \sqrt{2}\exp\left(\mathrm{LPF}_{\sigma_\mathrm{f}}\left\{\log\left|M(\mathbf{x}) - \mathbb{E}\left\{M(\mathbf{x})\right\}\right|\right\} + \frac{\gamma}{2}\right)\exp\left(-\varphi(\theta)\right), \tag{4.48}$$

where $\mathrm{LPF}_{\sigma_\mathrm{f}}\{\cdot\}$ is a low-pass Gaussian filter with standard deviation σ_f, $\mathbb{E}\{M(\mathbf{x})\}$ denotes the expectation value in each point of the image, $\varphi(\cdot)$ is the correction function in terms of local SNR $\theta = \mathrm{SNR}(\mathbf{x})$ (see Fig. 4.3b) and γ is the Euler-Mascheroni constant defined as:

$$\gamma = \lim_{n\to\infty}\left(\sum_{k=1}^{n}\frac{1}{k} - \log(n)\right) \approx 0.57721. \tag{4.49}$$

Note that the estimators (4.47) and (4.48) need an estimation procedure of the parameter $\mathbb{E}\{M(\mathbf{x})\}$. If the estimation is carried out by local sample moments (4.3), the local stationarity of the data is implicitly assumed. This assumption is not valid in regions with more than one tissue, particularly on transitions, and therefore the estimation can be biased.

4.3.2 Estimation along multiple MRI scans

These methods estimate the noise map $\sigma(\mathbf{x})$ (or equivalently the noise variance map $\sigma^2(\mathbf{x})$) using multiple replicas (repetitions) $M_{(k)}(\mathbf{x})$ for $k = 1, 2, \ldots, K$ (see the scheme in Fig. 4.4). The results obtained with the methods serve as *silver standard* references in the evaluation processes of spatially variant noise estimation algorithms from a one single image.

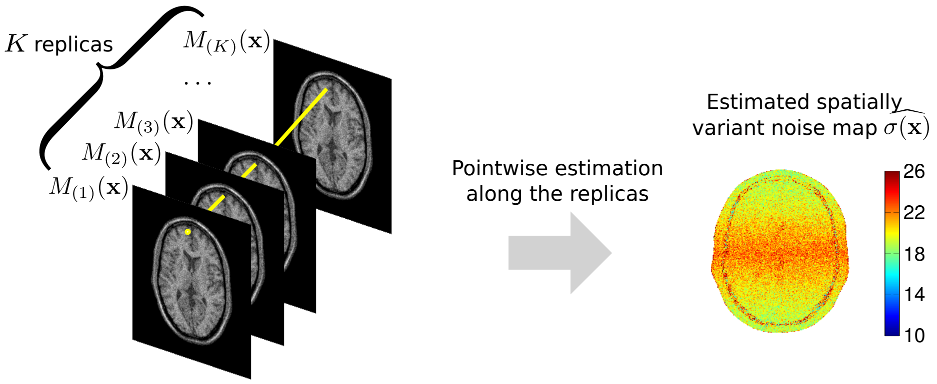

Figure 4.4: The general scheme of the noise estimation along the replicas. The estimation is performed pointwisely along the images $M_{(k)}(\mathbf{x})$.

1. DeVore et al. 2000
   The noise variance map $\sigma^2(\mathbf{x})$ is estimated along with the underlying signal amplitude $A_T(\mathbf{x})$ across the replicas $M_{(k)}(\mathbf{x})$ in an iterative way:

$$\widehat{A_{k+1}(\mathbf{x})} = \left\langle \frac{I_1\left(\frac{\widehat{A_k(\mathbf{x})}}{\widehat{\sigma_k^2(\mathbf{x})}} M_{(k)}(\mathbf{x})\right)}{I_0\left(\frac{\widehat{A_k(\mathbf{x})}}{\widehat{\sigma_k^2(\mathbf{x})}} M_{(k)}(\mathbf{x})\right)} M_{(k)}(\mathbf{x}) \right\rangle_k \tag{4.50}$$

   and

$$\widehat{\sigma_{k+1}^2(\mathbf{x})} = \max\left\{ \frac{1}{2}\langle M_{(k)}^2(\mathbf{x})\rangle_k - \frac{1}{2}\widehat{A_k^2(\mathbf{x})},\ 0 \right\}, \tag{4.51}$$

   where $\langle M_{(k)}^p(\mathbf{x})\rangle_k$ is defined as follows:

$$\langle M_{(k)}^p(\mathbf{x})\rangle_k = \frac{1}{K} \sum_{k\in\{1,2,\ldots,K\}} M_{(k)}^p(\mathbf{x}), \quad p \in \mathbb{Z}. \tag{4.52}$$

   The initialization process of the EM algorithm is obtained by the method of moments:

$$\widehat{A_0(\mathbf{x})} = \left[2\left(\langle M_{(k)}^2(\mathbf{x})\rangle_k\right)^2 - \langle M_{(k)}^4(\mathbf{x})\rangle_k \right]^{\frac{1}{4}}, \tag{4.53}$$

$$\widehat{\sigma_0^2(\mathbf{x})} = \frac{1}{2}\left[\langle M_{(k)}^2(\mathbf{x})\rangle_k - \widehat{A_0^2(\mathbf{x})} \right]. \tag{4.54}$$

   The algorithm stops after reaching k_{max} iterations.

2. Landman et al. 2009b
   The noise map $\sigma(\mathbf{x})$ is estimated using Q_n estimator (4.10):

$$\widehat{\sigma(\mathbf{x})} = Q_n\left(\{k \in \{1,2,\ldots,K\} : \varepsilon_{(k)}(\mathbf{x})\}\right), \tag{4.55}$$

   where $\varepsilon_{(k)}(\mathbf{x})$ is the residual, which we define as follows[10]:

$$\varepsilon_{(k)}(\mathbf{x}) = M_{(k)}(\mathbf{x}) - \langle M_{(k)}(\mathbf{x})\rangle_k. \tag{4.56}$$

   Again, the re-estimation procedure is applied after removing the observations $M_{(k)}(\mathbf{x})$ with lower local SNR than the adaptive computed threshold $t(\mathbf{x})$:

$$t(\mathbf{x}) = \min\left\{ 5,\ \underset{k\in\{1,2,\ldots,K\}}{\text{median}} \left(\frac{M_{(k)}(\mathbf{x})}{\widehat{\sigma(\mathbf{x})}} \right) - 3 \right\}. \tag{4.57}$$

3. Maximov et al. 2012
   The raw noise map $\sigma_{\text{raw}}(\mathbf{x})$ is obtained using MAD estimator along the repetitions $M_{(k)}(\mathbf{x})$ as follows:

$$\widehat{\sigma_{\text{raw}}(\mathbf{x})} = 1.4826 \cdot \underset{k\in\{1,2,\ldots,K\}}{\text{median}} \left| M_{(k)}(\mathbf{x}) - \underset{l\in\{1,2,\ldots,K\}}{\text{median}} \left(M_{(l)}(\mathbf{x}) \right) \right|. \tag{4.58}$$

   The correction factor (4.15) is also applied to (4.58) to obtain the final noise map $\widehat{\sigma(\mathbf{x})}$. However, the sample estimator of the mean in (4.17) is calculated along the replicas $M_{(k)}(\mathbf{x})$ using (4.52) rather than in a local neighbourhood.

---

[10] Landman et al. 2009b assume multiple contrast type examinations to estimate the noise map. Since we use the same contrast type for all images $M_{(k)}(\mathbf{x})$ we can define the biophysical model to be the pointwise average along all the replicas.

Table 4.2: Extra parameters used by the state-of-the-art methods in our experiments.

Method	Parameters
Estimation from a single image $M(\mathbf{x})$	
DeVore et al. 2000	$k_{\max} = 10$
Goossens et al. 2006	Daubechies7 (db7) wavelet is used for the SWT decomposition
Delakis et al. 2007	db7 wavelet is used for the SWT decomposition, the directional analysis is not used (see Delakis et al. 2007 for more details)
Landman et al. 2009b	BM4D algorithm is used to provide the biophysical model of the MRI data, BM4D algorithm uses default parameters (Maggioni and Foi 2012)
Manjón et al. 2010	the image $M(\mathbf{x})$ is smoothed in a 3×3 window to obtain $\langle M(\mathbf{x})\rangle_{\mathbf{x}}$ for eq. (4.13), NLM: size of patches equals 5×5, size of the search window equals 11×11, $\theta_{\mathrm{ERR}} = 1.0 \times 10^{-6}$, the formula (4.17) uses 5×5 windows to estimate $\langle M(\mathbf{x})\rangle_{\mathbf{x}}$
Rajan et al. 2011	NLM: size of patches equals 5×5, size of the search window equals 11×11, $n_b = 1000$, the range filter (4.22) is applied in a 3×3 window
Pan et al. 2012	8×8 DCT bases are used for (4.23), local sample estimators of p–th raw moments in (4.25) and (4.26) are calculated in 5×5 windows,
Maggioni and Foi 2012	the parameters are set according to the authors recommendations
Maximov et al. 2012	$\theta_{\mathrm{ERR}} = 1.0 \times 10^{-6}$, the formula (4.17) uses 5×5 windows to estimate $\langle M(\mathbf{x})\rangle_{\mathbf{x}}$
Liu et al. 2014	$\theta_{\mathrm{ERR}} = 1.0 \times 10^{-6}$, the formula (4.17) uses 5×5 windows to estimate $\langle M(\mathbf{x})\rangle_{\mathbf{x}}$
Borrelli et al. 2014	NLM: size of patches equals 5×5, size of the search window equals 11×11, median filter (4.36) uses 5×5 windows, $\theta_{\mathrm{ERR}} = 1.0 \times 10^{-6}$, the formula (4.17) uses 5×5 windows to estimate $\langle M(\mathbf{x})\rangle_{\mathbf{x}}$
Tabelow et al. 2015	$k_{\max} = 10$, the number of the receiver coils is assumed to be one (i.e., $L = 1$), other parameters are set according to the authors recommendations
Manjón et al. 2015	NLM: size of patches equals 5×5, size of the search window equals 11×11, $N = K = 25$, the guided image (4.43) is calculated in a 3×3 window, the parameter θ in (4.46) is calculated as $\theta = \mathrm{SNR}(\mathbf{x}) = \frac{\langle M(\mathbf{x})\rangle_{\mathbf{x}}}{\widehat{\sigma_{\mathrm{raw}}(\mathbf{x})}}$, 5×5 window is used to calculate $\langle M(\mathbf{x})\rangle_{\mathbf{x}}$ for local SNR, final smoothing of the noise map (4.45) is performed in a 11×11 window as $\langle\widehat{\sigma(\mathbf{x})}\rangle_{\mathbf{x}}$
Aja-Fernández et al. 2015b	$\sigma_{\mathrm{f}} = 3.4$, DeVore's EM algorithm (4.1, 4.2) is used to calculate $\mathbb{E}\{M(\mathbf{x})\}$ for T_1-weighted MRI data, and the SWT decomposition with db7 wavelet is arranged for T_2- and PD-weighted MRI data, local SNR is estimated using DeVore's EM algorithm (4.1–4.2) with $k_{\max} = 10$ as $\mathrm{SNR}(\mathbf{x}) = \widehat{A_k(\mathbf{x})}/\widehat{\sigma_k(\mathbf{x})}$, 3×3 window is used for DeVore's algorithm
Estimation along multiple scans $M_{(k)}(\mathbf{x})$	
DeVore et al. 2000	$k_{\max} = 10$
Landman et al. 2009b	no parameters required
Maximov et al. 2012	$\theta_{\mathrm{ERR}} = 1.0 \times 10^{-6}$
Glenn et al. 2015	the raw noise variance map is smoothed using isotropic Gaussian filter of size 5×5 with standard deviation set to $\sigma_{\mathrm{Glenn}} = 5$
Sample standard deviation along the replicas	no parameters required

4. Glenn et al. 2015
   The raw noise variance map is estimated using the formula[11]:

$$\widehat{\sigma^2_{\mathrm{raw}}(\mathbf{x})} = \left(\frac{K}{K-1}\right)\left[\langle M^2_{(k)}(\mathbf{x})\rangle_k - \left(\langle M_{(k)}(\mathbf{x})\rangle_k\right)^2\right]. \tag{4.59}$$

Then, the raw noise variance map (4.59) is smoothed using Gaussian low-pass filter to obtain the final noise variance pattern $\widehat{\sigma^2(\mathbf{x})}$. The coefficients of circularly symmetric

---

[11] Glenn et al. 2015 calculate the noise variance map for each diffusion-sensitizing gradient direction followed by averaging the results along all directions. Since we have only one contrast type data, we skip this step.

Gaussian filter can be defined for any $\mathbf{p} \in \eta(\mathbf{x})$ as follows:

$$G_{\sigma_{\text{Glenn}}}(\mathbf{p}) = \frac{1}{2\pi\sigma^2_{\text{Glenn}}} \exp\left(-\frac{\|\mathbf{x}-\mathbf{p}\|_2^2}{2\sigma^2_{\text{Glenn}}}\right), \tag{4.60}$$

where $\|\cdot\|$ is the ℓ^2–norm and σ_{Glenn} is the standard deviation (same for both directions).

5. Sample standard deviation along the replicas
   We refer to this simple approach as a *silver standard* method for spatially variant nc-χ estimation. The straightforward way to estimate the noise standard deviation $\sigma(\mathbf{x})$ might be:

$$\widehat{\sigma(\mathbf{x})} = \sqrt{\langle M^2_{(k)}(\mathbf{x})\rangle_k - \left(\langle M_{(k)}(\mathbf{x})\rangle_k\right)^2}. \tag{4.61}$$

   Note that the estimator (4.61) is biased for Rician and nc-χ signals for low SNR, and it should be applied to AWGN data only.

4.3.3 Specific parameters used by the state-of-the-art methods

All reference techniques presented in section 4.3.1 use squared windows of size 5×5 to obtain the noise estimate in a local neighbourhood $\eta(\mathbf{x})$ except for DeVore's EM algorithm, where 3×3 window is observed to be optimal. A short characterization of additional parameters used by the state-of-the-art methods is included in Table 4.2:

4.4 Quantitative evaluation of the methods

The accuracy of noise estimators in synthetic MRI data experiments is evaluated using pointwise relative error (RE) of an estimate $\widehat{\sigma_i(\mathbf{x})}$ for i–th repetition of the experiment (Fig. 4.5):

$$\text{RE}_i(\mathbf{x}) = \frac{\left|\widehat{\sigma_i(\mathbf{x})} - \sigma(\mathbf{x})\right|}{\sigma(\mathbf{x})}, \tag{4.62}$$

where $\sigma(\mathbf{x})$ is the *ground truth* noise map. Then, the REs are pointwisely averaged along R repetitions:

$$\text{RE}(\mathbf{x}) = \frac{1}{R}\sum_{i=1}^{R} \text{RE}_i(\mathbf{x}). \tag{4.63}$$

While the former measure is used in visual inspections of the methods, the latter one is employed in quantitative numerical evaluations. To this end, the parameter $\text{RE}(\mathbf{x})$ is spatially averaged across the foreground area Ω_Δ of the image to get one single value for a given SNR level. We refer to this spatially averaged parameter as $\overline{\text{RE}}$.

Furthermore, we define the variance (VAR) of the parameter $\text{RE}(\mathbf{x})$ as the pointwise variance along the repetitions (Fig. 4.5):

$$\text{VAR}(\mathbf{x}) = \frac{1}{R-1}\sum_{i=1}^{R} \left(\text{RE}_i(\mathbf{x}) - \text{RE}(\mathbf{x})\right)^2. \tag{4.64}$$

In a similar fashion to $\text{RE}(\mathbf{x})$, we spatially average $\text{VAR}(\mathbf{x})$ over the area Ω_Δ to get the variance of the estimator for a given SNR. The spatially averaged parameter is referred then as $\overline{\text{VAR}}$.

To detect the foreground area Ω_Δ of the image $M(\mathbf{x})$, we used a simple thresholding followed by a morphological closing operator. This operator removes small objects and fills the holes in a thresholded binary image.

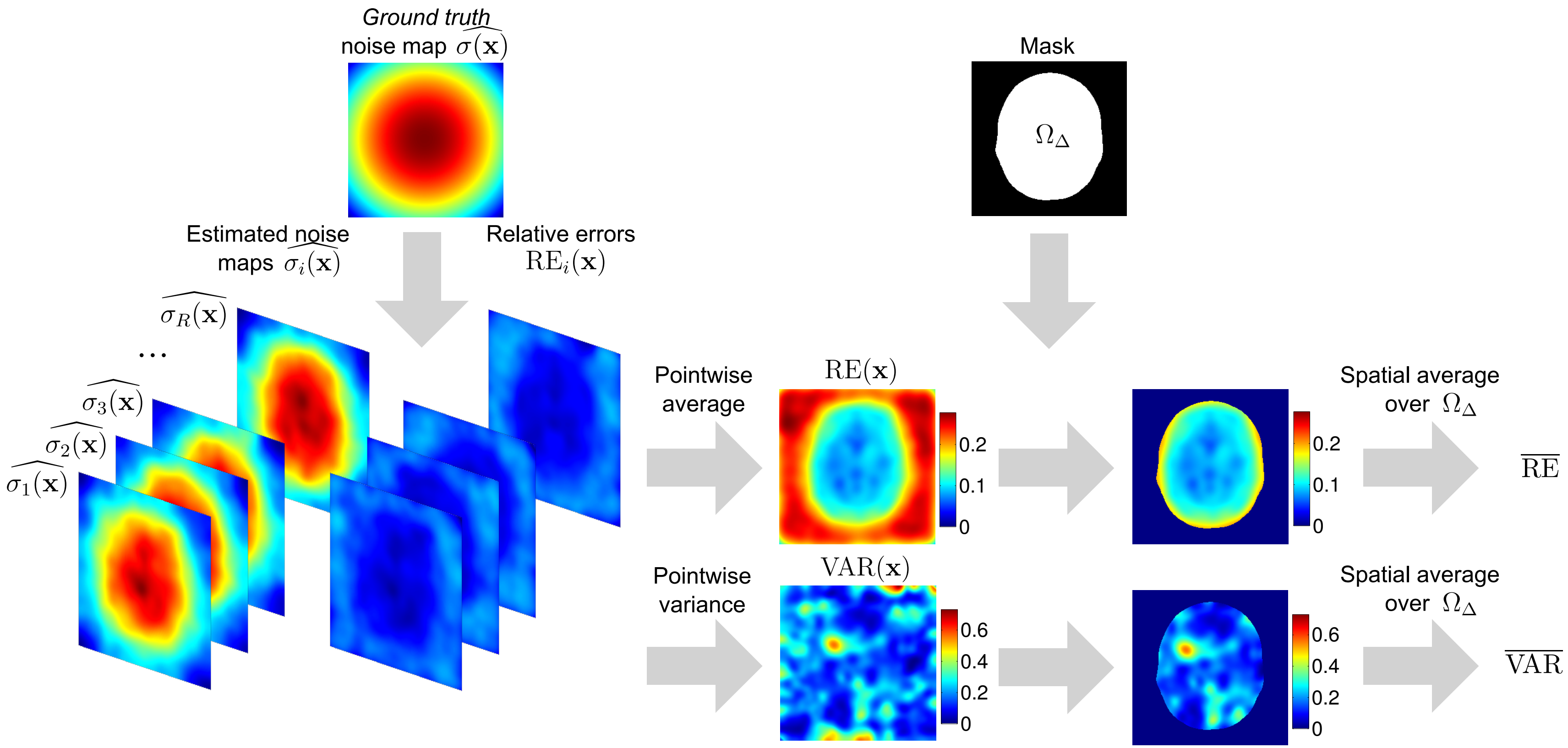

Figure 4.5: Averaging process of the quantitative parameters $\mathrm{RE}(\mathbf{x})$ (4.63) and $\mathrm{VAR}(\mathbf{x})$ (4.64). The white pixels of the binary mask determine the foreground area Ω_Δ of the image $M(\mathbf{x})$.

The morphological closing operator is defined as follows (Gonzalez and Woods 2008, Parker 1997):

$$M_{\mathrm{fg}} = (M_{\mathrm{b}} \oplus \mathcal{S}) \ominus \mathcal{S}, \tag{4.65}$$

where $M_{\mathrm{b}} = M_{\mathrm{b}}(\mathbf{x})$ is the thresholded binary image, $\mathcal{S}$ is the structuring element and $M_{\mathrm{fg}} = M_{\mathrm{fg}}(\mathbf{x})$ is the final mask of the foreground area Ω_{Δ} of the image $M(\mathbf{x})$. Two operations are needed for (4.65) namely the dilation and the erosion of the image. The dilation of the binary image M_{b} using the structuring element $\mathcal{S}$ is given by:

$$M_{\mathrm{b}} \oplus \mathcal{S} = \left\{\mathbf{p} \colon \mathcal{S}'(\mathbf{p}) \cap M_{\mathrm{b}}(\mathbf{x}) \neq \emptyset\right\}, \tag{4.66}$$

where $\mathcal{S}'$ is the reflection of $\mathcal{S}$ defined as:

$$\mathcal{S}' = \{\mathbf{w} \colon \mathbf{w} = -\mathbf{p}, \quad \text{for} \quad \mathbf{p} \in \mathcal{S}\}. \tag{4.67}$$

The erosion of the binary image M_{b} by $\mathcal{S}$ is defined then by:

$$M_{\mathrm{b}} \ominus \mathcal{S} = \{\mathbf{p} \colon \mathcal{S}(\mathbf{p}) \subseteq M_{\mathrm{b}}(\mathbf{x})\}. \tag{4.68}$$

4.5 Conclusions and remarks

In this chapter we presented the most up-to-date state-of-the-art survey of noise estimation in non-stationary Rician, nc-χ and Gaussian distributed signals. These methods are employed then to estimate spatially variant noise patterns in accelerated parallel MRI acquisitions in the contribution part of the thesis.

The methods extensively illustrated in section 4.3.1 are used to infer about noise characteristics from a single image without any additional information about the acquisition process. The algorithms from section 4.3.2 are arranged to provide *silver standard* references along multiple repetitions (replicas) of the data. The estimators are used for those experiments, where the repeated acquisitions are available.

In section 4.3.3 we provided a complete list of extra parameters used by the state-of-the-art methods from sections 4.3.1 and 4.3.2. Although the methods use different paradigms and tunable parameters to estimate local noise level, we tried to find a common denominator for all of them. For Maggioni and Foi 2012, Tabelow et al. 2015 and Aja-Fernández et al. 2015b we used the third-party code along with standard parameters suggested by the authors. We note that not all of the authors exactly specify the parameters of the methods used in their experiments. For example, Pan et al. 2012 do not define the size of a DCT basis, while Rajan et al. 2011 do not provide the number of bins n_b used for the histogram (4.21).

Eventually, the noise variance estimates $\widehat{\sigma^2(\mathbf{x})}$ coming from DeVore et al. 2000, Goossens et al. 2006, Delakis et al. 2007, Rajan et al. 2011, Pan et al. 2012, Borrelli et al. 2014 and Glenn et al. 2015 are squared for consistent comparisons with other methods in all experiments. Moreover, some methods presented in section 4.3.1 (Rajan et al. 2011, Maggioni and Foi 2012, Tabelow et al. 2015, Manjón et al. 2015) were originally proposed to deal with stacked images. We apply them for single MRI slices in our experiments. Last but not least, although the estimated noise maps are reliable in the foreground areas only, we calculate them also in the background regions in some quantitative experiments.

Part II

Contributions

Chapter 5

Non-stationary Rician noise estimation

Contents

5.1 Introduction

In this chapter we propose a new method to automatically retrieve spatially variant noise patterns from non-stationary Rician distributed images. This kind of non-stationary noise is particularly interesting, since we can find it in accelerated parallel SENSE MRI acquisitions.

Our proposal is developed by defining a variance-stabilizing transformation (VST) for Rician distribution. The VST enables to transform the magnitude MRI data from a non-stationary variate to a stationary Gaussian variate. Afterwards, the spatially variant noise pattern is estimated by a homomorphic filtering procedure. The proposal is compared to fourteen most relevant state-of-the-art methods in non-stationary Rician and Gaussian noise estimation and additionally to four methods providing *silver standard* references using multiple replicas of the data.

Compared to the previous noise estimation methods, the pioneering nature and the main advantages of our proposal over the state-of-the-art are as follows:

1. It uses the exact theoretical transformation (the variance-stabilizing transformation) from Rician to Gaussian distribution rather than Gaussian assumptions followed by empirical corrections. Consequently, the noise estimation method is robust for the whole range of SNRs (from very low SNRs – non-stationary Rayleigh distribution to very high SNRs – non-stationary Gaussian distribution).
2. It estimates the noise patterns using only a single image without the need to extract the background or foreground regions.
3. Pre-scans, repeated acquisitions or a biophysical model of the MRI data are not required for the estimation procedure.
4. Any additional information from the acquisition process like sensitivity profiles or noise matrices of the receiver coils is also unnecessary. Clearly, a method is vendor independent and it works for a retrospectively reconstructed MRI data.
5. The proposal can be applied to different contrast type examinations including T_1-, T_2-, and PD-weighted MRI data sets.
6. The method is not affected by the granular effect as the final step of the algorithms is the homomorphic filtering procedure.
7. The proposal is fast since it is implemented using discrete convolutions and pointwise operations.

This chapter is organized as follows. In section 5.2 we introduce the VST methodology, the asymptotic stabilizer for Rician distribution and present numerical models proposed by Foi 2011. Then, we derive a new transformation for stationary Rician distribution, which provides a robust stabilization in the whole set of SNRs in comparison with Foi's models. Later on, in section 5.3, we adapt the proposed VST to non-stationary Rician distribution and introduce the spatially variant Rician noise estimation scheme in the VST framework. In section 5.4 we present the set of synthetic and real MRI data sets employed in the evaluation process of our proposal against the state-of-the-art. Section 5.5 is devoted to experimental verification of our proposal. At first, we confirm the robustness of the proposed VST procedure for the whole range of SNRs throughout the statistical hypothesis testing. Then, we show several quantitative and qualitative experiments in comparison with the state-of-the-art methods presented in section 4.3. Finally, in the last paragraph of the chapter the concluding remarks are drawn.

5.2 The variance-stabilizing transformation

The VST principle has recently gained a lot of attention in digital image processing field, both in theoretical and application aspects. Although the VST is usually applicable to medical and astronomical data, it is not only limited to these sources, and it can also be related to modelling the raw data from a charge-coupled device (CCD) sensor (Foi 2009a, Pyatykh and Hesser 2014 and Zhang et al. 2015a) or lossy compression of hyperspectral images (Zemliachenko et al. 2014). In the field of medical imaging, the VST is principally used to deal with Poisson (Makitalo and Foi 2011, Zhang et al. 2008), Poisson-Gaussian (Boulanger et al. 2010, Mäkitalo and Foi 2013, Bajic et al. 2016), and Rician noise (Foi 2011). In this chapter, however, we are interested in modelling Rician distributed signals. The VST in context of processing the MRI data is a particularly useful methodology, since it has been applied to efficiently solve various signal and image processing problems, e.g., stationary signal-dependent noise estimation (Foi 2011), image denoising (Maggioni et al. 2013, Yang et al. 2015, Zhang et al. 2015b), diffusion-weighted MRI data reconstructions (Shafiee et al. 2015) and the analysis of resting-state fMRI data (Thompson and Fransson 2016).

5.2.1 Asymptotic stabilizer for Rician distributed data

In this section we briefly present the basic definition of VST and therefore we put the VST into the context of modelling Rician distributed noise. Without loss of generality, we use the symbol $M\colon \Omega \to \mathbb{R}$ to denote both a real-valued Rician RV and its realization (an observation). For the sake of argument, let us assume now that M follows **stationary** Rician distribution with noncentrality parameter A_T and scale σ (i.e., $M \sim \mathrm{Rice}(A_T, \sigma)$). The PDF of this RV is defined as follows:

$$p(M|A_T,\sigma) = \frac{M}{\sigma^2}\exp\left(-\frac{M^2+A_T^2}{2\sigma^2}\right) I_0\left(\frac{A_T M}{\sigma^2}\right), \quad M \geqslant 0, \tag{5.1}$$

where $I_0(\cdot)$ is the modified Bessel function of the first kind and zeroth order.

The fundamental inconvenience of modelling Rician distributed data is the signal-dependence of the second-order central moment (the variance). Let us recall this functional dependence of the variance $\mathrm{Var}\{M\}$ on the underlying signal A_T:

$$\mathrm{Var}\{M\} = \mathrm{Var}\left\{M|A_T,\sigma\right\} = A_T^2 + 2\sigma^2 - \frac{\pi\sigma^2}{2}\,{}_1F_1^2\left(-\frac{1}{2};1;-\frac{A_T^2}{2\sigma^2}\right). \tag{5.2}$$

Our goal here is to change the signal-dependent nature of Rician noise to a signal-independent one. Specifically, we are interested in a function $f_{\mathrm{stab}}\colon \mathbb{R} \mapsto \mathbb{R}$, which transforms the Rician RV to another RV with a constant variate, i.e., $\mathrm{Var}\left\{f_{\mathrm{stab}}(M|\sigma)\right\} = 1$. Moreover, the new RV $f_{\mathrm{stab}}(M|\sigma)$ should not depend on the noncentrality parameter A_T anymore (Bartlett 1947).

In the most fundamental way, this transform can be found using the first-order Taylor approximation of $f_{\mathrm{stab}}(M|\sigma)$ about a point $M = M_0$:

$$f_{\mathrm{stab}}(M|\sigma) = f_{\mathrm{stab}}(M_0|\sigma) + (M - M_0)\left.\frac{df_{\mathrm{stab}}}{dM}\right|_{M=M_0} + R_1(M), \tag{5.3}$$

where $R_1(M)$ is the remainder term of the expansion.

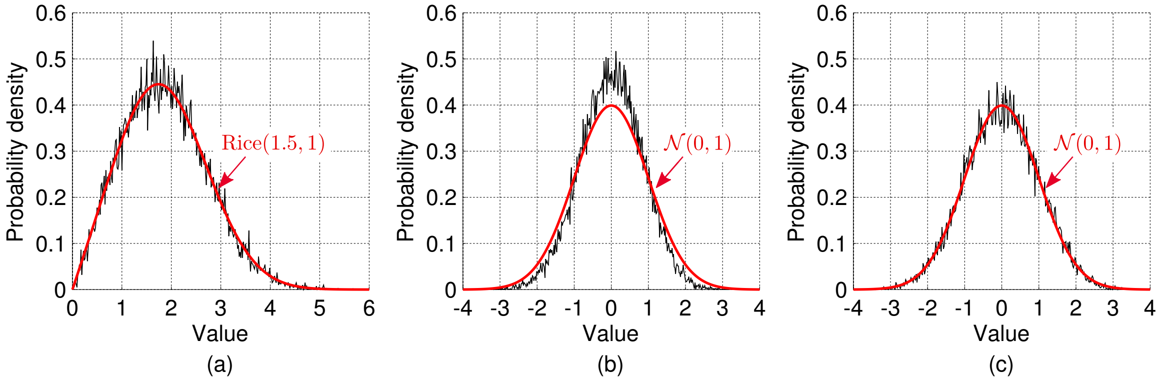

Figure 5.1: (a) The PDF of Rician RV and the normalized histogram of simulated Rician distributed data with a noncentrality parameter $A_T = 1.5$ and the scale $\sigma = 1$. (b) The normalized histogram of noise component retrieved from Rician distributed sample and (c) the normalized histogram of noise component retrieved from variance-stabilized Rician sample. The evaluation uses $N = 25000$ samples and $n_b = 350$ bins for all histograms.

Neglecting the remainder term $R_1(M)$ and taking the variance on both sides of eq. (5.3) result in[1]:

$$\mathrm{Var}\{f_{\mathrm{stab}}(M|\sigma)\} \approx \mathrm{Var}\{M\} \cdot \left(\frac{df_{\mathrm{stab}}}{dM} \bigg|_{M=M_0} \right)^2 . \tag{5.4}$$

Finally, imposing $\mathrm{Var}\{f_{\mathrm{stab}}(M|\sigma)\} = 1$ and $M_0 = \widetilde{A}$, and taking the indefinite integral of (5.4) we have the general formula of VST for Rician RV (Foi 2011):

$$f_{\mathrm{stab}}(M|\sigma) = \int^{M} \frac{1}{\sqrt{\mathrm{Var}\{M|\widetilde{A},\sigma\}}} d\widetilde{A}, \tag{5.5}$$

where $\mathrm{Var}\{M|\widetilde{A},\sigma\}$ is the conditional variance of M, i.e., the variance of the RV M is expressed in the function of the parameter $\widetilde{A}$. The formula (5.5) defines the transformation f_{stab}, which turns the signal-dependent Rician RV into a signal-independent RV i.e., the RV with a constant and finite variance. Henceforth, the extracted noise component from Rician distributed data may be considered as AWGN process (e.g., standard normal distribution $\mathcal{N}(0,1)$). This is depicted in Fig. 5.1, where the noise component was extracted from simulated Rician distributed data and the variance-stabilized Rician data. Therefore, Gaussianity assumptions can be applied at further stages of the data processing pipeline, e.g., noise estimation, tissue classification.

5.2.2 Foi's approach

In Foi 2011, the asymptotic stabilizer for Rician distributed RV inferring from the integral definition (5.5) and the approximation of the conditional variance for large values of A_T has been derived:

$$f_{\mathrm{stab}}(M|\sigma) = \sqrt{\frac{M^2}{\sigma^2} - \frac{1}{2} + a}, \quad a \in \mathbb{R}, \tag{5.6}$$

---

[1] We use two basic properties of variance operator:

- $\mathrm{Var}\{cM\} = c^2\mathrm{Var}\{M\}$ for $c \in \mathbb{R}$,
- $\mathrm{Var}\{c + M\} = \mathrm{Var}\{M\}$ for $c \in \mathbb{R}$.

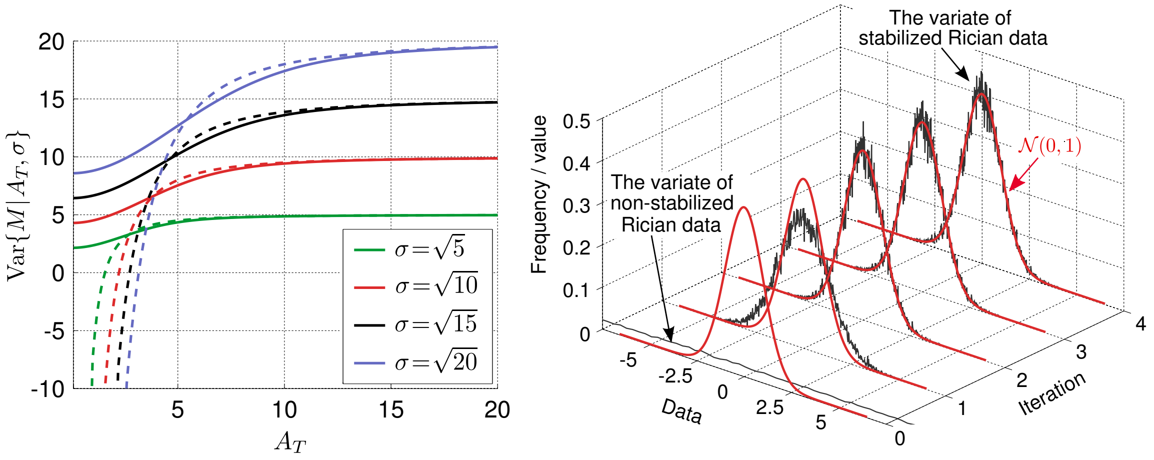

(a) (b)

Figure 5.2: (a) The conditional variance of Rician RV Var $\{M|A_T,\sigma\}$ for different values of σ. The solid lines present the theoretical variance (5.2), while dashed lines show the approximation of the conditional variance for larger values of A_T (5.7). (b) The results of the iterative stabilization scheme (5.9) for stationary Rician distribution. The variate of the stabilized Rician data follows standard normal distribution $\mathcal{N}(0,1)$.

where $M \geqslant \frac{\sqrt{2}}{2}\sigma$ and $a \in \mathbb{R}$ is an arbitrary constant. The conditional variance Var $\{M|A_T,\sigma\}$ used in the derivation procedure (5.5) is given by (see Fig. 5.2a):

$$\mathrm{Var}\,\{M|A_T,\sigma\} \approx \sigma^2 - \frac{\sigma^4}{2A_T^2}. \tag{5.7}$$

The transformation (5.6) is correct for higher SNR levels, however, it does not work satisfactorily for lower SNR (i.e., SNR < 5). To handle low SNRs properly, Foi resorts to numerical models of the stabilizer f obtained from a direct optimization procedure (Foi 2009b). The optimization procedure incorporates the accuracy of stabilization in terms of standard deviation, smoothness of the transformation f, proximity of f to (5.6) as M approaches $M_{\max}$ and the closeness of the inverse transformation to Rician ML estimate of the parameter A_T:

$$\begin{aligned} F(f) = \int_0^{A_{\max}} \left(\mathrm{std}\{f(M)|\widetilde{A},1\} - 1\right)^2 d\widetilde{A} + \lambda_{\mathrm{smooth}} \int_0^{M_{\max}} \left(\frac{d^2 f}{d\widetilde{M}^2}\right)^2 d\widetilde{M} \\ + \lambda_{\mathrm{asympt}} \int_0^{M_{\max}} \frac{1}{(M_{\max} - \widetilde{M} + \varepsilon)^4} \left(f(\widetilde{M}) - f_{\mathrm{stab}}(\widetilde{M}|1)\right)^2 d\widetilde{M} \\ + \lambda_{\mathrm{inverse}} \int_0^{M_{\max}} \left(\mathcal{V}_f(f(\widetilde{M})) - \widehat{A_{\mathrm{ML}}}(\widetilde{M})\right)^2 d\widetilde{M}, \end{aligned} \tag{5.8}$$

where:

- $\mathrm{std}\{f(M)|\widetilde{A},1\}$ is the standard deviation of the stabilized data M by the function f,
- $\varepsilon = 2.0 \times 10^{-16}$ is used to ensure the well-posedness of the solution,
- $\mathcal{V}_f\colon \mathbb{E}\{f(M)|A_T,1\} \to A_T$ is the exact unbiased inverse for the estimation of A_T, where $\mathbb{E}\{f(M)|A_T,1\}$ is the conditional expectation,
- $\widehat{A_{\mathrm{ML}}}$ is the Rician ML estimate obtained from a single sample M as the solution of the equation $\frac{M}{A_T}\frac{I_1(A_T M)}{I_0(A_T M)} = 1$ for $M > \sqrt{2}$ and $\widehat{A_{\mathrm{ML}}} = 0$ for $M \leqslant \sqrt{2}$,

- $\lambda_{\text{smooth}} \geqslant 0$, $\lambda_{\text{asympt}} \geqslant 0$, $\lambda_{\text{inverse}} \geqslant 0$ are the penalty parameters of different factors in the cost function (5.8).

Note that the cost function f in (5.8) is defined for the finite range of the parameter A_T (i.e., $A_T \in [0, A_{\max}]$) and $\sigma = 1$. Consequently, the variable M is considered for $[0, M_{\max}]$ because of the exponential decay of the PDF (5.1).

The numerically precalculated function $f(M)$ from eq. (5.8) along with the asymptotic stabilizer $f_{\text{stab}}(M)$ (5.6) are iteratively applied to stationary Rician distributed data M turning it into the equivalent one with standard AWGN component (Fig. 5.2b):

$$\begin{cases} \widehat{\sigma}_1 = \mathfrak{C}\{M\}, \\ \widehat{\sigma}_{k+1} = \widehat{\sigma}_k \mathfrak{C}\{f_{\widehat{\sigma}_k}(M)\} \quad \text{for} \quad k \geqslant 1, \end{cases} \tag{5.9}$$

where $f_{\widehat{\sigma}_k}$ is the VST with the noise level parameter $\sigma = \widehat{\sigma}_k$ and $\mathfrak{C}\{\cdot\}$ is an estimator of standard deviation of the data, e.g., MAD estimator.

The approach is computationally intensive, since the stabilization is achieved in the presented iterative scheme (5.9). Specifically, each k–th iteration of the algorithm requires the estimation of the parameter σ to stabilize the data M in $(k+1)$–th iteration in a more efficient way. Although the method is acceptable for stationary Rician noise as it was originally proposed, the estimation of the parameter σ locally leads to significant under- or overestimations due to a small number of samples used by MAD estimator. As long as the procedure is applied for stationary Rician noise (a single value σ), it delivers the state-of-the-art results. However, applying Foi's approach to the non-stationary Rician distributed data (like those observed in SENSE MRI acquisitions) requires the estimation of σ in a local manner. This potential generalization of Foi's approach leads to a biased estimator of σ, especially near edges and tissue transitions. For that reason, the Rician data are further incorrectly stabilized, i.e., the variate of the transformed data does not exactly follow Gaussian distribution.

5.2.3 Robust numerical model

In this section, we present our proposal of VST for Rician distributed data. We present a single-shot VST, which overcomes the main problems of conventional stabilizers for Rician distributed data:

- it does not need an iterative scheme to estimate the parameter σ,
- it stabilizes robustly the data for the whole range of SNRs.

This proposal requires an additional parameter to be estimated namely the local SNR. Though the inclusion of an additional parameter in the derivation of the stabilizer could seem an inconvenience, we will show that both the initialization of σ and the estimation of the SNR per pixel can be efficiently achieved avoiding main problems of other solutions.

Firstly, we start with the parametrization of eq. (5.6) using a vector parameter $\mathbf{\Theta} = (\theta_1, \theta_2)$ as follows:

$$f_{\text{stab}}(M|\sigma, \mathbf{\Theta}) = \sqrt{\max\left\{\theta_1^2 \frac{M^2}{\sigma^2} - \theta_2,\ 0\right\}} + a, \quad a \in \mathbb{R}, \tag{5.10}$$

where the operator $\max\{\cdot,\cdot\}$ avoids a negative argument of the square root function. Note that for $(\theta_1, \theta_2) = (1, 0.5)$ the parametrized eq. (5.10) becomes the asymptotic one (5.6).

Table 5.1: The parameters of the optimization cost function (5.8) used by Foi 2011.

	Model A	Model B
λ_{asympt}	1	1
λ_{smooth}	10^{-2}	10^{-4}
λ_{inverse}	$10^{-\frac{1}{2}}$	0

In order to cope with different behaviours of the stabilizer, the parameters θ_1 and θ_2 should be tuned accordingly to the SNR of the signal M. This can be efficiently achieved by using a numerical optimization procedure providing θ_1 and θ_2 as a function of the SNR with the following optimization criterion:

$$\boldsymbol{\Theta}_{\text{opt}} = \arg\min_{\boldsymbol{\Theta}} J\left(f_{\text{stab}}(M|\sigma, \boldsymbol{\Theta})\right) \tag{5.11}$$

with $\boldsymbol{\Theta}_{\text{opt}} = (\theta_{1\text{opt}}, \theta_{2\text{opt}})$ and $J\colon \mathbb{R}^2 \mapsto \mathbb{R}$ being a cost function to be minimized:

$$\begin{aligned} J\left(f_{\text{stab}}(M|\sigma, \boldsymbol{\Theta})\right) = {} & \lambda_1 \cdot \varphi(1 - \operatorname{Var}\left\{f_{\text{stab}}(M|\sigma, \boldsymbol{\Theta})\right\}) \\ & + \lambda_2 \cdot \varphi(\text{Skewness}\{f_{\text{stab}}(M|\sigma, \boldsymbol{\Theta})\}) \\ & + \lambda_3 \cdot \varphi(\text{ExcessKurtosis}\{f_{\text{stab}}(M|\sigma, \boldsymbol{\Theta})\}), \end{aligned} \tag{5.12}$$

where the weighting parameters meet the condition $\lambda_1 + \lambda_2 + \lambda_3 = 1$ and $\varphi\colon \mathbb{R} \to \mathbb{R}$ is a non-negative convex function, e.g., $\varphi(x) = x^2$.

Secondly, we define the components of (5.12) in terms of r–th raw moments of f_{stab}–transformed Rician distribution:

$$\begin{aligned} \operatorname{Var}\left\{f_{\text{stab}}(M|\sigma, \boldsymbol{\Theta})\right\} &= m_2 - m_1^2, \\ \text{Skewness}\left\{f_{\text{stab}}(M|\sigma, \boldsymbol{\Theta})\right\} &= \frac{m_3 - 3m_1m_2 + 2m_1^3}{(m_2 - m_1^2)^{\frac{3}{2}}}, \\ \text{ExcessKurtosis}\left\{f_{\text{stab}}(M|\sigma, \boldsymbol{\Theta})\right\} &= \frac{m_4 - 4m_1m_3 + 6m_1^2m_2 - 3m_1^4}{(m_2 - m_1^2)^2} - 3, \end{aligned} \tag{5.13}$$

where r–th raw moment for Rician distribution is given by:

$$\begin{aligned} m_r = \mathbb{E}\left\{f^r_{\text{stab}}(M|\sigma, \boldsymbol{\Theta})\right\} &= \int_0^\infty f^r_{\text{stab}}(\widetilde{M}|\sigma, \boldsymbol{\Theta}) p(\widetilde{M}|A_T, \sigma) d\widetilde{M} \\ &= \int_0^\infty f^r_{\text{stab}}(\widetilde{M}|\sigma, \boldsymbol{\Theta}) \frac{\widetilde{M}}{\sigma^2} \exp\left(-\frac{\widetilde{M}^2 + A_T^2}{2\sigma^2}\right) I_0\left(\frac{A_T\widetilde{M}}{\sigma^2}\right) d\widetilde{M}. \end{aligned} \tag{5.14}$$

The cost function (5.12) favours a unitary variance, zero skewness and zero excess kurtosis[2], enforcing the desired Gaussian behaviour of the transformed RV. Note that one can also resort to additional parameters, which potentially can be used in the optimization cost function (5.12), e.g., higher order moments or measures of the shape of a probability distribution like L–moments (Hosking 1992).

The numerical optimization of (5.11) has been carried out for $\sigma = 1$ and logarithmically increasing A_T between 0.001 and 20. We used Nelder-Mead optimization method and the adaptive Gauss-Kronrod quadrature to numerically evaluate the integrals defined by (5.14) over the interval $M \in [0;\ 30]$ (Nelder and Mead 1965, Shampine 2008).

---

[2] The excess kurtosis is defined as $\text{ExcessKurtosis}\{X\} = \text{Kurtosis}\{X\} - 3$. The kurtosis of a Gaussian RV equals three.

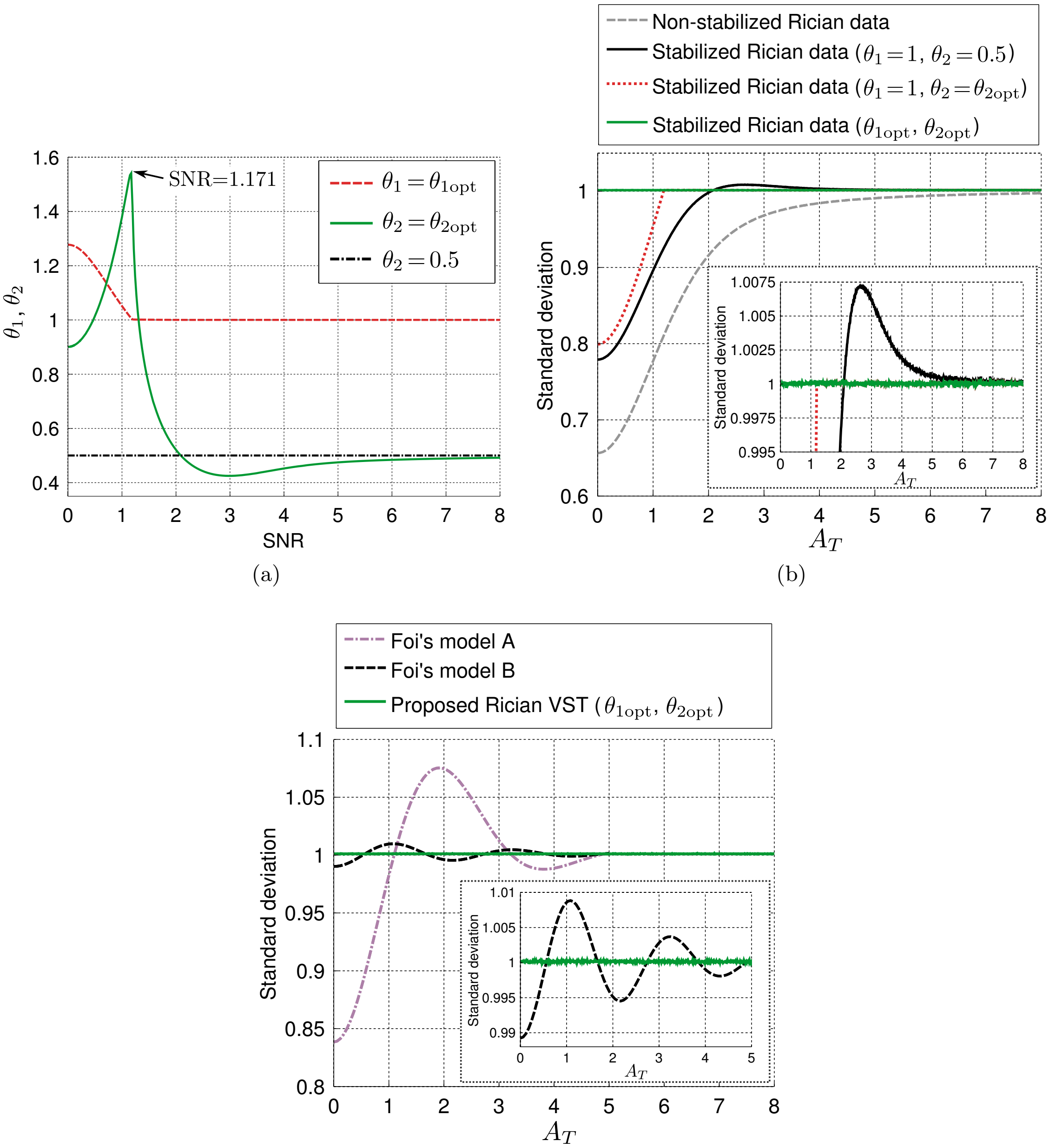

(a)

(b)

(c)

Figure 5.3: (a) Optimized parameters $\theta_{1\mathrm{opt}}$ and $\theta_{2\mathrm{opt}}$ of eq. (5.12) in terms of SNR for $(\lambda_1, \lambda_2, \lambda_3) = (0.998, 0.001, 0.001)$, (b) comparison of standard deviations between non-stabilized Rician distributed data and the stabilized ones using different parameters θ_1 and θ_2, and (c) standard deviation of the variance-stabilizing parametric approach $f_{\mathrm{stab}}(M|\sigma, \mathbf{\Theta}_{\mathrm{opt}})$ compared to Foi's stabilizers A and B (see the Table 5.1). The parameter $\sigma = 1$ is used for all simulations.

The results of the optimization procedure for $(\lambda_1, \lambda_2, \lambda_3) = (0.998, 0.001, 0.001)$ and the convex function $\varphi(x) = x^2$ in terms of SNR of the signal (SNR $= A_T/\sigma$) are shown in Fig. 5.3a. The set of parameters $(\lambda_1, \lambda_2, \lambda_3)$ for the optimization procedure was found in an empirical way. We remark that higher values of the parameters λ_2 and λ_3 lead to a better fitting process of skewness and excess kurtosis to Gaussian case. However, due to the trade-off between variance and skewness/kurtosis, the variate of the variance-stabilized Rician data is no longer unitary. Note that a breakdown point at SNR $= 1.171$ is observed

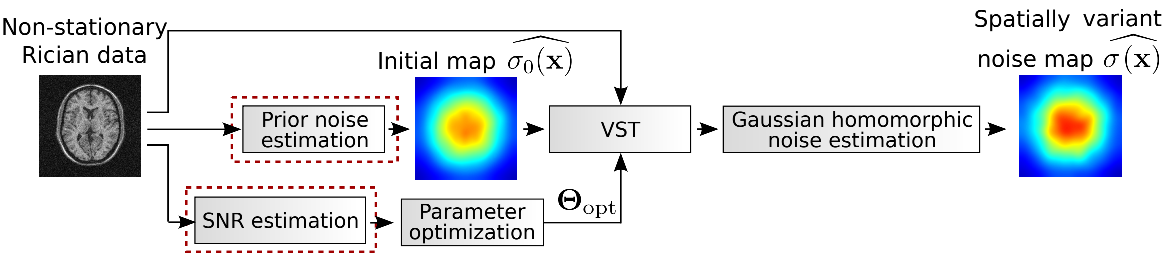

Figure 5.4: General scheme of our proposal in non-stationary Rician noise estimation. The method requires the prior noise map estimate $\widehat{\sigma_0(\mathbf{x})}$ and the SNR map to stabilize the data (VST block). The red rectangles indicate the interchangeable modules of the algorithm.

for $\theta_{2\text{opt}}$. Next, we compare the standard deviations of variance-non-stabilized and variance-stabilized Rician data including different variants of the parameters θ_1 and θ_2 (Fig. 5.3b). For $(\theta_1, \theta_2) = (1, \theta_{2\text{opt}})$, the accuracy of variance-stabilizing procedure slightly improved in comparison with asymptotic stabilizer $(\theta_1, \theta_2) = (1, 0.5)$, however, the solution is still not the optimal one at low SNRs (SNR < 1.171). Substantial improvements of the stabilization results can be observed simultaneously applying the optimized pair of the parameters θ_1 and θ_2 to eq. (5.10), i.e., $(\theta_1, \theta_2) = (\theta_{1\text{opt}}, \theta_{2\text{opt}})$. The results obtained from the proposed parametric VST are then compared to Foi's models A and B (Fig. 5.3c, Table 5.1)[3]. The new parametric form of VST efficiently achieved the stabilization of the Rician RV for the whole range of SNRs from very low SNRs – Rayleigh RV to very high SNRs – Gaussian RV.

The strong point of our proposal is that the stabilization of the data is obtained in a single-shot, i.e., the data are transformed in a non-iterative way. To apply the transformation f_{stab} on a real MR image we need a prior noise map $\sigma_0(\mathbf{x})$ and the local SNR of the image SNR($\mathbf{x}$). Since the main application of the VST in this work is the noise estimation, the monotonicity of the function f_{stab} is not required. Finally, we remind, although the comparison with Foi's models was carried out for stationary Rician distributed data, our proposal will be employed for non-stationary Rician distributed images (see section 5.3.1).

5.3 Non-stationary Rician noise estimation

In this section, we define the spatially variant noise estimation scheme for non-stationary Rician data using the proposed VST framework. To our best knowledge, the VST has not been used in any form in context of modelling the non-stationary signal-dependent Rician noise.

5.3.1 Spatially variant Rician noise estimation

We propose a new methodology to estimate the non-stationary Rician noise following the pipeline presented in Fig. 5.4.

The first step of the process is the application of the parametric VST (5.10) to the magnitude MR image. The VST transforms signal-dependent Rician data to a signal-independent Gaussian-like equivalent. Once the data are stabilized, we can use a non-stationary Gaussian noise estimator to extract the local noise level from the image. In this work, we will make use of the Gaussian homomorphic approach, recently proposed in Aja-Fernández et al. 2015b, since it has proved its accuracy and robustness.

---

[3] The MATLAB source code of the variance-stabilizing transformation proposed by Foi is available at `http://www.cs.tut.fi/~foi/RiceOptVST/`.

Firstly, the above-mentioned parametric VST is applied pointwisely to the raw noisy magnitude MR image $M(\mathbf{x})$ as follows:

$$\widetilde{M}(\mathbf{x}) = \widehat{\sigma_0(\mathbf{x})} \cdot f_{\text{stab}}(M(\mathbf{x})|\widehat{\sigma_0(\mathbf{x})}, \theta_{1\text{opt}}(\mathbf{x}), \theta_{2\text{opt}}(\mathbf{x})), \tag{5.15}$$

where $\widehat{\sigma_0(\mathbf{x})}$ is the prior (pre-estimated) noise map, $\theta_{1\text{opt}}(\mathbf{x})$ and $\theta_{2\text{opt}}(\mathbf{x})$ are the optimized to local SNR transformation parameters:

$$\begin{aligned} \theta_{1\text{opt}}(\mathbf{x}) &= (\theta_1 \circ \text{SNR})(\mathbf{x}), \\ \theta_{2\text{opt}}(\mathbf{x}) &= (\theta_2 \circ \text{SNR})(\mathbf{x}) \end{aligned} \tag{5.16}$$

with the pointwise SNR defined as:

$$\text{SNR}(\mathbf{x}) = \frac{A_T(\mathbf{x})}{\sigma(\mathbf{x})}. \tag{5.17}$$

Using the formula (5.10) and assuming $a = 0$, we can express eq. (5.15) as follows:

$$\widetilde{M}(\mathbf{x}) = \widehat{\sigma_0(\mathbf{x})} \sqrt{\max\left\{ \theta^2_{1\text{opt}}(\mathbf{x}) \frac{M^2(\mathbf{x})}{\widehat{\sigma^2_0(\mathbf{x})}} - \theta_{2\text{opt}}(\mathbf{x}),\ 0 \right\}}, \tag{5.18}$$

where $\widetilde{M}(\mathbf{x})$ is the variance-stabilized MR image multiplied by the initial noise map estimate $\widehat{\sigma_0(\mathbf{x})}$. Henceforth, the transformed image (5.18) can be assumed as a noise-free component $\widetilde{A_T}(\mathbf{x})$ corrupted with additive Gaussian distributed noise $N(\mathbf{x}; 0, \sigma^2(\mathbf{x}))$ with zero mean and spatially variant variance $\sigma^2(\mathbf{x})$:

$$\widetilde{M}(\mathbf{x}) \approx \widetilde{A_T}(\mathbf{x}) + N(\mathbf{x}; 0, \sigma^2(\mathbf{x})) = \widetilde{A_T}(\mathbf{x}) + \sigma(\mathbf{x}) \cdot N(\mathbf{x}; 0, 1). \tag{5.19}$$

In the **second** stage of the noise estimation algorithm, we need to separate the low-frequency component $\sigma(\mathbf{x})$ from (5.19). Earlier, however, we remove a DC component (center the data) from the signal $\widetilde{M}(\mathbf{x})$ (5.19):

$$\widetilde{M_{\text{C}}}(\mathbf{x}) = \widetilde{M}(\mathbf{x}) - \mathbb{E}\{\widetilde{M}(\mathbf{x})\} = \sigma(\mathbf{x}) \cdot N(\mathbf{x}; 0, 1), \tag{5.20}$$

where $\mathbb{E}\{\cdot\}$ is the expectation operator applied to the variance-stabilized image, e.g., an edge preservation low-pass filter (see section 5.3.3 for details). Next, we resort to the homomorphic filtering principle for multiplicative components (Aja-Fernández et al. 2015b). Specifically, we apply the transformation $g(x) = \log x$ to (5.20), separate the low-frequency noise map and finally return to the spatial domain of the image using inverse transformation $g^{-1}(y) = \exp(y)$. So, we apply g to the absolute value of the centered data (5.20) and then we separate the components as follows:

$$\log|\widetilde{M_{\text{C}}}(\mathbf{x})| = \log|\sigma(\mathbf{x}) \cdot N(\mathbf{x}; 0, 1)| = \underbrace{\log \sigma(\mathbf{x})}_{\text{low frequency}} + \underbrace{\log|N(\mathbf{x}; 0, 1)|}_{\text{high frequency}}. \tag{5.21}$$

Since the multiplicative character of noise (5.20) can be represented as two additive components in log domain (5.21), we resort to low-pass filter $\text{LPF}_{\sigma_\text{f}}$ to clear out the high-frequency contribution of $\log|N(\mathbf{x}; 0, 1)|$:

$$\text{LPF}_{\sigma_\text{f}}\left\{\log\left|\widetilde{M_{\text{C}}}(\mathbf{x})\right|\right\} \approx \log \sigma(\mathbf{x}) - \text{LPF}_{\sigma_\text{f}}\left\{\log|N(\mathbf{x}; 0, 1)|\right\}, \tag{5.22}$$

where $\text{LPF}_{\sigma_\text{f}}\{\log|N(\mathbf{x}; 0, 1)|\} \approx \mathbb{E}\{\log|N(\mathbf{x}; 0, 1)|\}$. Considering that $|N(\mathbf{x}; 0, 1)|$ follows a half-Gaussian distribution and assuming that the low-pass filter $\text{LPF}_{\sigma_\text{f}}$ is a good approximation of the mean, we can write:

$$\text{LPF}_{\sigma_\text{f}}\left\{\log\left|\widetilde{M_{\text{C}}}(\mathbf{x})\right|\right\} \approx \log \sigma(\mathbf{x}) - \log\sqrt{2} - \frac{\gamma}{2} \tag{5.23}$$

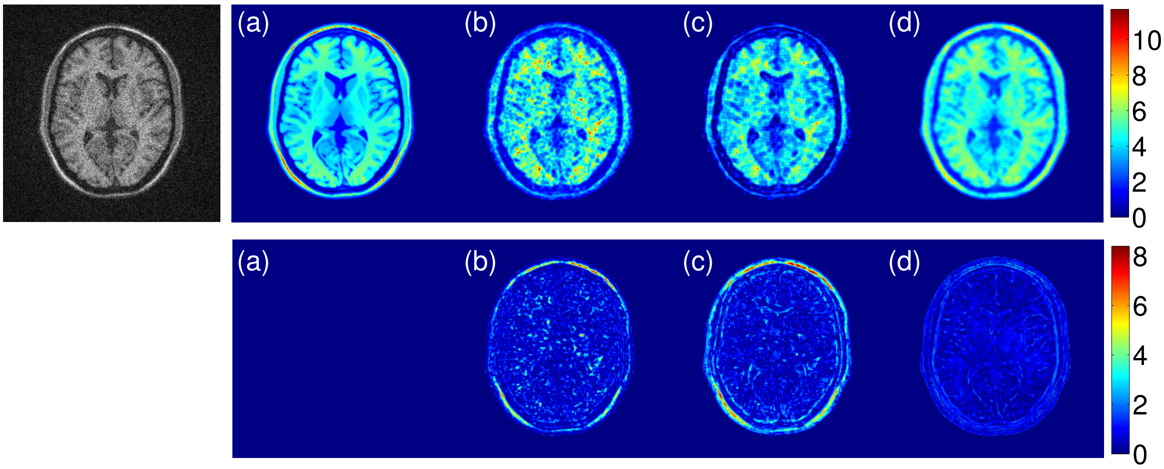

Figure 5.5: Estimated local SNR maps from synthetic noisy T_1-weighted MR image (top row) and absolute differences between the *ground truth* and the estimated SNR maps (bottom row): (a) the *ground truth*, (b) DeVore et al. 2000, (c) Koay and Basser 2006, (d) **our proposal**. The estimation is carried out in 5×5 windows. The maximum SNR of the noisy MR image in the foreground area equals $\mathrm{SNR}_{\mathrm{max}} = 10.64$.

with γ being the Euler-Mascheroni constant. After some basic rearrangements of (5.23) we have:

$$\mathrm{LPF}_{\sigma_{\mathrm{f}}}\left\{\log\left|\widetilde{M_{\mathrm{C}}}(\mathbf{x})\right|\right\} + \frac{\gamma}{2} \approx \log\left(\frac{\sigma(\mathbf{x})}{\sqrt{2}}\right). \tag{5.24}$$

Finally, the inverse transformation $g^{-1}(y) = \exp(y)$ of (5.24) leads to a new spatially variant Rician noise estimator defined by the formula:

$$\widehat{\sigma(\mathbf{x})} = \sqrt{2}\exp\left(\mathrm{LPF}_{\sigma_{\mathrm{f}}}\left\{\log\left|\widetilde{M_{\mathrm{C}}}(\mathbf{x})\right|\right\} + \frac{\gamma}{2}\right). \tag{5.25}$$

with $\mathrm{LPF}_{\sigma_{\mathrm{f}}}$ being a low-pass Gaussian filter with a standard deviation σ_{f}.

5.3.2 SNR estimation

The reliable estimation of local SNR is a key issue of our proposal of spatially variant Rician noise estimation. Both factors of the SNR definition (5.17) namely $A_T(\mathbf{x})$ and $\sigma(\mathbf{x})$ can be estimated simultaneously using EM algorithm as demonstrated in DeVore et al. 2000 (see section 4.3.1 for more details). This approach is characterized by a high level of granularity of the estimated parameters $\widehat{A_T(\mathbf{x})}$ and $\widehat{\sigma(\mathbf{x})}$, thus, it leads to significant under- and overestimations of the division $\widehat{A_T(\mathbf{x})}/\widehat{\sigma(\mathbf{x})}$. In this work, however, we use a local mean of the magnitude image $M(\mathbf{x})$ as the estimate of the underlying signal, $\widehat{A_T(\mathbf{x})}$. Then, we employ the method proposed by Aja-Fernández et al. 2015b to obtain the estimate of a prior noise map, $\widehat{\sigma_0(\mathbf{x})}$. This simple strategy avoids granularities of the SNR map, usually observed with DeVore et al. 2000 or Koay and Basser 2006, and it provides a more realistic SNR representation (Fig. 5.5).

5.3.3 Noise extraction procedures

Last but not least, it is important to choose a right centering procedure of the variance-stabilized data in (5.20). One straightforward approximation would be the local average in a neighborhood, as was recently shown in Aja-Fernández et al. 2015b. However, this method is prone to provide inaccurate estimates due to the presence of tissue inhomogeneities within

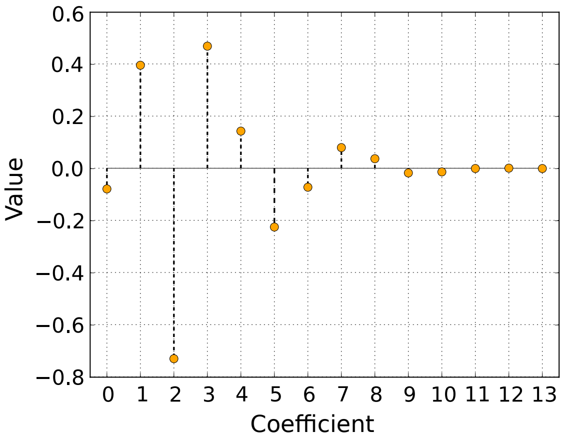

Figure 5.6: Coefficients of a decomposition high-pass filter (db7) used in 2D SWT to center the data (filtering process of the variance-stabilized image along the rows and columns).

the local window. Once again, different methods from literature could be used here. In this work, we employ two approaches: the edge-preserving bilateral filter for grayscale images (Tomasi and Manduchi 1998) and 2D SWT (Mallat 2008). One can also apply other edge-preserving and AWGN-compliant methods like non-local means filter (Buades et al. 2005) or recent advances in this field, e.g., robust guided filter (He et al. 2013) or strengthen-operate-subtract methodology (Romano and Elad 2015).

The first method used in our proposal, namely the bilateral filter, is applied to the magnitude of variance-stabilized MR image $\widetilde{M}(\mathbf{x})$ as follows:

$$\Psi(\mathbf{x}) = \frac{\sum_{\mathbf{p}\in\eta(\mathbf{x})} \psi_{\sigma_{\mathrm{g}}}(\|\mathbf{p}-\mathbf{x}\|)\psi_{\sigma_{\mathrm{r}}}(|\widetilde{M}(\mathbf{p})-\widetilde{M}(\mathbf{x})|)\widetilde{M}(\mathbf{p})}{\sum_{\mathbf{p}\in\eta(\mathbf{x})} \psi_{\sigma_{\mathrm{g}}}(\|\mathbf{p}-\mathbf{x}\|)\psi_{\sigma_{\mathrm{r}}}(|\widetilde{M}(\mathbf{p})-\widetilde{M}(\mathbf{x})|)}, \tag{5.26}$$

where $\eta(\mathbf{x})$ is a neighbourhood centered at the pixel $\mathbf{x}$, $\psi_{\sigma_{\mathrm{g}}}$ and $\psi_{\sigma_{\mathrm{r}}}$ are geometric and radiometric distances, respectively. In the basic variant of the algorithm, $\psi_{\sigma_{\mathrm{g}}}$ and $\psi_{\sigma_{\mathrm{r}}}$ are defined to be:

$$\psi_{\sigma}(x) = \exp\left(-\frac{x^2}{2\sigma^2}\right), \tag{5.27}$$

where σ is the scale parameter (standard deviation). Therefore, the results of the filtering procedure (5.26) can be subtracted from the noisy variance-stabilized image $\widetilde{M}(\mathbf{x})$ as follows:

$$\widetilde{M_{\mathrm{C}}}(\mathbf{x}) = \widetilde{M}(\mathbf{x}) - \Psi(\mathbf{x}). \tag{5.28}$$

The centering of the data can alternatively be done by the SWT, since it extracts the noise component from $\widetilde{M}(\mathbf{x})$ using the HH subband of the SWT of the image at the first scale (Mallat 2008). Specifically, to extract the noise component from the image $\widetilde{M}(\mathbf{x})$ we refer to diagonal details coefficients of the SWT decomposition:

$$\widetilde{M_{\mathrm{C}}}(\mathbf{x}) = ((\widetilde{M} \circledast g^{(r)}) \circledast g^{(c)})(\mathbf{x}), \tag{5.29}$$

where “$\circledast$” denotes the convolution operator. The convolution procedure (5.29) is performed with separable one-dimensional high-pass filter g (see Fig. 5.6), i.e., the first convolution is applied along the rows $g^{(r)}$, and the second one is applied along the columns $g^{(c)}$ of the image.

5.4 Materials and methods

In this section, we present the MRI data and spatially variant noise patterns used for the numerical experiments.

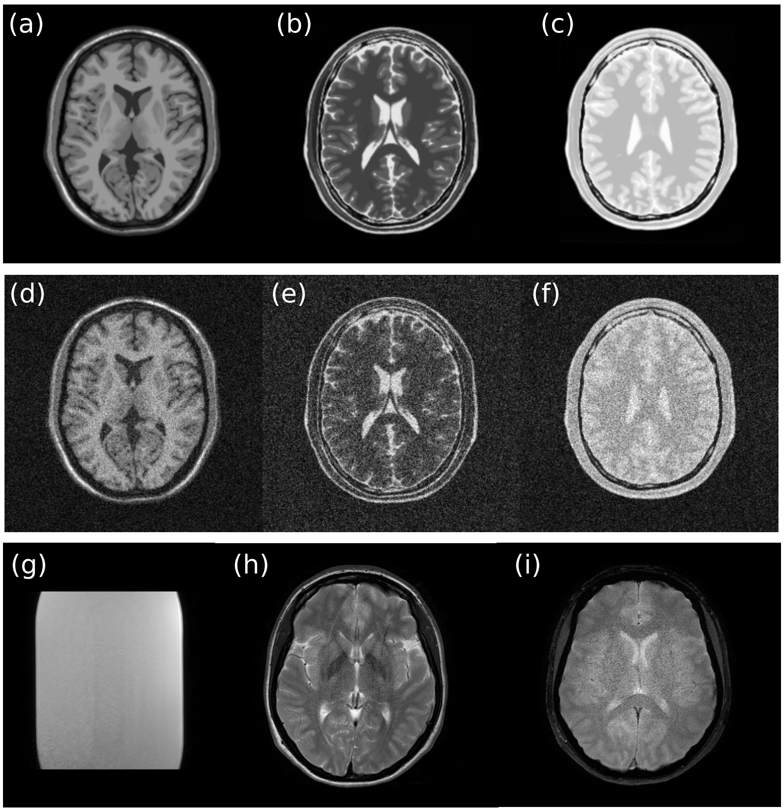

Figure 5.7: Data sets used in the experiments: (a) synthetic noise-free T_1-, (b) T_2- and (c) PD-weighted MRI data, (d) simulated noisy T_1-, (e) T_2- and (f) PD-weighted SENSE MRI data (all with $r = 2$), (g) real noisy T_1-weighted TFE SENSE MRI phantom ($r = 2$), (h) real noisy T_2-weighted TSE SENSE MRI brain data ($r = 4$) and (i) real noisy T_2-weighted FFE SENSE MRI brain data ($r = 4$).

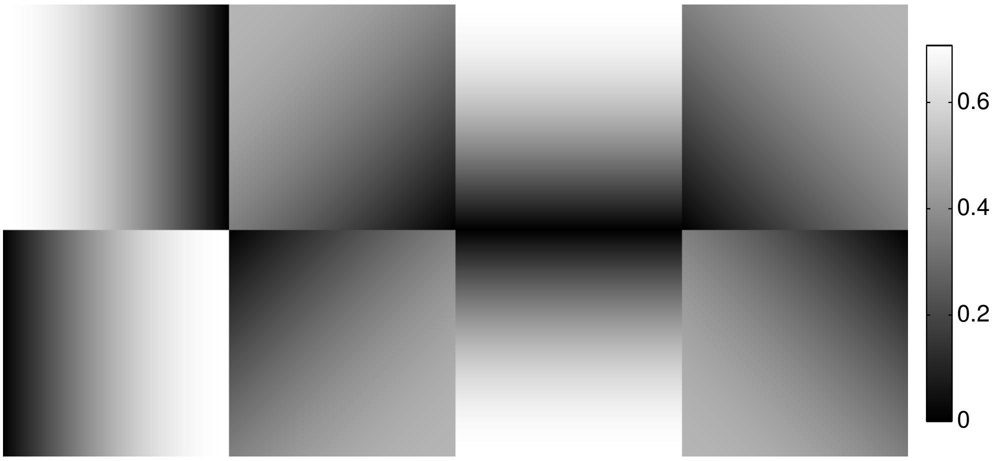

Figure 5.8: Sensitivity maps used to generate synthetic SENSE MRI data from eight receiver coils (see Fig. 5.7d–f).

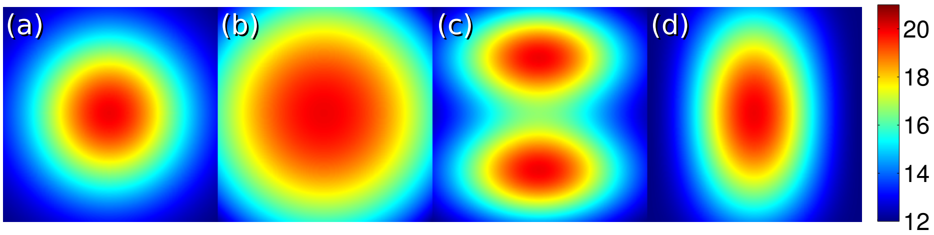

Figure 5.9: Spatially variant noise patterns used in the experiments for synthetic MRI data.

5.4.1 Materials

To verify our proposal in non-stationary Rician noise estimation, we carry out some numerical experiments using both synthetic and real MRI data. Below, we provide a brief description of the data sets used in our experiments.

1. Synthetic MR images: three brain MRI slices at different transverse planes are used, i.e., T_1-, T_2- and PD-weighted MRI data (all with intensity non-uniformity INU=0%). The data are free of noise, the background areas are set to zero, the slice thickness equals 1 mm and the intensity range of the images is normalized to $[0 - 255]$ (Fig. 5.7a–c). The synthetic data sets come from BrainWeb simulated database (Collins et al. 1998).

2. Synthetic SENSE MR images[4]: synthetic noisy T_1-, T_2- and PD-weighted MR images from BrainWeb are used to simulate Cartesian SENSE MRI reconstructions from eight receiver coils ($L = 8$) with correlations between k–th and l–th receiver coil ($k \neq l$) defined to be $\rho_{kl} = \rho$, the variance of the noise set to $\sigma_l^2(\mathbf{x}) = \sigma_l^2$ (the correlations and the noise level are the same for all L coils) and SENSE reduction factor set to $r = 2$ (Fig. 5.7d–f). The sensitivity maps used for Cartesian SENSE reconstruction are depicted in Fig. 5.8.

3. Real SENSE MRI phantom data: twenty repetitions of T_1-weighted scan of a doped ball phantom were performed using Philips Achieva 3.0T TX device (Philips Medical Systems, Best, the Netherlands) provided with a 32-channel coil system using Turbo Field Echo (TFE) sequence[5], volume size $224 \times 224 \times 59$, TR=5.264 ms / TE=2.569 ms, slice thickness 3.20 mm, and reduction factor $r = 2$ (Fig. 5.7g).

4. *In vivo* SENSE MRI brain data: two T_2-weighted scans of the brain in transverse planes were acquired by Philips Achieva 3.0T TX scanner provided with the 32-channel head coil. The first data set was acquired using Fast Field Echo (FFE) sequence[6], volume size $240 \times 180 \times 161$, TR=3000 ms / TE=80 ms, slice thickness 3.20 mm (Fig. 5.7h), while the second one was obtained using Turbo Spin Echo (TSE)[7] (Fig. 5.7i). The $\mathbf{k}$–space was subsampled by the reduction factor $r = 4$ for both acquisitions.

The background areas of real SENSE MRI data have been automatically suppressed by the scanner during the acquisition process (see Figs. 5.7g–i).

---

[4] We used Aja-Fernández's parallel MRI simulator available at `https://www.mathworks.com/matlabcentral/fileexchange/36893-parallel-mri-noisy-phantom-simulator`.

[5] TFE is the vendor acronym for Ultrafast Gradient Echo sequence (Philips).

[6] FFE is the vendor acronym for Gradient Echo sequence (Philips).

[7] TSE is the vendor acronym for Fast Spin Echo sequence (Philips).

5.4.2 Spatially variant noise maps

In the first two synthetic noise estimation experiments, we simulate spatially variant noise patterns as shown in Fig. 5.9. These noise patterns are typically observed in accelerated parallel MRI acquisitions of the brain (Landman et al. 2009b, Manjón et al. 2010, Aja-Fernández et al. 2014a). To generate the synthetic MR image, we add complex Gaussian noise to the $\mathbf{x}$–space domain of noise-free MRI phantom, and then, we reconstruct the final magnitude noisy image $M(\mathbf{x})$ as follows:

$$M(\mathbf{x}) = \left| A_{\mathrm{re}}(\mathbf{x}) + N_{\mathrm{re}}(\mathbf{x}) + j \cdot (A_{\mathrm{im}}(\mathbf{x}) + N_{\mathrm{im}}(\mathbf{x})) \right| , \tag{5.30}$$

where $N_{\mathrm{re}}(\mathbf{x}), N_{\mathrm{im}}(\mathbf{x}) \sim \mathcal{N}\left(0, \sigma^2(\mathbf{x})\right)$ are uncorrelated Gaussian distributed noise components with scale parameter $\sigma^2(\mathbf{x})$ varying across the image and $A_{\mathrm{re}}(\mathbf{x})$, $A_{\mathrm{im}}(\mathbf{x})$ are the components of the noise-free MRI data.

5.4.3 The state-of-the-art methods and our proposal

For the sake of comparison, we used fourteen spatially variant noise estimation methods presented in section 4.3.1. These methods estimate the noise map $\sigma(\mathbf{x})$ from a single MR image $M(\mathbf{x})$ wihout any additional information from the acquisition process. Moreover, we employed four methods (section 4.3.2), which estimate the noise map $\sigma(\mathbf{x})$ from multiple scans of the same object. The methods are treated as *silver standard* references, and they are applied for those experiments, where multiple repetitions are available.

Regarding our proposal, we set the following parameters in the evaluation process:

- SNR estimation is carried out in 5 × 5 windows,
- bilateral filter (5.26) uses 5 × 5 windows, $\psi_{\sigma_{\mathrm{g}}} = 15$, $\psi_{\sigma_{\mathrm{r}}} = 120$,
- SWT (5.29) uses the db7 wavelet,
- the low pass filter (5.25) uses $\sigma_{\mathrm{f}} = 3.4$ to generate circularly symmetric Gaussian mask.

Finally, note that we used morphological operators for the detection procedure of the foreground area of the image (see section 4.4 for more details).

5.5 Experimental results and discussion

In this section we evaluate our proposal against the aforementioned state-of-the-art techniques in non-stationary Rician noise estimation. We carry out several experiments including both synthetic and real MRI data presented in section 5.4.1.

5.5.1 Statistical analysis of the underlying assumption

Before testing the quantitative and qualitative performance of proposed noise estimation method, we verified the underlying assumption of Gaussianity of the variate after stabilizing Rician distributed signal. To extract the noise component from the variance-stabilized Rician signal, we employed SWT decomposition with high-pass filter related to db7 wavelet (see Fig. 5.6). We carried out three statistical experiments on variance-stabilized Rician data:

1. Chi-square goodness-of-fit test (χ^2–test),
2. Anderson-Darling (AD) normality test,
3. Quantile-quantile (QQ) plot.

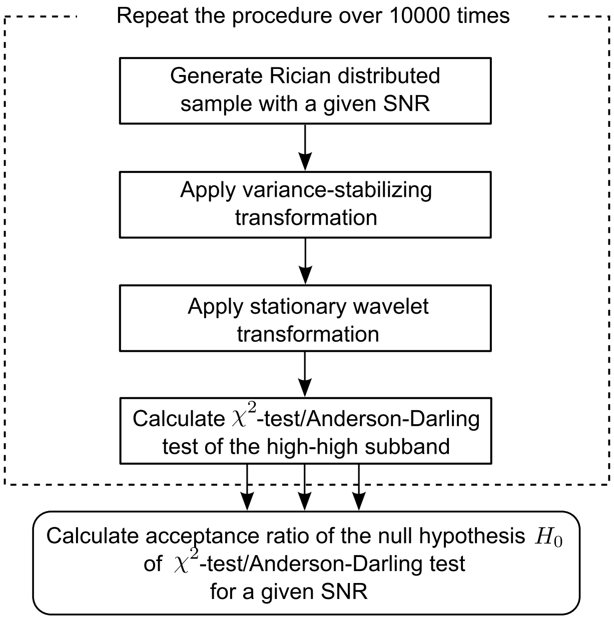

Figure 5.10: The evaluation scheme of the noise component in variance-stabilized Rician data for a given SNR level (SNR $= A_T/\sigma$) using a statistical hypothesis testing.

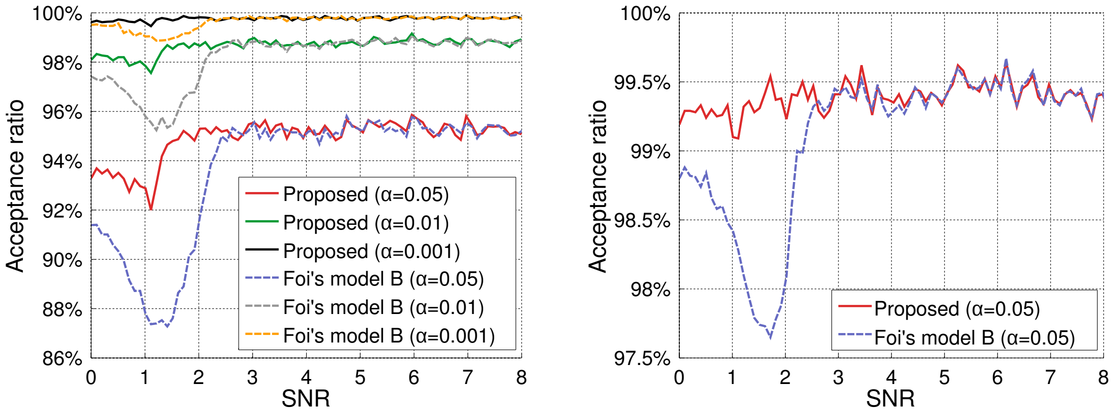

(a) (b)

Figure 5.11: Statistical tests for noise component in variance-stabilized Rician distributed signal: (a) acceptance ratio of null hypothesis H_0 in χ^2–test that the noise in variance-stabilized signal follows standard normal distribution (three significance levels are used in the experiment $\alpha \in \{0.05, 0.01, 0.001\}$) and (b) acceptance ratio of the AD normality test of the noise component at the significance level $\alpha = 0.05$.

In the **first statistical experiment**, we calculate the acceptance ratio of χ^2–test[8]. The null hypothesis H_0 states that the noise in variance-stabilized Rician distributed signal follows standard normal distribution, while the alternative hypothesis H_1 is the opposite. We repeat χ^2–test over 10000 iterations for each SNR step with sample size $N = 256$, and then we calculate the acceptance ratio of H_0 for each SNR level individually. The scheme of the experiment is summarized in Fig. 5.10. Three significance levels are used $\alpha \in \{0.05, 0.01, 0.001\}$. The results of the experiment exhibit increased acceptances of the hypothesis H_0 (for SNR < 3) using proposed VST in comparison with Foi's model B (Fig. 5.11a). The acceptances of H_0

---

[8] The routine `chi2gof` is used in the simulation (The MathWorks, Inc., Natick, MA).

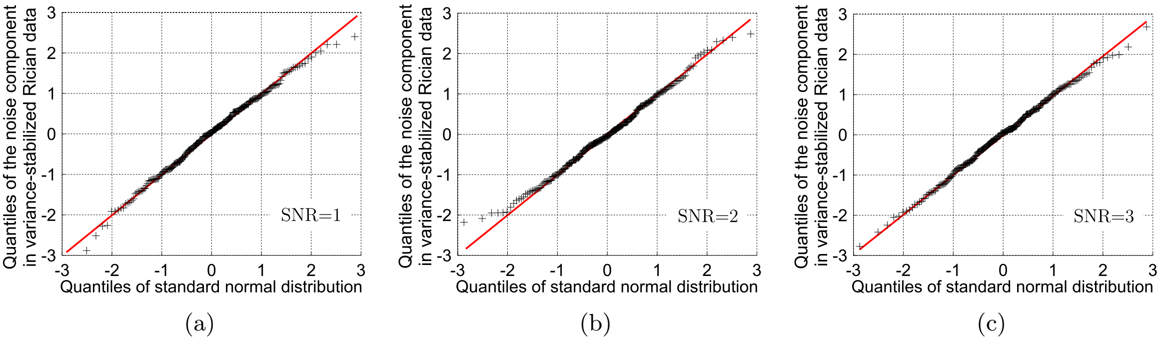

(a) (b) (c)

Figure 5.12: Quantile-Quantile plots of the stabilized noise component in Rician distributed signal using the proposed VST for different SNRs of the signal: (a) SNR $= 1$, (b) SNR $= 2$ and (c) SNR $= 3$. The red lines indicate the reference function $y = x$.

for our proposal reach at least 92%, 97.56%, 99.46% for $\alpha = 0.05$, $\alpha = 0.01$ and $\alpha = 0.001$, respectively. Note that we apply only Foi's model B for the clarity of the figures, since the model A presents much worse behaviour than the model B (compare to Fig. 5.3c).

Since χ^2–test is applied to binned data, it requires sufficiently large samples for an adequate convergence to a χ^2 distribution and it depends on selected number of bins n_b, e.g., $n_b = 1 + \log_2 N$, where N is the sample size. In the **second statistical experiment**, we employ AD test[9] to verify if the noise component in variance-stabilized Rician signal come from standard normal distributed population (see Fig. 5.10). The same statistical hypotheses H_0 and H_1 are used as in χ^2–test. The results of AD test for the significance level $\alpha = 0.05$ are depicted in Fig. 5.11b. Again, our proposal overcomes Foi's model B for low SNR and it attains at least 99.1% of H_0 acceptances.

Finally, in the **third statistical experiment**, we show QQ plot for the noise component in variance-stabilized Rician distributed data for a sample with $N = 256$ and SNR $\in \{1, 2, 3\}$ (Fig. 5.12). We relate quantiles of standard normal distribution (horizontal axis) to the quantiles of the noise component extracted from variance-stabilized Rician distributed data (vertical axis). As we can see, the points obtained from QQ experiment approximately lie on the reference line $y = x$, i.e., the noise in variance-stabilized Rician signal follows standard normal distribution.

The results obtained from three statistical experiments assure us that:

1. the assumption of normality of the noise component in variance-stabilized Rician signal by the proposed method holds for low SNRs,
2. Gaussian-dedicated methods like the SWT can be employed to recover the noise component from variance-stabilized Rician data,
3. post-correction factors proposed by Koay and Basser 2006, Manjón et al. 2015 and Aja-Fernández et al. 2015b are no longer required for Rician distribution.

---

[9] The routine `adtest` is used in the simulation (The MathWorks, Inc., Natick, MA).

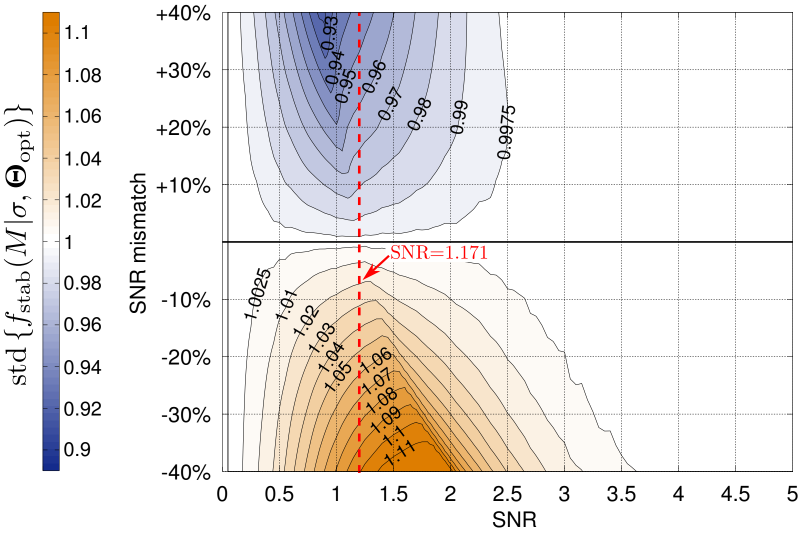

Figure 5.13: Influence of SNR mismatch on standard deviation of variance-stabilized Rician data for $\mathbf{\Theta}_{\mathrm{opt}} = (\theta_{1\mathrm{opt}}, \theta_{2\mathrm{opt}})$ (5.31). The red dashed line indicates the breakdown point of the parameter $\theta_{2\mathrm{opt}}$ (defined as in eq. (5.16)) at $\mathrm{SNR} = 1.171$ (see also Fig. 5.3a).

5.5.2 Analysis of SNR mismatch on VST procedure

In this section, we study the influence of SNR mismatch on the accuracy of the variance-stabilizing process. To this end, we generate stationary Rician distributed images of size 256×256 with SNRs between $\mathrm{SNR} = 0$ and $\mathrm{SNR} = 5$. We apply the proposed VST (5.10) with $\mathbf{\Theta}_{\mathrm{opt}}$, which is optimized to the intentionally modified SNRs between -40% and $+40\%$ of the original value. We define $\theta_{1\mathrm{opt}}$ and $\theta_{2\mathrm{opt}}$ in this experiment to be:

$$\begin{aligned} \theta_{1\mathrm{opt}}(\mathbf{x}) &= (\theta_1 \circ \mathrm{SNR}_{\mathrm{modified}})(\mathbf{x}), \\ \theta_{2\mathrm{opt}}(\mathbf{x}) &= (\theta_2 \circ \mathrm{SNR}_{\mathrm{modified}})(\mathbf{x}) \end{aligned} \tag{5.31}$$

with the modified pointwise SNR given by $\mathrm{SNR}_{\mathrm{modified}}(\mathbf{x}) = p \cdot \mathrm{SNR}(\mathbf{x})$ for $p \in [0.6;\ 1.4]$.

The results of the experiment are depicted in Fig. 5.13. The contour plot presents over-/underestimation of the sample standard deviation of variance-stabilized Rician data. We relate the underlying SNR (horizontal axis) to the SNR mismatch ($\mathrm{SNR}_{\mathrm{modified}}$), which is subsequently used to obtain the parameters $\theta_{1\mathrm{opt}}$ and $\theta_{2\mathrm{opt}}$ from eq. (5.31). As we expected, the accuracy of the stabilization process for low SNR depends on the precision of the estimated SNR level. For positive (negative) SNR mismatch, some underestimations (overestimations) of the sample standard deviation are observed in the variance-stabilized Rician data. Note that the experiment shows that a $\pm 20\%$ of SNR mismatch produces around 5% of error in the standard deviation of the stabilized data. Interestingly, the proposed VST is very robust for $\mathrm{SNR} > 3.5$ against $\pm 40\%$ SNR mismatch, where the error of the stabilized standard deviation is less than 0.25%.

5.5.3 Robustness analysis of the proposed algorithm

In this section, we analyse the robustness of the proposed variance-stabilizing homomorphic filter. Before, however, we present the qualitative results from the stabilization process and we evaluate different procedures used to extract the noise component from synthetic brain MRI data. Then, we study the state-of-the-art methods, which potentially can be employed to obtain the noise map estimate $\widehat{\sigma_0(\mathbf{x})}$. The initial noise map $\widehat{\sigma_0(\mathbf{x})}$ is used then to stabilize the noisy MRI data as shown in Fig. 5.4.

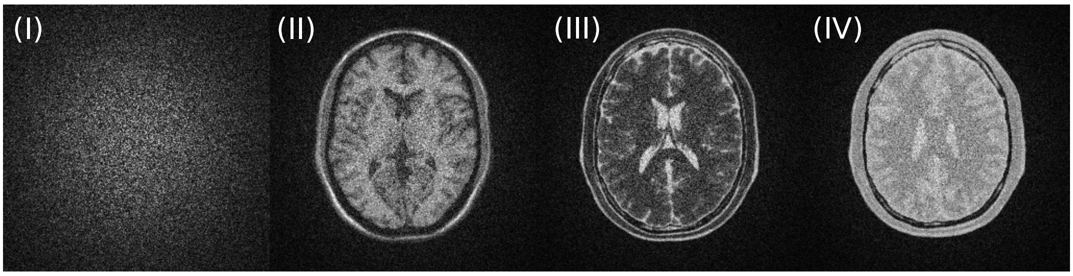

(a) Noisy data (non-stationary Rician noise follows the noise pattern from Fig. 5.9a)

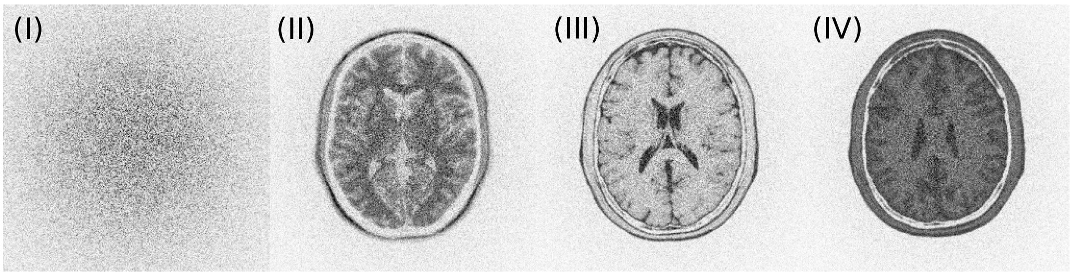

(b) Noisy data (non-stationary Rician noise follows the noise pattern from Fig. 5.9a) – negative image

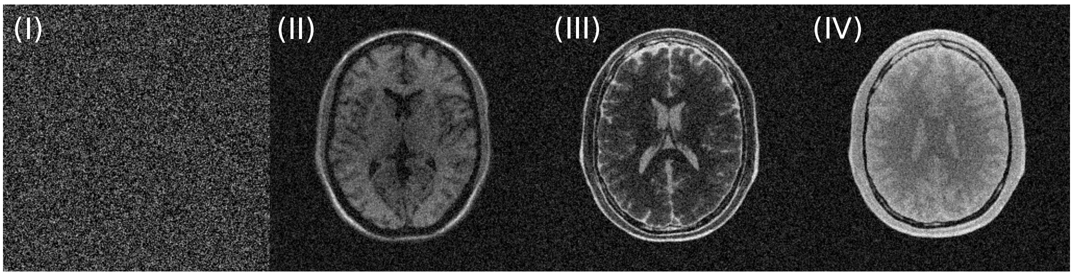

(c) Variance-stabilized data using our proposal

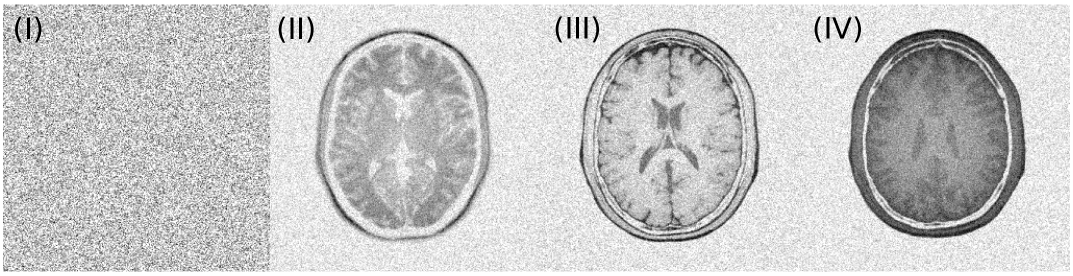

(d) Variance-stabilized data using our proposal – negative image

Figure 5.14: (a, b) The noisy non-stationary Rician distributed data and (c, d) the corresponding variance-stabilized equivalents using the proposed VST: (I) non-stationary Rayleigh noise (SNR = 0), (II) synthetic T_1-, (III) T_2- and (IV) PD-weighted brain MRI data. Note that we provide negatives of the noisy images, which might be more visually acceptable rather than the orginal images.

In the **first robustness test**, we visually relate noisy non-stationary Rician distributed data to the variance-stabilized equivalents using the proposed approach (Fig. 5.14). We generate the non-stationary Rician data using synthetic T_1-, T_2- and PD-weighted brain MRI data sets and the noise pattern from Fig. 5.9a. The reconstruction of the magnitude Rician data follows eq. (5.30). The proposed VST stabilizes the magnitude data even if the underlying signal amplitude equals zero, i.e., the data follows a non-stationary Rayleigh distribution (Fig. 5.14I).

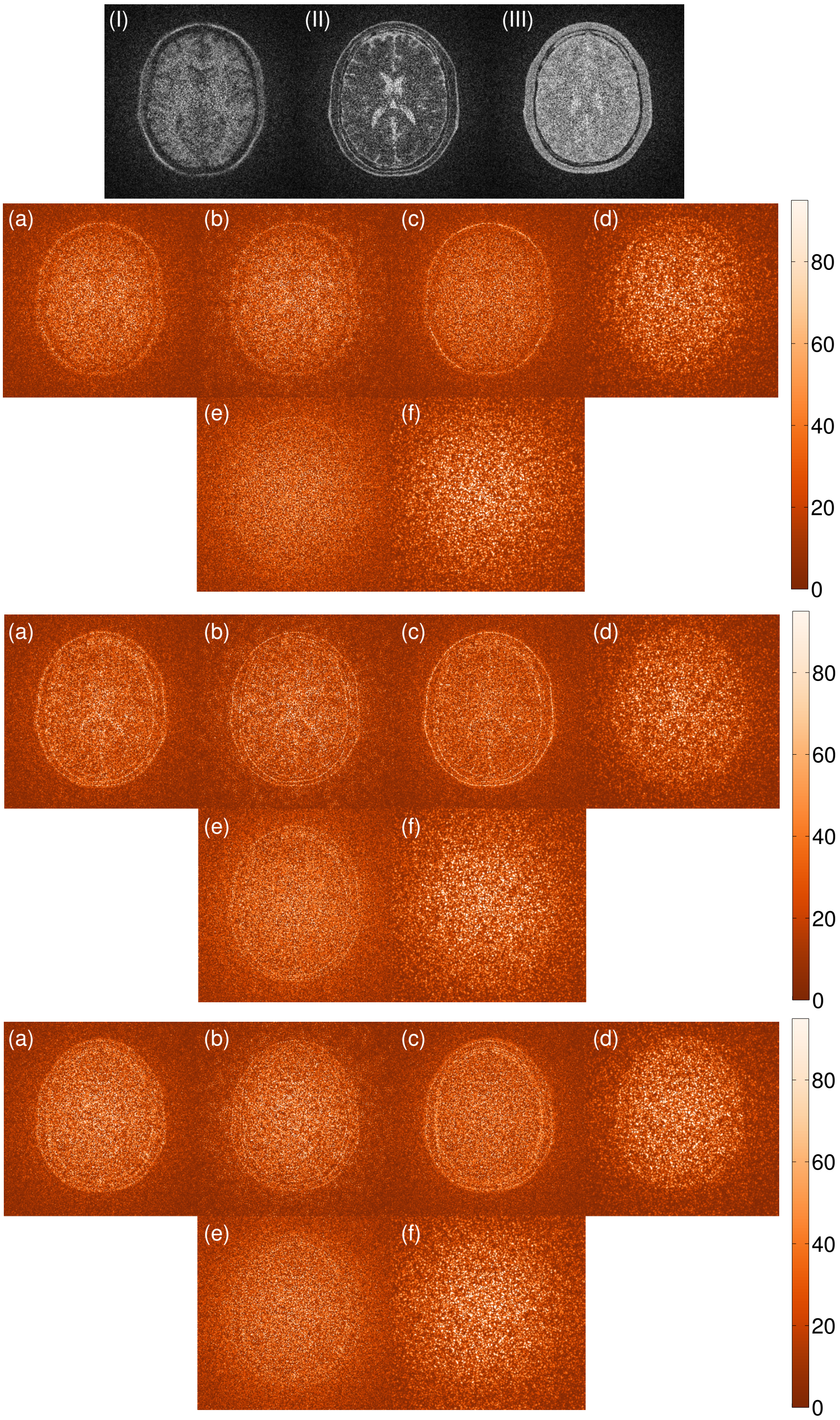

Figure 5.15: Noise components retrieved from synthetic (I) T_1-, (II) T_2- and (III) PD-weighted brain MRI data: (a) local mean (Aja-Fernández et al. 2015b), (b) local EM algorithm (Aja-Fernández et al. 2015b), (c) edge-preservation bilateral filter, (d) HH subband of the SWT of the image (Aja-Fernández and Vegas-Sánchez-Ferrero 2015), (e) VST + edge-preservation bilateral filter (**proposed**) and (f) VST + HH subband of the SWT (**proposed**). All images represent absolute value of the noise component. The maximum SNR of the foreground area equals $\mathrm{SNR}_{\max} = 5.63$, $\mathrm{SNR}_{\max} = 5.14$ and $\mathrm{SNR}_{\max} = 5.50$ for T_1-, T_2- and PD-weighted data, respectively.

Table 5.2: Averaged relative errors of the proposed noise estimation scheme with different state-of-the-art techniques used to initialize $\sigma_0(\mathbf{x})$ in eq. (5.18). The columns "w/o VST" (without VST) present the errors of state-of-the-art methods, while the columns "w VST" (with VST) relate to our proposal initialized by state-of-the-art methods. The last record presents an ideal estimate $\widehat{\sigma_0(\mathbf{x})} = \sigma(\mathbf{x})$. The best performance for each $\mathrm{SNR}_{\max}$ is in bold letters.

Method used to estimate $\sigma_0(\mathbf{x})$	$\mathrm{SNR}_{\max} = 5.63$		$\mathrm{SNR}_{\max} = 8.71$		$\mathrm{SNR}_{\max} = 11.79$		$\mathrm{SNR}_{\max} = 14.87$	
	w/o VST	w VST	w/o VST	w VST	w/o VST	w VST	w/o VST	w VST
DeVore et al. 2000	0.1763	0.0477	0.1910	0.0441	0.2331	0.0446	0.2955	0.0453
Goossens et al. 2006	0.2276	0.0552	0.2073	0.0493	0.2001	0.0481	0.1974	0.0451
Delakis et al. 2007	0.1682	0.0453	0.2115	0.0459	0.2388	0.0448	0.2616	0.0441
Landman et al. 2009a	0.1853	0.0523	0.1635	0.0480	0.1554	0.0468	0.1535	0.0437
Manjón et al. 2010	0.1325	0.0456	0.1285	0.0420	0.1248	0.0423	0.1221	0.0403
Rajan et al. 2011	0.2004	0.0583	0.1689	0.0507	0.1583	0.0460	0.1773	0.0457
Pan et al. 2012	0.2507	0.0609	0.1861	0.0516	0.1524	0.0493	0.1302	0.0454
Maggioni and Foi 2012	0.1915	0.0557	0.1217	0.0481	0.0919	0.0466	0.0820	0.0435
Maximov et al. 2012	0.1971	0.0460	0.2083	0.0448	0.2212	0.0445	0.2365	0.0436
Liu et al. 2014	0.2704	0.0462	0.2711	0.0464	0.2686	0.0441	0.2671	0.0435
Borrelli et al. 2014	0.1129	0.0453	0.1162	0.0419	0.1192	0.0425	0.1208	0.0403
Tabelow et al. 2015	0.1568	0.0618	0.1083	0.0556	0.0990	0.0542	0.1020	0.0503
Manjón et al. 2015	0.0915	0.0464	0.0738	0.0431	0.0692	0.0437	0.0665	0.0413
Aja-Fernández et al. 2015b	0.1248	**0.0451**	0.1090	**0.0410**	0.0930	**0.0415**	0.0765	**0.0390**
$\widehat{\sigma_0(\mathbf{x})} = \sigma(\mathbf{x})$	–	0.0417	–	0.0395	–	0.0411	–	0.0387

In the **second robustness test**, we visually compare noise components extracted from variance-non-stabilized and variance-stabilized T_1-, T_2-, and PD-weighted brain MR images. To this end, we generate noisy images as in eq. (5.30) using the spatially variant noise pattern from Fig. 5.9a. Following the underlying assumptions, the proposed VST should change the character of signal-dependent Rician noise to AWGN equivalent and therefore it should enable to apply Gaussian-dedicated noise extraction procedures like the SWT decomposition. In Figs. 5.15a–d, we show the noise components, which were retrieved from variance-non-stabilized MR images, while in Figs. 5.15e,f we present the noise components extracted from variance-stabilized images. Introducing the VST visibly improved the performance of noise extraction procedures. Moreover, variance-non-stabilized approaches not only underestimate the noise in low SNR areas, but they also lead to the intensification of the noise component near skull edges.

Finally, in the **third robustness test**, we use fourteen state-of-the-art methods presented in section 4.3.1 to study the influence of the initial estimate $\widehat{\sigma_0(\mathbf{x})}$ on the final noise map $\widehat{\sigma(\mathbf{x})}$. To carry out the evaluation process, we use synthetic T_1-weighted brain MR image, four $\mathrm{SNR}_{\max}$ levels (5.63, 8.71, 11.79, 14.87) and $R = 100$ repetitions of the experiment for each $\mathrm{SNR}_{\max}$ level. The $\overline{\mathrm{RE}}$s (see section 4.4 for more details) of the proposed noise estimation scheme are compared to the state-of-the-art in Table 5.2. The proposal is able to estimate the final noise map $\widehat{\sigma(\mathbf{x})}$ even if the prior noise estimation step gives the relative error around $0.2 - 0.3$. Moreover, the $\overline{\mathrm{RE}}$ of our proposal is nearly constant among all verified methods and $\mathrm{SNR}_{\max}$ levels, obtaining the accuracy of 5%, close to the error that would be achieved with an ideal estimate $\widehat{\sigma_0(\mathbf{x})} = \sigma(\mathbf{x})$. **Note that the highest $\overline{\mathbf{RE}}$ obtained with our proposal is always lower than the best results got with any of the state-of-the-art method.** This means that almost any estimation approach presented in section 4.3.1 can be effectively employed to provide the initial guess $\widehat{\sigma_0(\mathbf{x})}$. Based on the experimental results, we plug Aja-Fernández et al. 2015b into the initialization step for our proposed methodology (Fig. 5.4).

Although we are not obligated to use the method proposed by Aja-Fernández et al. 2015b, we decided to employ it for two reasons:

1. it gives a reasonable results over all verified $\mathrm{SNR}_{\max}$ levels,
2. the algorithm is computationally tractable.

5.5.4 Synthetic MRI data experiments

In this section, we evaluate our proposal using synthetic T_1-, T_2- and PD-weighted brain MRI data from BrainWeb database (see section 5.4.1 for more details).

As the **first noise estimation experiment** we quantitatively contrast the proposed noise estimation algorithm to the state-of-the art methods from section 4.3.1. We add spatially variant complex noise to the noise-free T_1-, T_2- and PD-weighted MR images and then we reconstruct the final envelopes of the images following the model given by eq. (5.30). The noise patterns from Fig. 5.9 are employed to evaluate the performance of the estimators in the function of maximum SNR of the foreground area Ω_Δ, $\mathrm{SNR}_{\max}$. Note that the upper bounds of the noise patterns were scaled for all contrast type data individually. This enables to reflect correct changes of $\mathrm{SNR}_{\max}$ over all noise patterns and then to average the results. One hundred repetitions ($R = 100$) of the experiment are considered for each noise pattern and single $\mathrm{SNR}_{\max}$ value except computationally intensive Rajan's method where only ten repetitions are performed (see Fig. 4.5 for the explanation of the averaging procedure). Exact SNR maps are known beforehand for this experiment and they are defined as $\mathrm{SNR}(\mathbf{x}) = A_T(\mathbf{x})/\sigma(\mathbf{x})$.

The averaged results for the third noise pattern from Fig. 5.9 are shown in Fig. 5.16. The local methods (DeVore et al. 2000, Delakis et al. 2007, Maximov et al. 2012 and Liu et al. 2014) mostly give poor results in terms of spatially averaged parameters $\mathrm{RE}(\mathbf{x})$ and $\mathrm{VAR}(\mathbf{x})$ ($\overline{\mathrm{RE}}$ and $\overline{\mathrm{VAR}}$) over all contrast type data. The parameter $\overline{\mathrm{RE}}$ of these estimators is unacceptable, since it exceeds the value of $\overline{\mathrm{RE}} = 0.2$ for $\mathrm{SNR}_{\max} > 10$. On the other hand, Goossens et al. 2006 yield almost fixed values of $\overline{\mathrm{RE}}$ and $\overline{\mathrm{VAR}}$ for $\mathrm{SNR}_{\max} > 10$ as a consequence of AWGN assumptions of the estimator. The highest precision among all local methods is achieved through robust Q_n estimator (Landman et al. 2009b). We remind here that methods by Landman et al. 2009b and Maximov et al. 2012 have been initially proposed to deal with repeated acquisitions and they do not show their considerable potential like in a voxelwise estimation. Note that Liu et al. 2014 is clearly outperformed by the proposed methodology, even though both Liu et al. 2014 and our proposal make use of the HH subband of the SWT of the image. This confirms the importance of the variance-stabilizing transformation prior to the noise estimation in non-stationary Rician distributed data.

The second group of the verified algorithms are non-local estimators arranging patch-based calculations. The leading role in this field plays Manjón et al. 2015, though, it is characterized by biased estimates for the images with low $\mathrm{SNR}_{\max}$. The results obtained from Manjón et al. 2015 can be even improved using stacked data. Nevertheless, since the acquisition of real MRI data is performed in 2D, the noise map is different for each slice. Therefore, the noise estimation methodology, which takes the consecutive slices into account, is valid for synthetic MRI data only. We pay a special attention to Borrelli et al. 2014, which is characterized by close to constant $\overline{\mathrm{RE}}$ and $\overline{\mathrm{VAR}}$ regardless of $\mathrm{SNR}_{\max}$ level. Other non-local methods (i.e., Manjón et al. 2010, Maggioni and Foi 2012) along with Pan et al. 2012, Borrelli et al. 2014, Tabelow et al. 2015 and Manjón et al. 2015 are characterized by an extremely low $\overline{\mathrm{VAR}}$ parameter. Consequently, they are preferred for adaptive denoising procedures of non-stationary Rician distributed data.

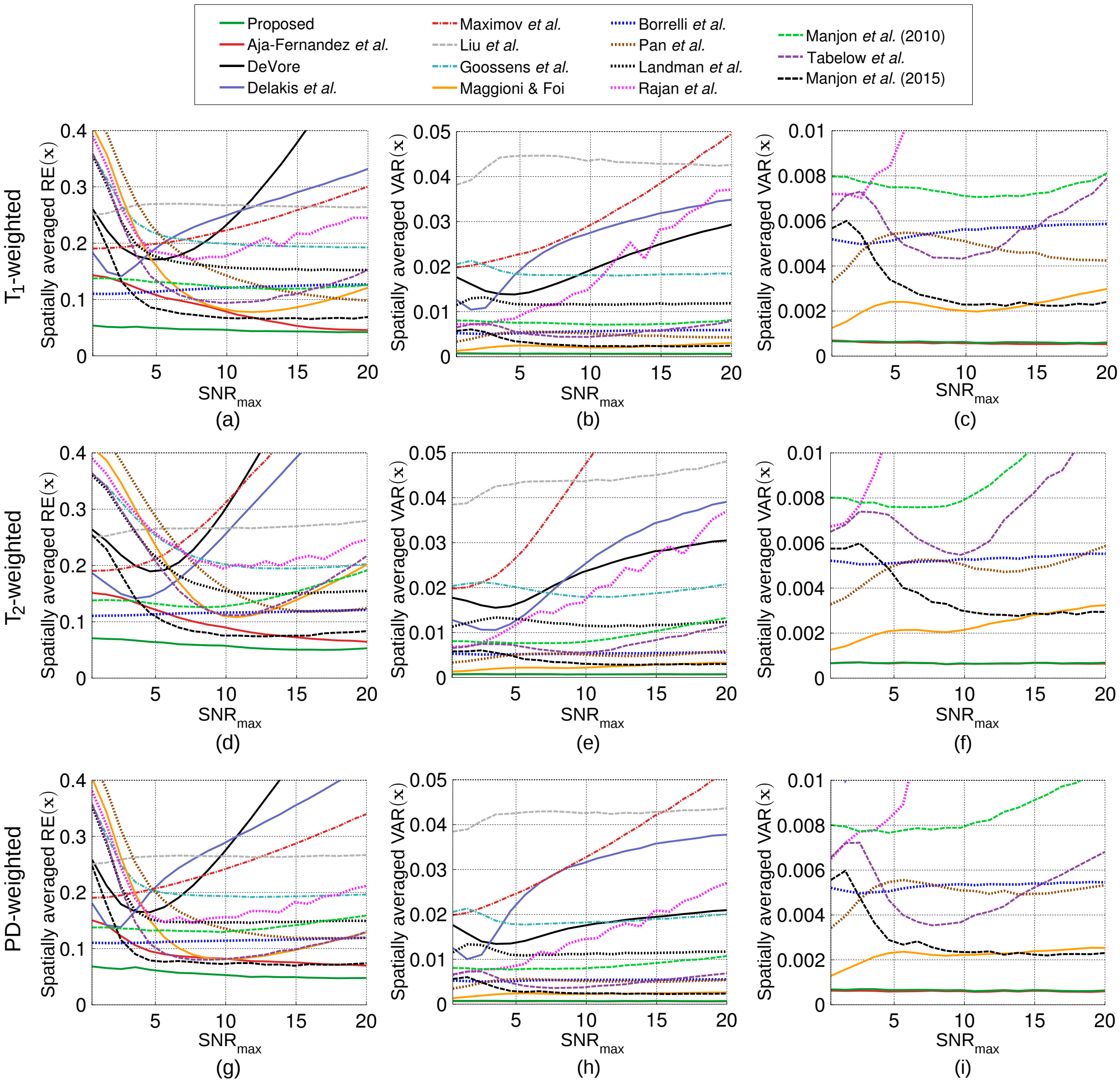

(a) (b) (c)
(d) (e) (f)
(g) (h) (i)

Figure 5.16: Comparison of noise estimators for synthetic MRI data contamined by non-stationary Rician noise following eq. (5.30) in the function of $\mathrm{SNR}_{\mathrm{max}}$ for the third noise pattern from Fig. 5.9. First column: spatially averaged relative error $\overline{\mathrm{RE}}$ of the estimators; Second column: spatially averaged variance $\overline{\mathrm{VAR}}$ of the estimators; Third column: the parameter $\overline{\mathrm{VAR}}$ from the second column zoomed to the range $[0 - 0.01]$. The first row corresponds to T_1-, the second row to T_2- and the third one to PD-weighted MRI data.

Regarding the proposed spatially variant Rician noise estimation scheme, the results show the outstanding performance of the method for the whole range of SNRs. Our proposal provides nearly constant $\overline{\mathrm{RE}}$ and $\overline{\mathrm{VAR}}$ over all $\mathrm{SNR}_{\mathrm{max}}$ levels, considerably lower than any other the state-of-the-art method. As we expected, the results of our proposal meet those from Aja-Fernández et al. 2015b for sufficiently high values of $\mathrm{SNR}_{\mathrm{max}}$ (usually around $\mathrm{SNR}_{\mathrm{max}} = 20$).

Eventually, we point out that the examined methods show consistent results over spatially variant noise patterns from Fig. 5.9 and all contrast type data, i.e., T_1-, T_2- and PD-weighted MRI. The results from another experiment, where the parameters $\overline{\mathrm{RE}}$ and $\overline{\mathrm{VAR}}$ are averaged over all noise patterns are shown in Fig. 5.17.

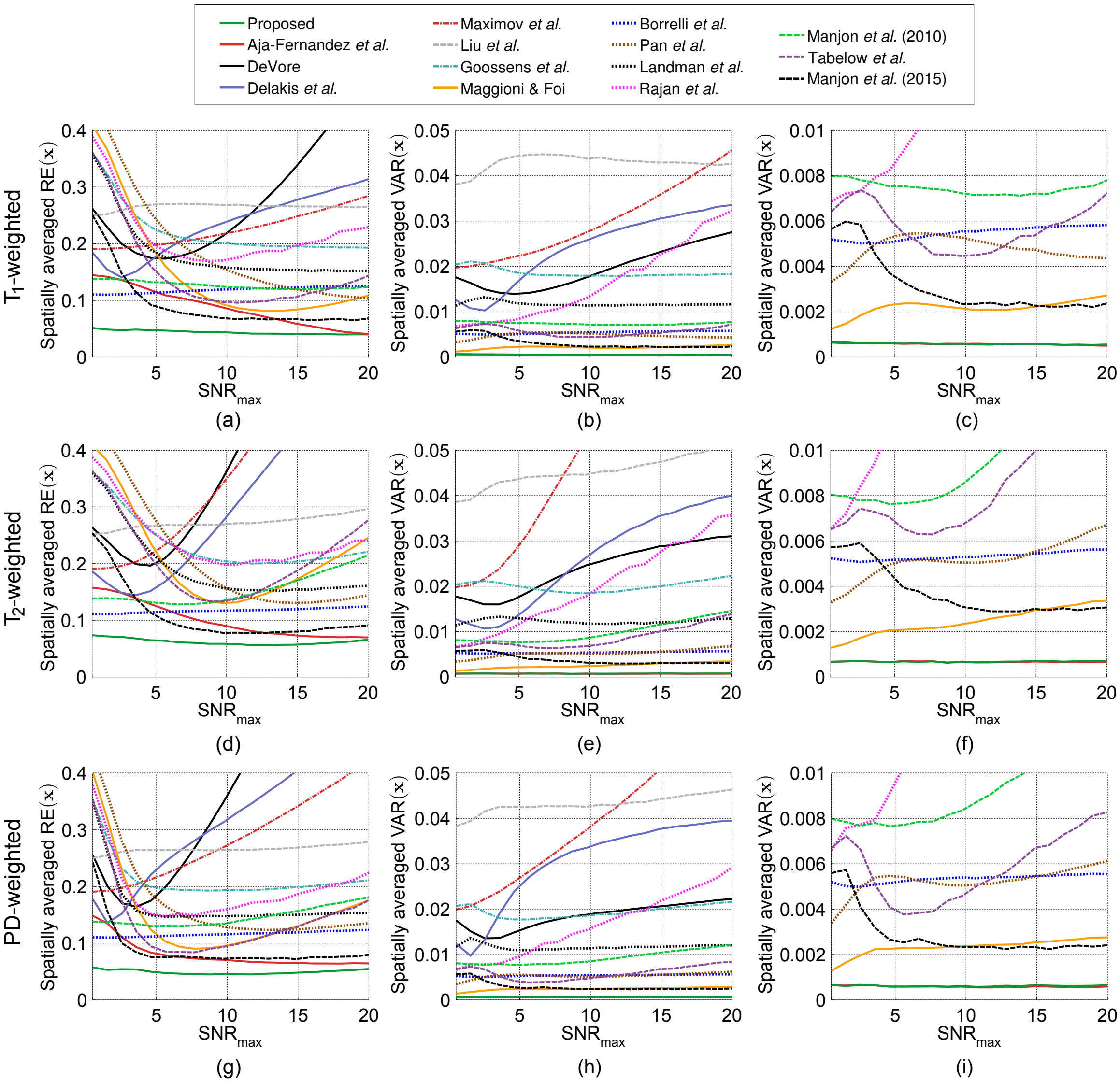

(a) (b) (c)

(d) (e) (f)

(g) (h) (i)

Figure 5.17: Comparison of noise estimators for synthetic MRI data contamined by non-stationary Rician noise following eq. (5.30) in the function of $\mathrm{SNR}_{\mathrm{max}}$. Each plot presents the averaged results over all synthetic noise maps from Fig. 5.9. First column: spatially averaged relative error $\overline{\mathrm{RE}}$ of the estimators; Second column: spatially averaged variance $\overline{\mathrm{VAR}}$ of the estimators; Third column: the parameter $\overline{\mathrm{VAR}}$ from the second column zoomed to the range $[0-0.01]$. The first row corresponds to T_1-, the second row to T_2- and the third one to PD-weighted MRI data.

Table 5.3: The parameters of synthetic MRI reconstructions used in the second experiment: noise pattern from Fig. 5.9, the variability degree of the underlying noise map $\sigma(\mathbf{x})$ and the maximum SNR of the image in the foreground area, $\mathrm{SNR}_{\mathrm{max}}$. The noise estimation results are shown in corresponding Figs. 5.18–5.20.

	T_1-weighted	T_2-weighted	PD-weighted
Noise pattern	first	third	fourth
$\sigma(\mathbf{x})$	$[5-20]$	$[8-20]$	$[12-20]$
$\mathrm{SNR}_{\mathrm{max}}$	8.73	7.49	8.09

In the **second experiment**, we focus on the qualitative evaluation of the estimators. The synthetic T_1-, T_2- and PD-weighted MR images are contamined by spatially variant noise following the model (5.30). Exact SNR maps are *a priori* known for the experiment. All the parameters used to simulate the artificial noise are included in Table 5.3.

The estimated noise maps and relative errors of the methods coming from this experiment are shown in Figs. 5.18–5.20. The local methods (DeVore et al. 2000, Delakis et al. 2007, Maximov et al. 2012, Liu et al. 2014, Goossens et al. 2006, Landman et al. 2009b) exhibit spatial granularities of the estimated noise maps due to the noise level calculations in fixed neighbourhoods, i.e., 5 × 5 windows (Fig. 5.18–5.20a–f).

In contrast to local methods, Manjón et al. 2010 and Maggioni and Foi 2012 use patch-based estimation, which leads to less granular and more reliable results (Fig. 5.18–5.20g, j). The similar results were obtained from Pan et al. 2012 with the advantage of a much less computational cost than the patch-based methods (Fig. 5.18–5.20i). Recent advances in spatially variant Rician noise estimation (Borrelli et al. 2014, Tabelow et al. 2015, Manjón et al. 2015) additionally carry out a post-relaxation step of the raw estimates (Fig. 5.18–5.20k–m). These methods yield fairly smoothed and reliable noise maps, though, the high-frequency components of the image (i.e., skull edges) are still observed (Fig. 5.18l, Fig. 5.19k, Fig. 5.20k).

Finally, Aja-Fernández et al. 2015b and our proposal provide granular-free noise estimates and they get rid of high-frequency components from the image at all (Fig. 5.18–5.20n, o). Some underestimations can be observed in Aja-Fernández et al. 2015b, especially in low SNR areas, nevertheless, the global patterns are reproduced correctly. Our proposal compensates these underestimations and provides the most reliable representation of underlying noise patterns (Fig. 5.18–5.20o). Moreover, our method can estimate the noise levels for background regions as well, where the data follow Rayleigh rather than Rician distribution. These improvements of our proposal are the consequences of introducing the VST to the conventional homomorphic filter.

To complete the whole set of experiments with synthetic MRI data, we provide the **third experiment**, where the performance of the algorithms is verified for synthetic SENSE MRI reconstructions. We simulate eight coils ($L = 8$) SENSE MRI data with subsampling rate $r = 2$. The data coming from each coil is contamined by AWGN with $\sigma_l^2(\mathbf{x})$ (see Table 5.4). Moreover, we introduce correlations between k–th and l–th receiver coil ($k \neq l$) to be ρ_{kl}. After recovering process of the image using Cartesian SENSE reconstruction, the magnitude is affected by non-stationary, correlated and signal-dependent Rician noise. In this experiment, the SNR is not known and it must be estimated by each algorithm individually.

Eventually, we pay attention to the variability degrees of underlying noise maps $\sigma(\mathbf{x})$ in the reconstructed images, which varies in a lesser extent than the noise maps from the previous visual evaluations (see Table 5.4).

Table 5.4: The parameters of synthetic SENSE MRI reconstructions used in the third experiment (see the corresponding Figs. 5.7d–f): $\sigma_l^2(\mathbf{x})$ – the noise level in l–th receiver coil before the magnitude reconstruction; ρ_{kl} – the correlations between k–th and l–th receiver coil ($k \neq l$) and the variability degree of the underlying noise map $\sigma(\mathbf{x})$. The noise estimation results are shown in Figs. 5.21 and 5.22.

	T_1-weighted	T_2-weighted	PD-weighted
$\sigma_l^2(\mathbf{x})$	75	225	175
ρ_{kl}	0.2	0.05	0.3
$\sigma(\mathbf{x})$	[18.77 – 22.26]	[35.20 – 36.69]	[27.03 – 35.03]

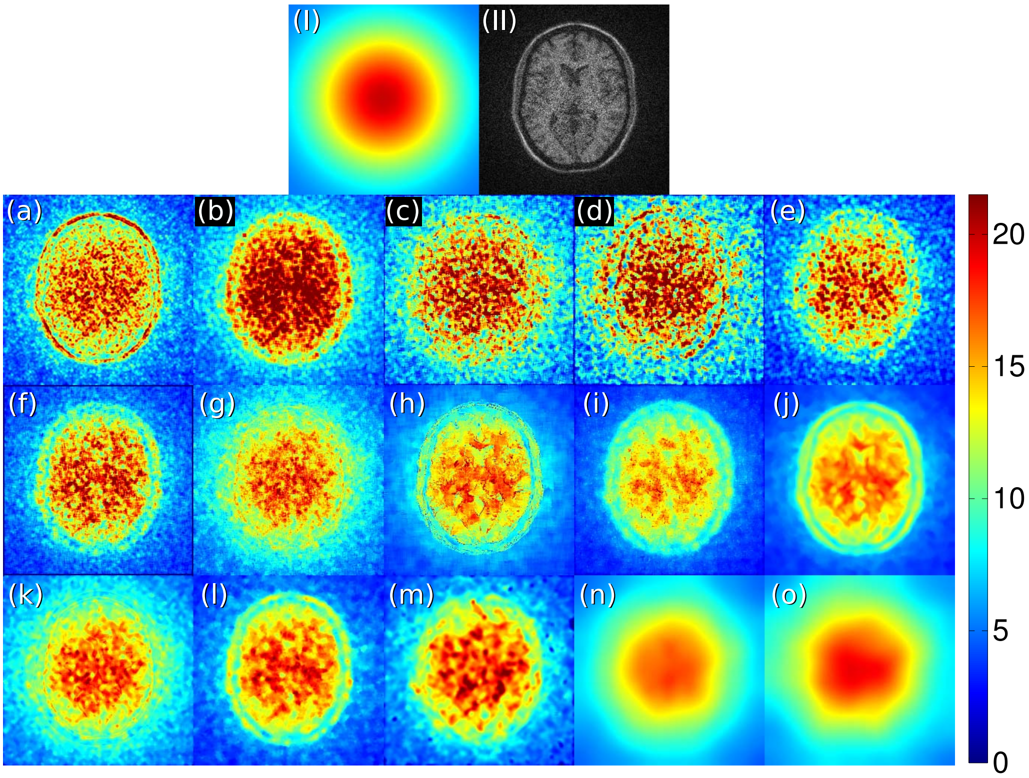

Estimated spatially variant noise maps

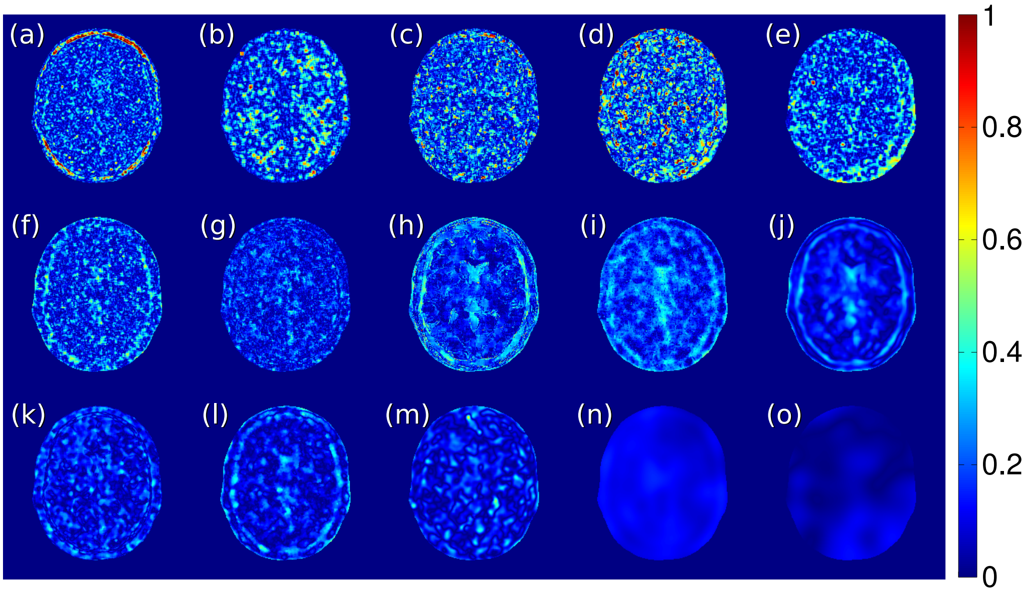

Relative errors of the estimators

Figure 5.18: Visual inspection of the methods for synthetic T_1-weighted MRI brain data distorted by non-stationary Rician noise following eq. (5.30) with $\mathrm{SNR}_{\mathrm{max}} = 8.73$ (top figure) and corresponding relative errors $\mathrm{RE}(\mathbf{x})$ of the estimators (bottom figure). (I) A reference noise map and (II) noisy image following eq. (5.30). Examined methods: (a) DeVore et al. 2000, (b) Delakis et al. 2007, (c) Maximov et al. 2012, (d) Liu et al. 2014, (e) Goossens et al. 2006, (f) Landman et al. 2009b, (g) Manjón et al. 2010, (h) Rajan et al. 2011, (i) Pan et al. 2012, (j) Maggioni and Foi 2012, (k) Borrelli et al. 2014, (l) Tabelow et al. 2015, (m) Manjón et al. 2015, (n) Aja-Fernández et al. 2015b and (o) **our proposal**.

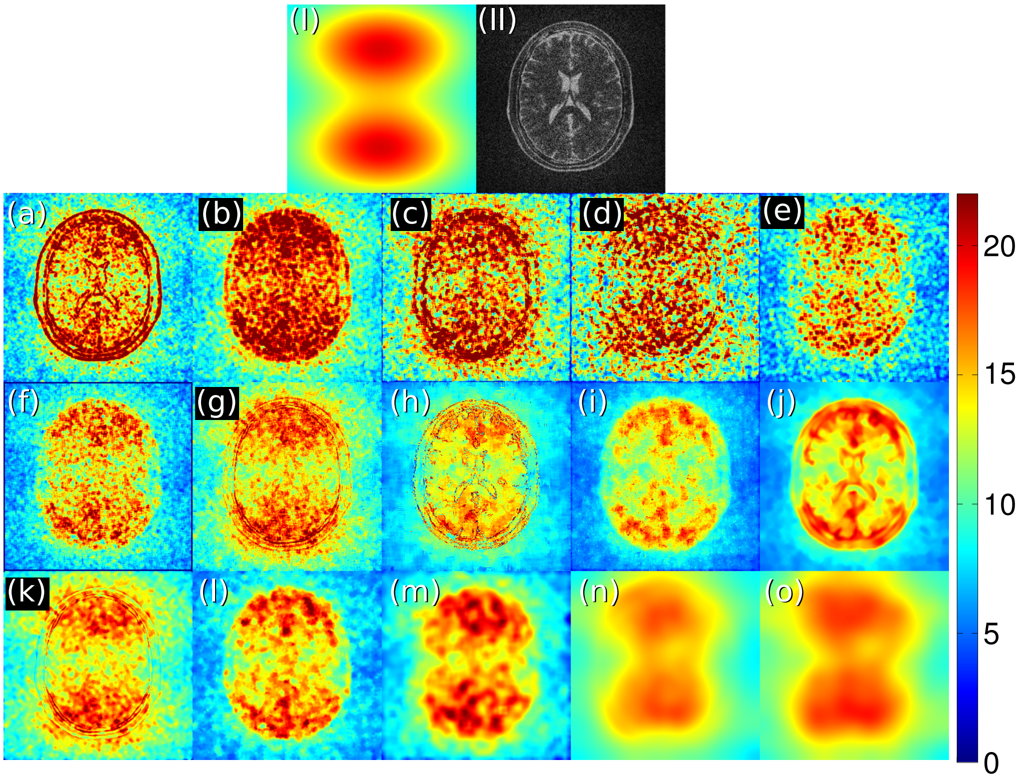

Estimated spatially variant noise maps

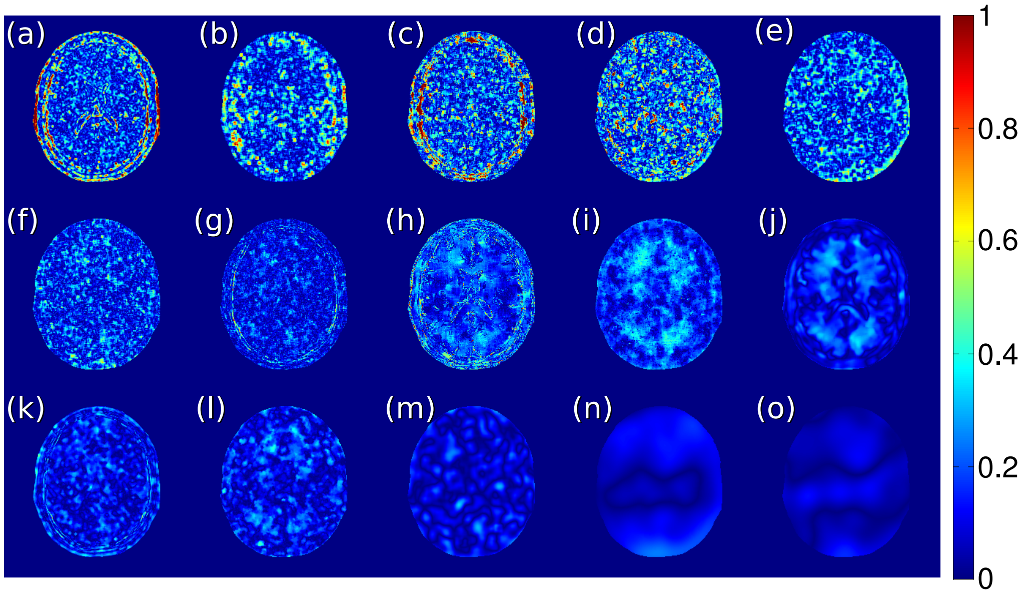

Relative errors of the estimators

Figure 5.19: Visual inspection of the methods for synthetic T_2-weighted MRI brain data distorted by non-stationary Rician noise following eq. (5.30) with $\text{SNR}_{\text{max}} = 7.49$ (top figure) and corresponding relative errors $\text{RE}(\mathbf{x})$ of the estimators (bottom figure). (I) A reference noise map and (II) noisy image following eq. (5.30). Examined methods: (a) DeVore et al. 2000, (b) Delakis et al. 2007, (c) Maximov et al. 2012, (d) Liu et al. 2014, (e) Goossens et al. 2006, (f) Landman et al. 2009b, (g) Manjón et al. 2010, (h) Rajan et al. 2011, (i) Pan et al. 2012, (j) Maggioni and Foi 2012, (k) Borrelli et al. 2014, (l) Tabelow et al. 2015, (m) Manjón et al. 2015, (n) Aja-Fernández et al. 2015b and (o) **our proposal**.

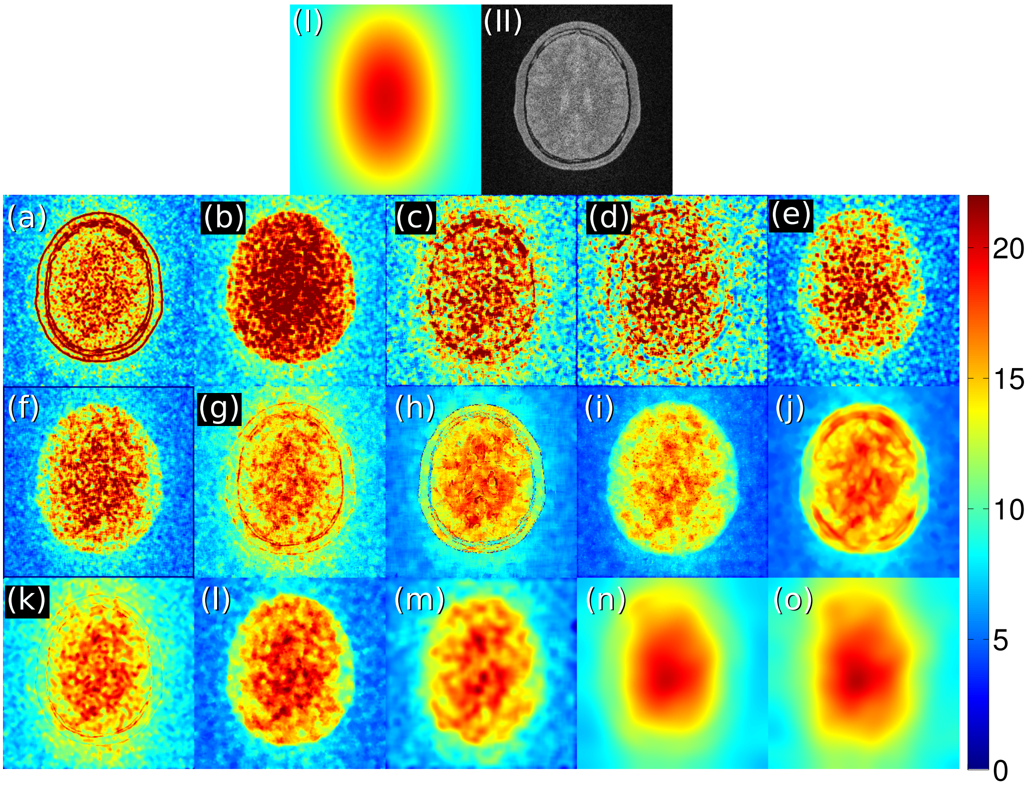

Estimated spatially variant noise maps

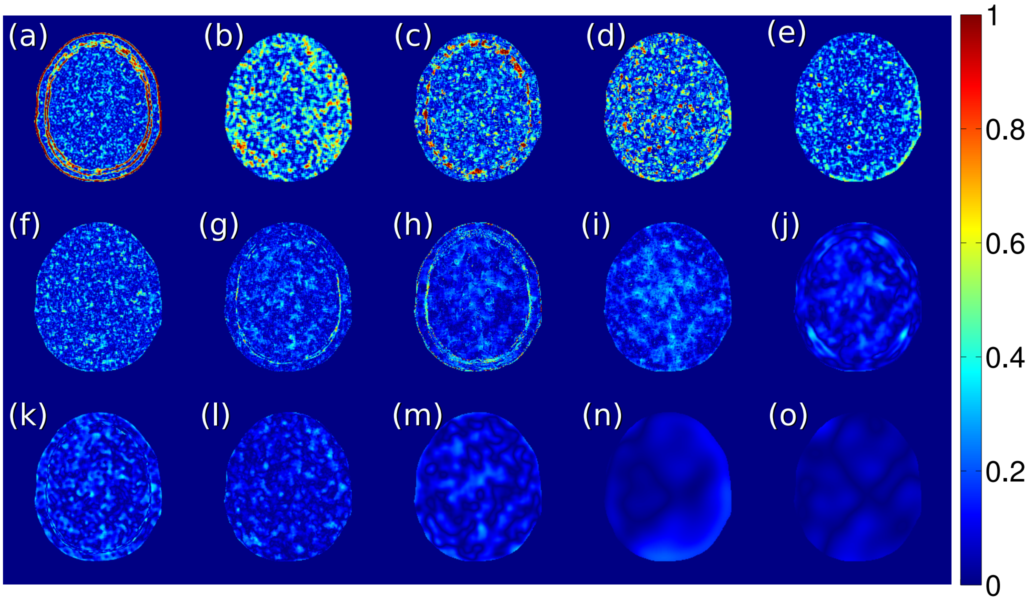

Relative errors of the estimators

Figure 5.20: Visual inspection of the methods for synthetic PD-weighted MRI brain data distorted by non-stationary Rician noise following eq. (5.30) with $\mathrm{SNR}_{\max} = 8.09$ (top figure) and corresponding relative errors $\mathrm{RE}(\mathbf{x})$ of the estimators (bottom figure). (I) A reference noise map and (II) noisy image following eq. (5.30). Examined methods: (a) DeVore et al. 2000, (b) Delakis et al. 2007, (c) Maximov et al. 2012, (d) Liu et al. 2014, (e) Goossens et al. 2006, (f) Landman et al. 2009b, (g) Manjón et al. 2010, (h) Rajan et al. 2011, (i) Pan et al. 2012, (j) Maggioni and Foi 2012, (k) Borrelli et al. 2014, (l) Tabelow et al. 2015, (m) Manjón et al. 2015, (n) Aja-Fernández et al. 2015b and (o) **our proposal**.

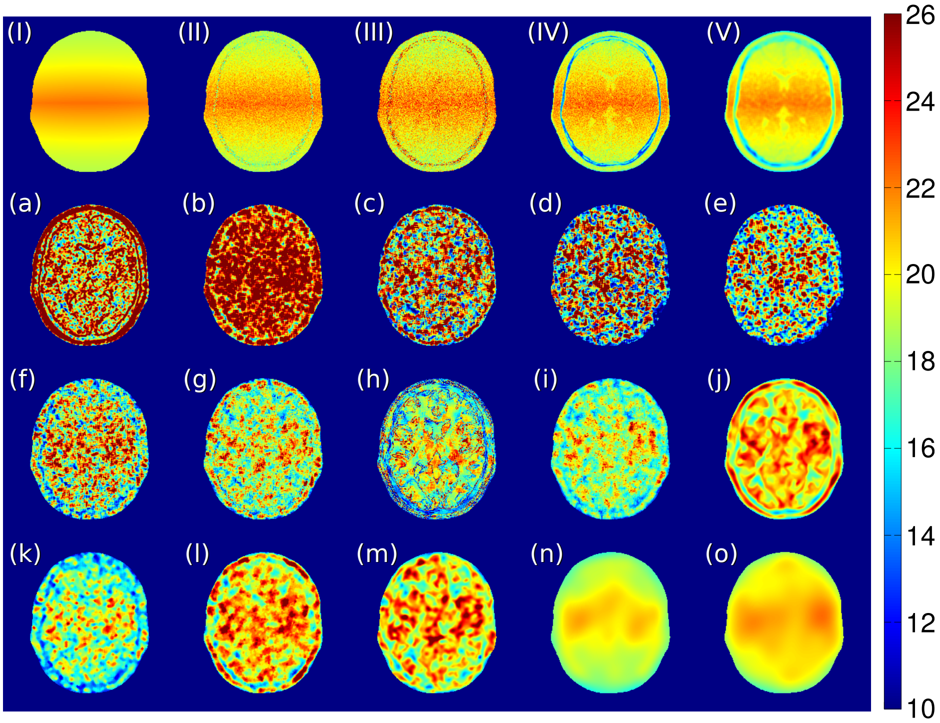

Results for T_1-weighted SENSE MRI brain data

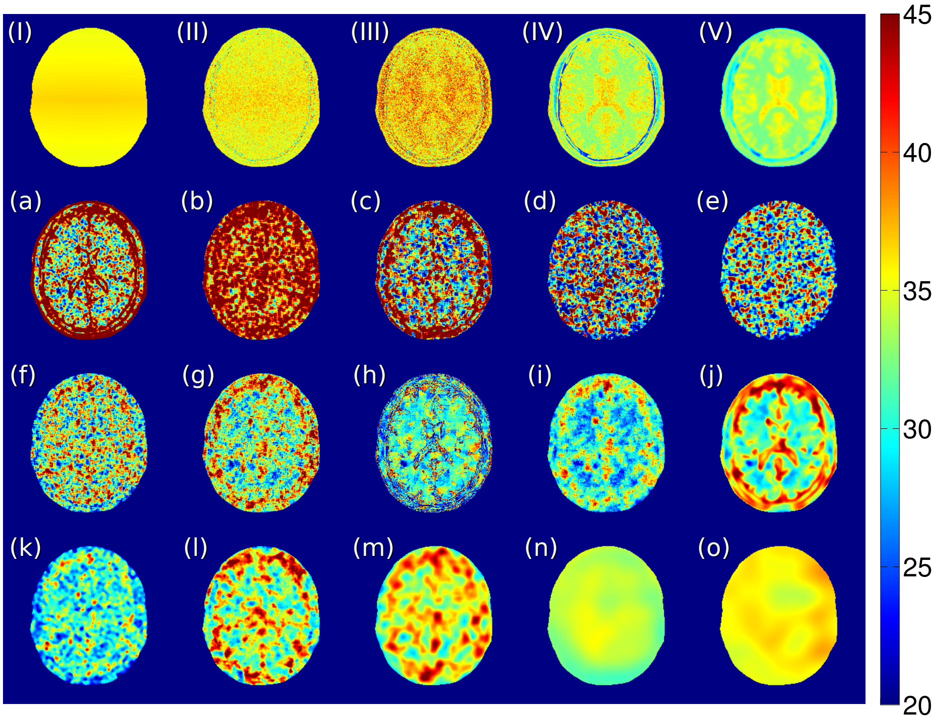

Results for T_2-weighted SENSE MRI brain data

Figure 5.21: Visual inspection of the methods for simulated SENSE MRI data. (I) *Ground truth* and silver standard methods along 500 repetitions: (II) DeVore et al. 2000, (III) Maximov et al. 2012, (IV) Landman et al. 2009b and (V) Glenn et al. 2015. Examined methods: (a) DeVore et al. 2000, (b) Delakis et al. 2007, (c) Maximov et al. 2012, (d) Liu et al. 2014, (e) Goossens et al. 2006, (f) Landman et al. 2009b, (g) Manjón et al. 2010, (h) Rajan et al. 2011, (i) Pan et al. 2012, (j) Maggioni and Foi 2012, (k) Borrelli et al. 2014, (l) Tabelow et al. 2015, (m) Manjón et al. 2015, (n) Aja-Fernández et al. 2015b and (o) **our proposal**.

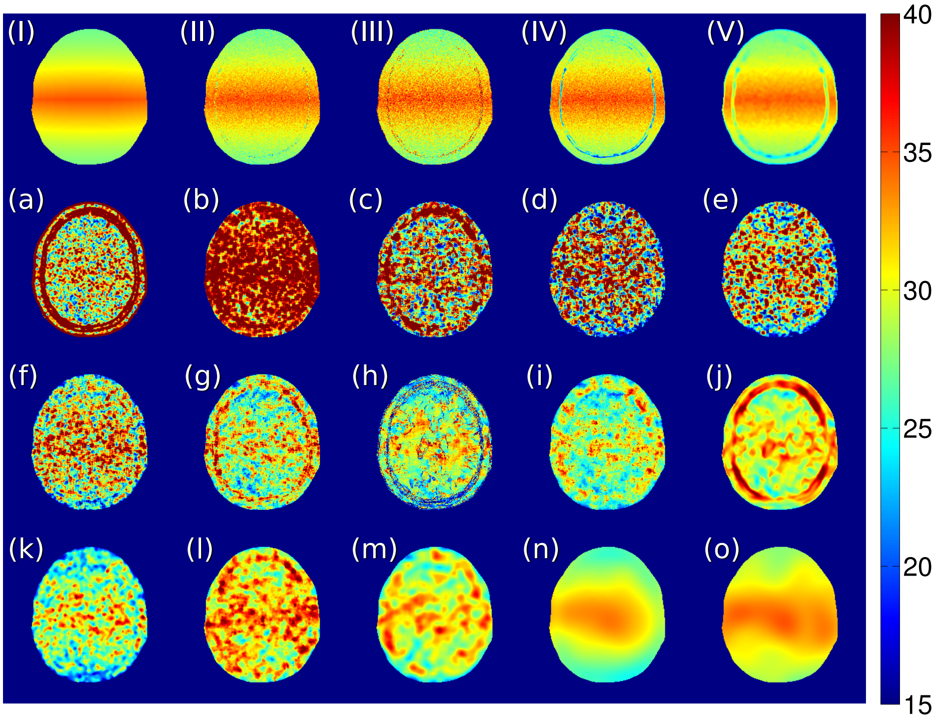

Figure 5.22: Visual inspection of the methods for simulated PD-weighted SENSE MRI brain data. (I) *Ground truth* and silver standard methods along 500 repetitions: (II) DeVore et al. 2000, (III) Maximov et al. 2012, (IV) Landman et al. 2009b and (V) Glenn et al. 2015. Examined methods: (a) DeVore et al. 2000, (b) Delakis et al. 2007, (c) Maximov et al. 2012, (d) Liu et al. 2014, (e) Goossens et al. 2006, (f) Landman et al. 2009b, (g) Manjón et al. 2010, (h) Rajan et al. 2011, (i) Pan et al. 2012, (j) Maggioni and Foi 2012, (k) Borrelli et al. 2014, (l) Tabelow et al. 2015, (m) Manjón et al. 2015, (n) Aja-Fernández et al. 2015b and (o) **our proposal**.

The qualitative results of the third experiment are shown in Figs. 5.21 and 5.22. Different references are considered: the *ground truth* for Cartesian SENSE, analytically derived by Aja-Fernández et al. 2014a (Figs. 5.21I and 5.22I) and the estimates defined for multiple repetitions along $R = 500$ independent replicas of the image defined in section 4.3.2: DeVore et al. 2000, Maximov et al. 2012, Landman et al. 2009b and Glenn et al. 2015 (Figs. 5.21II–V and 5.22II–V). These pseudo-reference maps are used then as *silver standards*, i.e., the noise maps that would be obtained, if the appropriate number of scans are available.

The results of this experiment significantly differ from the previous one, though the same phantoms were arranged to generate the noisy images. Almost all examined methods presented in section 4.3.1 failed in this experiment. There are two reasons for this: 1) spatial correlations of the noise component, which are introduced by Cartesian SENSE reconstructions, and, 2) much smaller variability degrees of the noise patterns. Note that local methods provide highly granular results and the patch based methods do not overcome this limitation as in previous qualitative experiment.

Aja-Fernández et al. 2015b provide smooth and granularity-free noise patterns, however, they are slightly underestimated once again (Figs. 5.21n and 5.22n). The reasonable results of the estimation process can be obtained using hereby proposed variance-stabilizing homomorphic approach (Figs. 5.21o and 5.22o). Finally, note, although we used different correlation ratios and variability degrees of the noise patterns, the results yielded by our proposal are consistent for all contrast type SENSE MRI data.

5.5.5 Real MRI data experiments

In the **fourth experiment**, we estimate the noise map for real noisy T_1-weighted TFE SENSE MRI phantom reconstructed from $L = 32$ coils with subsampling rate $r = 2$ in phase encoding direction (Fig. 5.7g). Since the *ground truth* is not available in this case, we resort to *silver standard* approaches (DeVore et al. 2000, Maximov et al. 2012, Landman et al. 2009b and Glenn et al. 2015) being pointwise estimators along twenty acquisitions ($R = 20$) of the same phantom. Again, the SNR map has to be estimated by each method individually in the experiment. Note that the final magnitude of this real SENSE MRI data set presents highly spatially correlated noise component.

The results of the experiment are presented in Fig. 5.23. Some of local methods (DeVore et al. 2000, Maximov et al. 2012 and Landman et al. 2009b) perform well enough inside the phantom due to the local homogeneity of the source (see Fig. 5.23a, c, f). The phantom used in this experiment does not consist of tissue transitions usually observed in a typical *in vivo* brain MRI examination, thus, the estimators are not affected by the outliers. Indeed, the granularities of the noise maps come from the small number of samples used in the estimation process (typically 25 samples are taken into account to provide a single noise level estimate). In comparison with the second experiment, the wavelet-based methods (Delakis et al. 2007, Liu et al. 2014 and Goossens et al. 2006) failed in this evaluation (Fig. 5.23b, d, e). This is due to the extraction of high-frequency components from already smoothed MR image.

Maggioni and Foi 2012 provide quite reasonable results inside the phantom, though, the noise map is significantly overestimated near edges of the object (Fig. 5.23j). Borrelli et al. 2014 and Tabelow et al. 2015 provide highly underestimated noise patterns, however, the structure of the map is still preserved (Fig. 5.23k, l). We draw attention to the results

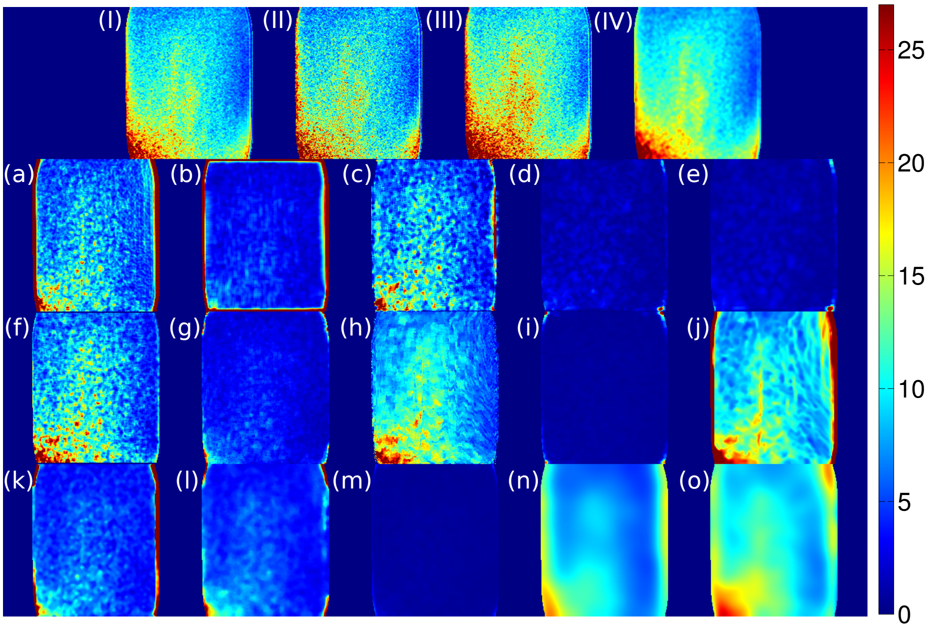

Figure 5.23: Visual inspection of the methods for real T_1-weighted TFE SENSE MRI phantom (Fig. 5.7g). Silver standard methods along 20 acquisitions: (I) DeVore et al. 2000, (II) Maximov et al. 2012, (III) Landman et al. 2009b and (IV) Glenn et al. 2015. Examined methods: (a) DeVore et al. 2000, (b) Delakis et al. 2007, (c) Maximov et al. 2012, (d) Liu et al. 2014, (e) Goossens et al. 2006, (f) Landman et al. 2009b, (g) Manjón et al. 2010, (h) Rajan et al. 2011, (i) Pan et al. 2012, (j) Maggioni and Foi 2012, (k) Borrelli et al. 2014, (l) Tabelow et al. 2015, (m) Manjón et al. 2015, (n) Aja-Fernández et al. 2015b and (o) **our proposal**.

obtained from Landman et al. 2009b and Rajan et al. 2011: the methods show good behaviour in the boundaries and inside the phantom, though the granularity is still a problem (Fig. 5.23f, h). Surprisingly, Manjón et al. 2015 failed in this experiment, probably due to the differences in eigenvalues distribution in non-local PCA decomposition between synthetic and real MRI data (Fig. 5.23m; see also eq. (4.44)). Finally, Aja-Fernández et al. 2015b give clear, smooth and granularity-free results, but nevertheless the noise patterns are slightly underestimated in comparison with *silver standards* (Fig. 5.23n).

The proposed method retrieves smooth and granularity-free results as well, and it does not underestimate the noise levels in the foreground area (Fig. 5.23o). A little overestimations can be still observed near edges of the phantom. These overestimations predominantly depend on the selected noise extraction procedure (a bilateral filter in this example), and they can be mitigated choosing other edge-preservation and AWGN-compliant image filtering procedure.

In the **fifth experiment**, we examine *in vivo* T_2-weighted TSE SENSE MRI brain data and *in vivo* T_2-weighted FFE SENSE MRI brain data (Fig. 5.7h, i). Neither *ground truth* nor pseudo-reference map is available in this case. So, we only visually verify the differences of noise patterns between the methods and compare the results to the previous experiments.

Some local methods (DeVore et al. 2000, Delakis et al. 2007 and Maximov et al. 2012) provide highly granular and overestimated noise maps especially near skull edges (Fig. 5.24a–c). Note that these results are compatible with previous results obtained from the second and the third experiment (compare with Figs. 5.18a–c, 5.19a–c, 5.20a–c, 5.21a–c, and 5.22a–c). Contrary, the methods by Liu et al. 2014, Goossens et al. 2006, Pan et al. 2012 and Manjón et al. 2015 show significant underestimations of the noise for *in vivo* SENSE MRI acquisitions (Fig. 5.24d, e, i, m). These results are also fully consistent with the fourth experiment on real MRI data (compare with Fig. 5.23d, e, i, m). Quite reasonable results in the foreground area of the brain generate Maggioni and Foi 2012, though, overestimations about the skull edges can be noticed in T_2-weighted TSE SENSE MRI data. These inaccuracies of the estimated maps have a little importance, since the skull is usually stripped prior to the data analysis step (e.g., image registration or image segmentation).

Finally, the results from the method by Aja-Fernández et al. 2015b and our proposal are shown in Fig. 5.24n and Fig. 5.24o, respectively. Note since a pseudo-reference map is not available in this experiment, we can only deduce that our proposal gives the acceptable results from the consistency with the previous experiments evaluated visually.

5.6 Computational cost of the noise estimation scheme

The computational cost of the noise estimation algorithm is crucial when processing the stacked slices of MRI data. The core of the algorithm, obviously, can be implemented in low-level programming language, which allows direct accessing to the memory, e.g., C programming language. We can go even further and employ parallel computing platforms like graphics processing unit (GPU) or field-programmable gate array (FPGA) to significantly speed-up the computations. However, when developing the noise estimation algorithm, one has to be well aware of the following facts:

- the noise estimation procedure is only a minor part of the whole MRI data processing and analysis pipeline, which usually includes other related steps, e.g., image denoising, parameter estimation, tissue segmentation and/or image registration,

- the noise estimation must be carried out for each slice individually as long as we consider 2D acquisition.

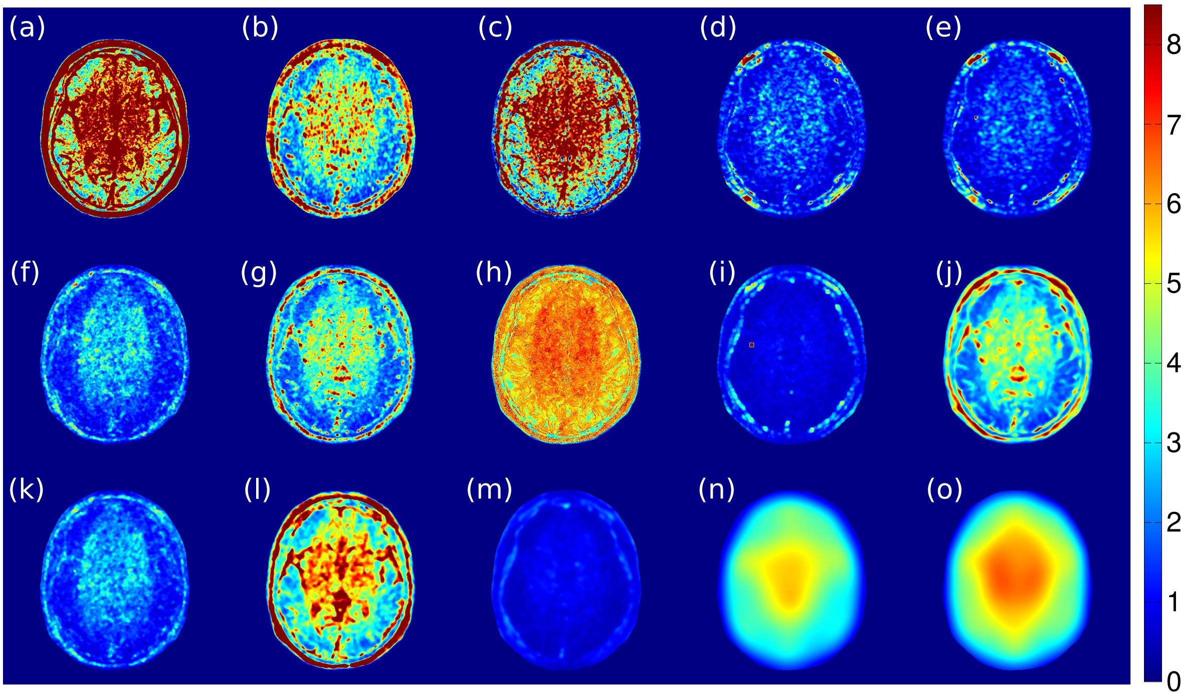

In vivo T_2-weighted TSE SENSE MRI brain data ($r = 4$)

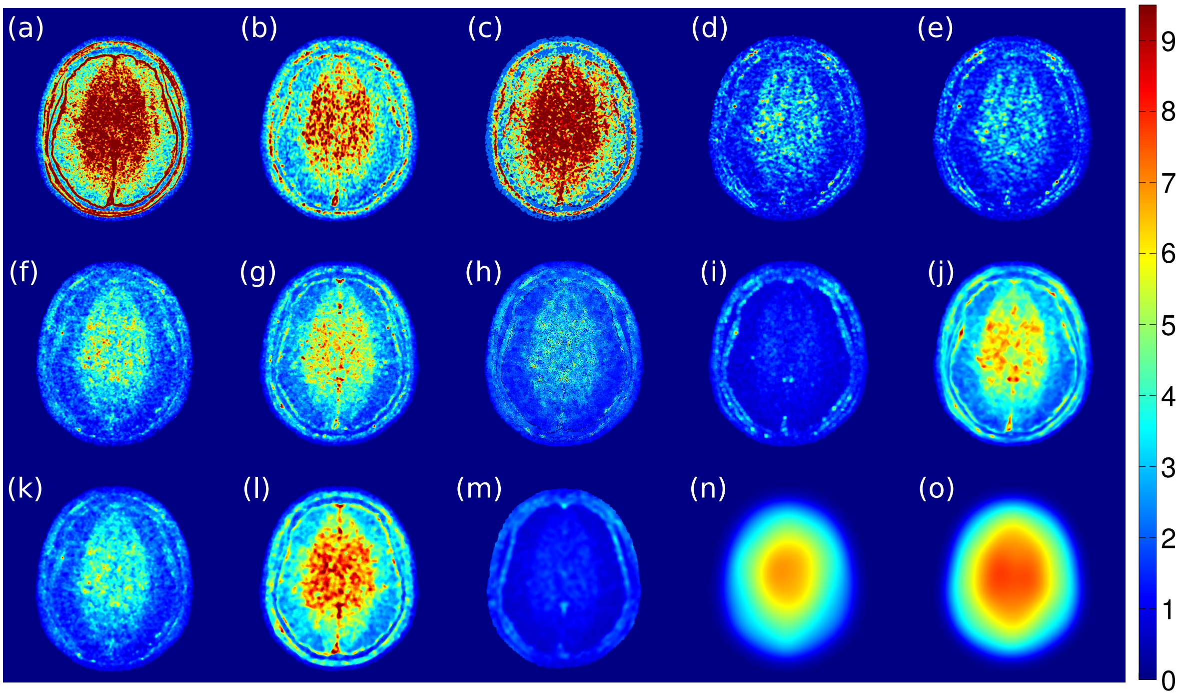

In vivo T_2-weighted FFE SENSE MRI brain data ($r = 4$)

Figure 5.24: Visual inspection of the methods for *in vivo* T_2-weighted TSE SENSE MRI slice from Fig. 5.7h (top figure) and *in vivo* T_2-weighted FFE SENSE MRI slice from Fig. 5.7i (bottom figure). Examined methods: (a) DeVore et al. 2000, (b) Delakis et al. 2007, (c) Maximov et al. 2012, (d) Liu et al. 2014, (e) Goossens et al. 2006, (f) Landman et al. 2009b, (g) Manjón et al. 2010, (h) Rajan et al. 2011, (i) Pan et al. 2012, (j) Maggioni and Foi 2012, (k) Borrelli et al. 2014, (l) Tabelow et al. 2015, (m) Manjón et al. 2015, (n) Aja-Fernández et al. 2015b and (o) **our proposal**.

In this research, we verify the averaged execution times of the algorithms studied in this chapter using two MRI slices of size 256×256 and 560×560 pixels, respectively. We examine the computational cost of the methods using their implementations in MathWorks MATLAB 2013b under GNU/Linux Debian operating system with kernel version 3.16.0. We remind that two methods, namely Maggioni and Foi 2012 and Tabelow et al. 2015, are verified using their original source code shared by the authors. These methods provide their cores in C programming language and GNU R environment, respectively. Additional scripts are written in MathWorks MATLAB environment and they are used only as wrappers to these routines.

The averaged results of the examinations for single MRI slices are presented in Table 5.5. As we expected, the computationally efficient methods are the local ones, since they are mostly implemented using a set of 2D convolutions. Opposite to local estimators, the patch-based methods (Manjón et al. 2010, Manjón et al. 2015 and Rajan et al. 2011) are the least computationally efficient due to the requirement of $|V(\mathbf{x})| - 1$ comparisons between the local patch $\eta(\mathbf{x})$ and the remaining patches $\eta(\mathbf{p})$ for each pixel of the image individually. Consequently, the computational complexity of NLM-based algorithm is of the order of $\mathcal{O}(|V(\mathbf{x})||\eta(\mathbf{x})|)$ for a single point of the image. Some speed-up strategies of the NLM scheme have been published so far (Chan et al. 2013, Bhujle and Chaudhuri 2014), but they usually refer to image denoising procedure rather than noise estimation.

The computational cost of our proposal largely depends on employed noise extraction procedure (see Fig. 5.25). Specifically, we can estimate the computational complexity of these noise extraction procedures as follows:

- SWT is of the order of $\mathcal{O}(2k)$, if separable convolutions are used as explained in eq. (5.29); k is the number of coefficients of the filter (see Fig. 5.6),
- bilateral filter is of the order of $\mathcal{O}(|\eta(\mathbf{x})|)$.

Table 5.5: Averaged execution times of the algorithms for a single image of size 256×256 and 560×560 pixels.

Method	Execution time	
	256 × 256	560 × 560
Goossens et al. 2006	6 ms	20 ms
Delakis et al. 2007	34 ms	116 ms
Maximov et al. 2012	58 ms	187 ms
Liu et al. 2014	61 ms	211 ms
DeVore et al. 2000	120 ms	457 ms
Aja-Fernández et al. 2015b	168 ms	762 ms
Proposal (SWT)	191 ms	863 ms
Pan et al. 2012	704 ms	3 s 129 ms
Proposal (bilateral filter)	1 s 160 ms	4 s 812 ms
Maggioni and Foi 2012 (÷)	1 s 289 ms	4 s 735 ms
Borrelli et al. 2014	1 s 323 ms	4 s 880 ms
Landman et al. 2009a	5 s 457 ms	26 s
Manjón et al. 2010	35 s	2 min 43 s
Tabelow et al. 2015 (⋆)	53 s	1 min 16 s
Manjón et al. 2015	1 min 15 s	6 min 26 s
Rajan et al. 2011	4 min 26 s	~ 1.5 h

(÷) The algorithm is partly delivered in C programming language.

(⋆) The algorithm is delivered in GNU R environment.

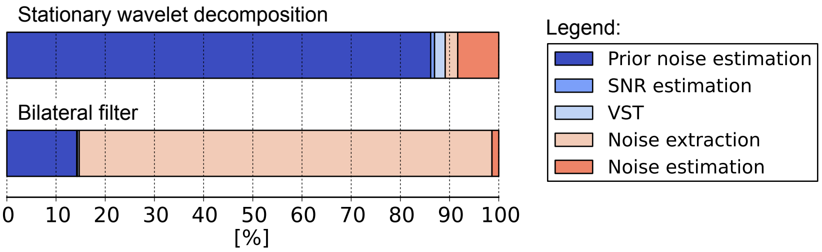

Figure 5.25: The percentage computational cost of two variants of the proposed noise estimation algorithm (compare to the scheme included in Fig. 5.4). Note that we split *Gaussian homomorphic noise estimation* module from Fig. 5.4 into two steps namely *noise extraction* and *noise estimation*.

At first glance, it looks as the results included in Table 5.5 were inconsistent with the theoretical considerations. However, note that we used build-in MathWorks MATLAB function to convolve the signal (single row/column of the image) with the kernel[10], while the core of the bilateral filter was prepared from scratch. Finally, note that we used a naive implementation of the bilateral filter instead of a fast algorithm of the order of $\mathcal{O}\left(\log\sqrt{|\eta(\mathbf{x})|}\right)$[11] or even $\mathcal{O}(1)$ (see Weiss 2006 and Porikli 2008 for more details).

5.7 Conclusions and remarks

In this chapter, we proposed a new variance-stabilizing transformation for Rician distributed random variable. This methodology allows transforming Rician distributed data to another data with Gaussian variate. Consequently, the signal-dependent Rician noise can be represented as a signal-independent AWGN component. We proved this transformation to be robust for the whole range of SNRs, i.e., from very low SNRs – Rayleigh distribution to very high SNRs – Gaussian distribution.

Then, we set up a variance-stabilizing homomorphic approach to estimate spatially variant noise patterns from non-stationary Rician distributed data. The non-stationary Rician noise is particularly interesting since we can find it in modern accelerated parallel MRI acquisitions like SENSE MRI. We adapted the proposed variance-stabilizing transformation to non-stationary Rician distributed data and then we combined the transformation with the homomorphic filtering scheme. **The proposed spatially variant Rician noise estimation method shows a remarkably better behaviour than all most relevant state-of-the-art methods including recent advances published in 2015**. The variance-stabilizing homomorphic filter is characterized by many advantages over recent state-of-the-art techniques estimating the noise from a single MR image. While the robustness of this estimator was justified in this chapter, we indicate the following superiorities of our proposal over the state-of-the-art:

- it takes signal-dependency of Rician noise into account rather than correction factors or rough assumptions of Gaussianity,
- it does not require pre-scans, multiple acquisitions, or a biophysical model of the data to retrieve the noise patterns,

---

[10] Actually, MathWorks MATLAB call the procedure `conv2.mex`, which is written in a low-level programming language rather than in MathWorks MATLAB itself.

[11] In comparison with commercial software, Adobe Photoshop CS2's Surface Blur module uses the algorithm in the order of $\mathcal{O}\left(\log\sqrt{|\eta(\mathbf{x})|}\right)$ (Porikli 2008).

- it is not affected by the granular effect,
- any technical details about the acqusition procedure like sensitivity profiles or noise matrices of the receiver coils are not required,
- it does not involve computationally intensive schemes like maximum likelihood or non-local means paradigm.

Our proposal is characterized also by some “soft” advantages:

1. **The algorithm is flexible** in comparison with other solutions. Specifically, different methodologies can be plugged into `prior noise estimation` and `SNR estimation` blocks of the pipeline included in Fig. 5.4. To verify this, we employed various methods to estimate a prior noise map $\sigma_0(\mathbf{x})$. These estimates are used then to stabilize the variance in non-stationary Rician distributed data (see Table 5.2). This experiment showed that almost any noise estimation approach presented in section 4.3.1 can be used as the initial guess $\widehat{\sigma_0(\mathbf{x})}$. Furthemore, we can substitute the noise extraction procedure included in `Gaussian homomorphic noise estimation` block by other edge-preservation and AWGN-compliant solution, e.g., the non-local means scheme (Buades et al. 2005) or guided filter (He et al. 2013).

2. **The software implementation of our proposal is straightforward**. It uses pointwise operations for variance-stabilizing transformation and discrete convolutions to extract the noise component from variance-stabilized non-stationary Rician distributed data. The noise estimation is carried out using the low-pass filter $\mathrm{LPF}_{\sigma_\mathrm{f}}$ as pointwise multiplication in DCT domain of the image. This enables to easily reimplement our proposal in almost any programming language or in an integrated circuit and finally place it inside the MRI scanner.

3. **The proposal is versatile and scalable**. It can be related to other engineering-related disciplines, where the signal follows (non-)stationary Rician distribution. The variance-stabilizing transformation and/or Rician noise estimation scheme can be employed in other scenarios:

    - SAR imaging: the data in SAR imaging follows Rician distribution and they are highly distorted by the noise (DeVore et al. 2000),
    - laser speckle: the intensity in speckle pattern phenomenon follows Rician distribution (Goodman 1975),
    - Rician fading channel: a model for radio propagation anomaly follows Rician distribution (Vandendorpe 1995).

Chapter 6

Non-stationary nc-χ noise estimation

Contents

6.1 Introduction

In this chapter we focus on non-stationary nc-χ distributed noise. This kind of noise is also relevant in MRI since it appears in accelerated parallel GRAPPA MRI magnitude data obtained with SoS and in multiple-coil acquisitions also reconstructed with SoS formula. Noise analysis in non-stationary nc-χ distributed data becomes more complicated than in non-stationary Rician data since additional parameter in statistical model appears, i.e., the parameter associated with the number of receiver coils. Moreover, the effective parameters must be introduced if accelerated parallel GRAPPA MRI or correlated multiple-coil is considered (both with SoS formula).

In this chapter, we propose the VST for nc-χ distributed RV. The VST is intentionally designed to generate Gaussian-like distributed variates from nc-χ data. As an application and proof of concept, we apply proposed VST framework to accurately estimate spatially variant noise patterns of accelerated parallel GRAPPA MR images obtained with SoS formula.

Analogously to Rician case, the proposal in spatially variant nc-χ noise estimation is characterized by many advantages over the state-of-the-art:

1. It is based on the VST procedure, which transforms the nc-χ data to Gaussian variates rather than Gaussian approximations. The noise estimation method is then accurate for the whole range of SNRs (from very low SNRs – non-stationary c-χ distribution to very high SNRs – non-stationary Gaussian distribution).

2. The single non-stationary nc-χ distributed image is used to retrieve a spatially variant noise pattern.

3. Our proposal does not require reconstruction coefficients for GRAPPA MRI and it works for retrospectively reconstructed magnitude data being a vendor independent method. Multiple acquisitions or pre-scans are not required to estimate the noise map.

4. Our proposal can be applied to different contrast type examinations including T_1-, T_2-, and PD-weighted MRI data sets.

5. The method is not affected by the granular effect as the final step of the algorithms is the homomorphic filtering procedure.

6. Our proposal is fast since it is implemented using discrete convolutions and pointwise operations.

7. Finally, the proposed VST allows using any Gaussian-compliant noise estimation method presented in Chapter 4.3 to retrieve spatially variant noise patterns from non-stationary nc-χ distributed data.

This chapter is organized as follows. In section 6.2, we present a mapping technique from nc-χ to Gaussian distributed signals, which was previously used in the MRI community. In section 6.3, we analytically derive the asymptotic VST for nc-χ distribution using squared nc-χ distributed RV. Then, we provide a robust numerical model in a similar fashion to Rician VST as presented in Chapter 5. This numerical model improves the performance of the asymptotic stabilizer for low SNRs. Next, in section 6.4, we adapt the proposed VST to non-stationary nc-χ distribution and we introduce noise estimation method for signal-dependent non-stationary nc-χ noise. Section 6.5 is devoted to present synthetic and real GRAPPA MRI data sets employed in the evaluation process of our proposal. In section 6.6, we verify the VSTs and the noise estimation algorithm in comparison with state-of-the-art methods. Firstly, we confirm the robustness of VSTs against the state-of-the-art

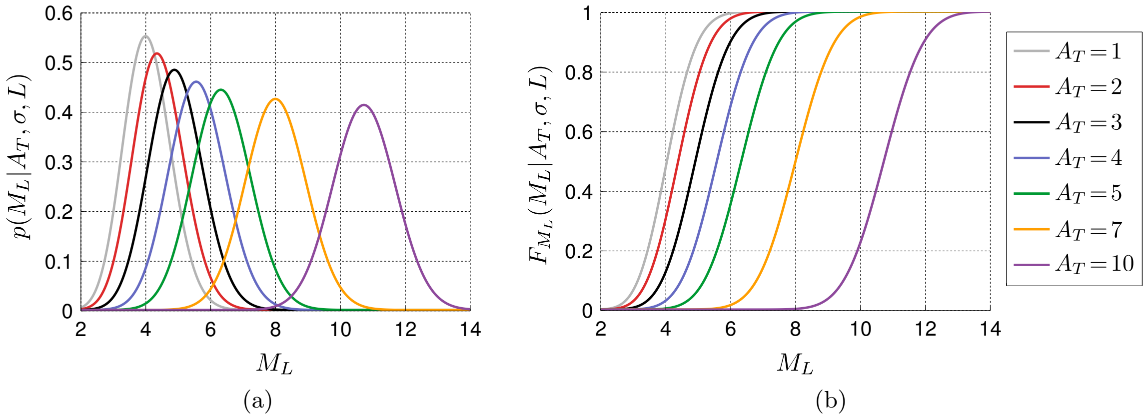

Figure 6.1: (a) The probability density functions and (b) the cumulative distribution functions for nc-χ distributed RV for different values of the amplitude A_T. The number of receiver coils L and the underlying noise variance σ^2 is the same for all plots, i.e., $L = 8$ and $\sigma^2 = 1$.

mapping technique from nc-χ to Gaussian distributed signals using statistical hypothesis testing, i.e., Chi-square goodness-of-fit test and Anderson-Darling test. Secondly, we show some quantitative experiments of the noise estimation algorithm using simulated accelerated parallel GRAPPA MRI data. Thirdly, the qualitative evaluations of our proposal are depicted for synthetic and real GRAPPA MRI data. Finally, we present experiments, which compare noise estimation results from a single image to the estimation process along the repeated scans. In the last paragraph of the chapter the concluding remarks are drawn.

6.2 Mapping from nc-χ to Gaussian distributed signals

In this section, we present a mapping method from a nc-χ distributed RV to a Gaussian distributed RV. This kind of methodology is well-known in probability theory and it was already used in context of digital signal processing including electroencephalography signals (Van Albada and Robinson 2007) and magnetic resonance imaging data (Koay et al. 2009a).

To explain the method, let us recall the PDF of nc-χ distributed RV M_L given by (3.25):

$$p(M_L|A_T,\sigma,L) = \frac{A_T^{1-L}}{\sigma^2} M_L^L \exp\left(-\frac{M_L^2+A_T^2}{2\sigma^2}\right) I_{L-1}\left(\frac{A_T M_L}{\sigma^2}\right), \quad M_L \geqslant 0, \tag{6.1}$$

where $M_L = M_L(\mathbf{x})$ is the magnitude signal, σ^2 is the underlying noise variance, L is the number of receiver coils and $A_T = A_T(\mathbf{x})$ is the noise-free amplitude signal. Consequently, the CDF corresponding to (6.1) is defined by the formula:

$$F_{M_L}(m|A_T,\sigma,L) = 1 - Q_L\left(\frac{A_T}{\sigma}, \frac{m}{\sigma}\right), \tag{6.2}$$

where $Q_L(\cdot,\cdot)$ is the generalized Marcum Q-function of L–th order (see Appendix A):

$$Q_L\left(\frac{A_T}{\sigma}, \frac{m}{\sigma}\right) = \left(\frac{\sigma}{A_T}\right)^{L-1} \int_{\frac{m}{\sigma}}^{\infty} t^L \exp\left(-\frac{\sigma^2 t^2 + A_T^2}{2\sigma^2}\right) I_{L-1}\left(\frac{A_T t}{\sigma}\right) dt. \tag{6.3}$$

The exemplary PDFs and the corresponding CDFs of nc-χ distributed RV for eight receiver coils ($L = 8$) are depicted in Fig. 6.1a and Fig. 6.1b, respectively.

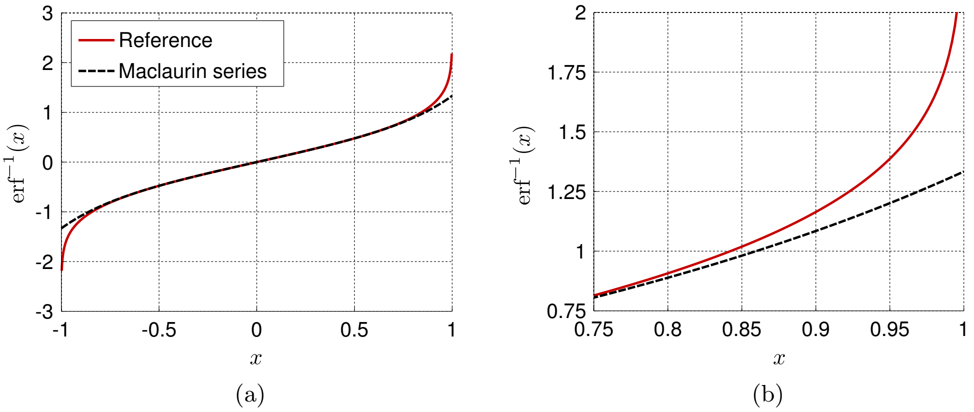

(a) (b)

Figure 6.2: (a) The inverse of the error function erf(x) (6.6) and its approximation using Maclaurin series (6.8). (b) The zoomed plot from figure (a).

To map a real-valued nc-χ distributed signal M_L to the Gaussian equivalent M_G, the following composition can be employed (Koay et al. 2009a)[1]:

$$M_G = F_{M_G}^{-1}\Big(F_{M_L}(M_L|A_T,\sigma,L)\Big|A_T,\sigma\Big), \tag{6.4}$$

where $F_{M_G}^{-1}(\cdot|A_T,\sigma)$ is the inverse CDF of a Gaussian RV with the expectation A_T and the standard deviation σ. The function $F_{M_G}^{-1}$ is given by the expression:

$$F_{M_G}^{-1}(y|A_T,\sigma) = A_T + \sigma\sqrt{2}\mathrm{erf}^{-1}(2y-1) \tag{6.5}$$

with $\mathrm{erf}^{-1}(x)$ being the inverse of the error function erf(x):

$$\mathrm{erf}(x) = \frac{2}{\sqrt{\pi}}\int_0^x e^{-t^2}\,dt. \tag{6.6}$$

Finally, an outlier-rejection step is recommended, which marks a sample M_G from eq. (6.4) to be an outlier if the following inequalities do not hold:

$$\frac{\varepsilon}{2} \leqslant F_{M_L}(M_L|A_T,\sigma,L) < 1-\frac{\varepsilon}{2}. \tag{6.7}$$

The parameter ε is user-defined, e.g., $\varepsilon = 0.005$. So, the method presented by Koay et al. 2009a can be summarized as follows:

1. firstly, the CDF (6.2) is applied to the nc-χ distributed data,
2. then, the inverse CDF (6.4) is calculated assuming Gaussianity of the data.

The presented method is straightforward, since it is only a pointwise operation. However, some further comments on the method are worth being pointed out here:

1. The method requires the parameters of the nc-χ distributed signal M_L to be known in advance, i.e., the noise-free signal A_T, the underlying noise standard deviation σ and the number of receiver coils L. These parameters are used to calculate the generalized Marcum Q-function (6.3) and the inverse CDF of a Gaussian RV (6.5), and they must be

---

[1] For the simplicity of the notation, we use the same symbol to refer both a Gaussian RV M_G and a particular realization of the RV.

estimated directly from the signal. Many methods can be arranged here, e.g., LMMSE estimator (Brion et al. 2011, Vegas-Sánchez-Ferrero et al. 2012), ML estimator (Rajan et al. 2012, Tabelow et al. 2015) or a fixed point formula (Koay and Basser 2006, Koay et al. 2009b).

2. The inverse of the error function $\mathrm{erf}^{-1}(x)$ and the generalized Marcum Q-function must be numerically evaluated. The former function can be approximated using the Maclaurin series as follows (Sloane et al. 2003, see Fig. 6.2):

$$\mathrm{erf}^{-1}(x) \approx \sqrt{\pi}\left(\frac{1}{2}x + \frac{1}{24}\pi x^3 + \frac{7}{960}\pi^2 x^5 + \frac{127}{80640}\pi^3 x^7\right). \tag{6.8}$$

Note that $\mathrm{erf}^{-1}(x)$ has three special values:

$$\mathrm{erf}^{-1}(x) = \begin{cases} -\infty & \text{for} \quad x = -1 \\ 0 & \text{for} \quad x = 0 \\ \infty & \text{for} \quad x = 1. \end{cases} \tag{6.9}$$

The approximation of the latter function becomes more complicated, since it requires the evaluation of the integral consisting the modified Bessel function of the first kind (6.3). Although many methods were proposed to approximate generalized Marcum Q-functions, we refer to the algorithm presented in Shnidman 1989 since it is computationally tractable. Note that numerical evaluations of generalized Marcum Q-functions are beyond the scope of the thesis and it might be an interesting topic for further research line.

3. The formula (6.4) is also valid for Rician RV with the CDF given by:

$$F_{M_L}(m|A_T,\sigma) = 1 - Q_1\left(\frac{A_T}{\sigma}, \frac{m}{\sigma}\right), \tag{6.10}$$

6.3 The variance-stabilizing transformation

In this section, we are looking for a function $f_{\mathrm{stab}}\colon \mathbb{R} \to \mathbb{R}$, which stabilizes the variate of nc-χ distributed RV M_L, i.e., it transforms the nc-χ distributed RV in such a way that the variance of the new RV $f_{\mathrm{stab}}(M_L)$ equals one. The main idea when stabilizing the variance in nc-χ distribution is similar to Rician case, however, additional parameter is introduced here, i.e., the number of the receiver coils L ($L \geqslant 1$). Note that the number of receiver coils equals one for Rician distribution.

In this section, we derive the asymptotic variance stabilizer, and then we propose a robust numerical scheme to improve the performance of the asymptotic model for low SNRs.

6.3.1 Asymptotic stabilizer for nc-χ distributed data

The variance of nc-χ data is in the functional dependence of the underlying (noise-free) signal A_T as stated in Chapter 3. Since the nc-χ distributed RV M_L (i.e., $M_L \sim \text{nc-}\chi(A_T,\sigma,L)$) does not have a closed-form expression for the expectation operator $\mathbb{E}\{M_L\}$, we refer to the squared random variable M_L^2, which follows a noncentral Chi-squared distribution, i.e., $M_L^2 \sim \text{nc-}\chi^2(A_T,\sigma,L)$. The PDF of M_L^2 distributed RV is given then by (Aja-Fernández et al. 2011; compare to eq. (6.1)):

$$p(M_L^2|A_T,\sigma,L) = \frac{A_T^{1-L}}{2\sigma^2} M_L^{L-1} \exp\left(-\frac{M_L^2 + A_T^2}{2\sigma^2}\right) I_{L-1}\left(\frac{A_T M_L}{\sigma^2}\right), \; M_L \geqslant 0, \tag{6.11}$$

where M_L^2 is the squared CMS and $A_T^2 = A_T^2(\mathbf{x})$ is defined by the formula $A_T^2(\mathbf{x}) = \sum_{l=1}^{L} |A_l(\mathbf{x})|^2$ with $A_l(\mathbf{x})$ being a noise-free signal from l–th receiver coil. Thenceforth, the odd raw moments can be expressed in closed-form expressions and consequently they are computationally tractable functions.

In what follows, the expectation value and the variance of M_L^2 distributed RV are given by (Simon 2007, Aja-Fernández and Tristán-Vega 2012):

$$\mathbb{E}\{M_L^2\} = A_T^2 + 2L\sigma^2, \tag{6.12}$$

$$\mathrm{Var}\{M_L^2\} = 4A_T^2\sigma^2 + 4L\sigma^4. \tag{6.13}$$

To derive the VST for squared nc-χ distributed RV, we use the first order Taylor expansion of the variance-stabilizing function $f_{\mathrm{stab}}(M_L^2|\sigma, L)$ about a point $M_L^2 = \widetilde{A_T^2}$:

$$f_{\mathrm{stab}}(M_L^2|\sigma, L) = f_{\mathrm{stab}}(\widetilde{A_T^2}|\sigma, L) + (M_L^2 - \widetilde{A_T^2}) \left.\frac{df_{\mathrm{stab}}}{dM_L^2}\right|_{M_L^2 = \widetilde{A_T^2}} + R_1(M_L^2), \tag{6.14}$$

where $R_1(M_L^2)$ is the remainder term of the expansion. We neglect this remainder term and take the variance on both sides of eq. (6.14):

$$\mathrm{Var}\{f_{\mathrm{stab}}(M_L^2|\sigma, L)\} \approx \mathrm{Var}\{M_L^2\} \cdot \left(\left.\frac{df_{\mathrm{stab}}}{dM_L^2}\right|_{M_L^2 = \widetilde{A_T^2}} \right)^2. \tag{6.15}$$

We impose now the constraint $\mathrm{Var}\{f_{\mathrm{stab}}(M_L^2|\sigma, L)\} = 1$ and calculate the integral of eq. (6.15) leading to a general formula of the asymptotic variance stabilizer for nc-χ^2 distributed RV M_L^2:

$$f_{\mathrm{stab}}(M_L^2|\sigma, L) = \int^{M_L^2} \frac{1}{\sqrt{\mathrm{Var}\{M_L^2|\widetilde{A_T}, \sigma, L\}}}\, d\widetilde{A_T}, \tag{6.16}$$

where $\mathrm{Var}\{M_L^2|\widetilde{A_T}, \sigma, L\}$ is the conditional variance of nc-χ^2 distributed RV, i.e., the variance in the function of the parameter $\widetilde{A_T}$. We derive this conditional variance referring to the expectation value and the variance of M_L^2 given by eqs. (6.12–6.13). From (6.12) we have $A_T^2 = \mathbb{E}\{M_L^2\} - 2L\sigma^2$, and then we put it into the eq. (6.13) leading to the formula:

$$\mathrm{Var}\{M_L^2\} = 4\left(\mathbb{E}\{M_L^2\} - 2L\sigma^2\right)\sigma^2 + 4L\sigma^4 = 4\sigma^2\left(\mathbb{E}\{M_L^2\} - L\sigma^2\right). \tag{6.17}$$

Note that the formula (6.17) depends on the noise variance parameter σ^2, the number of receiver coils L and the expectation value of M_L^2. We assume now that $\mu_2 = \mathbb{E}\{M_L^2\}$ and rewrite the formula (6.17) leading to the conditional variance of M_L^2:

$$\mathrm{Var}\{M_L^2|\mu_2, \sigma, L\} = 4\sigma^2\left(\mu_2 - L\sigma^2\right). \tag{6.18}$$

We plug now the eq. (6.18) into the integral (6.16):

$$f_{\mathrm{stab}}(M_L^2|\sigma, L) = \frac{1}{2\sigma}\int^{M_L^2} \frac{1}{\sqrt{\mu_2 - L\sigma^2}}\, d\mu_2. \tag{6.19}$$

To compute the integral (6.19), we refer to u-substitution rule. Let us assume that $u = \mu_2 - L\sigma^2$ and $du = d\mu_2$. Then, we have:

$$\int \frac{1}{\sqrt{\mu_2 - L\sigma^2}}\, d\mu_2 = \int u^{-\frac{1}{2}}\, du = 2\sqrt{u} + C = 2\sqrt{\mu_2 - L\sigma^2} + C, \quad C \in \mathbb{R}. \tag{6.20}$$

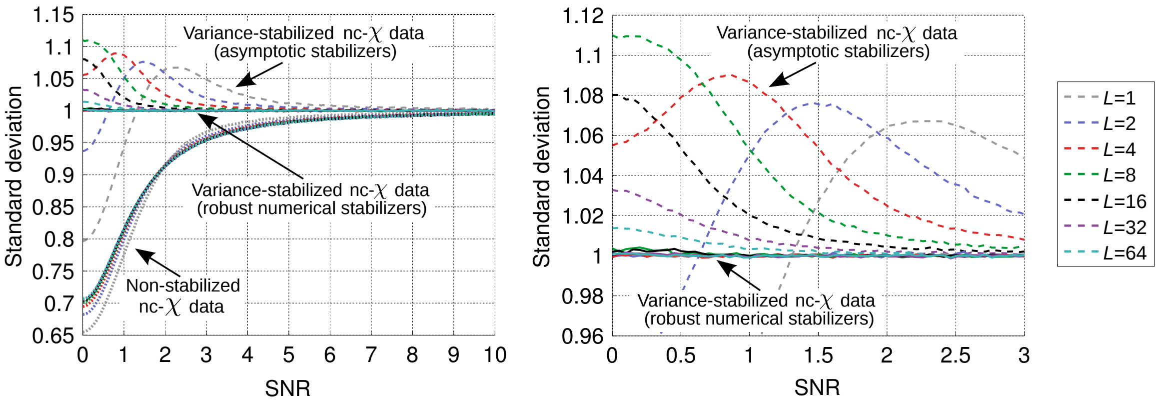

(a) (b)

Figure 6.3: (a) Comparison of standard deviations in terms of SNR (SNR $= A_T/\sqrt{L\sigma^2}$) between non-stabilized nc-χ data (dotted lines), variance-stabilized nc-χ data using asymptotic model (dashed lines) and robust numerical model (solid lines) for different number of receiver coils L. (b) The zoomed figure for SNR $\in [0;3]$.

Finally, the asymptotic stabilization formula (6.19) becomes the form:

$$f_{\text{stab}}(M_L^2|\sigma, L) = \frac{1}{\sigma}\sqrt{M_L^2 - L\sigma^2} = \sqrt{\frac{M_L^2}{\sigma^2} - L}. \tag{6.21}$$

The transformation (6.21) provides the asymptotic variance stabilizer for squared nc-χ distributed RV. Two issues must be addressed here:

1. The formula (6.21) does not depend on the underlying noise-free signal A_T anymore. So, to stabilize the variance in nc-χ distributed data, we need the square operation of the data and two parameters to be known in advance: the noise standard deviation σ and the number of receiver coils L. Note that the mapping technique from nc-χ to Gaussian distributed signals, previously presented in section 6.2, requires three parameters to be known beforehand: A_T, σ and L.

2. The formula (6.21) is not consistent with Rician VST for $L = 1$ (compare to eq. (5.6)), since we used nc-χ^2 distributed RV to obtain the closed-form expression for the expectation operator (6.12) and the variance (6.13) rather than the asymptotic approximation.

6.3.2 Robust numerical model

In the previous section, we derived the asymptotic model, which stabilizes the variance in nc-χ distributed data. The model requires the square operation of the data and two parameters to be known before the stabilization process namely the noise standard deviation σ and the number of the receiver coils L. Nevertheless, due to the simplifications implicit in the transformation, the previous model could not optimally work for low SNRs (see Fig. 6.3).

In this section, we propose a robust numerical model, which improves the accuracy of VST for low SNRs, while keeping the properties of asymptotic transformation for high SNRs. To that end, we redefine the eq. (6.21) using a vector parameter $\boldsymbol{\Theta} = (\theta_1, \theta_2)$:

$$f_{\text{stab}}(M_L^2|\sigma, L, \boldsymbol{\Theta}) = \frac{1}{\sigma}\sqrt{\max\{\theta_1^2 M_L^2 - \theta_2 L\sigma^2,\ 0\}}. \tag{6.22}$$

The vector parameter $\boldsymbol{\Theta}$ must be tuned accordingly to the SNR of the signal defined as:

$$\mathrm{SNR} = \frac{A_T}{\sqrt{L\sigma^2}}. \tag{6.23}$$

We introduce the maximum operator $\max\{\cdot,\cdot\}$ in eq. (6.22) to avoid a negative value under the square root sign. Then, the numerical optimization procedure is applied with the following criterion:

$$\boldsymbol{\Theta}_{\mathrm{opt}} = \arg\min_{\boldsymbol{\Theta}} J\left(f_{\mathrm{stab}}(M_L^2|\sigma, L, \boldsymbol{\Theta})\right), \tag{6.24}$$

where $J\colon \mathbb{R}^2 \mapsto \mathbb{R}$ is a cost function to be minimized:

$$\begin{aligned} J\left(f_{\mathrm{stab}}(M_L^2|\sigma, L, \boldsymbol{\Theta})\right) &= \lambda_1 \cdot \varphi(1 - \mathrm{Var}\{f_{\mathrm{stab}}(M_L^2|\sigma, L, \boldsymbol{\Theta})\}) \\ &+ \lambda_2 \cdot \varphi(\mathrm{Skewness}\{f_{\mathrm{stab}}(M_L^2|\sigma, L, \boldsymbol{\Theta})\}) \\ &+ \lambda_3 \cdot \varphi(\mathrm{ExcessKurtosis}\{f_{\mathrm{stab}}(M_L^2|\sigma, L, \boldsymbol{\Theta})\}), \end{aligned} \tag{6.25}$$

where $\lambda_1 + \lambda_2 + \lambda_3 = 1$ and $\varphi(x)$ is a convex function, e.g., $\varphi(x) = x^2$. Clearly, we impose the variance of the variance-stabilized data to be unitary, while the skewness and the excess kurtosis to be zero. Note that similarly to Rician case, additional parameters can be included in the cost function (6.25), e.g., higher order moments or measures of the shape of a probability distribution like L–moments (Hosking 1992).

We define now the components of the cost function (6.25) in terms of the raw moments for f_{stab}–transformed nc-χ^2 distribution:

$$\begin{aligned} \mathrm{Var}\left\{f_{\mathrm{stab}}(M_L^2|\sigma, L, \boldsymbol{\Theta})\right\} &= m_2 - m_1^2, \\ \mathrm{Skewness}\left\{f_{\mathrm{stab}}(M_L^2|\sigma, L, \boldsymbol{\Theta})\right\} &= \frac{m_3 - 3m_1m_2 + 2m_1^3}{(m_2 - m_1^2)^{\frac{3}{2}}}, \\ \mathrm{ExcessKurtosis}\left\{f_{\mathrm{stab}}(M_L^2|\sigma, L, \boldsymbol{\Theta})\right\} &= \frac{m_4 - 4m_1m_3 + 6m_1^2m_2 - 3m_1^4}{(m_2 - m_1^2)^2} - 3, \end{aligned} \tag{6.26}$$

where r–th raw moment for f_{stab}–transformed nc-χ^2 distributed RV is defined now as follows:

$$\begin{aligned} m_r &= \mathbb{E}\{f_{\mathrm{stab}}^r(M_L^2|\sigma, L, \boldsymbol{\Theta})\} \\ &= \int_0^\infty f_{\mathrm{stab}}^r(\widetilde{M_L^2}|\sigma, L, \boldsymbol{\Theta}) p(\widetilde{M_L^2}|A_T, \sigma, L) d\widetilde{M_L^2} \\ &= \int_0^\infty f_{\mathrm{stab}}^r(\widetilde{M_L^2}|\sigma, L, \boldsymbol{\Theta}) \frac{A_T^{1-L}}{2\sigma^2} \widetilde{M_L^{L-1}} \exp\left(-\frac{\widetilde{M_L^2} + A_T^2}{2\sigma^2}\right) I_{L-1}\left(\frac{A_T\widetilde{M_L}}{\sigma^2}\right) d\widetilde{M_L^2}. \end{aligned} \tag{6.27}$$

The optimization of the cost function (6.25) is performed by calculating the raw moments defined by (6.27) of the stabilized nc-χ^2 distributed RV by means of the adaptive Gauss-Kronrod quadrature over the interval $M_L \in [0,\ 30]$. We used Nelder-Mead optimization method assuming $\sigma = 1$ and logarithmically increasing parameter A_T between 0.001 and 15.

The performance of the resulting optimization procedure for the convex function $\varphi(x) = x^2$, weighting parameters $(\lambda_1, \lambda_2, \lambda_3) = (0.998, 0.001, 0.001)$ and different number of the receiver coils L is shown in Fig. 6.3. The results obtained with the asymptotic VST is satisfactory for high SNRs only. The robust numerical model stabilizes the nc-χ data in the whole range of SNRs for all the cases considered ($L \in \{1, 2, 4, 8, 16, 32, 64\}$), though, the knowledge about the SNR of the signal is required. The accuracy of the asymptotic model improves with the increasing number of receiver coils L and it can be a good alternative to the numerical approach for $L \geqslant 32$, especially assuming that it does not require the SNR

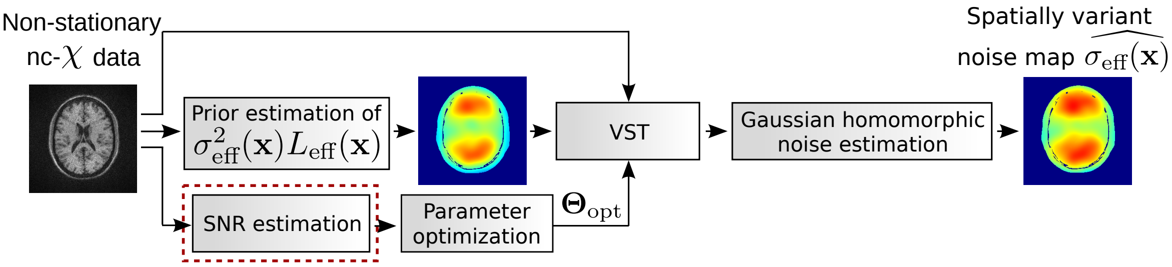

Figure 6.4: General scheme of our proposal in non-stationary nc-χ noise estimation. The method requires the initial estimate of $\sigma^2_{\text{eff}}(\mathbf{x})L_{\text{eff}}(\mathbf{x})$ and the SNR map to stabilize the data (the block VST), and then to retrieve the spatially variant noise map estimate $\widehat{\sigma_{\text{eff}}(\mathbf{x})}$ using the Gaussian homomorphic filter. The optimal vector parameter $\mathbf{\Theta}_{\text{opt}}$ is obtained from the numerical optimization procedure (6.24). The red rectangle indicates the interchangeable module of the pipeline.

of the signal to be known. Note that we assumed that the SNRs for numerical model are exactly known for this experiment.

The optimized version of the formula (6.22) finally becomes the form:

$$f_{\text{stab}}(M_L^2|\sigma, L, \mathbf{\Theta}_{\text{opt}}) = \frac{1}{\sigma}\sqrt{\max\{\theta^2_{1\text{opt}}M_L^2 - \theta_{2\text{opt}}L\sigma^2,\ 0\}}, \tag{6.28}$$

where $\mathbf{\Theta}_{\text{opt}} = (\theta_{1\text{opt}}, \theta_{2\text{opt}})$ is the optimized vector parameter $\mathbf{\Theta}$.

6.4 Non-stationary nc-χ noise estimation

In section 6.3, we proposed transformations to stabilize the variance of nc-χ distributed RV:

1. the asymptotic stabilizer (6.21) in a closed-form formula,
2. the numerical model (6.28), which boosts the accuracy of the asymptotic transformation for low SNRs.

These transformations change a signal-dependent nc-χ distributed noise to the Gaussian equivalent. In this section, we present a non-stationary nc-χ noise estimation approach employing proposed VSTs and the homomorphic Gaussian filter (Aja-Fernández et al. 2015b, Aja-Fernández and Vegas-Sánchez-Ferrero 2015).

6.4.1 Spatially variant nc-χ noise estimation

The VSTs derived in section 6.3 are intended for nc-χ distributed RV. However, a typical MRI acquisition shows a certain level of correlation between the receiver coils (Aja-Fernández et al. 2011, Aja-Fernández and Tristán-Vega 2012, Algarin et al. 2015). Consequently, the VST (6.28) must be corrected taking the correlations between the coils into account, when applied to the magnitude signal $M_L(\mathbf{x})$ obtained from accelerated parallel GRAPPA MRI or a multiple-coil acquisition (both reconstructed with SoS). To this end, we introduce the effective parameters to eq. (6.28) leading to the formula:

$$f_{\text{stab}}(M_L^2|\sigma_{\text{eff}}, L_{\text{eff}}, \mathbf{\Theta}_{\text{opt}}) = \frac{1}{\sigma_{\text{eff}}}\sqrt{\max\{\theta^2_{1\text{opt}}M_L^2 - \theta_{2\text{opt}}L_{\text{eff}}\sigma^2_{\text{eff}},\ 0\}}. \tag{6.29}$$

Once the VST is adapted to the squared CMS signal $M_L^2 = M_L^2(\mathbf{x})$, we can follow the pipeline depicted in Fig. 6.4. This figure summarizes the spatially variant noise estimation procedure for nc-χ distributed data and it is employed to estimate the noise patterns for accelerated parallel GRAPPA MRI with SoS reconstruction in this chapter.

Firstly, we pointwisely apply the VST (6.29) to the magnitude image $M_L(\mathbf{x})$ as follows (the block `VST` in Fig. 6.4):

$$\begin{aligned} \widetilde{M_L}(\mathbf{x}) &= \widehat{\sigma_{\text{eff}}(\mathbf{x})} \cdot f_{\text{stab}}(M_L^2(\mathbf{x}) | \widehat{\sigma_{\text{eff}}(\mathbf{x})}, \widehat{L_{\text{eff}}(\mathbf{x})}, \boldsymbol{\Theta}_{\text{opt}}(\mathbf{x})) \\ &= \sqrt{\max\{\theta_{1\text{opt}}^2(\mathbf{x}) M_L^2(\mathbf{x}) - \theta_{2\text{opt}}(\mathbf{x}) \widehat{L_{\text{eff}}(\mathbf{x})} \widehat{\sigma_{\text{eff}}^2(\mathbf{x})},\ 0\}}, \end{aligned} \tag{6.30}$$

where $\widehat{L_{\text{eff}}(\mathbf{x})}$ and $\widehat{\sigma_{\text{eff}}^2(\mathbf{x})}$ are the estimates of the effective number of coils and the effective variance of noise, respectively, and $\boldsymbol{\Theta}_{\text{opt}}(\mathbf{x}) = (\theta_{1\text{opt}}(\mathbf{x}), \theta_{2\text{opt}}(\mathbf{x}))$ is the vector parameter $\boldsymbol{\Theta}$ optimized to local SNR. The optimization procedure (6.24) requires the SNR level, which is defined for accelerated parallel GRAPPA MRI with SoS reconstruction as follows (Aja-Fernández et al. 2014a):

$$\text{SNR}_{M_L}(\mathbf{x}) = \frac{A_T(\mathbf{x})}{\sqrt{\frac{L_{\text{eff}}(\mathbf{x}) \sigma_{\text{eff}}^2(\mathbf{x})}{r}}}, \tag{6.31}$$

where r is the subsampling rate of the raw data in $\mathbf{k}$–space domain. The parameters $\theta_{1\text{opt}}(\mathbf{x})$ and $\theta_{2\text{opt}}(\mathbf{x})$ are defined now in terms of local SNR level:

$$\begin{aligned} \theta_{1\text{opt}}(\mathbf{x}) &= (\theta_1 \circ \text{SNR}_{M_L})(\mathbf{x}), \\ \theta_{2\text{opt}}(\mathbf{x}) &= (\theta_2 \circ \text{SNR}_{M_L})(\mathbf{x}). \end{aligned} \tag{6.32}$$

Note, that if the asymptotic VST is used instead (i.e., $\theta_{1\text{opt}}(\mathbf{x}) \equiv 1$ and $\theta_{2\text{opt}}(\mathbf{x}) \equiv 1$), the stabilization (6.30) is reduced to the formula:

$$\widetilde{M_L}(\mathbf{x}) = \sqrt{\max\{M_L^2(\mathbf{x}) - \widehat{L_{\text{eff}}(\mathbf{x})} \widehat{\sigma_{\text{eff}}^2(\mathbf{x})},\ 0\}}. \tag{6.33}$$

After the variance-stabilizing procedure, $\widetilde{M_L}(\mathbf{x})$ can be seen as a noise-free signal $\widetilde{A_T}(\mathbf{x})$ corrupted with additive Gaussian noise $N(\mathbf{x}; 0, \sigma_{\text{eff}}^2(\mathbf{x}))$ with zero mean and spatially variant variance $\sigma_{\text{eff}}^2(\mathbf{x})$:

$$\widetilde{M_L}(\mathbf{x}) \approx \widetilde{A_T}(\mathbf{x}) + N(\mathbf{x}; 0, \sigma_{\text{eff}}^2(\mathbf{x})) = \widetilde{A_T}(\mathbf{x}) + \sigma_{\text{eff}}(\mathbf{x}) \cdot N(\mathbf{x}; 0, 1). \tag{6.34}$$

Secondly, we extract the noise component from the stabilized image $\widetilde{M_L}(\mathbf{x})$ and estimate the noise map out of Gaussian data (the block `Gaussian homomorphic noise estimation` in Fig. 6.4). We adapt Gaussian homomorphic approach recently presented in section 5.3.1, since it has proved its accuracy and robustness. Therefore, the noise map can be estimated as follows:

$$\widehat{\sigma_{\text{eff}}(\mathbf{x})} = \sqrt{2} \exp\left(\text{LPF}_{\sigma_{\text{f}}} \left\{ \log \left| \widetilde{M_{L_{\text{C}}}}(\mathbf{x}) \right| \right\} + \frac{\gamma}{2} \right), \tag{6.35}$$

where $\text{LPF}_{\sigma_{\text{f}}}$ is a low-pass filter with standard deviation σ_{f}, γ is the Euler-Mascheroni constant and $\widetilde{M_{L_{\text{C}}}}(\mathbf{x}) = \mathbb{E}\{\widetilde{M_L}(\mathbf{x})\}$ is a centered version of the image $\widetilde{M_L}(\mathbf{x})$, where $\mathbb{E}\{\cdot\}$ is the expectation operator that must be locally approximated for practical implementation.

6.4.2 Noise extraction procedures

The second step of the algorithm presented in section 6.4.1 requires the centering procedure of the data $\widetilde{M_L}(\mathbf{x})$ prior to the final noise estimation. Although many edge-preservation and AWGN-compliant solutions can be arranged here, we employ the SWT of the image $\widetilde{M_L}(\mathbf{x})$ using HH subband at the scale $s = 1$. Again, we refer to the diagonal details coefficients:

$$\widetilde{M_{L_{\text{C}}}}(\mathbf{x}) = ((\widetilde{M_L} \circledast g^{(r)}) \circledast g^{(c)})(\mathbf{x}), \tag{6.36}$$

where "$\circledast$" denotes the convolution operator. The convolution procedure (6.36) is performed with separable one-dimensional high-pass filter g using db7 wavelet (see Fig.5.6). The first convolution is applied along the rows of the image $\widetilde{M_L}(\mathbf{x})$ (denoted as $g^{(r)}$), while the second convolution is applied along the columns of the pre-filtered image (denoted as $g^{(c)}$).

Once again, we are not obligated to use the SWT to extract the noise component from the stabilized image $\widetilde{M_L}(\mathbf{x})$ (6.34). However, by employing the SWT we can relatively compare our proposal with recent advances in noise estimation for GRAPPA MRI presented in Aja-Fernández and Vegas-Sánchez-Ferrero 2015, i.e., we can relate the estimation results *with* and *without* the variance-stabilization step.

6.4.3 Local SNR estimation

The presented numerical VST procedure requires the SNR to be known in advance. For accelerated parallel GRAPPA MRI reconstructed with SoS, the SNR map of the magnitude image $M_L(\mathbf{x})$ is defined as in eq. (6.31). The denominator of eq. (6.31) can be estimated using the procedure proposed by Aja-Fernández et al. 2013. However, we still need the method to obtain the estimate of the underlying noise-free signal $A_T(\mathbf{x})$. Different techniques for nc-χ data can be arranged here including LMMSE estimator (Brion et al. 2011), ML estimator (Rajan et al. 2012) and the majorize-minimize framework (Varadarajan and Haldar 2015). In this work, we use a local mean of the magnitude image $M_L(\mathbf{x})$ as the estimator of the underlying signal $A_T(\mathbf{x})$ since it is computationally tractable approach.

6.5 Materials and methods

In this section we present the data sets employed in the evaluation process of our proposal and we provide the details of the methods arranged in our experiments.

6.5.1 Materials

To verify our proposal in non-stationary nc-χ noise estimation, we carry out numerical experiments using both synthetic and real GRAPPA MRI data obtained with SoS formula. Below, a brief description of the data used in our experiments is given.

1. Synthetic MR images: three brain MRI slices at different transverse planes are used, i.e., T_1-, T_2- and PD-weighted MRI data (all with INU=0%). The data are free of noise, the background areas are set to zero, the slice thickness equals 1 mm and the intensity range of the images is normalized to $[0-255]$ (Fig. 6.5a–c). The synthetic data sets come from BrainWeb simulated database (Collins et al. 1998). These images are used then to simulate synthetic noisy accelerated parallel GRAPPA MRI data with SoS reconstruction.

2. Synthetic GRAPPA MR images[2]: simulated noisy T_1-, T_2- and PD-weighted GRAPPA MRI data with SoS reconstruction. The Cartesian GRAPPA reconstruction uses eight receiver coils ($L = 8$) with correlations between k–th and l–th receiver coil ($k \neq l$) defined to be ρ_{kl}, the variance of the noise is set to $\sigma_l^2 = \sigma^2$ for all receiver coils (the noise is the same for all L coils) and GRAPPA reduction factor is set to $r = 2$ (Fig. 6.5d–f). The **k**–space is uniformly sampled and 32 ACS lines are preserved. These data are used for qualitative evaluation of noise estimation methods.

---

[2] We used Aja-Fernández's parallel MRI simulator available at `https://www.mathworks.com/matlabcentral/fileexchange/36893-parallel-mri-noisy-phantom-simulator`.

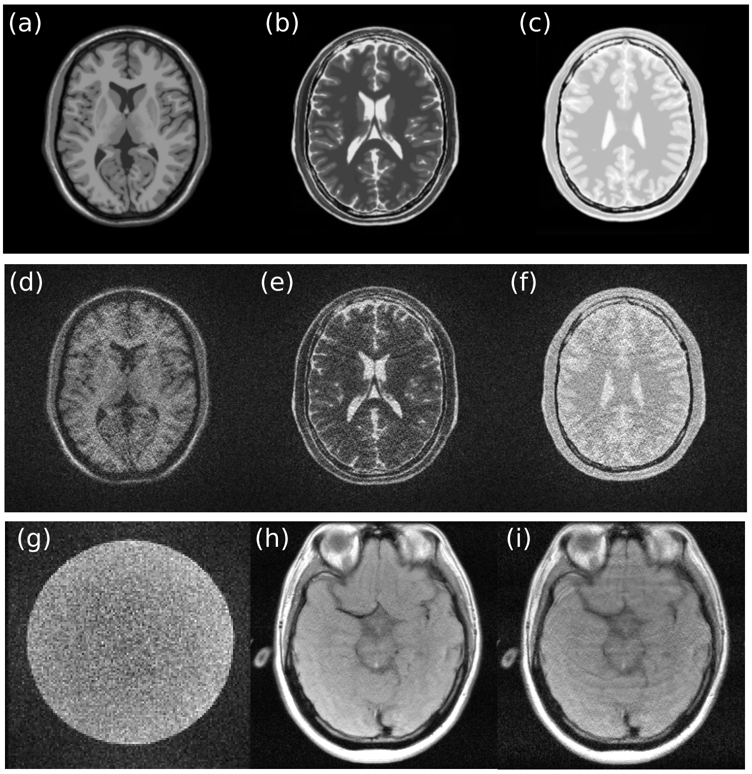

Figure 6.5: Data sets used in the experiments: (a) synthetic noise-free T_1-, (b) T_2- and (c) PD-weighted MRI data, (d) simulated noisy T_1-, (e) T_2- and (f) PD-weighted GRAPPA MRI data (all with $L = 8$ and $r = 2$), (g) real noisy T_1-weighted FGRE GRAPPA MRI phantom ($L = 8$, $r = 2$), (h) *in vivo* noisy T_1-weighted FSPGR GRAPPA MRI brain data ($L = 8$, $r = 2$) and (i) *in vivo* noisy T_1-weighted FSPGR GRAPPA MRI brain data ($L = 8$, $r = 4$).

3. Real GRAPPA MRI phantom: one hundred repetitions of T_1-weighted scan of a phantom were performed using GE Signa 1.5T EXCITE 12m4 scanner (General Electric Healthcare, Waukesha, WI) with an eight-channel head coil using Fast Gradient Echo (FGRE) sequence, matrix size equals 128×128, TR=8.6 ms / TE=3.38 ms, slice thickness equals 1 mm, FOV is set to $\text{FOV}_x \times \text{FOV}_y = 21 \times 21$ cm and the reduction factor equals $r = 2$ (Fig. 6.5g). The $\mathbf{k}$–space is uniformly sampled and 32 ACS lines are preserved.

4. *In vivo* GRAPPA MRI brain data: two T_1-weighted scans of the brain in transverse plane are acquired by GE 3.0T scanner provided with an eight-channel head coil. The data sets were acquired using Fast Spoiled Gradient Echo (FSPGR) sequence, matrix size equals 256×256, TR=300 ms / TE=10 ms, FOV is set to $\text{FOV}_x \times \text{FOV}_y = 22 \times 22$ cm and the reduction factor equals $r = 2/r = 4$ (Fig. 6.5h, i). The $\mathbf{k}$–space is uniformly sampled and 64 ACS lines are preserved. This data come from PULSAR parallel MRI simulator (Ji et al. 2007).

6.5.2 Methods

For the sake of evaluation of our proposal, we use four noise estimation methods, which assume the noise component to be non-stationary Gaussian (Goossens et al. 2006, Pan et al. 2012, Maggioni and Foi 2012 and Aja-Fernández and Vegas-Sánchez-Ferrero 2015) and one method dealing with non-stationary nc-χ distributed noise (Tabelow et al. 2015). For more details about these noise estimation algorithms, see section 4.3.1.

The state-of-the-art Gaussian methods are used twice during the evaluation process:

1. the algorithms are applied directly to the magnitude GRAPPA MRI data,
2. the VST given by eq. (6.29) is applied to the magnitude GRAPPA MRI data prior to noise estimation.

All Gaussian methods employed in the evaluation procedure retrieve spatially variant noise pattern from a single image without any additional information about the acquisition process. One parameter is needed by Tabelow et al. 2015 – the number of receiver coils L, which is assumed to be constant over the FOV.

Regarding our proposal, we use the same parameters as with Rician distributed noise:

- the SWT given by eq. (6.36) uses db7 wavelet,
- the low pass filter (6.35) uses the parameter $\sigma_{\mathrm{f}} = 3.4$ to generate circularly symmetric Gaussian mask,
- the noise estimation is performed in a 5×5 window,
- the estimation of local SNR is carried out in a 5×5 window.

Finally, note that we used morphological operators for the detection procedure of the foreground area of the image (see section 4.4 for more details).

6.6 Experimental results and discussion

In this section, we numerically examine proposed VSTs for nc-χ distribution and we quantitatively/qualitatively evaluate noise estimation algorithms. At first, we carry on some statistical experiments to verify the underlying assumption of Gaussianity of the noise in variance-stabilized data. Then, we show the applications of VST for nc-χ distributed data in context of spatially variant noise estimation for GRAPPA MRI data obtained with SoS.

6.6.1 Statistical analysis of VSTs

In this section, we evaluate the proposed asymptotic and numerical variants of VST for nc-χ distributed data. To this end, the following experiments are considered:

1. Chi-square goodness-of-fit test (χ^2-test) and Anderson-Darling (AD) test to verify if the noise in variance-stabilized nc-χ data follows the standard normal distribution.
2. Quantile-quantile (QQ) plots of the noise in variance-stabilized nc-χ data.

In the **first statistical experiment**, we verify the normality of the noise in variance-stabilized nc-χ data. To extract the noise component from variance-stabilized nc-χ distributed signal, we use the SWT with high-pass filter associated with db7 wavelet (see Fig. 5.6). We perform 10000 repetitions of χ^2-test[3] and AD test[4] for simulated nc-χ data with SNR $\in [0;\ 3]$ and different number of receiver coils $L \in \{8, 16, 32, 64\}$.

The null hypothesis H_0 of statistical tests states that "*the noise in variance-stabilized nc-χ data follows standard normal distribution*", while the alternative hypothesis H_1 is the opposite. The significance level equals $\alpha = 0.05$ and sample size is $N = 256$ for both tests. The pipeline of the experiment is summarized in Fig. 6.6. We additionally compared our proposals to Koay's mapping technique presented in section 6.2. The parameters A_T and σ are exactly known for the methods in this experiment.

---

[3] The routine `chi2gof` is used in the simulation (The MathWorks, Inc., Natick, MA).

[4] The routine `adtest` is used in the simulation (The MathWorks, Inc., Natick, MA).

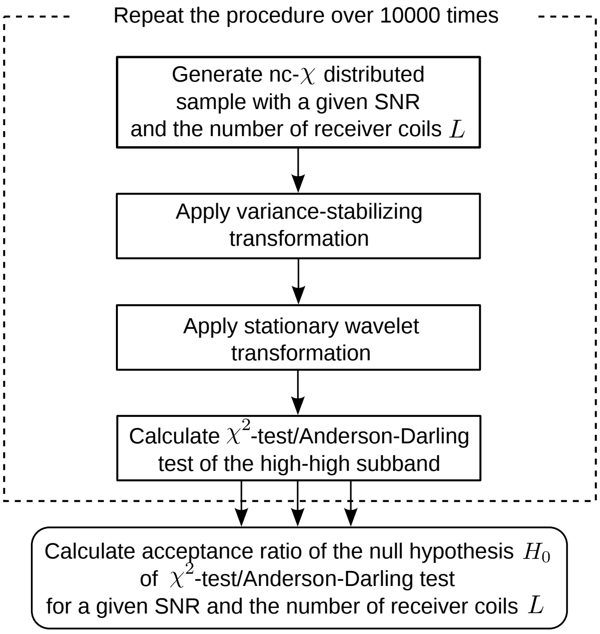

Figure 6.6: The evaluation scheme of the noise component in variance-stabilized nc-χ data for a given SNR level (SNR $= A_T/\sqrt{L\sigma^2}$) and the number of receiver coils L using a statistical hypothesis testing.

The acceptance ratios of H_0 for the experiment in terms of SNR of the signal are depicted in Fig. 6.7 and Fig. 6.8. The results show the high performance of the robust numerical model regardless of SNR level, i.e., at least 92.70% and 98.98% acceptance ratios for χ^2-test and AD test, respectively. Nevertheless, the asymptotic model tends to be also valid in terms of statistical hypothesis testing for increasing number of receiver coils, especially for $L = 32$ and $L = 64$. Clearly, the noise component in variance-stabilized nc-χ data can be treated as Gaussian distributed and the algorithms assuming Gaussianity of the data can then be employed. Note that the acceptance ratios of χ^2-test are lower than the acceptance ratios of AD tests, since the χ^2-test depends on the data binning process. Finally, note that the proposed numerical model outperforms Koay's mapping technique for all the cases. Furthermore, the asymptotic model shows also much better performance for $L \geqslant 16$ than Koay's technique.

In the **second statistical experiment**, we show QQ plots for the noise component in variance-stabilized nc-χ data by robust numerical model. In comparison to the previous experiments, the purpose of this evaluation is to show the Gaussianity of the noise in variance-stabilized nc-χ data rather than compare the VSTs models to each other. To this end, we generate the samples of size $N = 256$ from nc-χ distribution with SNR $\in \{1, 2, 5\}$ and different number of receiver coils $L \in \{8, 16, 32, 64\}$. Then, we relate the quantiles of standard normal distribution (theoretical quantiles) to the quantiles of the noise in variance-stabilized nc-χ samples using the robust numerical VST model (empirical quantiles).

The results of the experiment show that the quantiles approximately lie on the reference line $y = x$ (see Fig. 6.9), assessing that the noise in variance-stabilized nc-χ data comes from the standard normal distribution $\mathcal{N}(0, 1)$. Note that our proposal does not interfere with the signal characterized by SNR $= 5$, where the nc-χ data can be approximated well-enough using Gaussian distribution. Such approximation of GRAPPA MRI signal for higher SNR was proposed by Aja-Fernández and Vegas-Sánchez-Ferrero 2015.

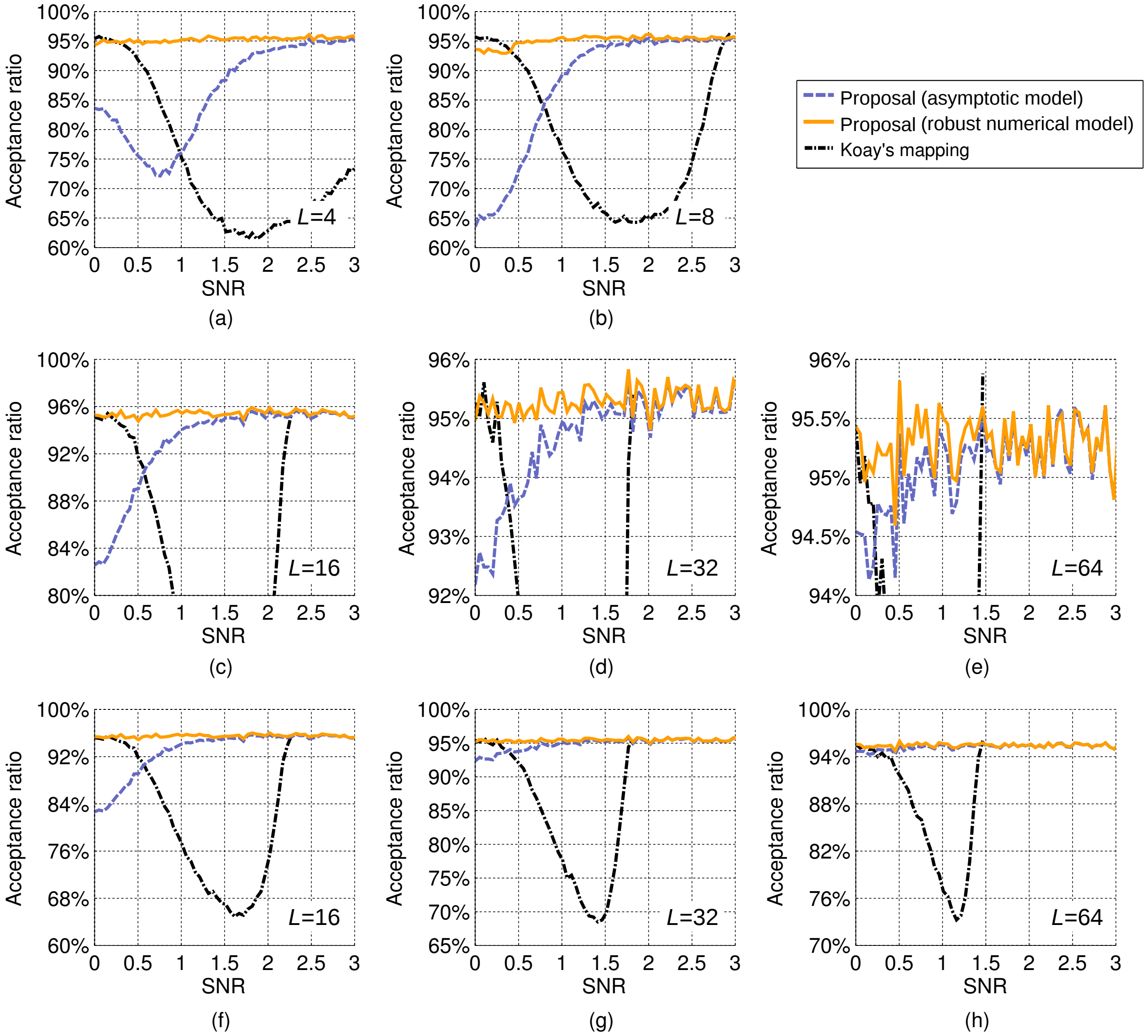

(a) (b) (c) (d) (e) (f) (g) (h)

Figure 6.7: (a–e) Acceptance ratios of χ^2-test of the noise component in variance-stabilized nc-χ distributed data using asymptotic and numerical models for different number of receiver coils L. Our proposals are compared then to Koay's mapping technique (6.4). (f–h) Zoomed out plots from figures (c–e).

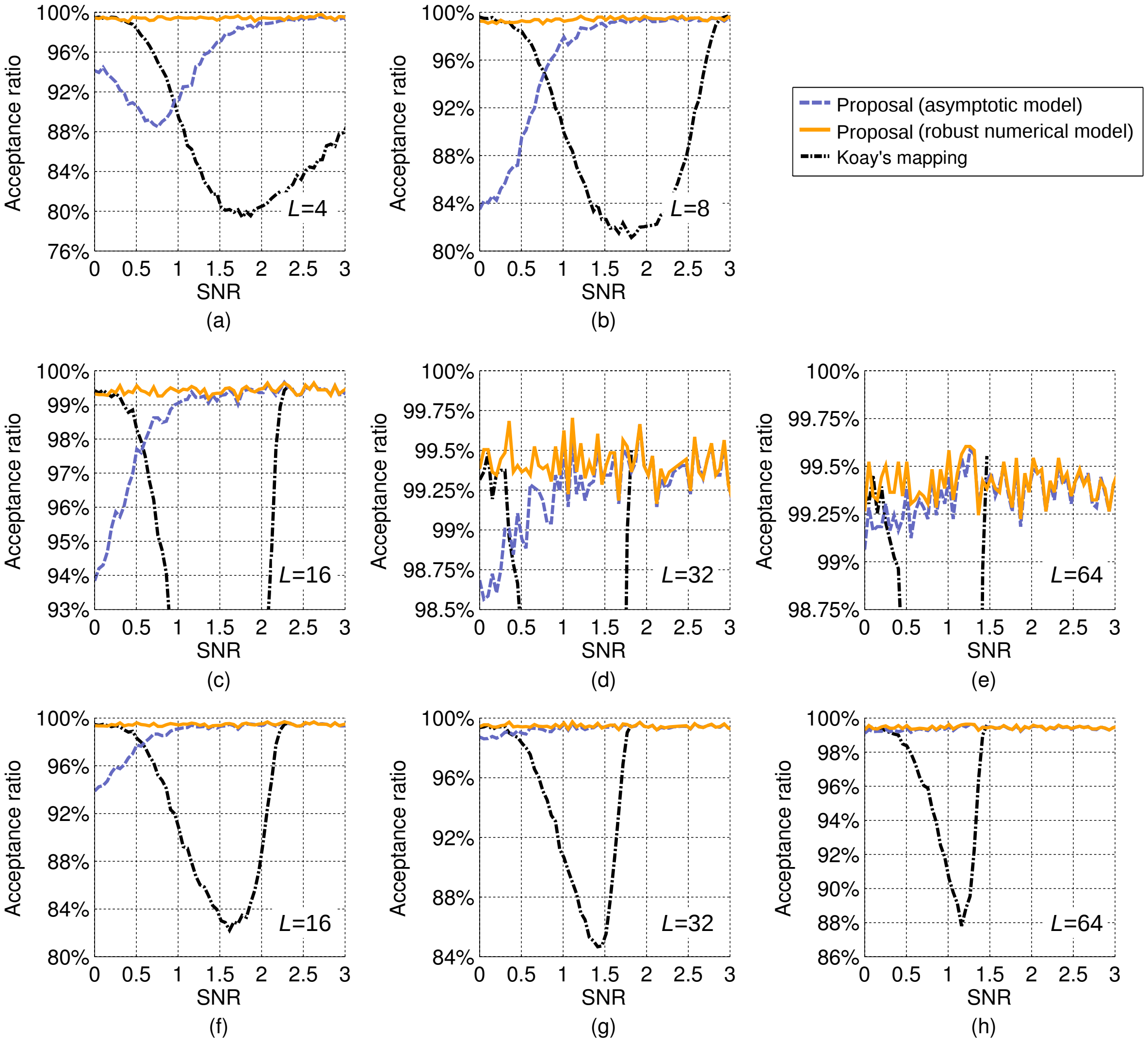

Figure 6.8: (a–e) Acceptance ratios of AD test of normality of the noise component in variance-stabilized nc-χ distributed data using asymptotic and numerical models for different number of receiver coils L. Our proposals are compared then to Koay's mapping technique (6.4). (f–h) Zoomed out plots from figures (c–e).

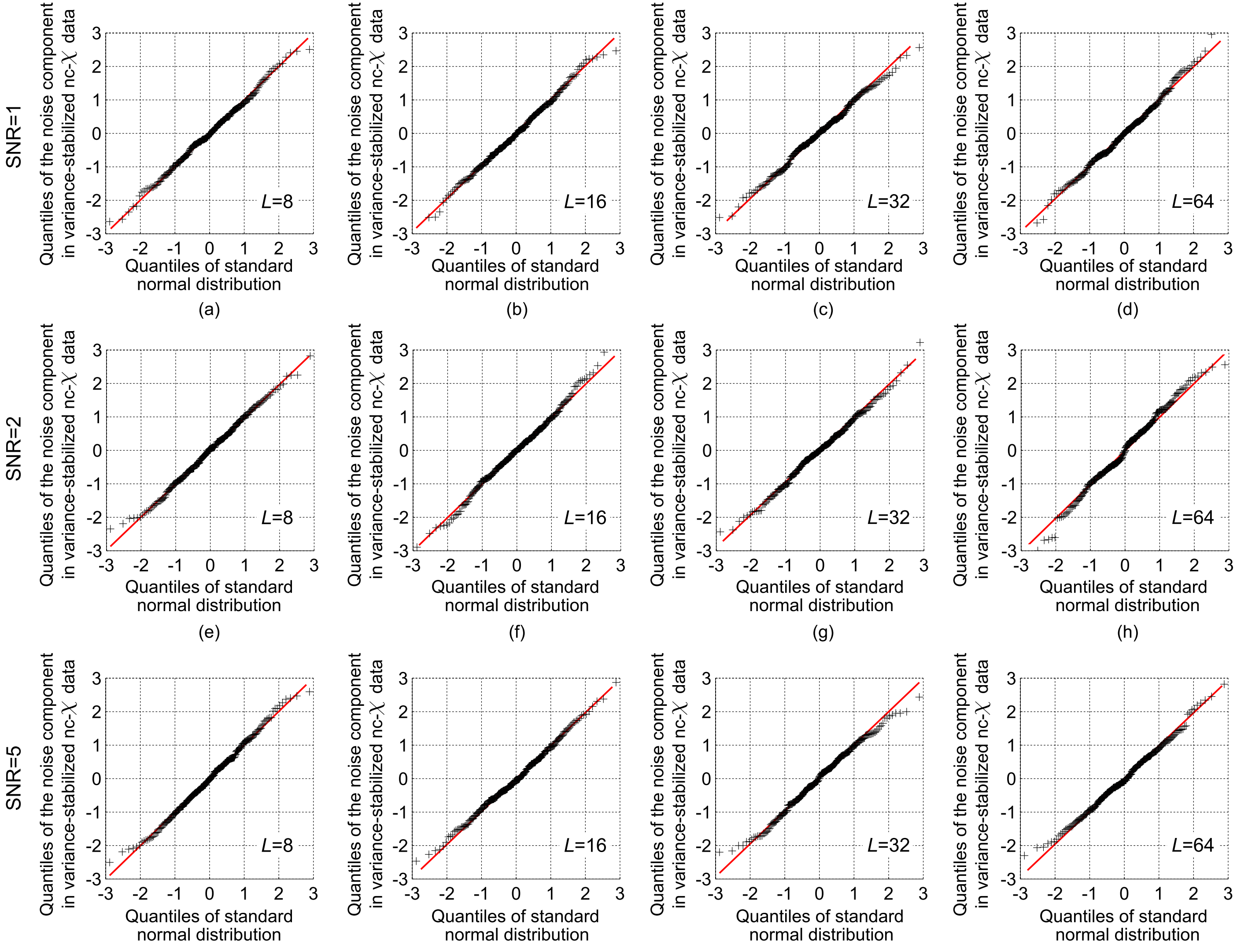

(a) (b) (c) (d)

(e) (f) (g) (h)

(i) (j) (k) (l)

Figure 6.9: QQ plots of the noise component in variance-stabilized nc-χ distributed data for different number of receiver coils $L \in \{8, 16, 32, 64\}$ and SNR level: (a–d) SNR $= 1$, (e–h) SNR $= 2$ and (i–l) SNR $= 5$. The red lines indicate the reference $y = x$. The sample size equals $N = 256$ for all experiments.

6.6.2 Synthetic GRAPPA MRI data experiments

In this section, we present three experiments with simulated T_1-, T_2-, and PD-weighted accelerated parallel GRAPPA MRI data reconstructed with SoS:

1. Quantitative evaluation of the methods in terms of the underlying noise variance $\sigma_l^2 = \sigma^2$. The underlying noise variance is assumed to be the same for all L coils.
2. Quantitative evaluation of the methods in terms of the correlation ratio between the receiver coils $\rho_{kl} = \rho$. The correlation ratio is the same between the receiver coils.
3. Qualitative evaluation of the methods.

For all experiments presented in this section, we employ synthetic BrainWeb noise-free T_1-, T_2- and PD-weighted MRI transverse slices recently presented in section 6.5.1 (see Fig. 6.5a–c). We simulate eight coils ($L = 8$) noisy GRAPPA MRI data with underlying noise level σ and correlations between receiver coils given by ρ. The **k**–space is uniformly sampled in frequency encoding direction and it is uniformly subsampled by the factor of $r = 2$ in phase encoding direction keeping 32 ACS lines. The local SNR maps are exactly known for this experiment. Finally, the reference noise patterns obtained from Aja-Fernández et al. 2011 are used to evaluate the accuracy of the estimators using the parameters $\mathrm{RE}(\mathbf{x})$ (4.63) and $\mathrm{VAR}(\mathbf{x})$ (4.64). Note that we additionally examine the state-of-the-art Gaussian methods combined with numerical VST procedure (6.29).

In the **first noise estimation experiment**, the behaviour of noise estimators for different values of the underlying noise standard deviation σ is tested. The correlations between the receiver coils are set to $\rho = 0.1$ for all simulations. One hundred repetitions ($R = 100$) of the estimation procedure are considered for each algorithm, noise level σ and contrast type examination (T_1-, T_2-, and PD-weighted scan). The estimation results are then averaged along the replicas, and the final values of $\overline{\mathrm{RE}}$ and $\overline{\mathrm{VAR}}$ are calculated as spatial averages of the parameters $\mathrm{RE}(\mathbf{x})$ and $\mathrm{VAR}(\mathbf{x})$ over the foreground area of the image Ω_Δ (see section 4.4 for more details about calculating the parameters $\overline{\mathrm{RE}}$ and $\overline{\mathrm{VAR}}$).

The results of the experiment are shown in Fig. 6.10. The first observation is clear: applying the VST procedure prior to noise estimation using Gaussian method leads to significant improvement of the results. The higher the underlying noise level σ is, the larger difference in the parameter $\overline{\mathrm{RE}}$ between a non-variance-stabilized and a variance-stabilized Gaussian estimator is observed. Contrary, the methods coincide for low value of noise standard deviation σ. These results are obvious, since the nc-χ distribution approximately follows Gaussian distribution for SNR $\to \infty$. The proposed methodology is the one with the greatest performance, showing almost constant values of $\overline{\mathrm{RE}}$ and $\overline{\mathrm{VAR}}$ for the whole range of the parameter σ. Finally, note that the method by Tabelow et al. 2015, initially proposed to deal with non-stationary nc-χ distributed data, generally shows a better performance in terms of the parameter $\overline{\mathrm{RE}}$ than Gaussian methods. However, it is still outperformed by our proposal (Fig. 6.10a, c, e) and some other Gaussian methods supported by the VST procedure, i.e., Pan et al. 2012 (Fig. 6.10a, c), Maggioni and Foi 2012 (Fig. 6.10a and Fig. 6.10c for higher noise level σ).

In the **second noise estimation experiment**, we quantitatively investigate the behaviour of noise estimators for different values of correlation ratio between receiver coils. All the reconstruction details of GRAPPA algorithm are the same as in the first experiment except the underlying noise variance, which is fixed now to $\sigma^2 = 225$ for all simulations. One hundread repetitions of the estimation procedure are considered for each algorithm, correlation ratio ρ and contrast type examination.

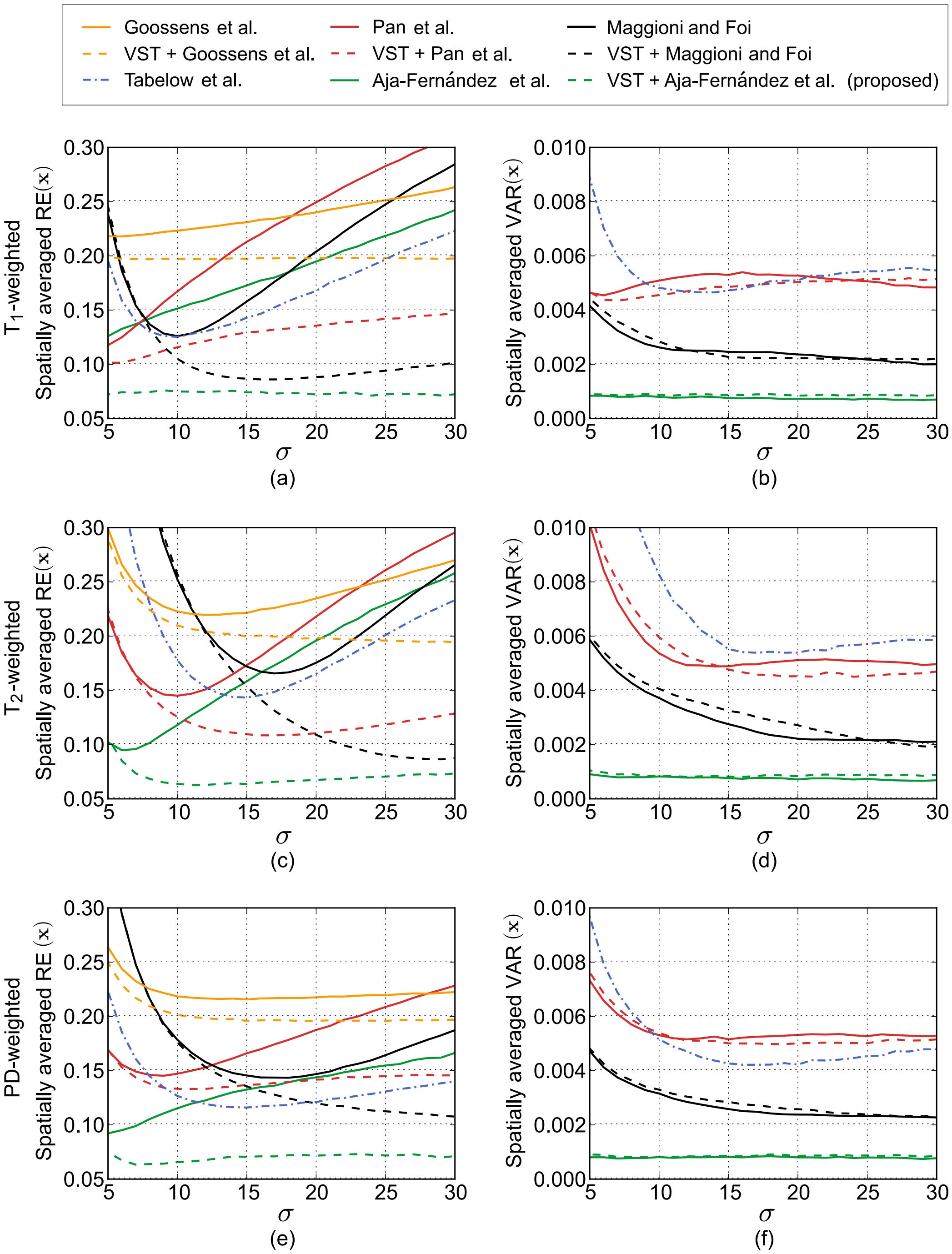

Figure 6.10: Comparison of noise estimators for synthetic GRAPPA MRI data contamined by non-stationary nc-χ distributed noise in the function of $\sigma_l = \sigma$. The reconstructions use eight receiver coils ($L = 8$), subsampling rate $r = 2$ and the correlations between the coils equals $\rho = 0.1$. Each plot presents the averaged results over $R = 100$ repetitions of the experiment. The first column shows spatially averaged relative error of the estimators, $\overline{\mathrm{RE}}$, while the second column presents spatially averaged variance of the estimators, $\overline{\mathrm{VAR}}$. The first row corresponds to T_1-, the second row to T_2- and the third one to PD-weighted GRAPPA MRI data. The acronym "VST + " means that the variance-stabilizing transformation is applied to the magnitude data before the estimation process.

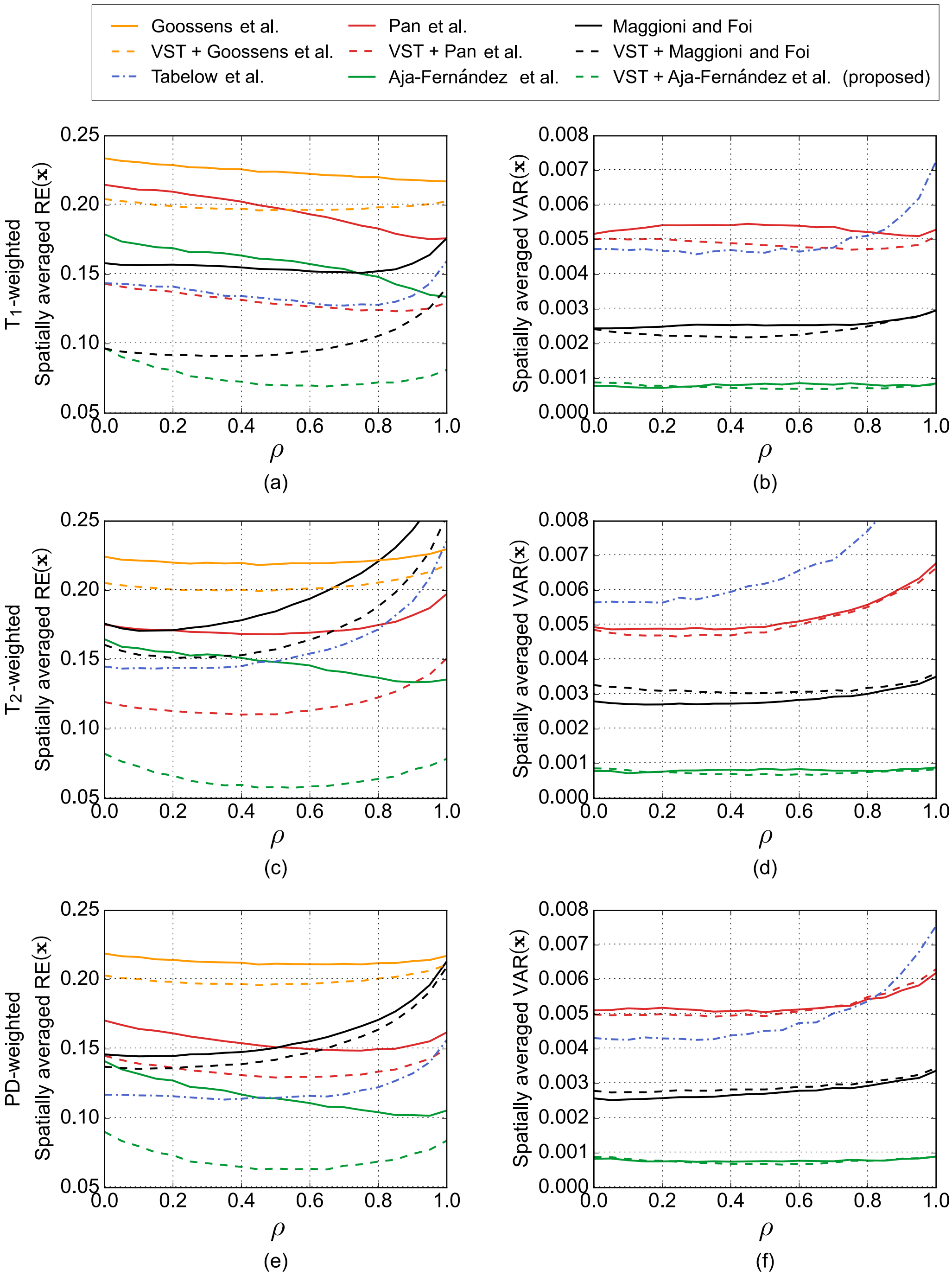

Figure 6.11: Comparison of noise estimators for synthetic GRAPPA MRI data contamined by non-stationary nc-χ distributed noise in the function of $\rho_{kl} = \rho$. The GRAPPA reconstructions use eight receiver coils ($L = 8$), subsampling rate $r = 2$ and the underlying noise variance equals $\sigma^2 = 225$. Each plot presents the averaged results over $R = 100$ repetitions of the experiment. The first column shows spatially averaged relative error of the estimators, $\overline{\mathrm{RE}}$, while the second column presents spatially averaged variance of the estimators, $\overline{\mathrm{VAR}}$. The first row corresponds to T_1-, the second row to T_2- and the third one to PD-weighted GRAPPA MRI data. The acronym "VST + " means that the variance-stabilizing transformation is applied to the magnitude data before the estimation process.

The parameters $\overline{\text{RE}}$ and $\overline{\text{VAR}}$ obtained in this experiment are shown in Fig. 6.11. Again, the variance-stabilization procedure improves the performance of any Gaussian estimator for the whole range of the parameter $\rho \in [0;\ 1]$. Finally, we point out that our proposal shows a great performance in comparison to the state-of-the-art methods when the variance-stabilization procedure is applied, i.e., it has the lowest $\overline{\text{RE}}$ and almost constant $\overline{\text{VAR}}$ parameter over all ρ levels.

As the **third noise estimation experiment**, we visually compare the estimated noise patterns and the corresponding REs of the estimators for simulated GRAPPA MRI data, i.e., T_1-, T_2- and PD-weighted transverse slices (see Fig. 6.5d–f). We fixed the underlying noise variance to $\sigma^2 = 225$ and the correlation ratio between receiver coils to $\rho = 0.1$. Other parameters of the image reconstruction procedure are the same as presented in the introductory part of this section. The reference (theoretical) noise maps are obtained according to Aja-Fernández et al. 2011. To evaluate the estimators, we use all non-stationary noise estimation algorithms engaged in previous quantitative experiments. The estimation with Gaussian methods is repeated then after applying the VST. Moreover, we refer to a *silver standard* method being a pointwise sample standard deviation calculated along twenty five ($R = 25$) repetitions (see eq. (4.61)).

The estimation results and the corresponding REs of the estimators for this experiment are shown in Figs. 6.12–6.14. Note that we use a binary mask to hide the parameter RE($\mathbf{x}$) for the background areas since it is not representative. The first conclusion is clear: in all the cases the use of the VST prior to a Gaussian estimation improves the accuracy of the estimator, while employing a Gaussian method directly on the non-stationary nc-χ distributed data leads to the underestimated results.

Similarly to the results obtained for SENSE MRI data, Goossens et al. 2006 lead to highly granular noise patterns, whether the method uses the VST or not. On the other hand, Pan et al. 2012 and Maggioni and Foi 2012 preceded by the VST show more reliable and less granular results in comparison with Goossens et al. 2006. Nevertheless, the estimators are still affected by the skull egdes (Fig. 6.12h,j and Fig. 6.14j) and the inhomogeneities of the tissues introduce a bias to the estimates (Fig. 6.13j). Supprisingly, a similar behaviour can be observed for Tabelow et al. 2015 (especially for T_1-weighted image; see Fig. 6.12b). Although the method by Tabelow et al. 2015 benefits from the nc-χ model, it assumes the number of receiver coils to be constant across the image, i.e., $L(\mathbf{x}) \equiv \text{const}$[5]. Note that the relative error of standard deviation along the variance-stabilized samples, RE($\mathbf{x}$), does not exhibit the influence of the MR signal (Figs. 6.12d, 6.13d, 6.14d). Finally, the hereby proposed method is the one showing the greatest fidelity with the *ground truth*, avoiding the granularity in the estimation and the influence of the edges (Figs. 6.12l, 6.13l, 6.14l).

6.6.3 Real GRAPPA MRI data experiments

In this section, we present qualitative evaluations of the methods for real accelerated parallel GRAPPA MRI data reconstructed with SoS formula. In comparison to the experiments presented in section 6.6.2, the reference maps are not available here and therefore we cannot use the quantitative measures.

In the **first noise estimation experiment**, we evaluate the estimators using real T_1-weighted FGRE GRAPPA MRI phantom data (see section 6.5.1 for more details). We refer to *silver standard* method (4.61) being a pointwise sample standard deviation along one hundred ($R = 100$) acquisitions of the same phantom.

---

[5] The authors suggest using the reduced value of L (or simply assume $L(\mathbf{x}) \equiv 1$) to avoid a model misspecification (see the section 2.6 in Tabelow et al. 2015 for more details).

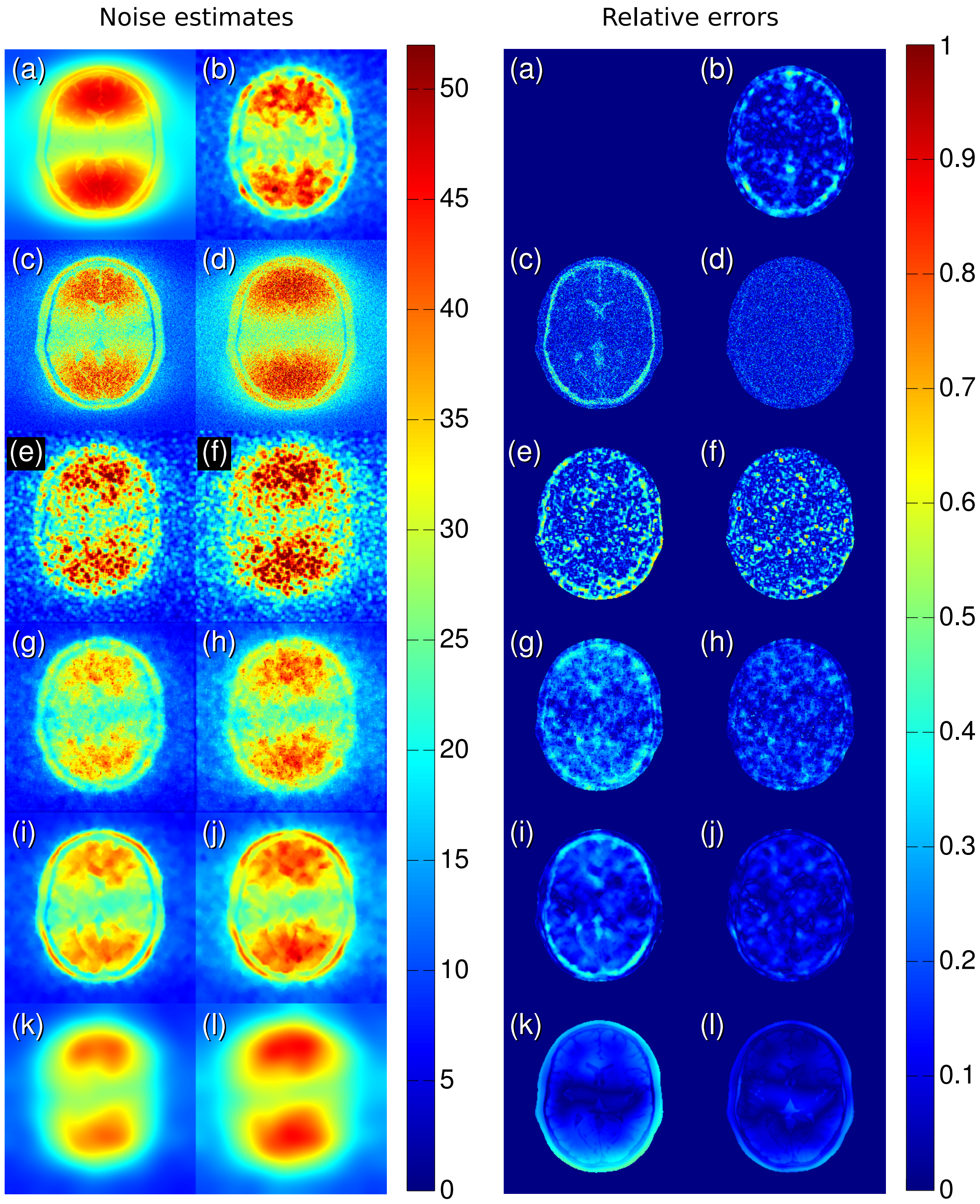

Figure 6.12: Noise estimation results and the relative errors of the estimators for synthetic T_1-weighted GRAPPA MR image reconstructed from eight receiver coils ($L = 8$), the correlation ratio between receiver coils $\rho = 0.1$ and the underlying noise variance $\sigma^2 = 225$ ($\mathrm{SNR}_{\max} = 6.92$) (Fig. 6.5d): (a) the *ground truth* (Aja-Fernández et al. 2011), (b) Tabelow et al. 2015, (c) standard deviations along the replicas ($R = 25$), (d) VST + standard deviations along the replicas ($R = 25$), (e) Goossens et al. 2006, (f) VST + Goossens et al. 2006, (g) Pan et al. 2012, (h) VST + Pan et al. 2012, (i) Maggioni and Foi 2012, (j) VST + Maggioni and Foi 2012, (k) Aja-Fernández and Vegas-Sánchez-Ferrero 2015 and (l) VST + Aja-Fernández and Vegas-Sánchez-Ferrero 2015 (**our proposal**).

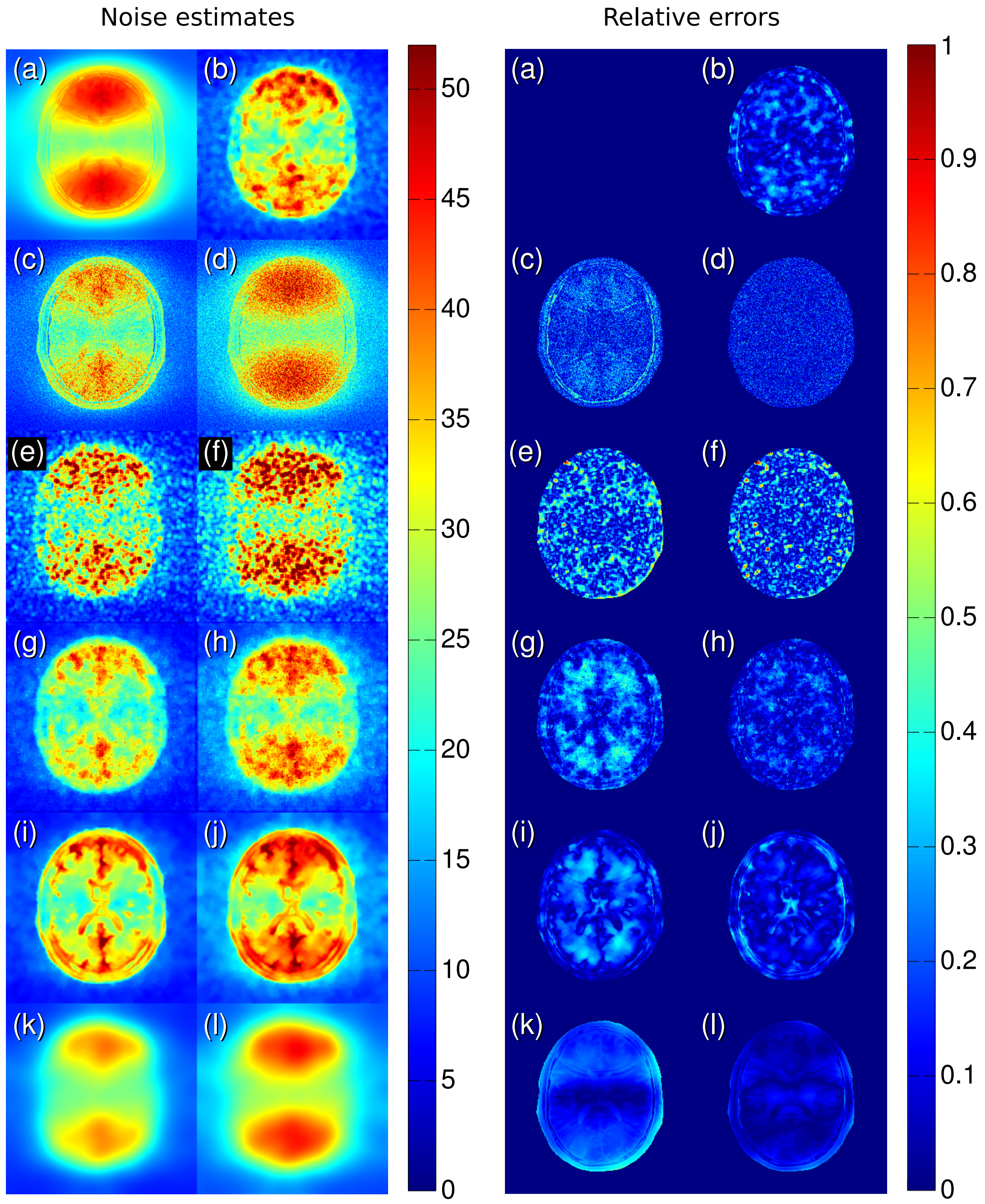

Figure 6.13: Noise estimation results and the relative errors of the estimators for synthetic T_2-weighted GRAPPA MR image reconstructed from eight receiver coils ($L = 8$), the correlation ratio between receiver coils $\rho = 0.1$ and the underlying noise variance $\sigma^2 = 225$ ($\text{SNR}_{\max} = 6.58$) (Fig. 6.5e): (a) the *ground truth* (Aja-Fernández et al. 2011), (b) Tabelow et al. 2015, (c) standard deviations along the replicas ($R = 25$), (d) VST + standard deviations along the replicas ($R = 25$), (e) Goossens et al. 2006, (f) VST + Goossens et al. 2006, (g) Pan et al. 2012, (h) VST + Pan et al. 2012, (i) Maggioni and Foi 2012, (j) VST + Maggioni and Foi 2012, (k) Aja-Fernández and Vegas-Sánchez-Ferrero 2015 and (l) VST + Aja-Fernández and Vegas-Sánchez-Ferrero 2015 (**our proposal**).

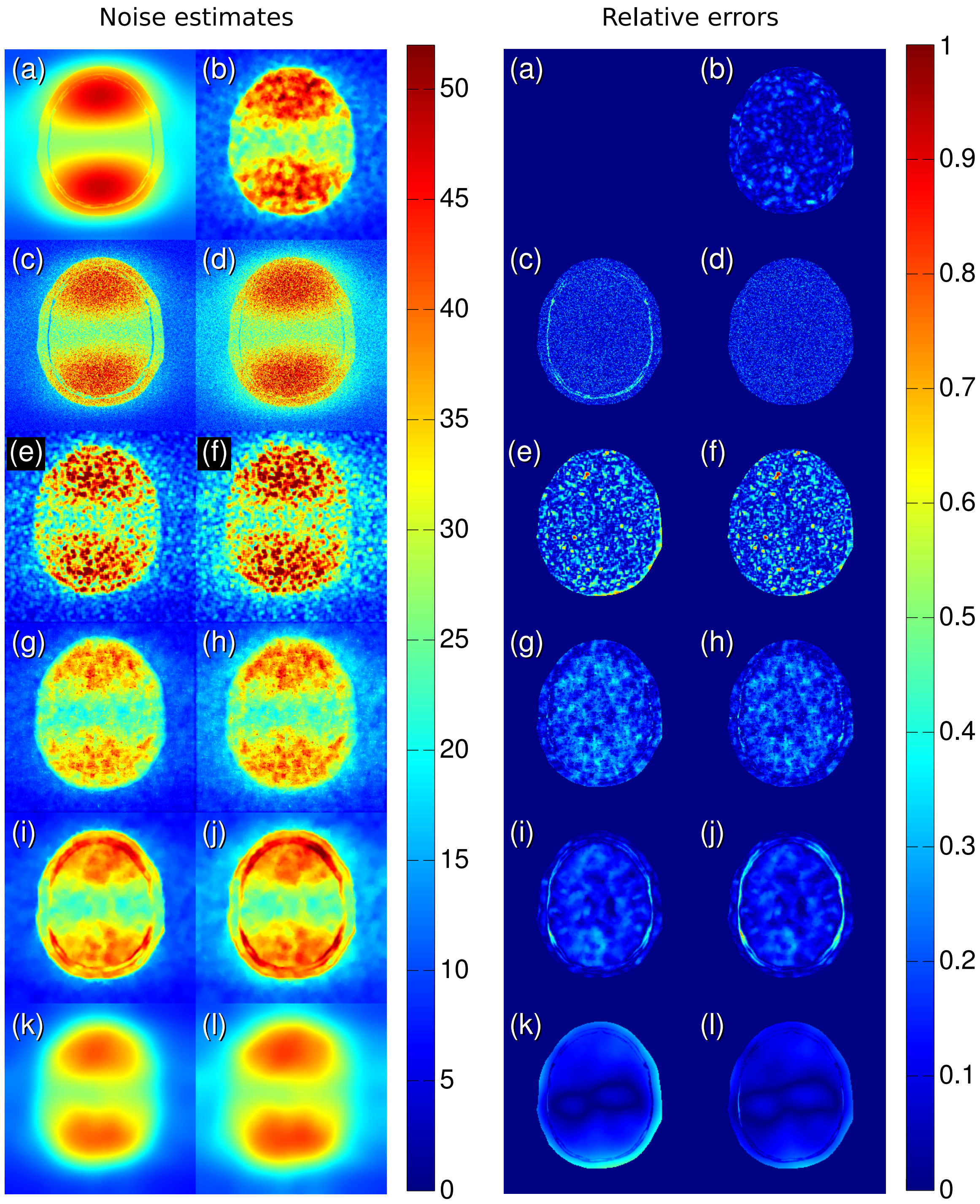

Figure 6.14: Noise estimation results and the relative errors of the estimators for synthetic PD-weighted GRAPPA MR image reconstructed from eight receiver coils ($L = 8$), the correlation ratio between receiver coils $\rho = 0.1$ and the underlying noise variance $\sigma^2 = 225$ ($\text{SNR}_{\text{max}} = 6.86$) (Fig. 6.5f): (a) the *ground truth* (Aja-Fernández et al. 2011), (b) Tabelow et al. 2015, (c) standard deviations along the replicas ($R = 25$), (d) VST + standard deviations along the replicas ($R = 25$), (e) Goossens et al. 2006, (f) VST + Goossens et al. 2006, (g) Pan et al. 2012, (h) VST + Pan et al. 2012, (i) Maggioni and Foi 2012, (j) VST + Maggioni and Foi 2012, (k) Aja-Fernández and Vegas-Sánchez-Ferrero 2015 and (l) VST + Aja-Fernández and Vegas-Sánchez-Ferrero 2015 (**our proposal**).

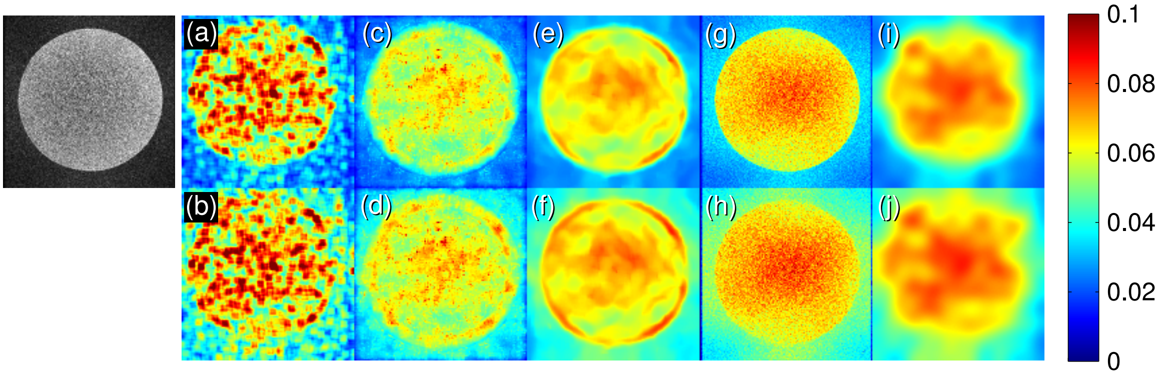

Figure 6.15: Visual inspections of the methods for real T_1-weighted FGRE GRAPPA MRI data: (a) Goossens et al. 2006, (b) VST + Goossens et al. 2006, (c) Pan et al. 2012, (d) VST + Pan et al. 2012, (e) Maggioni and Foi 2012, (f) VST + Maggioni and Foi 2012, (g) standard deviations along the replicas ($R = 100$), (h) VST + standard deviations along the replicas ($R = 100$), (i) Aja-Fernández and Vegas-Sánchez-Ferrero 2015 and (j) VST + Aja-Fernández and Vegas-Sánchez-Ferrero 2015 (**our proposal**).

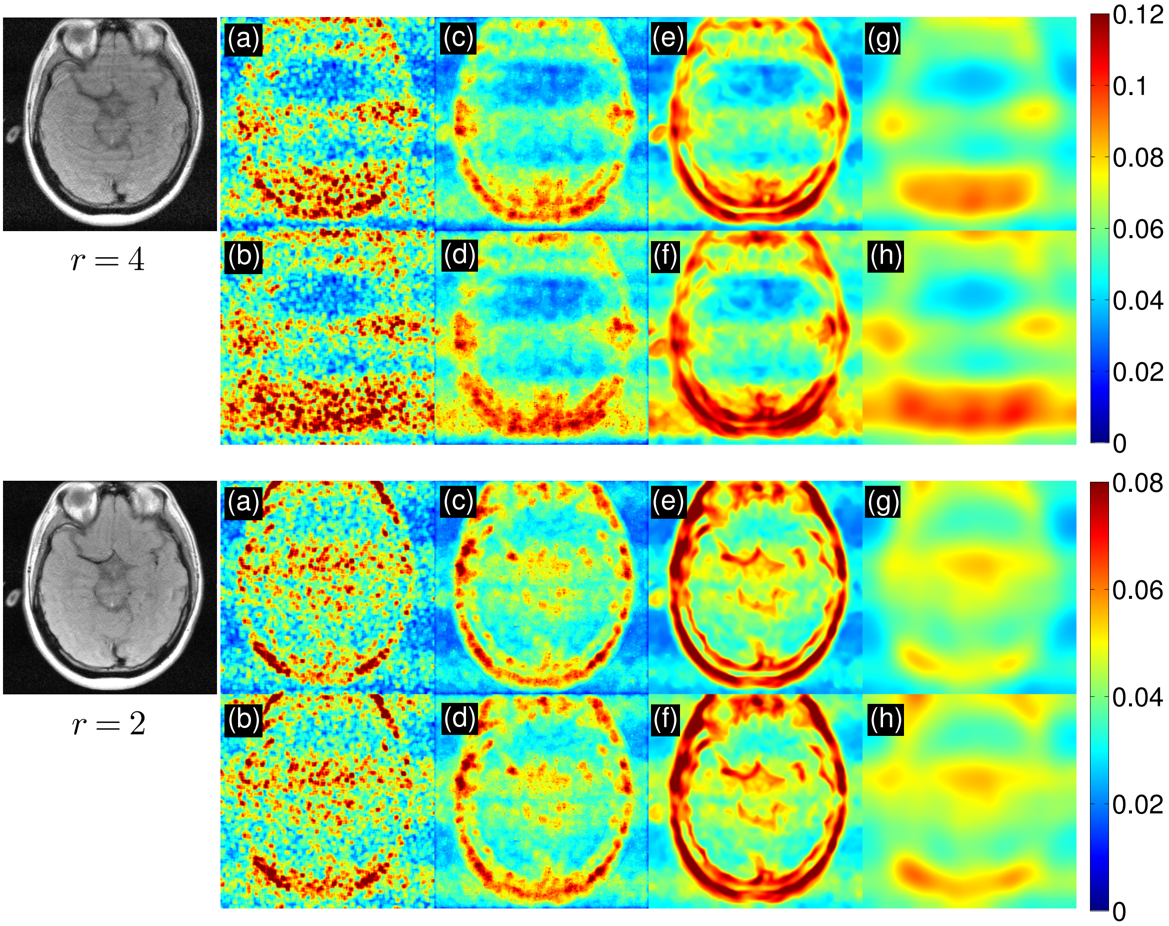

Figure 6.16: Visual inspections of the methods for *in vivo* T_1-weighted FSPGR GRAPPA MRI brain data for $r = 4$ and $r = 2$: (a) Goossens et al. 2006, (b) VST + Goossens et al. 2006, (c) Pan et al. 2012, (d) VST + Pan et al. 2012, (e) Maggioni and Foi 2012, (f) VST + Maggioni and Foi 2012, (g) Aja-Fernández and Vegas-Sánchez-Ferrero 2015 and (h) VST + Aja-Fernández and Vegas-Sánchez-Ferrero 2015 (**our proposal**).

We calculate twice this pseudo-reference map along the samples:

1. we apply the estimator (4.61) along the replicas,
2. we stabilize the data using (6.29) and then we apply the estimator (4.61) to the variance-stabilized images.

The results of the estimation process are depicted in Fig. 6.15. Generally, the behaviour of the estimators are similar to those presented for synthetic GRAPPA MRI data. In comparison with previous qualitative experiments (see Figs. 6.12–6.14), the evaluated image[6] does not consist tissues inhomogeneities inside the phantom, and therefore the estimators should not be affected by the outliers. Nevertheless, the edges of the phantom are still visible in retrieved noise patterns for some methods, e.g., Pan et al. 2012 (Fig. 6.15c, d) and Maggioni and Foi 2012 (Fig. 6.15e, f). Note also that Pan et al. 2012 and Maggioni and Foi 2012 provide highly underestimated noise patterns, when compared to *silver standard* references. Again, our proposal exhibits best performance, improving the results of the estimator presented by Aja-Fernández and Vegas-Sánchez-Ferrero 2015.

In the **second noise estimation experiment**, we compare the performance of the estimators for PULSAR *in vivo* T_1-weighted FSPGR GRAPPA MRI brain data (see section 6.5.1 for more details). In comparison to the previous experiments, neither a reference map nor a pseudo-reference map is available here. Consequently, a subjective comparison between the methods is the only the possible variant. Then, the results can be confronted to the previous evaluations, if they produce reasonable results.

The results from this experiment are shown in Fig. 6.16. The results are fully consistent with previous qualitative evaluations of the estimators, i.e., the employment of the VST procedure prior to Gaussian estimator strengthened observed noise maps, but it simultaneously intensified border effects (Fig. 6.16d, f). Regarding our proposal, it avoids granularities of the estimates as usually observed with Goossens et al. 2006 and it attenuates border effects coming from the skull areas (compare to Pan et al. 2012 and Maggioni and Foi 2012).

Finally, note although the results are compatible with previous visual evaluations, multiple acquisitions of the brain should be also considered to confirm the results from this experiment. However, due to a long scan time and the lack of patient's comfort, it might be a difficult task to acquire the data in real conditions.

6.6.4 Evaluation against the estimator along the samples

In this section, we evaluate our proposal and state-of-the art methods using a single GRAPPA MR image in relation to the estimation procedure along the replicas. Specifically, we estimate the noise pattern from a single image, and then we compare the results with the estimator (4.61) for the increasing number of repetitions (acquisitions).

In the **first experiment**, we employ simulated synthetic T_1-weighted GRAPPA MRI data with the following parameters $L = 8$, $r = 2$ and $\rho = 0.1$. The $\mathbf{k}$–space domain is uniformly sampled and 32 ACS lines are preserved. The SoS formula is used to reconstruct the magnitude data. Eighty GRAPPA MRI reconstructions ($R = 80$) with underlying noise variances $\sigma^2 = 100$ and $\sigma^2 = 400$ are considered for this experiment. The results of the evaluation process are depicted in Fig. 6.17. The horizontal (constant) lines refer to spatially averaged $\mathrm{RE}(\mathbf{x})$ (i.e., the parameter $\overline{\mathrm{RE}}$) calculated from a single noise map. Two versions of the estimator (4.61) for the increasing number of samples are considered: *without* and *with* the

---

[6] The Gaussian estimators use only a single slice, while the *silver standard* method arranges stacked images to provide a pseudo-reference map.

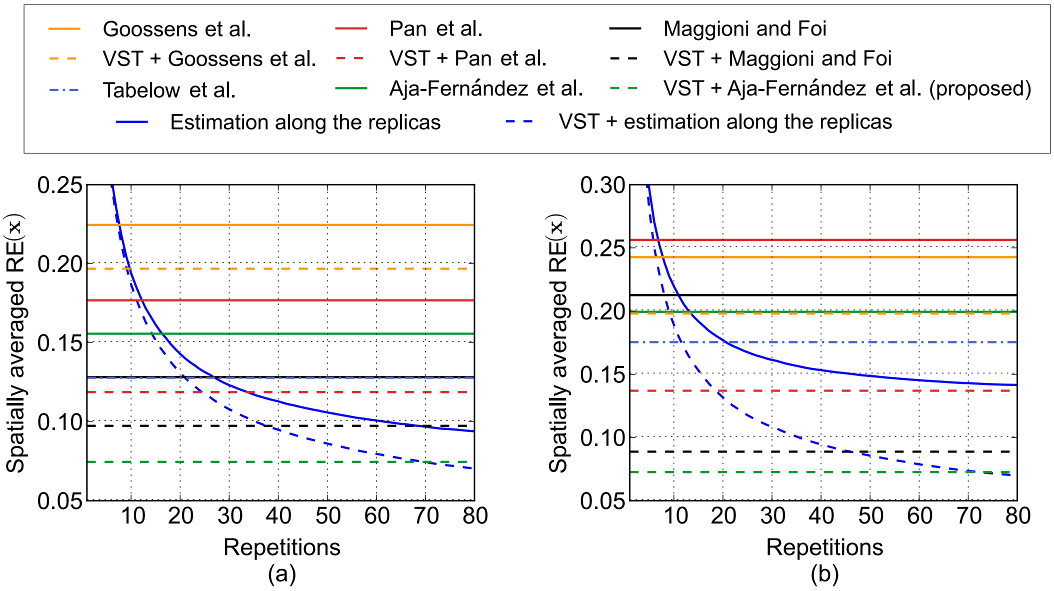

Figure 6.17: Comparison of spatially averaged relative error $\mathrm{RE}(\mathbf{x})$ between our proposal and state-of-the-art methods using a single synthetic T_1-weighted GRAPPA MRI slice (Fig. 6.5a), and the estimation along the increasing number of images (pointwise standard deviation along the replicas). The underlying noise variance levels are: (a) $\sigma^2 = 100$ and (b) $\sigma^2 = 400$. Two versions of Gaussian estimators are considered: *without* and *with* the variance-stabilizing transformation (the acronym "VST +").

VST procedure (6.29). The estimator (4.61) preceded by the VST mechanism needs at least seventy replicas of the data to provide better results than our proposal from a single slice. Note that this experiment not only shows the robustness of the proposed noise estimator, but it particularly verifies the number of replicas, which must be taken into account when providing a pseudo-reference map for real GRAPPA MRI acquisitions. Hence, the noise patterns estimated from one hundred repetitions can be assumed to be relevant pseudo-references for the first experiment presented in section 6.6.3 (see Fig. 6.15g, h).

In the **second experiment**, we calculate the ratio of pixels of real T_1-weighted FGRE GRAPPA MRI data, whose estimated variance from one single slice lays within the confidence interval (CI) for increasing number of samples R (replicas). Clearly, we apply the VST (6.29) and estimate the noise patterns using Gaussian estimators from one single image. Then, we stabilize all replicas and pointwisely fit normal distributions for increasing number of samples using ML approach[7]. If the underlying samples are i.i.d. and normally distributed (i.e., $X_i \sim \mathcal{N}(\mu, \sigma^2)$), the statistics $(R-1)s^2/\sigma^2$ follows a χ^2 distribution with $(R-1)$ degrees of freedom with s^2 being a sample variance. Assuming that $\chi^2_{R-1,\beta}$ is the β quantile of the χ^2 distribution with $(R-1)$ degrees of freedom the following formula holds:

$$P\left(\chi^2_{R-1,1-\alpha/2} \leqslant \frac{(R-1)s^2}{\sigma^2} \leqslant \chi^2_{R-1,\alpha/2}\right) = 1-\alpha, \tag{6.37}$$

where P is the probability that the RV falls within a given range.

We construct now $100(1-\alpha)\%$ CI for the variance, when the underlying data are normally distributed:

$$\frac{(R-1)\widehat{s^2_R(\mathbf{x})}}{\chi^2_{R-1,\alpha/2}} \leqslant \widehat{\sigma^2_{\text{eff}}(\mathbf{x})} \leqslant \frac{(R-1)\widehat{s^2_R(\mathbf{x})}}{\chi^2_{R-1,1-\alpha/2}}, \tag{6.38}$$

---

[7] The ML reduces to least squares estimation for Gaussian distributed data.

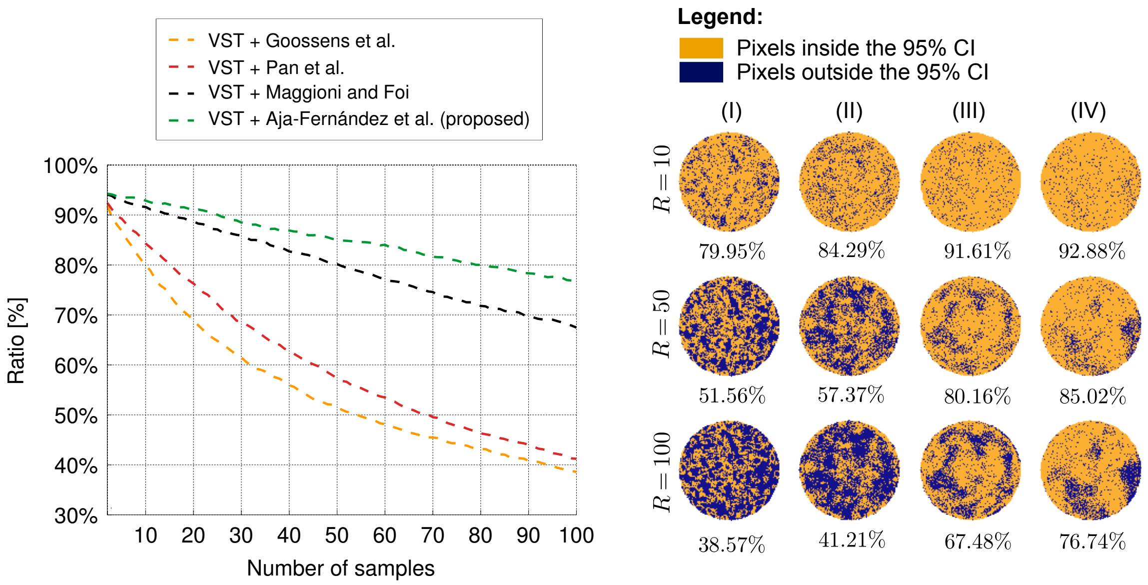

(a) (b)

Figure 6.18: (a) The ratio of pixels in the foreground area of T_1-weighted FGRE GRAPPA MRI phantom (Fig. 6.5g), whose estimated variance from one single slice lays within the 95% confidence interval (CI) for increasing number of samples R (replicas). (b) The visual representation of the quantitative experiment and the percentage ratios for $R = 10$, $R = 50$ and $R = 100$: (I) VST + Goossens et al. 2006, (II) VST + Pan et al. 2012, (III) VST + Maggioni and Foi 2012 and (IV) VST + Aja-Fernández and Vegas-Sánchez-Ferrero 2015 (**proposed**).

where $\widehat{s_R^2(\mathbf{x})}$ is the sample variance obtained with the estimator (4.61) from R replicas of the stabilized data at the location $\mathbf{x}$. Note that contrary to CI for the mean, the CI for the variance is skewed and it has the support on $[0;\ \infty)$.

The quantitative and qualitative results of the experiment for $\alpha = 0.05$ (95% CI) are shown in Fig. 6.18. Note that the ratios of the pixels laying inside the confidence inverval (6.38) concern the foreground area of the phantom only. The results show that our proposal outperforms state-of-the art methods for all number of samples R, which are taken into account by the estimator (4.61). The proposal reaches the ratios 92.88%, 85.02% and 76.74% for $R = 10$, $R = 50$ and $R = 100$, respectively. In other words, the new spatially variant noise estimation method provides the noise pattern from a single image, where $X\%$ of the estimated points from the foreground area lay inside the CIs constructed for R samples.

These two experiments evidence that the spatially variant noise patterns can be estimated from non-stationary nc-χ distributed data using only a single image. Furthermore, our proposal achieves it in best way when compared to state-of-the-art methods.

6.7 Conclusions and remarks

In this chapter, we proposed new variance-stabilizing transformations for nc-χ distributed random variable. The transformations enable to convert a nc-χ distributed random variable into another random variable, where the noise component can be assumed to be Gaussian distributed. In other words, the transformations allows removing signal-dependency of the noise, i.e., the variance-stabilized data no longer depends on the underlying amplitude signal A_T.

Two variants of the variance-stabilizing transformation were proposed:

1. the asymptotic model (6.21) inferred from the first-order Taylor expansion of the variance-stabilizing function $f_{\text{stab}}(M_L^2|\sigma, L)$,
2. the robust numerical model (6.28), which allows stabilizing the variance for the whole range of SNRs, i.e., from very low SNRs – c-χ distribution to very high SNRs – Gaussian distribution.

The variance-stabilizing transformations were verified then with the mapping technique from nc-χ to Gaussian distribution using a statistical hypothesis testing, i.e., χ^2-test and Anderson-Darling test. Statistical tests showed high acceptance ratios for the whole range of SNR of the proposed numerical VST, i.e., at least 92.70% and 98.98% acceptances for χ^2-test and Anderson-Darling test, respectively. This means that the noise component in variance-stabilized nc-χ data can be assumed to be Gaussian distributed.

Next, we presented signal-dependent non-stationary nc-χ distributed noise estimation scheme in variance-stabilizing framework. This approach allows estimating spatially variant noise component in non-stationary nc-χ distributed data like accelerated parallel GRAPPA MRI obtained with SoS reconstruction. Our proposal uses the numerical VST to stabilize the nc-χ data and Gaussian homomorphic filtering procedure to retrieve smooth and granularity-free noise patterns. The noise estimation method is validated over simulated synthetic and real accelerated parallel GRAPPA MRI examinations. **The method was compared to main state-of-the-art methods showing best performance among others for the whole range of underlying noise standard deviation σ and correlation ratio between receiver coils ρ.** The estimator was then verified using real accelerated parallel GRAPPA MRI acquisitions proving reasonable results, when contrasted to the studies on simulated synthetic data.

The proposed non-stationary nc-χ noise estimation scheme is characterized by the following advantages over state-of-the art methods:

- it does not require multiple acquisitions (like Veraart et al. 2013) or pre-scans to estimate the noise pattern; a single image is sufficient to provide a reliable noise map,
- any technical details about the acqusition procedure like reconstruction coefficients for GRAPPA MRI are not required (Aja-Fernández et al. 2014a),
- it is not affected by the granular effect (Goossens et al. 2006) or a bias coming from the transitions between the tissues (Maggioni and Foi 2012, Pan et al. 2012),
- it does not involve computationally intensive approaches like weighted maximum likelihood estimation (Tabelow et al. 2015) or non-local scheme (Maggioni and Foi 2012),
- it uses exact theoretical model rather than Gaussian approximations (Goossens et al. 2006, Maggioni and Foi 2012, Pan et al. 2012) and consequently the noise estimation algorithm is robust for the whole range of SNRs (from very low SNRs – non-stationary c-χ distribution to very high SNRs – non-stationary Gaussian distribution).

Finally, it is worth mentioning that any Gaussian-compliant noise estimation method presented in Chapter 4 can be arranged to retrieve spatially variant noise patterns in the proposed variance-stabilizing framework. Furthermore, although the asymptotic model is biased for low SNRs, it can be used in denoising procedures of nc-χ distributed data using Gaussian filters.

Chapter 7

Final conclusions and remarks

The main assumption behind this PhD thesis was to estimate a spatially variant noise map from a single MR image only without repeated scans or extra information needed about the acquisition process. In this work, we particularly focused on non-stationary Rician and non-stationary nc-χ distributed signals since we can find them in accelerated parallel MRI acquisitions. As an application and proof of concept, we used SENSE MRI and GRAPPA MRI with SoS reconstruction. These modalities allow obtaining the final MR image from subsampled **k**–space raw MRI data if the redundant data from many receiver coils are available. Consequently, the scan time is significantly reduced when compared to single-coil acquisition. The SENSE and GRAPPA reconstructions, however, lead to non-stationarity of the noise in the final magnitude data. In this thesis, we were interested in estimating the noise patterns from a one single magnitude MR image.

Potential applications of the estimated noise patterns can be found at different stages of MRI data processing pipeline including:

- adaptive noise-driven noise removal procedures (e.g., LMMSE estimator),
- parameters estimation in DTI/DKI (e.g., LMMSE and ML estimator),
- image segmentation using statistical models (e.g., mixture models),
- estimation of diffusion profiles from HARDI data,
- quality evaluation of the MRI data using SNR/CNR parameter.

The presented PhD thesis was divided into two parts: the **background** and the **contributions**. In the **background** part of the thesis, we presented basic information about nuclear magnetic resonance phenomena, image formation processes and statistical distributions employed to model the MR signal. Then, we carried out an extensive review of state-of-the-art methods in non-stationary Gaussian, Rician and nc-χ noise estimation schemes intended for MRI, especially focusing on accelerated parallel MRI acqusitions. The author identified main drawbacks of reviewed noise estimation methods particularly considering the methods estimating the noise pattern from a single image. The state-of-the-art chapter indicates also the underlying criteria that should be met when proposing a new or extending current noise estimation schemes to deal with non-stationarity of the noise in Rician and nc-χ distributed signals. Furthermore, a comprehensive comparison of the state-of-the-art included in Table 4.1 is intended to serve as a starting point for further research in noise modelling in accelerated parallel MRI. We believe it allows selecting the most relevant noise estimation solution for a particular research or clinical application.

We pay attention that our proposals are not strictly limited to MRI and they can be applied to other imaging techniques like synthetic aperture radar imaging, modelling the intensity in speckle pattern phenomenon or modelling the fading channels in wireless communication.

The second part of the PhD thesis is devoted to **our contributions** of which the most important are:

1. **Improved variance-stabilizing transformation for Rician distributed signal.**
   The proposed numerical optimized transformation changes Rician distributed random variable to another random variable with a constant variate. This means that the variance-stabilized Rician noise is no longer signal-dependent and it can be assumed to be Gaussian distributed. Our proposal is robust for the whole range of SNRs, i.e., from very low SNRs – Rayleigh distribution to very high SNRs – Gaussian distribution.

   Our proposal was shown to outperform the state-of-the-art Foi's numerical models for Rician distributed data.

2. **Asymptotic variance-stabilizing transformation for nc-χ distributed signal.**
   The analytically derived transformation changes squared nc-χ distributed random variable to another random variable with a constant variate. Again, the variance-stabilized nc-χ distributed noise is no longer signal-dependent and it can be treated as Gaussian distributed. Contrary to Rician case, this transformation is reversible and it can be implemented as a pointwise operator with the computational complexity of the order of $\mathcal{O}(1)$ given the estimated effective parameters.

3. **Robust numerical variance-stabilizing transformation for nc-χ distributed signal.**
   The proposed numerical variance-stabilizing transformation improves the performance of analytically derived asymptotic model for low SNRs. The numerical scheme allows robustly stabilizing the nc-χ distributed signal for the whole range of SNRs, i.e., from very low SNRs – c-χ distribution to very high SNRs – Gaussian distribution. In comparison to the asymptotic model, this transformation is no longer reversible.

   Our proposal was shown to outperform the state-of-the-art Koay's mapping technique for nc-χ distributed data.

4. **Spatially variant noise estimation scheme for Rician distributed data**.
   The proposed noise estimation scheme allows estimating spatially variant noise patterns from non-stationary Rician distributed data. The noise estimation scheme employs the proposed variance-stabilizing transformation for Rician distributed data to remove the signal-dependency of the noise. Then, the Gaussian homomorphic filter retrieves smooth and granularity-free noise pattern. This noise estimation method was used then to obtain the noise patterns from accelerated parallel SENSE MRI acquisitions.

   The proposed noise estimation approach was shown to outperform fourteen state-of-the-art methods for the whole range od SNRs.

5. **Spatially variant noise estimation scheme for nc-χ distributed data**.
   The proposed noise estimation scheme provides accurate estimation of noise patterns from non-stationary nc-χ distributed data. Again, the scheme uses the variance-stabilizing transformation (i.e., the robust numerical model for nc-χ distributed data) and Gaussian homomorphic filter. The framework was used then to retrieve spatially variant noise patterns from accelerated parallel GRAPPA MRI with SoS reconstruction.

The proposed method was shown to outperform state-of-the-art methods for the whole range od SNRs.

Moreover, we shown that **Gaussian-compliant methods preceeded by the variance-stabilizing transformation can be arranged to estimate spatially variant noise patterns from non-stationary nc-χ distributed data**. Note also that each Gaussian noise estimation method, which is preceeded by the variance-stabilizing transformation, provides the results not worse than those without the stabilization step.

In this work, the following thesis was defined: "*Maps of non-stationary noise generated by parallel MRI reconstruction can be accurately estimated from a single acquisition without any additional information needed*".

To prove this thesis, the author showed that the estimation of spatially variant noise pattern from a one single image is possible. It was verified for non-stationary Rician and non-stationary nc-χ distributed data with a particular application in SENSE MRI and GRAPPA MRI with SoS reconstruction, respectively. The estimation can be done better than the state-of-the-art methods for the whole range of SNRs. This was confirmed using quantitative and qualitative experiments. Furthermore, the robustness of the proposals was verified in comparison with *silver standard* methods, i.e., the results were confronted with the methods estimating the noise patterns along multiple scans.

To sum up, the most important advantages of proposed spatially variant noise estimation schemes over the state-of-the-art are:

1. the methods take signal-dependency of the noise into account rather than correction factors or rough assumptions of Gaussianity,
2. the noise estimates are not affected by granular effects or a significant bias,
3. the estimators are robust for the whole range of SNRs,
4. the methods do not require repeated acquisitions, pre-scans, or a physical model of the MRI data,
5. any additional information from the reconstruction process of the MRI data like sensitivity profiles of the receiver coils (SENSE) or reconstruction coefficients (GRAPPA) is no longer needed,
6. post-correction factors (Koay and Basser 2006, Manjón et al. 2015 or Aja-Fernández et al. 2015b) are no longer required for Rician/nc-χ distributed data,
7. any Gaussian noise estimation method can be employed now in the VST framework for spatially variant noise estimation in non-stationary nc-χ distributed data,
8. software implementations are straightforward since they are based on discrete convolutions and pointwise operations,
9. finally, note that the variance-stabilizing frameworks open a new way of thinking in MRI, where various data processing algorithms (e.g., image segmentation using mixture models) can be performed in variance-stabilized domain of the MR image rather than in the image domain using computationally intensive Rician/nc-χ schemes or Gaussian approximations.

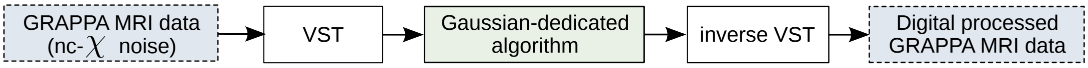

Figure 7.1: The data processing in a reversible variance-stabilization framework.

The future research directions in spatially variant noise estimation in MRI should primarily focus on blind estimation procedures (estimation without any assumptions about the noise distribution) or making use of the redundant information from the acquisition process, e.g., diffusion data or successive dynamic image series.

Below, we characterize selected problems in statistical models of the noise in MRI and noise estimation in non-stationary Rician and nc-χ distributed data which **are still open**:

1. **A reversible VST for nc-χ distribution.**
   In (section 6), we derived the reversible asymptotic VST for nc-χ distribution using squared random variable M_L^2. Although the asymptotic methodology uses a closed-form formula for the expectation operator and the variance of nc-χ^2 distributed random variable, it is biased for low SNRs.

   In the future research, the unbiased reversible VST for nc-χ distribution should be analytically derived. The asymptotic approximations of the expectation operator $\mathbb{E}\{M_L\}$ and the variance $\mathrm{Var}\{M_L\}$ of nc-χ distributed random variable should be used in the derivation procedure. Moreover, one might consider higher-order Taylor expansions of the VST definition instead of the first order approximation. This will avoid a systematic bias of the stabilizer for low SNRs as previously observed for non-optimized variant of the VST. In comparison with our numerical VST, this transformation will not depend on any optimization procedure or local SNR estimation. Clearly, while the VST for nc-χ distribution allows transforming the noise from nc-χ to Gaussian distribution, the inverse VST should enable to transform the noise from Gaussian to nc-χ distribution.

   A wide range of potential applications of unbiased reversible VST for nc-χ distribution can be found in data processing from accelerated parallel MRI acquisitions, not only in case of non-stationary nc-χ noise estimation. Specifically, one can adapt Gaussian-dedicated noise removal or image resampling (upsampling) algorithms for GRAPPA MRI data (obtained with SoS) in the pipeline as shown in Fig. 7.1. Such noise removal procedures employing Rician VST framework have been proposed recently (see Maggioni et al. 2013, Yang et al. 2015 and Zhang et al. 2015b).

2. **Statistical modelling of non-Cartesian sampled accelerated parallel MRI data.**
   All scientific reports considering both stationary and non-stationary noise estimation in MRI assume Cartesian sampling of $\mathbf{k}-$space domain. This enable to define exact statistical model of the final magnitude data coming from single-coil (Gudbjartsson and Patz 1995), multiple-coil (Constantinides et al. 1997, Aja-Fernández and Tristán-Vega 2012 and Aja-Fernández et al. 2013), and accelerated parallel SENSE MRI and GRAPPA MRI (Aja-Fernández et al. 2011, Aja-Fernández et al. 2014b and Aja-Fernández et al. 2014a). Even the image is reconstructed by a non-linear POCS algorithm (Sabati et al. 2013), the Cartesian sampling of the raw MR signal is still assumed.

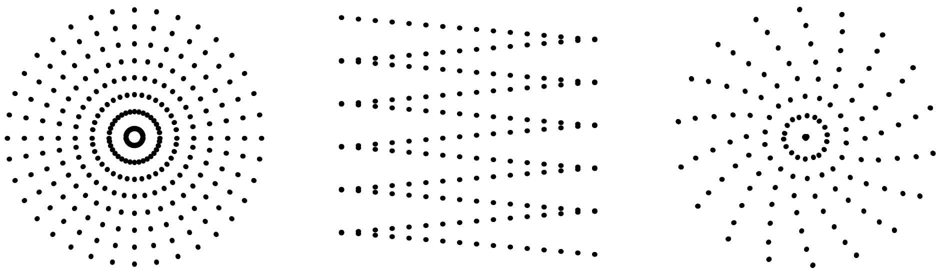

(a) (b) (c)

Figure 7.2: Non-Cartesian sampling trajectories of MR signal in **k**–space domain: (a) polar, (b) zig-zag, and (c) spiral.

As other than Cartesian sampling trajectories of **k**–space domain get more attention in clinical and research accelerated parallel MRI examinations (Lustig and Pauly 2010, Weller et al. 2014, Wright et al. 2014), the future research should focus on analysis of statistical models, which potentially can be employed to approximate noisy magnitude MR signal obtained from accelerated parallel MRI reconstructions with non-Cartesian sampling of **k**–space domain (see Fig. 7.2).

Note that the results coming from this research may be the following:

- The Rician and nc-χ distributions are roughly correct for the representation of magnitude non-Cartesian accelerated parallel MRI data.
- The Rician and nc-χ models need a correction factor, e.g., a similar one as proposed by Aja-Fernández et al. 2011 to adapt nc-χ model in context of GRAPPA MRI with SoS reconstruction.
- Other statistical models fit the data better than Rician and nc-χ models.

3. **The analysis of intensity non-uniformity on statistical properties of the noise.**
   In this thesis we employed synthetic T_1-, T_2- and PD-weighted MRI data with INU=0% to quantitatively evaluate the estimators. Since the non-uniformity of intensity of the magnitude MR signal can be observed in real acquisitions (see Fig. 5.7g), it might be interesting to examine this effect on statistical properties of the signal. Recently, similar analyses were performed in context of modelling the statistical texture properties in magnitude MRI data (see Materka and Strzelecki 2015). Another interesting problem might be the evaluation of popular intensity non-uniformity correction techniques on statistical properties of the noise in magnitude MRI data (e.g., Vovk et al. 2007).

4. **The non-stationary signal-dependent Rician/nc-χ noise estimation for DTI**.
   The diffusion-weighted accelerated parallel MRI examinations are particularly prone to noise due to involuntary motions of human body (Anderson 2001, Tristán-Vega et al. 2012a). Consequently, the noise affects also the underlying fibre structure derived from diffusion tensor tractography algorithms. The future research should focus on non-stationary Rician/nc-χ noise estimation from redundant diffusion accelerated parallel MRI data. Since the spatially variant noise pattern is retrieved, it can be used for noise-driven diffusion tensor estimation.

5. **A fast implementation of the noise estimation procedure.**
   In this thesis we were considering single slices of MRI data. Since clinical applications usually arrange a whole stacked dataset (e.g., diffusion images to reconstruct the fiber structure of the brain/spine), the noise estimation method should provide the results for each slice individually. Consequently, software implementations of some noise estimation methods might no longer be applicable for real-time imaging. To speed-up the computations a GPU with OpenCL/CUDA can be employed as the implementation platform of noise estimation algorithms. Finally, note that recent advances in cross platform acceleration of computer vision algorithms like OpenVX standard from Khronos Group[1] allows preparing a platform-independent source code.

6. **A blind noise estimation procedure.**
   The main assumption behind all noise estimation algorithms in MRI is that the statistical model of the noise is known in advance or assumed to be Gaussian (see Table 4.1 in section 4). The future research should involve a *blind noise estimation* procedure, i.e., the estimation without any *a priori* assumptions about the acquisition details or distributional properties of the noise.

   Two problems must be addressed here:

   - the detection of stationarity/non-stationarity of the noise,
   - the identification of statistical distribution of the underlying noise.

   Note that two works on blind noise estimation were already proposed – Pan et al. 2012 and Aja-Fernández and Vegas-Sánchez-Ferrero 2015. Nevertheless, both methods assume that MR signal can be approximated by Gaussian distribution. This assumption leads to highly biased noise map estimates for low SNRs as shown in Chapter 6.

---

[1] `https://www.khronos.org/`

Appendix A

Appendix

A.1 The Marcum Q-function definition for nc-χ distribution

In this appendix, we show a representation of a Marcum Q-function for nc-χ distribution. Let us recall the PDF of a real-valued nc-χ distributed random variable M_L (3.25):

$$p(M_L|A_T,\sigma,L) = \frac{A_T^{1-L}}{\sigma^2} M_L^L \exp\left(-\frac{M_L^2+A_T^2}{2\sigma^2}\right) I_{L-1}\left(\frac{A_T M_L}{\sigma^2}\right), M_L \geqslant 0, \tag{A.1}$$

where M_L is the CMS (2.15), σ^2 is the underlying noise variance, L is the number of receiver coils, A_T is the noise-free signal and $I_k(\cdot)$ is the modified Bessel function of the first kind and k–th order. The CDF of nc-χ distributed random variable M_L is given then as follows:

$$\begin{aligned} F_{M_L}\left(m|A_T,\sigma,L\right) &= \int_0^m p(\widetilde{M_L}|A_T,\sigma,L)\, d\widetilde{M_L} \\ &= \int_0^m \frac{A_T^{1-L}}{\sigma^2}\widetilde{M_L^L} \exp\left(-\frac{\widetilde{M_L^2}+A_T^2}{2\sigma^2}\right) I_{L-1}\left(\frac{A_T\widetilde{M_L}}{\sigma^2}\right) d\widetilde{M_L} \\ &= 1-\int_m^\infty \frac{A_T^{1-L}}{\sigma^2}\widetilde{M_L^L} \exp\left(-\frac{\widetilde{M_L^2}+A_T^2}{2\sigma^2}\right) I_{L-1}\left(\frac{A_T\widetilde{M_L}}{\sigma^2}\right) d\widetilde{M_L}. \end{aligned} \tag{A.2}$$

Using a substitution $t=\frac{\widetilde{M_L}}{\sigma}$ and basic integral properties, we express eq. (A.2) as follows:

$$\begin{aligned} F_{M_L}\left(m|A_T,\sigma,L\right) &= 1-\left(\frac{\sigma}{A_T}\right)^{L-1}\int_{\frac{m}{\sigma}}^\infty t^L \exp\left(-\frac{\sigma^2t^2+A_T^2}{2\sigma^2}\right) I_{L-1}\left(\frac{A_T t}{\sigma}\right) dt \\ &= 1-Q_L\left(\frac{A_T}{\sigma},\frac{m}{\sigma}\right) \end{aligned} \tag{A.3}$$

where $Q_L(\cdot,\cdot)$ is called the generalized Marcum Q-function of L–th order. □

References

Aja-Fernández, S., Alberola-López, C., and Westin, C. (2008). Noise and signal estimation in magnitude MRI and Rician distributed images: A LMMSE approach. *IEEE Trans. Image Process.*, 17(8):1383–1398. (cited at pages 11, 12 and 37)

Aja-Fernández, S., Brion, V., and Tristán-Vega, A. (2013). Effective noise estimation and filtering from correlated multiple-coil MR data. *Magn. Reson. Imaging*, 31(2):272–285. (cited at pages 40, 46, 48, 56, 111 and 133)

Aja-Fernández, S., Martín, D. G., Tristán-Vega, A., and Vegas-Sánchez-Ferrero, G. (2015a). Improving GRAPPA reconstruction by frequency discrimination in the ACS lines. *Int. J. Comput. Assist. Radiol. Surg.*, 10(10):1–12. (cited at pages 25, 29 and 30)

Aja-Fernández, S., Pieciak, T., and Vegas-Sánchez-Ferrero, G. (2015b). Spatially variant noise estimation in MRI: A homomorphic approach. *Med. Imag. Anal.*, 20(1):184–197. (cited at pages 13, 47, 48, 50, 58, 60, 63, 73, 74, 75, 81, 84, 85, 86, 87, 89, 90, 91, 92, 93, 94, 95, 96, 97, 98, 109, 132, 153, 154 and 155)

Aja-Fernández, S. and Tristán-Vega, A. (2012). Influence of noise correlation in multiple-coil statistical models with sum of squares reconstruction. *Magn. Reson. Med.*, 67(2):580–585. (cited at pages 23, 25, 34, 38, 39, 43, 106, 109 and 133)

Aja-Fernández, S. and Tristán-Vega, A. (2013). A review on statistical noise models for magnetic resonance imaging. *LPI, ETSI Telecomunicacion, Universidad de Valladolid, Spain, Tech. Rep*, pages 1–27. (cited at pages 10 and 34)

Aja-Fernández, S., Tristán-Vega, A., and Alberola-López, C. (2009). Noise estimation in single- and multiple-coil magnetic resonance data based on statistical models. *Magn. Reson. Imaging*, 27(10):1397–1409. (cited at pages 11, 12, 34, 35 and 38)

Aja-Fernández, S., Tristán-Vega, A., and Hoge, W. (2011). Statistical noise analysis in GRAPPA using a parametrized noncentral Chi approximation model. *Magn. Reson. Med.*, 65(4):1195–1206. (cited at pages 11, 34, 35, 42, 43, 56, 105, 109, 118, 121, 122, 123, 124, 133, 134 and 157)

Aja-Fernández, S. and Vegas-Sánchez-Ferrero, G. (2015). Blind estimation of spatially variant noise in GRAPPA MRI. In *IEEE International Symposium on Biomedical Imaging (ISBI)*, pages 1478–1481. (cited at pages 47, 48, 58, 84, 109, 111, 112, 114, 122, 123, 124, 125, 126, 128, 135, 153, 157 and 158)

Aja-Fernández, S., Vegas-Sánchez-Ferrero, G., and Tristán-Vega, A. (2010). About the background distribution in MR data: A local variance study. *Magn. Reson. Imaging*, 28(5):739–752. (cited at pages 34 and 37)

Aja-Fernández, S., Vegas-Sánchez-Ferrero, G., and Tristán-Vega, A. (2014a). Noise estimation in parallel MRI: GRAPPA and SENSE. *Magn. Reson. Imaging*, 32(3):281–290. (cited at pages 11, 26, 27, 34, 35, 40, 41, 43, 47, 48, 79, 94, 110, 129 and 133)

Aja-Fernández, S., Vegas-Sánchez-Ferrero, G., and Trsitan-Vega, A. (2014b). Statistical noise analysis in SENSE parallel MRI. *arXiv preprint arXiv:1402.4067*. (cited at pages 11, 34, 40, 41, 43 and 133)

Algarin, J., Breuer, F., Behr, V., and Freire, M. (2015). Analysis of the noise correlation in MRI coil arrays loaded with metamaterial magnetoinductive lenses. *IEEE Trans. Med. Imag.*, 34(5):1148–1154. (cited at page 109)

Anderson, A. W. (2001). Theoretical analysis of the effects of noise on diffusion tensor imaging. *Magn. Reson. Med.*, 46(6):1174–1188. (cited at pages 10 and 134)

Bajic, B., Lindblad, J., and Sladoje, N. (2016). Blind restoration of images degraded with mixed Poisson-Gaussian noise with application in transmission electron microscopy. In *IEEE International Symposium on Biomedical Imaging (ISBI)*, pages 123–127. (cited at page 67)

Bartlett, M. S. (1947). The use of transformations. *Biometrics*, 3(1):39–52. (cited at page 67)

Berger, A. (2002). How does it work?: Magnetic resonance imaging. *BMJ*, 324(7328):35. (cited at page 17)

Bhujle, H. and Chaudhuri, S. (2014). Novel speed-up strategies for non-local means denoising with patch and edge patch based dictionaries. *IEEE Trans. Image Process.*, 23(1):356–365. (cited at page 98)

Blaimer, M., Breuer, F., Mueller, M., Heidemann, R. M., Griswold, M. A., and Jakob, P. M. (2004). SMASH, SENSE, PILS, GRAPPA: How to choose the optimal method. *Top. Magn. Reson. Imag.*, 15(4):223–236. (cited at pages 26 and 30)

Blaimer, M., Breuer, F. A., Mueller, M., Seiberlich, N., Ebel, D., Heidemann, R. M., Griswold, M. A., and Jakob, P. M. (2006). 2D-GRAPPA-operator for faster 3D parallel MRI. *Magn. Reson. Med.*, 56(6):1359–1364. (cited at page 30)

Bloch, F. (1946). Nuclear induction. *Phys. Rev.*, 70(7-8):460–474. (cited at page 17)

Borrelli, P., Palma, G., Comerci, M., and Alfano, B. (2014). Unbiased noise estimation and denoising in parallel magnetic resonance imaging. In *IEEE International Conference on Acoustics, Speech and Signal Processing (ICASSP)*, pages 1230–1234. (cited at pages 46, 47, 48, 55, 60, 63, 85, 86, 89, 90, 91, 92, 93, 94, 95, 97, 98, 154 and 155)

Boulanger, J., Kervrann, C., Bouthemy, P., Elbau, P., Sibarita, J.-B., and Salamero, J. (2010). Patch-based nonlocal functional for denoising fluorescence microscopy image sequences. *IEEE Trans. Med. Imag.*, 29(2):442–454. (cited at page 67)

Brau, A. (2007). New parallel imaging method enhances imaging speed and accuracy. *GE Signa Pulse*, pages 36–38. (cited at page 25)

Breuer, F. A., Kannengiesser, S. A., Blaimer, M., Seiberlich, N., Jakob, P. M., and Griswold, M. A. (2009). General formulation for quantitative G-factor calculation in GRAPPA reconstructions. *Magn. Reson. Med.*, 62(3):739–746. (cited at page 29)

Brion, V., Poupon, C., Riff, O., Aja-Fernández, S., Tristán-Vega, A., Mangin, J.-F., Le Bihan, D., and Poupon, F. (2011). Parallel MRI noise correction: An extension of the LMMSE to non central χ distributions. In *Medical Image Computing and Computer-Assisted Intervention (MICCAI)*, pages 226–233. Springer. (cited at pages 105 and 111)

Brown, R. W., Cheng, Y.-C. N., Haacke, E. M., Thompson, M. R., and Venkatesan, R. (2014). *Magnetic resonance imaging: Physical principles and sequence design.* John Wiley & Sons. (cited at page 34)

Buades, A., Coll, B., and Morel, J.-M. (2005). A non-local algorithm for image denoising. In *IEEE Computer Society Conference on Computer Vision and Pattern Recognition (CVPR)*, volume 2, pages 60–65. (cited at pages 52, 53, 56, 76 and 100)

Casaseca-de-la Higuera, P., Tristán-Vega, A., Aja-Fernández, S., Alberola-López, C., Westin, C.-F., and Estépar, R. S. J. (2012). Optimal real-time estimation in diffusion tensor imaging. *Magn. Reson. Imaging*, 30(4):506–517. (cited at page 12)

Chaâri, L., Pesquet, J.-C., Benazza-Benyahia, A., and Ciuciu, P. (2011). A wavelet-based regularized reconstruction algorithm for SENSE parallel MRI with applications to neuroimaging. *Med. Imag. Anal.*, 15(2):185–201. (cited at pages 27, 32 and 38)

Chan, S. H., Zickler, T., and Lu, Y. M. (2013). Fast non-local filtering by random sampling: It works, especially for large images. In *IEEE International Conference on Acoustics, Speech and Signal Processing (ICASSP)*, pages 1603–1607. (cited at page 98)

Chang, Y., Liang, D., and Ying, L. (2012). Nonlinear GRAPPA: A kernel approach to parallel MRI reconstruction. *Magn. Reson. Med.*, 68(3):730–740. (cited at pages 30 and 43)

Collins, D., Zijdenbos, A., Kollokian, V., Sled, J., Kabani, N., Holmes, C., and Evans, A. (1998). Design and construction of a realistic digital brain phantom. *IEEE Trans. on Med. Imag.*, 17(3):463–468. (cited at pages 78 and 111)

Constantinides, C., Atalar, E., and McVeigh, E. (1997). Signal-to-noise measurements in magnitude images from NMR phased arrays. *Magn. Reson. Med.*, 38(5):852–857. (cited at pages 11, 23, 34, 43 and 133)

Constantinides, C. D., Westgate, C. R., O'Dell, W. G., Zerhouni, E. A., and McVeigh, E. R. (1995). A phased array coil for human cardiac imaging. *Magn. Reson. Med.*, 34(1):92–98. (cited at page 11)

Coupé, P., Manjón, J. V., Gedamu, E., Arnold, D., Robles, M., and Collins, D. L. (2010). Robust Rician noise estimation for MR images. *Med. Imag. Anal.*, 14(4):483–493. (cited at pages 47 and 55)

Czajkowska, J. and Pietka, E. (2014). A new parametric model-based technique in bone tumour analysis. *Comput. Med. Imaging Graph.*, 38(5):315–325. (cited at page 12)

Dabov, K., Foi, A., Katkovnik, V., and Egiazarian, K. (2007). Image denoising by sparse 3-D transform-domain collaborative filtering. *IEEE Trans. Image Process.*, 16(8):2080–2095. (cited at page 54)

Davids, M., Zöllner, F. G., Ruttorf, M., Nees, F., Flor, H., Schumann, G., and Schad, L. R. (2014). Fully-automated quality assurance in multi-center studies using MRI phantom measurements. *Magn. Reson. Imaging*, 32(6):771–780. (cited at page 12)

Delakis, I., Hammad, O., and Kitney, R. I. (2007). Wavelet-based de-noising algorithm for images acquired with parallel magnetic resonance imaging (MRI). *Phys. Med. Biol.*, 52(13):3741. (cited at pages 45, 48, 51, 60, 63, 85, 86, 89, 90, 91, 92, 93, 94, 95, 96, 97, 98, 154 and 155)

den Dekker, A. and Sijbers, J. (2014). Data distributions in magnetic resonance images: A review. *Phys. Medica*, 30(7):725–741. (cited at pages 34, 35 and 37)

DeVore, M. D., Lanterman, A. D., and O'Sullivan, J. A. (2000). ATR performance of a Rician model for SAR images. In *AeroSense 2000*, pages 34–45. International Society for Optics and Photonics. (cited at pages 45, 48, 50, 59, 60, 63, 75, 85, 86, 89, 90, 91, 92, 93, 94, 95, 96, 97, 98, 100, 153, 154 and 155)

Dietrich, O., Raya, J. G., Reeder, S. B., Ingrisch, M., Reiser, M. F., and Schoenberg, S. O. (2008). Influence of multichannel combination, parallel imaging and other reconstruction techniques on MRI noise characteristics. *Magn. Reson. Imaging*, 26(6):754–762. (cited at page 34)

Dikaios, N., Punwani, S., Hamy, V., Purpura, P., Rice, S., Forster, M., Mendes, R., Taylor, S., and Atkinson, D. (2014). Noise estimation from averaged diffusion weighted images: Can unbiased quantitative decay parameters assist cancer evaluation? *Magn. Reson. Med.*, 71(6):2105–2117. (cited at pages 10, 47 and 48)

Ding, Y., Chung, Y.-C., and Simonetti, O. P. (2010). A method to assess spatially variant noise in dynamic MR image series. *Magn. Reson. Med.*, 63(3):782–789. (cited at pages 46 and 48)

Feng, L., Srichai, M. B., Lim, R. P., Harrison, A., King, W., Adluru, G., Dibella, E. V., Sodickson, D. K., Otazo, R., and Kim, D. (2013). Highly accelerated real-time cardiac cine MRI using k–t SPARSE-SENSE. *Magn. Reson. Med.*, 70(1):64–74. (cited at pages 25 and 28)

Fessler, J. A. and Sutton, B. P. (2003). Nonuniform fast Fourier transforms using min-max interpolation. *IEEE Trans. Med. Imag.*, 51(2):560–574. (cited at page 21)

Foi, A. (2009a). Clipped noisy images: Heteroskedastic modeling and practical denoising. *Signal Process.*, 89(12):2609–2629. (cited at page 67)

Foi, A. (2009b). Optimization of variance-stabilizing transformations. *Preprint, 2009b*, 94:1–20. (cited at page 69)

Foi, A. (2011). Noise estimation and removal in MR imaging: the variance-stabilization approach. In *IEEE International Symposium on Biomedical Imaging (ISBI)*, pages 1809–1814. (cited at pages 66, 67, 68, 71 and 159)

Fratini, M., Moraschi, M., Maraviglia, B., and Giove, F. (2014). On the impact of physiological noise in spinal cord functional MRI. *J. Magn. Reson. Imaging*, 40(4):770–777. (cited at page 10)

Gahm, J. K., Kindlmann, G., and Ennis, D. B. (2014). The effects of noise over the complete space of diffusion tensor shape. *Med. Imag. Anal.*, 18(1):197–210. (cited at page 10)

Glenn, G. R., Tabesh, A., and Jensen, J. H. (2015). A simple noise correction scheme for diffusional kurtosis imaging. *Magn. Reson. Imaging*, 33(1):124–133. (cited at pages 46, 47, 48, 60, 63, 93, 94, 95 and 155)

Gonzalez, R. C. and Woods, R. E. (2008). *Digital image processing.* Pearson Education India. (cited at page 63)

Goodman, J. W. (1975). Statistical properties of laser speckle patterns. In *Laser speckle and related phenomena*, pages 9–75. Springer. (cited at page 100)

Goossens, B., Pizurica, A., and Philips, W. (2006). Wavelet domain image denoising for non-stationary noise and signal-dependent noise. In *IEEE International Conference on Image Processing (ICIP)*, pages 1425–1428. (cited at pages 46, 48, 51, 60, 63, 85, 86, 89, 90, 91, 92, 93, 94, 95, 96, 97, 98, 112, 121, 122, 123, 124, 125, 126, 128, 129, 154, 155, 157 and 158)

Greenspan, H., Ruf, A., and Goldberger, J. (2006). Constrained gaussian mixture model framework for automatic segmentation of MR brain images. *IEEE Trans. Med. Imag.*, 25(9):1233–1245. (cited at page 12)

Griswold, M. A., Jakob, P. M., Heidemann, R. M., Nittka, M., Jellus, V., Wang, J., Kiefer, B., and Haase, A. (2002). Generalized autocalibrating partially parallel acquisitions (GRAPPA). *Magn. Reson. Med.*, 47(6):1202–1210. (cited at pages 11 and 29)

Griswold, M. A., Jakob, P. M., Nittka, M., Goldfarb, J. W., and Haase, A. (2000). Partially parallel imaging with localized sensitivities (PILS). *Magn. Reson. Med.*, 44(4):602–609. (cited at page 30)

Gudbjartsson, H. and Patz, S. (1995). The Rician distribution of noisy MRI data. *Magn. Reson. Med.*, 34(6):910–914. (cited at pages 34, 36, 37, 43 and 133)

Guo, W. and Huang, F. (2009). Adaptive total variation based filtering for MRI images with spatially inhomogeneous noise and artifacts. In *IEEE International Symposium on Biomedical Imaging (ISBI)*, pages 101–104. (cited at pages 46 and 48)

Hampel, F. R. (1974). The influence curve and its role in robust estimation. *J. Amer. Statist. Assoc.*, 69(346):383–393. (cited at pages 46 and 55)

Hansen, M. S., Inati, S. J., and Kellman, P. (2015). Noise propagation in region of interest measurements. *Magn. Reson. Med.*, 73(3):1300–13008. (cited at pages 47 and 48)

Hashemi, R. H., Bradley, W. G., and Lisanti, C. J. (2012). *MRI: The basics.* Lippincott Williams & Wilkins. (cited at page 18)

He, K., Sun, J., and Tang, X. (2013). Guided image filtering. *IEEE Trans. Pattern Anal. Mach. Intell.*, 35(6):1397–1409. (cited at pages 76 and 100)

He, L. and Greenshields, I. (2009). A nonlocal maximum likelihood estimation method for Rician noise reduction in MR images. *IEEE Trans. Med. Imag.*, 28(2):165–172. (cited at page 12)

Heidemann, R. M., Anwander, A., Feiweier, T., Knösche, T. R., and Turner, R. (2012). k-space and q-space: combining ultra-high spatial and angular resolution in diffusion imaging using ZOOPPA at 7T. *NeuroImage*, 60(2):967–978. (cited at page 25)

Henkelman, M. (1985). Measurement of signal intensities in the presence of noise in MR images. *Med. Phys.*, 12:232–233. (cited at pages 10, 20 and 34)

Hoge, W. S. and Brooks, D. H. (2006). On the complimentarity of SENSE and GRAPPA in parallel MR imaging. In *IEEE Engineering in Medicine and Biology Society (EMBS)*, pages 755–758. (cited at page 25)

Hoge, W. S., Brooks, D. H., Madore, B., and Kyriakos, W. E. (2005). A tour of accelerated parallel MR imaging from a linear systems perspective. *Concept. Magn. Reson. A*, 27(1):17–37. (cited at pages 19 and 22)

Hosking, J. (1992). Moments or L moments? An example comparing two measures of distributional shape. *Am. Stat.*, 46(3):186–189. (cited at pages 71 and 108)

Jackson, J. I., Meyer, C. H., Nishimura, D. G., and Macovski, A. (1991). Selection of a convolution function for Fourier inversion using gridding [computerised tomography application]. *IEEE Trans. Med. Imag.*, 10(3):473–478. (cited at page 21)

Jeong, H.-K., Gore, J. C., and Anderson, A. W. (2013). High-resolution human diffusion tensor imaging using 2-D navigated multishot SENSE EPI at 7 T. *Magn. Reson. Med.*, 69(3):793–802. (cited at page 25)

Ji, J. X., Son, J. B., and Rane, S. D. (2007). PULSAR: A Matlab toolbox for parallel magnetic resonance imaging using array coils and multiple channel receivers. *Concept. Magn. Reson. B*, 31(1):24–36. (cited at page 112)

Jin, K. H., Lee, D., and Ye, J. C. (2015). A novel k-space annihilating filter method for unification between compressed sensing and parallel MRI. In *IEEE International Symposium on Biomedical Imaging (ISBI)*, pages 327–330. (cited at page 30)

Kay, S. M. (1993). *Fundamentals of statistical signal processing, volume I: Estimation theory.* Prentice Hall. (cited at pages 24, 25 and 27)

Koay, C. G. and Basser, P. J. (2006). Analytically exact correction scheme for signal extraction from noisy magnitude MR signals. *J. Magn. Reson.*, 179(2):317–322. (cited at pages 46, 47, 53, 75, 81, 105, 132 and 153)

Koay, C. G., Özarslan, E., and Basser, P. J. (2009a). A signal transformational framework for breaking the noise floor and its applications in MRI. *JMRI-J. Magn. Rreson. Im.*, 197(2):108–119. (cited at pages 103 and 104)

Koay, C. G., Özarslan, E., and Pierpaoli, C. (2009b). Probabilistic identification and estimation of noise (PIESNO): A self-consistent approach and its applications in MRI. *JMRI-J. Magn. Rreson. Im.*, 199(1):94–103. (cited at page 105)

Krissian, K. and Aja-Fernández, S. (2009). Noise-driven anisotropic diffusion filtering of MRI. *IEEE Trans. Image Process.*, 18(10):2265–2274. (cited at page 12)

Kyriakos, W. E., Panych, L. P., Kacher, D. F., Westin, C.-F., Bao, S. M., Mulkern, R. V., and Jolesz, F. A. (2000). Sensitivity profiles from an array of coils for encoding and reconstruction in parallel (SPACE RIP). *Magnet. Reson. Med.*, 44(2):301–308. (cited at page 30)

Landman, B. A., Bazin, P.-L., and Prince, J. L. (2009a). Estimation and application of spatially variable noise fields in diffusion tensor imaging. *Magn. Reson. Imaging*, 27(6):741–751. (cited at pages 45, 47, 48, 85 and 98)

Landman, B. A., Bazin, P.-L., Smith, S. A., and Prince, J. L. (2009b). Robust estimation of spatially variable noise fields. *Magn. Reson. Med.*, 62(2):500–509. (cited at pages 45, 47, 48, 52, 59, 60, 79, 86, 89, 90, 91, 92, 93, 94, 95, 96, 97, 154 and 155)

Larkman, D. J. and Nunes, R. G. (2007). Parallel magnetic resonance imaging. *Phys. Med. Biol.*, 52(7):R15. (cited at page 26)

Lauterbur, P. C. (1973). Image formation by induced local interactions: Examples employing nuclear magnetic resonance. *Nature*, 242:190–191. (cited at page 17)

Liang, D., Wang, H., Chang, Y., and Ying, L. (2011). Sensitivity encoding reconstruction with nonlocal total variation regularization. *Magn. Reson. Med.*, 65(5):1384–1392. (cited at page 27)

Ling, Q., Li, Z., Song, K., and Li, F. (2014). An iterative method for coil sensitivity estimation in multi-coil MRI systems. *Magn. Reson. Imaging*, 32(10):1365–1376. (cited at page 25)

Liu, B., King, K., Steckner, M., Xie, J., Sheng, J., and Ying, L. (2009). Regularized sensitivity encoding (SENSE) reconstruction using Bregman iterations. *Magn. Reson. Med.*, 61(1):145–152. (cited at pages 27 and 28)

Liu, R. W., Shi, L., Huang, W., Xu, J., Yu, S. C. H., and Wang, D. (2014). Generalized total variation-based MRI Rician denoising model with spatially adaptive regularization parameters. *Magn. Reson. Imaging*, 32(6):702–720. (cited at pages 47, 48, 55, 60, 85, 86, 89, 90, 91, 92, 93, 94, 95, 96, 97, 98, 154 and 155)

Lustig, M., Donoho, D., and Pauly, J. M. (2007). Sparse MRI: The application of compressed sensing for rapid MR imaging. *Magn. Reson. Med.*, 58(6):1182–1195. (cited at page 28)

Lustig, M. and Pauly, J. M. (2010). SPIRiT: Iterative self-consistent parallel imaging reconstruction from arbitrary k-space. *Magn. Reson. Med.*, 64(2):457–471. (cited at page 134)

Macovski, A. (1996). Noise in MRI. *Magn. Reson. Med.*, 36(3):494–497. (cited at page 10)

Maggioni, M. and Foi, A. (2012). Nonlocal transform-domain denoising of volumetric data with groupwise adaptive variance estimation. In *IS&T/SPIE Electronic Imaging*, pages 82960O–82960O–8. International Society for Optics and Photonics. (cited at pages 46, 48, 50, 54, 57, 60, 63, 85, 86, 89, 90, 91, 92, 93, 94, 95, 96, 97, 98, 112, 118, 121, 122, 123, 124, 125, 126, 128, 129, 154, 155, 157 and 158)

Maggioni, M., Katkovnik, V., Egiazarian, K., and Foi, A. (2013). Nonlocal transform-domain filter for volumetric data denoising and reconstruction. *IEEE Trans. Image Process.*, 22(1):119–133. (cited at pages 54, 67 and 133)

Makitalo, M. and Foi, A. (2011). Optimal inversion of the Anscombe transformation in low-count poisson image denoising. *IEEE Trans. Image Process.*, 20(1):99–109. (cited at page 67)

Mäkitalo, M. and Foi, A. (2013). Optimal inversion of the generalized Anscombe transformation for Poisson-Gaussian noise. *IEEE Trans. Image Process.*, 22(1):91–103. (cited at page 67)

Mallat, S. (2008). *A wavelet tour of signal processing: The sparse way.* Academic press. (cited at page 76)

Manjón, J. V., Coupé, P., and Buades, A. (2015). MRI noise estimation and denoising using non-local PCA. *Med. Imag. Anal.*, 22(1):35–47. (cited at pages 48, 49, 50, 57, 60, 63, 81, 85, 86, 89, 90, 91, 92, 93, 94, 95, 96, 97, 98, 132, 154 and 155)

Manjón, J. V., Coupé, P., Martí-Bonmatí, L., Collins, D. L., and Robles, M. (2010). Adaptive non-local means denoising of MR images with spatially varying noise levels. *JMRI-J. Magn. Reson. Im.*, 31(1):192–203. (cited at pages 12, 46, 48, 52, 55, 60, 79, 85, 86, 89, 90, 91, 92, 93, 94, 95, 97, 98, 154 and 155)

Mansfield, P. and Grannell, P. K. (1973). Nmr 'diffraction' in solids? *Journal of Physics C: Solid State Physics*, 6(22):422–426. (cited at page 17)

Martín-Fernández, M., Muñoz-Moreno, E., Cammoun, L., Thiran, J.-P., Westin, C.-F., and Alberola-López, C. (2009a). Addendum to sequential anisotropic multichannel Wiener filtering with Rician bias correction applied to 3D regularization of DWI data [Medical Image Analysis 13 (2009) 19-35]. *Med. Imag. Anal.*, 13(6). (cited at page 53)

Martín-Fernández, M., Muñoz-Moreno, E., Cammoun, L., Thiran, J.-P., Westin, C.-F., and Alberola-López, C. (2009b). Sequential anisotropic multichannel Wiener filtering with Rician bias correction applied to 3D regularization of DWI data. *Med. Imag. Anal.*, 13(1):19–35. (cited at page 53)

Marzetta, T. L. (1995). EM algorithm for estimating the parameters of a multivariate complex Rician density for polarimetric SAR. In *International Conference on Acoustics, Speech, and Signal Processing (ICASSP)*, volume 5, pages 3651–3654. (cited at pages 45, 48 and 50)

Materka, A. and Strzelecki, M. (2015). On the effect of image brightness and contrast nonuniformity on statistical texture parameters. *Found. Comput. Decision Sci.*, 40(3):163–185. (cited at page 134)

Maximov, I. I., Farrher, E., Grinberg, F., and Jon Shah, N. (2012). Spatially variable Rician noise in magnetic resonance imaging. *Med. Imag. Anal.*, 16(2):536–548. (cited at pages 46, 47, 48, 55, 59, 60, 85, 86, 89, 90, 91, 92, 93, 94, 95, 96, 97, 98, 154 and 155)

McRobbie, D. W., Moore, E. A., Graves, M. J., and Prince, M. R. (2003). *MRI from Picture to Proton*. Cambridge University Press. (cited at page 20)

McVeigh, E., Henkelman, R., and Bronskill, M. (1985). Noise and filtration in magnetic resonance imaging. *Med. Phys.*, 12(5):586–591. (cited at pages 10 and 34)

Moeller, S., Yacoub, E., Olman, C. A., Auerbach, E., Strupp, J., Harel, N., and Uğurbil, K. (2010). Multiband multislice GE-EPI at 7 Tesla, with 16-fold acceleration using partial parallel imaging with application to high spatial and temporal whole-brain fMRI. *Magn. Reson. Med.*, 63(5):1144–1153. (cited at page 25)

Muckley, M. J., Noll, D. C., Fessler, J., et al. (2015). Fast parallel MR image reconstruction via B1-based, adaptive restart, iterative soft thresholding algorithms (BARISTA). *IEEE Trans. Med. Imag.*, 34(2):578–588. (cited at page 25)

Nelder, J. A. and Mead, R. (1965). A simplex method for function minimization. *Comput. J.*, 7(4):308–313. (cited at page 71)

Pan, X., Zhang, X., and Lyu, S. (2012). Blind local noise estimation for medical images reconstructed from rapid acquisition. In *SPIE Medical Imaging*, pages 83143R–83143R. (cited at pages 46, 48, 54, 60, 63, 85, 86, 89, 90, 91, 92, 93, 94, 95, 96, 97, 98, 112, 118, 121, 122, 123, 124, 125, 126, 128, 129, 135, 154, 155, 157 and 158)

Parker, J. R. (1997). *Algorithms for image processing and computer vision.* John Wiley & Sons. (cited at page 63)

Pauluzzi, D. R. and Beaulieu, N. C. (2000). A comparison of SNR estimation techniques for the AWGN channel. *IEEE Trans. Commun.*, 48(10):1681–1691. (cited at page 54)

Peng, Z., Xu, Z., and Huang, J. (2016). RSPIRiT: Robust self-consistent parallel imaging reconstruction based on generalized LASSO. In *IEEE International Symposium on Biomedical Imaging (ISBI)*, pages 318–321. (cited at page 30)

Petr, J., Kybic, J., Bock, M., Müller, S., and Hlaváč, V. (2007). Parallel image reconstruction using b-spline approximation (PROBER). *Magnet. Reson. Med.*, 58(3):582–591. (cited at page 30)

PhilipsHealthcare (2012). dS-SENSE propels Ingenia's imaging speed. *FieldStrength*, 2(46):4. (cited at pages 25, 31 and 151)

Pieciak, T. (2014). The maximum spacing noise estimation in single-coil background MRI data. In *IEEE International Conference on Image Processing (ICIP)*, pages 1743–1747. (cited at pages 11 and 13)

Pieciak, T., Vegas-Sánchez-Ferrero, G., and Aja-Fernández, S. (2016a). Non-stationary Rician noise estimation in parallel MRI using a single image: A variance-stabilizing approach. *IEEE Trans. Pattern Anal. Mach. Intell.* (cited at page 13)

Pieciak, T., Vegas-Sánchez-Ferrero, G., and Aja-Fernández, S. (2016b). Variance stabilization of noncentral-Chi data: Application to noise estimation in MRI. In *IEEE International Symposium on Biomedical Imaging (ISBI)*, pages 1376–1379. (cited at page 13)

Polzehl, J. and Spokoiny, V. (2006). Propagation-separation approach for local likelihood estimation. *Probab. Theory Related Fields*, 135(3):335–362. (cited at pages 47 and 56)

Poot, D. and Klein, S. (2015). Detecting statistically significant differences in quantitative MRI experiments, applied to diffusion tensor imaging. *IEEE Trans. Med. Imag.*, 34(5):1164–1176. (cited at pages 48 and 49)

Porikli, F. (2008). Constant time O(1) bilateral filtering. In *IEEE Conference on Computer Vision and Pattern Recognition (CVPR)*, pages 1–8. IEEE. (cited at page 99)

Pruessmann, K. P., Weiger, M., Börnert, P., and Boesiger, P. (2001). Advances in sensitivity encoding with arbitrary k-space trajectories. *Magn. Reson. Med.*, 46(4):638–651. (cited at page 28)

Pruessmann, K. P., Weiger, M., Scheidegger, M. B., Boesiger, P., et al. (1999). SENSE: Sensitivity encoding for fast MRI. *Magn. Reson. Med.*, 42(5):952–962. (cited at pages 11, 26, 27 and 28)

Purcell, E. M., Torrey, H., and Pound, R. V. (1946). Resonance absorption by nuclear magnetic moments in a solid. *Phys. Rev.*, 69(1-2):37. (cited at page 17)

Pyatykh, S. and Hesser, J. (2014). Image sensor noise parameter estimation by variance stabilization and normality assessment. *IEEE Trans. Image Process.*, 23(9):3990–3998. (cited at page 67)

Rajan, J., Poot, D., Juntu, J., and Sijbers, J. (2011). Maximum likelihood estimation-based denoising of magnetic resonance images using restricted local neighborhoods. *Phys. Med. Biol.*, 56(16):5221–5234. (cited at pages 46, 48, 50, 53, 60, 63, 85, 90, 91, 92, 93, 94, 95, 96, 97, 98, 154 and 155)

Rajan, J., Veraart, J., Van Audekerke, J., Verhoye, M., and Sijbers, J. (2012). Nonlocal maximum likelihood estimation method for denoising multiple-coil magnetic resonance images. *Magn. Reson. Med.*, 30(10):1512–1518. (cited at pages 105 and 111)

Reichenbach, A., Hlawitschka, M., Tittgemeyer, M., and Scheuermann, G. (2014). Choosing a tractography algorithm: On the effects of measurement noise. In *Computational Diffusion MRI and Brain Connectivity*, pages 115–128. Springer. (cited at page 10)

Rice, S. O. (1944). Mathematical analysis of random noise. *Bell Syst. Tech. J.*, 23(3):282–332. (cited at page 36)

Roemer, P. B., Edelstein, W. A., Hayes, C. E., Souza, S. P., and Mueller, O. M. (1990). The NMR phased array. *Magn. Reson. Med.*, 16(2):192–225. (cited at pages 21 and 23)

Rohde, G. K., Barnett, A. S., Basser, P. J., and Pierpaoli, C. (2005). Estimating intensity variance due to noise in registered images: Applications to diffusion tensor MRI. *NeuroImage*, 26(3):673–684. (cited at page 10)

Romano, Y. and Elad, M. (2015). Boosting of image denoising algorithms. *SIAM J. Imaging Sci.*, 8(2):1187–1219. (cited at page 76)

Rousseeuw, P. J. and Croux, C. (1993). Alternatives to the median absolute deviation. *J. Amer. Statist. Assoc.*, 88(424):1273–1283. (cited at pages 45 and 52)

Roy, S., Carass, A., Bazin, P.-L., Resnick, S., and Prince, J. L. (2012). Consistent segmentation using a Rician classifier. *Med. Imag. Anal.*, 16(2):524–535. (cited at page 12)

Royuela-Del-Val, J., Cordero-Grande, L., Simmross-Wattenberg, F., Martín-Fernández, M., and Alberola-López, C. (2016). Jacobian weighted temporal total variation for motion compensated compressed sensing reconstruction of dynamic MRI. *Magn. Reson. Med.* (cited at page 32)

Sabati, M., Peng, H., Lauzon, M. L., and Frayne, R. (2013). A statistical method for characterizing the noise in nonlinearly reconstructed images from undersampled MR data: The POCS example. *Magn. Reson. Imaging*, 31(9):1587–1598. (cited at pages 43 and 133)

Samsonov, A. A. and Johnson, C. R. (2004). Noise-adaptive nonlinear diffusion filtering of MR images with spatially varying noise levels. *Magn. Reson. Med.*, 52(4):798–806. (cited at pages 45 and 48)

Sandino, C. M., Kellman, P., Arai, A. E., Hansen, M. S., and Xue, H. (2015). Myocardial T2* mapping: Influence of noise on accuracy and precision. *J. Cardiovasc. Magn. Reson.*, 17(1):7. (cited at page 10)

Sedarat, H. and Nishimura, D. G. (2000). On the optimality of the gridding reconstruction algorithm. *IEEE Trans. Med. Imag.*, 19(4):306–317. (cited at page 21)

Shafiee, M., Haider, S., Wong, A., Lui, D., Cameron, A., Modhafar, A., Fieguth, P., and Haider, M. (2015). Apparent ultra-high b-value diffusion-weighted image reconstruction via hidden conditional random fields. *IEEE Trans. Med. Imag.*, 34(5):1111–1124. (cited at page 67)

Shampine, L. F. (2008). Vectorized adaptive quadrature in MATLAB. *J. Comput. Appl. Math.*, 211(2):131–140. (cited at page 71)

Shnidman, D. A. (1989). The calculation of the probability of detection and the generalized Marcum Q-function. *IEEE Trans. Inf. Theory*, 35(2):389–400. (cited at page 105)

Sijbers, J. and Dekker, A. D. (2004). Maximum likelihood estimation of signal amplitude and noise variance from MR data. *Magn. Reson. Med.*, 51(3):586–594. (cited at pages 46, 48 and 53)

Sijbers, J., den Dekker, A., Scheunders, P., and Dyck, D. V. (1998). Maximum-likelihood estimation of Rician distribution parameters. *IEEE Trans. Med. Imag.*, 17(3):357–361. (cited at pages 36 and 46)

Simon, M. K. (2007). *Probability distributions involving Gaussian random variables: A handbook for engineers and scientists*. Springer Science & Business Media. (cited at page 106)

Sloane, N. J. et al. (2003). The on-line encyclopedia of integer sequences. (cited at page 105)

Sodickson, D. K. and Manning, W. J. (1997). Simultaneous acquisition of spatial harmonics (SMASH): Fast imaging with radiofrequency coil arrays. *Magn. Reson. Med.*, 38(4):591–603. (cited at pages 19, 20 and 30)

Tabelow, K., Voss, H. U., and Polzehl, J. (2015). Local estimation of the noise level in MRI using structural adaptation. *Med. Imag. Anal.*, 20(1):76–86. (cited at pages 47, 48, 50, 56, 60, 63, 85, 86, 89, 90, 91, 92, 93, 94, 95, 97, 98, 105, 112, 113, 118, 121, 122, 123, 124, 129, 154, 155 and 157)

Thompson, W. H. and Fransson, P. (2016). On stabilizing the variance of dynamic functional brain connectivity time series. *arXiv preprint arXiv:1603.00201*. (cited at page 67)

Tomasi, C. and Manduchi, R. (1998). Bilateral filtering for gray and color images. In *Sixth International Conference on Computer Vision (ICCV*, pages 839–846. (cited at page 76)

Trefethen, L. N. and Bau III, D. (1997). *Numerical linear algebra*, volume 50. SIAM. (cited at page 24)

Triantafyllou, C., Polimeni, J. R., and Wald, L. L. (2011). Physiological noise and signal-to-noise ratio in fMRI with multi-channel array coils. *NeuroImage*, 55(2):597–606. (cited at page 10)

Tristán-Vega, A. and Aja-Fernández, S. (2010). DWI filtering using joint information for DTI and HARDI. *Med. Imag. Anal.*, 14(2):205–218. (cited at page 12)

Tristán-Vega, A., Aja-Fernández, S., and Westin, C.-F. (2012a). Least squares for diffusion tensor estimation revisited: Propagation of uncertainty with Rician and non-Rician signals. *NeuroImage*, 59(4):4032–4043. (cited at pages 10 and 134)

Tristán-Vega, A., García-Pérez, V., Aja-Fernández, S., and Westin, C.-F. (2012b). Efficient and robust nonlocal means denoising of MR data based on salient features matching. *Comput. Meth. Prog. Bio.*, 105(2):131–144. (cited at page 12)

Tristan-Vega, A., Westin, C.-F., and Aja-Fernandez, S. (2010). A new methodology for the estimation of fiber populations in the white matter of the brain with the Funk–Radon transform. *NeuroImage*, 49(2):1301–1315. (cited at page 12)

Uecker, M., Lai, P., Murphy, M. J., Virtue, P., Elad, M., Pauly, J. M., Vasanawala, S. S., and Lustig, M. (2014). ESPIRiT–An eigenvalue approach to autocalibrating parallel MRI: Where SENSE meets GRAPPA. *Magn. Reson. Med.*, 71(3):990–1001. (cited at pages 25 and 30)

Van Albada, S. and Robinson, P. (2007). Transformation of arbitrary distributions to the normal distribution with application to EEG test–retest reliability. *J. Neurosci. Methods*, 161(2):205–211. (cited at page 103)

Vandendorpe, L. (1995). Multitone spread spectrum multiple access communications system in a multipath rician fading channel. *IEEE Trans. Veh. Technol.*, 44(2):327–337. (cited at page 100)

Varadarajan, D. and Haldar, J. P. (2015). A majorize-minimize framework for Rician and Non-central chi MR images. *IEEE Trans. Med. Imag.*, 34(10):2191–2202. (cited at pages 12 and 111)

Vegas-Sánchez-Ferrero, G., Tristán-Vega, A., Aja-Fernández, S., Martín-Fernández, M., Palencia, C., and Deriche, R. (2012). Anisotropic LMMSE denoising of MRI based on statistical tissue models. In *IEEE International Symposium on Biomedical Imaging (ISBI)*, pages 1519–1522. (cited at page 105)

Veraart, J., Fieremans, E., and Novikov, D. (2016). Diffusion MRI noise mapping using random matrix theory. *Magn. Reson. Med.* (cited at pages 47 and 48)

Veraart, J., Rajan, J., Peeters, R. R., Leemans, A., Sunaert, S., and Sijbers, J. (2013). Comprehensive framework for accurate diffusion MRI parameter estimation. *Magn. Reson. Med.*, 70(4):972–984. (cited at pages 12, 47, 48 and 129)

Veraart, J., Van Hecke, W., and Sijbers, J. (2011). Constrained maximum likelihood estimation of the diffusion kurtosis tensor using a Rician noise model. *Magn. Reson. Med.*, 66(3):678–686. (cited at page 12)

Vovk, U., Pernuš, F., and Likar, B. (2007). A review of methods for correction of intensity inhomogeneity in MRI. *IEEE Trans. Med. Imag.*, 26(3):405–421. (cited at page 134)

Vymazal, J. (2004). *Cardiovascular MRI: Angiography and perfusion studies with 1-molar Gadolinium-Based Contrast Agent.* MEDCORE Europe Publisher, Prague. (cited at page 20)

Walsh, D. O., Gmitro, A. F., and Marcellin, M. W. (2000). Adaptive reconstruction of phased array MR imagery. *Magn. Reson. Med.*, 43(5):682–690. (cited at page 24)

Wang, Y. (2000). Description of parallel imaging in MRI using multiple coils. *Magn. Reson. Med.*, 44(3):495–499. (cited at page 22)

Weiger, M., Pruessmann, K. P., and Boesiger, P. (2002). 2D SENSE for faster 3D MRI. *Magn. Reson. Mater. Phy.*, 14(1):10–19. (cited at page 28)

Weiss, B. (2006). Fast median and bilateral filtering. *ACM Transactions on Graphics (TOG)*, 25(3):519–526. (cited at page 99)

Weller, D. S., Ramani, S., Fessler, J., et al. (2014). Augmented Lagrangian with variable splitting for faster non-Cartesian-SPIRiT MR image reconstruction. *IEEE Trans. Med. Imag.*, 33(2):351–361. (cited at page 134)

Wright, K. L., Hamilton, J. I., Griswold, M. A., Gulani, V., and Seiberlich, N. (2014). Non-Cartesian parallel imaging reconstruction. *JMRI-J. Magn. Reson. Im.*, 40(5):1022–1040. (cited at pages 28 and 134)

Yang, J., Fan, J., Ai, D., Zhou, S., Tang, S., and Wang, Y. (2015). Brain MR image denoising for Rician noise using pre-smooth non-local means filter. *Biomed. Eng. OnLine*, 14(2):1–20. (cited at pages 67 and 133)

Ying, L. and Liang, Z.-P. (2010). Parallel MRI using phased array coils. *IEEE Signal Proc. Mag.*, 27(4):90–98. (cited at pages 19, 20 and 35)

Ying, L. and Sheng, J. (2007). Joint image reconstruction and sensitivity estimation in SENSE (JSENSE). *Magn. Reson. Med.*, 57(6):1196–1202. (cited at page 28)

Ying, L., Xu, D., and Liang, Z.-P. (2004). On Tikhonov regularization for image reconstruction in parallel MRI. In *Annual International Conference of the IEEE Engineering in Medicine and Biology Society (EMBC)*, volume 1, pages 1056–1059. (cited at pages 27 and 28)

Yu, J., Agarwal, H., Stuber, M., and Schär, M. (2011). Practical signal-to-noise ratio quantification for sensitivity encoding: Application to coronary MR angiography. *J. Magn. Reson. Imaging*, 33(6):1330–1340. (cited at pages 10 and 12)

Zemliachenko, A. N., Kozhemiakin, R. A., Uss, M. L., Abramov, S. K., Ponomarenko, N. N., Lukin, V. V., Vozel, B., and Chehdi, K. (2014). Lossy compression of hyperspectral images based on noise parameters estimation and variance stabilizing transform. *J. Appl. Remote Sens.*, 8(1):083571–083571. (cited at page 67)

Zhang, B., Fadili, J. M., and Starck, J.-L. (2008). Wavelets, ridgelets, and curvelets for Poisson noise removal. *IEEE Trans. Image Process.*, 17(7):1093–1108. (cited at page 67)

Zhang, J., Hirakawa, K., and Jin, X. (2015a). Quantile analysis of image sensor noise distribution. In *IEEE International Conference on Acoustics, Speech and Signal Processing (ICASSP)*, pages 1598–1602. (cited at page 67)

Zhang, X., Xu, Z., Jia, N., Yang, W., Feng, Q., Chen, W., and Feng, Y. (2015b). Denoising of 3D magnetic resonance images by using higher-order singular value decomposition. *Med. Imag. Anal.*, 19(1):75–86. (cited at pages 67 and 133)

Zhang, Y., Brady, M., and Smith, S. (2001). Segmentation of brain MR images through a hidden Markov random field model and the expectation-maximization algorithm. *IEEE Trans. Med. Imag.*, 20(1):45–57. (cited at page 10)

Zoran, D. and Weiss, Y. (2009). Scale invariance and noise in natural images. In *IEEE International Conference on Computer Vision (ICCV)*, pages 2209–2216. (cited at page 46)

Zwillinger, D. (2014). *Table of integrals, series, and products.* Elsevier. (cited at pages 36 and 39)

List of Figures

List of Tables

Academic overview of the author

The author of the thesis spent eight months in **Laboratorio de Procesado de Imagen** (LPI) research team under the supervision of **Santiago Aja-Fernández, Ph.D**. During the stays at LPI (2014, 2015), the author was working on parallel accelerated magnetic resonance imaging techniques and non-stationary noise estimation algorithms intended for accelerated parallel MRI.

The author of the thesis took part in the following workshops and summer school lectures connected with the topics presented in the thesis:

1. *Designing Benchmarks and Challenges for Measuring Algorithm Performance in Biomedical Image Analysis* – by Michal Kozubek, April 13th–16th, 2016, Prague, Czech Republic.

2. *MRI simulation for sequence development, protocol optimisation, and education* – by Lars G. Hanson and Tony Stöcker. An official European Society of Magnetic Resonance in Medicine (ESMRM) course, June 29th–July 1st, 2015, Copenhagen, Denmark.

3. *Signal-Dependent noise and stabilization of variance* by Alessandro Foi, October 27th–30th, 2014, Paris, France,

4. *Quantitative analysis in cellular and biomedical imaging* by Jean-Christophe Olivo-Marin and Habib Zaidi, October 27th–30th, 2014, Paris, France,

5. Cardiac Imaging Workshop – CT, MRI, SPECT and PET, June 21th, 2013, Cracow, Poland.

Awards:

- *IEEE Signal Processing Society Travel Grant* – a highly competitive IEEE Signal Processing Society Travel Grant to attend IEEE International Conference on Image Processing, Paris, 2014.

The author of the thesis is **a reviewer** for the following scientific journals:

1. Magnetic Resonance in Medicine (Wiley, Impact factor: 3.571),

2. Pattern Analysis and Applications (Springer, Impact factor: 0.646).